UNITED STATES AIR FORCE

SUMMER RESEARCH PROGRAM -- 1997

GRADUATE STUDENT RESEARCH PROGRAM FINAL REPORTS

VOLUME 10B

WRIGHT LABORATORY

RESEARCH & DEVELOPMENT LABORATORIES

5800 Uplander Way

Culver City, CA 90230-6608

Program Director, RDL
Gary Moore

Program Manager, AFOSR
Major Linda Steel-Goodwin

Program Manager, RDL
Scott Licoscos

Program Administrator, RDL
Johnetta Thompson

Program Administrator, RDL
Rebecca Kelly

Submitted to:

AIR FORCE OFFICE OF SCIENTIFIC RESEARCH

Bolling Air Force Base

Washington, D.C.

December 1997

REPORT DOCUMENTATION PAGE

AFRL-SR-BL-TR-00-
0766

1. AGENCY USE ONLY *(Leave blank)*	2. REPORT DATE
	December, 1997

4. TITLE AND SUBTITLE
1997 Summer Research Program (SRP), Graduate Student Research Program (GSRP), Final Reports, Volume 10B, Wright Laboratory

5. FUNDING NUMBERS
F49620-93-C-0063

6. AUTHOR(S)
Gary Moore

7. PERFORMING ORGANIZATION NAME(S) AND ADDRESS(ES)
Research & Development Laboratories (RDL)
5800 Uplander Way
Culver City, CA 90230-6608

8. PERFORMING ORGANIZATION REPORT NUMBER

9. SPONSORING/MONITORING AGENCY NAME(S) AND ADDRESS(ES)
Air Force Office of Scientific Research (AFOSR)
801 N. Randolph St.
Arlington, VA 22203-1977

10. SPONSORING/MONITORING AGENCY REPORT NUMBER

11. SUPPLEMENTARY NOTES

12a. DISTRIBUTION AVAILABILITY STATEMENT
Approved for Public Release

12b. DISTRIBUTION CODE

13. ABSTRACT *(Maximum 200 words)*

The United States Air Force Summer Research Program (USAF-SRP) is designed to introduce university, college, and technical institute faculty members, graduate students, and high school students to Air Force research. This is accomplished by the faculty members (Summer Faculty Research Program, (SFRP)), graduate students (Graduate Student Research Program (GSRP)), and high school students (High School Apprenticeship Program (HSAP)) being selected on a nationally advertised competitive basis during the summer intersession period to perform research at Air Force Research Laboratory (AFRL) Technical Directorates, Air Force Air Logistics Centers (ALC), and other AF Laboratories. This volume consists of a program overview, program management statistics, and the final technical reports from the GSRP participants at the Wright Laboratory.

14. SUBJECT TERMS
Air Force Research, Air Force, Engineering, Laboratories, Reports, Summer, Universities, Faculty, Graduate Student, High School Student

15. NUMBER OF PAGES

16. PRICE CODE

17. SECURITY CLASSIFICATION OF REPORT	18. SECURITY CLASSIFICATION OF THIS PAGE	19. SECURITY CLASSIFICATION OF ABSTRACT	20. LIMITATION OF ABSTRACT
Unclassified	Unclassified	Unclassified	UL

PREFACE

Reports in this volume are numbered consecutively beginning with number 1. Each report is paginated with the report number followed by consecutive page numbers, e.g., 1-1, 1-2, 1-3; 2-1, 2-2, 2-3.

Due to its length, Volume 10A is bound in two parts, 10A and 10B. Volume 10A contains #1-17. Volume 10B contains reports #18-35. The Table of Contents for Volume 10 is included in all parts.

This document is one of a set of 16 volumes describing the 1997 AFOSR Summer Research Program. The following volumes comprise the set:

VOLUME	TITLE
1	Program Management Report
	Summer Faculty Research Program (SFRP) Reports
2A & 2B	Armstrong Laboratory
3A & 3B	Phillips Laboratory
4A & 4B	Rome Laboratory
5A , 5B & 5C	Wright Laboratory
6	Arnold Engineering Development Center, United States Air Force Academy and Air Logistics Centers
	Graduate Student Research Program (GSRP) Reports
7A & 7B	Armstrong Laboratory
8	Phillips Laboratory
9	Rome Laboratory
10A & 10B	Wright Laboratory
11	Arnold Engineering Development Center, Wilford Hall Medical Center and Air Logistics Centers
	High School Apprenticeship Program (HSAP) Reports
12A & 12B	Armstrong Laboratory
13	Phillips Laboratory
14	Rome Laboratory
15B&15B	Wright Laboratory
16	Arnold Engineering Development Center

SRP Final Report Table of Contents

SRP Final Report Table of Contents

SRP Final Report Table of Contents

SRP Final Report Table of Contents

SRP Final Report Table of Contents

SRP Final Report Table of Contents

SRP Final Report Table of Contents

SRP Final Report Table of Contents

SRP Final Report Table of Contents

SRP Final Report Table of Contents

SRP Final Report Table of Contents

1. INTRODUCTION

The Summer Research Program (SRP), sponsored by the Air Force Office of Scientific Research (AFOSR), offers paid opportunities for university faculty, graduate students, and high school students to conduct research in U.S. Air Force research laboratories nationwide during the summer.

Introduced by AFOSR in 1978, this innovative program is based on the concept of teaming academic researchers with Air Force scientists in the same disciplines using laboratory facilities and equipment not often available at associates' institutions.

The Summer Faculty Research Program (SFRP) is open annually to approximately 150 faculty members with at least two years of teaching and/or research experience in accredited U.S. colleges, universities, or technical institutions. SFRP associates must be either U.S. citizens or permanent residents.

The Graduate Student Research Program (GSRP) is open annually to approximately 100 graduate students holding a bachelor's or a master's degree; GSRP associates must be U.S. citizens enrolled full time at an accredited institution.

The High School Apprentice Program (HSAP) annually selects about 125 high school students located within a twenty mile commuting distance of participating Air Force laboratories.

AFOSR also offers its research associates an opportunity, under the Summer Research Extension Program (SREP), to continue their AFOSR-sponsored research at their home institutions through the award of research grants. In 1994 the maximum amount of each grant was increased from $20,000 to $25,000, and the number of AFOSR-sponsored grants decreased from 75 to 60. A separate annual report is compiled on the SREP.

The numbers of projected summer research participants in each of the three categories and SREP "grants" are usually increased through direct sponsorship by participating laboratories.

AFOSR's SRP has well served its objectives of building critical links between Air Force research laboratories and the academic community. opening avenues of communications and forging new research relationships between Air Force and academic technical experts in areas of national interest, and strengthening the nation's efforts to sustain careers in science and engineering. The success of the SRP can be gauged from its growth from inception (see Table 1) and from the favorable responses the 1997 participants expressed in end-of-tour SRP evaluations (Appendix B).

AFOSR contracts for administration of the SRP by civilian contractors. The contract was first awarded to Research & Development Laboratories (RDL) in September 1990. After completion of the

1990 contract, RDL (in 1993) won the recompetition for the basic year and four 1-year options.

2. PARTICIPATION IN THE SUMMER RESEARCH PROGRAM

The SRP began with faculty associates in 1979; graduate students were added in 1982 and high school students in 1986. The following table shows the number of associates in the program each year.

YEAR	SRP Participation, by Year			TOTAL
	SFRP	GSRP	HSAP	
1979	70			70
1980	87			87
1981	87			87
1982	91	17		108
1983	101	53		154
1984	152	84		236
1985	154	92		246
1986	158	100	42	300
1987	159	101	73	333
1988	153	107	101	361
1989	168	102	103	373
1990	165	121	132	418
1991	170	142	132	444
1992	185	121	159	464
1993	187	117	136	440
1994	192	117	133	442
1995	190	115	137	442
1996	188	109	138	435
1997	148	98	140	427

Beginning in 1993, due to budget cuts, some of the laboratories weren't able to afford to fund as many associates as in previous years. Since then, the number of funded positions has remained fairly constant at a slightly lower level.

3. RECRUITING AND SELECTION

The SRP is conducted on a nationally advertised and competitive-selection basis. The advertising for faculty and graduate students consisted primarily of the mailing of 8,000 52-page SRP brochures to chairpersons of departments relevant to AFOSR research and to administrators of grants in accredited universities, colleges, and technical institutions. Historically Black Colleges and Universities (HBCUs) and Minority Institutions (MIs) were included. Brochures also went to all participating USAF laboratories, the previous year's participants, and numerous individual requesters (over 1000 annually).

RDL placed advertisements in the following publications: *Black Issues in Higher Education, Winds of Change,* and *IEEE Spectrum.* Because no participants list either *Physics Today* or *Chemical & Engineering News* as being their source of learning about the program for the past several years, advertisements in these magazines were dropped, and the funds were used to cover increases in brochure printing costs.

High school applicants can participate only in laboratories located no more than 20 miles from their residence. Tailored brochures on the HSAP were sent to the head counselors of 180 high schools in the vicinity of participating laboratories, with instructions for publicizing the program in their schools. High school students selected to serve at Wright Laboratory's Armament Directorate (Eglin Air Force Base, Florida) serve eleven weeks as opposed to the eight weeks normally worked by high school students at all other participating laboratories.

Each SFRP or GSRP applicant is given a first, second, and third choice of laboratory. High school students who have more than one laboratory or directorate near their homes are also given first, second, and third choices.

Laboratories make their selections and prioritize their nominees. AFOSR then determines the number to be funded at each laboratory and approves laboratories' selections.

Subsequently, laboratories use their own funds to sponsor additional candidates. Some selectees do not accept the appointment, so alternate candidates are chosen. This multi-step selection procedure results in some candidates being notified of their acceptance after scheduled deadlines. The total applicants and participants for 1997 are shown in this table.

1997 Applicants and Participants			
PARTICIPANT CATEGORY	TOTAL APPLICANTS	SELECTEES	DECLINING SELECTEES
SFRP	490	188	32
(HBCU/MI)	(0)	(0)	(0)
GSRP	202	98	9
(HBCU/MI)	(0)	(0)	(0)
HSAP	433	140	14
TOTAL	1125	426	55

4. SITE VISITS

During June and July of 1997, representatives of both AFOSR/NI and RDL visited each participating laboratory to provide briefings, answer questions. and resolve problems for both laboratory personnel and participants. The objective was to ensure that the SRP would be as constructive as possible for all participants. Both SRP participants and RDL representatives found these visits beneficial. At many of the laboratories, this was the only opportunity for all participants to meet at one time to share their experiences and exchange ideas.

5. HISTORICALLY BLACK COLLEGES AND UNIVERSITIES AND MINORITY INSTITUTIONS (HBCU/MIs)

Before 1993, an RDL program representative visited from seven to ten different HBCU/MIs annually to promote interest in the SRP among the faculty and graduate students. These efforts were marginally effective, yielding a doubling of HBCI/MI applicants. In an effort to achieve AFOSR's goal of 10% of all applicants and selectees being HBCU/MI qualified, the RDL team decided to try other avenues of approach to increase the number of qualified applicants. Through the combined efforts of the AFOSR Program Office at Bolling AFB and RDL, two very active minority groups were found, HACU (Hispanic American Colleges and Universities) and AISES (American Indian Science and Engineering Society). RDL is in communication with representatives of each of these organizations on a monthly basis to keep up with the their activities and special events. Both organizations have widely-distributed magazines/quarterlies in which RDL placed ads.

Since 1994 the number of both SFRP and GSRP HBCU/MI applicants and participants has increased ten-fold, from about two dozen SFRP applicants and a half dozen selectees to over 100 applicants and two dozen selectees, and a half-dozen GSRP applicants and two or three selectees to 18 applicants and 7 or 8 selectees. Since 1993, the SFRP had a two-fold applicant increase and a two-fold selectee increase. Since 1993, the GSRP had a three-fold applicant increase and a three to four-fold increase in selectees.

In addition to RDL's special recruiting efforts, AFOSR attempts each year to obtain additional funding or use leftover funding from cancellations the past year to fund HBCU/MI associates. This year, 5 HBCU/MI SFRPs declined after they were selected (and there was no one qualified to replace them with). The following table records HBCU/MI participation in this program.

SRP HBCU/MI Participation, By Year				
YEAR	SFRP		GSRP	
	Applicants	Participants	Applicants	Participants
1985	76	23	15	11
1986	70	18	20	10
1987	82	32	32	10
1988	53	17	23	14
1989	39	15	13	4
1990	43	14	17	3
1991	42	13	8	5
1992	70	13	9	5
1993	60	13	6	2
1994	90	16	11	6
1995	90	21	20	8
1996	119	27	18	7

6. SRP FUNDING SOURCES

Funding sources for the 1997 SRP were the AFOSR-provided slots for the basic contract and laboratory funds. Funding sources by category for the 1997 SRP selected participants are shown here.

1997 SRP FUNDING CATEGORY	SFRP	GSRP	HSAP
AFOSR Basic Allocation Funds	141	89	123
USAF Laboratory Funds	48	9	17
HBCU/MI By AFOSR (Using Procured Addn'l Funds)	0	0	N/A
TOTAL	9	98	140

SFRP - 188 were selected, but thirty two canceled too late to be replaced.
GSRP - 98 were selected, but nine canceled too late to be replaced.
HSAP - 140 were selected, but fourteen canceled too late to be replaced.

7. COMPENSATION FOR PARTICIPANTS

Compensation for SRP participants, per five-day work week, is shown in this table.

1997 SRP Associate Compensation

PARTICIPANT CATEGORY	1991	1992	1993	1994	1995	1996	1997
Faculty Members	$690	$718	$740	$740	$740	$770	$770
Graduate Student (Master's Degree)	$425	$442	$455	$455	$455	$470	$470
Graduate Student (Bachelor's Degree)	$365	$380	$391	$391	$391	$400	$400
High School Student (First Year)	$200	$200	$200	$200	$200	$200	$200
High School Student (Subsequent Years)	$240	$240	$240	$240	$240	$240	$240

The program also offered associates whose homes were more than 50 miles from the laboratory an expense allowance (seven days per week) of $50/day for faculty and $40/day for graduate students. Transportation to the laboratory at the beginning of their tour and back to their home destinations at the end was also reimbursed for these participants. Of the combined SFRP and GSRP associates, 65 % (194 out of 286) claimed travel reimbursements at an average round-trip cost of $776.

Faculty members were encouraged to visit their laboratories before their summer tour began. All costs of these orientation visits were reimbursed. Forty-three percent (85 out of 188) of faculty associates took orientation trips at an average cost of $388. By contrast, in 1993, 58 % of SFRP associates took

orientation visits at an average cost of $685; that was the highest percentage of associates opting to take an orientation trip since RDL has administered the SRP, and the highest average cost of an orientation trip. These 1993 numbers are included to show the fluctuation which can occur in these numbers for planning purposes.

Program participants submitted biweekly vouchers countersigned by their laboratory research focal point, and RDL issued paychecks so as to arrive in associates' hands two weeks later.

This is the second year of using direct deposit for the SFRP and GSRP associates. The process went much more smoothly with respect to obtaining required information from the associates, only 7% of the associates' information needed clarification in order for direct deposit to properly function as opposed to 10% from last year. The remaining associates received their stipend and expense payments via checks sent in the US mail.

HSAP program participants were considered actual RDL employees, and their respective state and federal income tax and Social Security were withheld from their paychecks. By the nature of their independent research, SFRP and GSRP program participants were considered to be consultants or independent contractors. As such, SFRP and GSRP associates were responsible for their own income taxes, Social Security, and insurance.

8. CONTENTS OF THE 1997 REPORT

The complete set of reports for the 1997 SRP includes this program management report (Volume 1) augmented by fifteen volumes of final research reports by the 1997 associates, as indicated below:

1997 SRP Final Report Volume Assignments

LABORATORY	SFRP	GSRP	HSAP
Armstrong	2	7	12
Phillips	3	8	13
Rome	4	9	14
Wright	5A, 5B	10	15
AEDC, ALCs, WHMC	6	11	16

APPENDIX A -- PROGRAM STATISTICAL SUMMARY

A. Colleges/Universities Represented

Selected SFRP associates represented 169 different colleges, universities, and institutions, GSRP associates represented 95 different colleges, universities, and institutions.

B. States Represented

SFRP -Applicants came from 47 states plus Washington D.C. Selectees represent 44 states.

GSRP - Applicants came from 44 states. Selectees represent 32 states.

HSAP - Applicants came from thirteen states. Selectees represent nine states.

Total Number of Participants	
SFRP	189
GSRP	97
HSAP	140
TOTAL	426

Degrees Represented			
	SFRP	GSRP	TOTAL
Doctoral	184	0	184
Master's	2	41	43
Bachelor's	0	56	56
TOTAL	186	97	298

SFRP Academic Titles	
Assistant Professor	64
Associate Professor	70
Professor	40
Instructor	0
Chairman	1
Visiting Professor	1
Visiting Assoc. Prof.	1
Research Associate	9
TOTAL	186

Source of Learning About the SRP		
Category	Applicants	Selectees
Applied/participated in prior years	28%	34%
Colleague familiar with SRP	19%	16%
Brochure mailed to institution	23%	17%
Contact with Air Force laboratory	17%	23%
IEEE Spectrum	2%	1%
BIIHE	1%	1%
Other source	10%	8%
TOTAL	100%	100%

APPENDIX B -- SRP EVALUATION RESPONSES

1. OVERVIEW

Evaluations were completed and returned to RDL by four groups at the completion of the SRP. The number of respondents in each group is shown below.

Table B-1. Total SRP Evaluations Received

Evaluation Group	Responses
SFRP & GSRPs	275
HSAPs	113
USAF Laboratory Focal Points	84
USAF Laboratory HSAP Mentors	6

All groups indicate unanimous enthusiasm for the SRP experience.

The summarized recommendations for program improvement from both associates and laboratory personnel are listed below:

A. Better preparation on the labs' part prior to associates' arrival (i.e., office space, computer assets, clearly defined scope of work).

B. Faculty Associates suggest higher stipends for SFRP associates.

C. Both HSAP Air Force laboratory mentors and associates would like the summer tour extended from the current 8 weeks to either 10 or 11 weeks; the groups state it takes 4-6 weeks just to get high school students up-to-speed on what's going on at laboratory. (Note: this same argument was used to raise the faculty and graduate student participation time a few years ago.)

2. 1997 USAF LABORATORY FOCAL POINT (LFP) EVALUATION RESPONSES

The summarized results listed below are from the 84 LFP evaluations received.

1. LFP evaluations received and associate preferences:

Table B-2. Air Force LFP Evaluation Responses (By Type)

		How Many Associates Would You Prefer To Get ? (% Response)											
		SFRP				GSRP (w/Univ Professor)				GSRP (w/o Univ Professor)			
Lab	Evals Recv'd	0	1	2	3+	0	1	2	3+	0	1	2	3+
AEDC	0	-	-	-	-	-	-	-	-	-	-	-	-
WHMC	0	-	-	-	-	-	-	-	-	-	-	-	-
AL	7	28	28	28	14	54	14	28	0	86	0	14	0
USAFA	1	0	100	0	0	100	0	0	0	0	100	0	0
PL	25	40	40	16	4	88	12	0	0	84	12	4	0
RL	5	60	40	0	0	80	10	0	0	100	0	0	0
WL	46	30	43	20	6	78	17	4	0	93	4	2	0
Total	84	32%	50%	13%	5%	80%	11%	6%	0%	73%	23%	4%	0%

LFP Evaluation Summary. The summarized responses, by laboratory, are listed on the following page. LFPs were asked to rate the following questions on a scale from 1 (below average) to 5 (above average).

2. LFPs involved in SRP associate application evaluation process:
   a. Time available for evaluation of applications:
   b. Adequacy of applications for selection process:
3. Value of orientation trips:
4. Length of research tour:
5. a. Benefits of associate's work to laboratory:
   b. Benefits of associate's work to Air Force:
6. a. Enhancement of research qualifications for LFP and staff:
   b. Enhancement of research qualifications for SFRP associate:
   c. Enhancement of research qualifications for GSRP associate:
7. a. Enhancement of knowledge for LFP and staff:
   b. Enhancement of knowledge for SFRP associate:
   c. Enhancement of knowledge for GSRP associate:
8. Value of Air Force and university links:
9. Potential for future collaboration:
10. a. Your working relationship with SFRP:
    b. Your working relationship with GSRP:
11. Expenditure of your time worthwhile:

(Continued on next page)

12. Quality of program literature for associate:
13. a. Quality of RDL's communications with you:
    b. Quality of RDL's communications with associates:
14. Overall assessment of SRP:

Table B-3. Laboratory Focal Point Reponses to above questions

	AEDC	*AL*	*USAFA*	*PL*	*RL*	*WHMC*	*WL*
# Evals Recv'd	0	7	1	14	5	0	46
Question #							
2	-	86 %	0 %	88 %	80 %	-	85 %
2a	-	4.3	n/a	3.8	4.0	-	3.6
2b	-	4.0	n/a	3.9	4.5	-	4.1
3	-	4.5	n/a	4.3	4.3	-	3.7
4	-	4.1	4.0	4.1	4.2	-	3.9
5a	-	4.3	5.0	4.3	4.6	-	4.4
5b	-	4.5	n/a	4.2	4.6	-	4.3
6a	-	4.5	5.0	4.0	4.4	-	4.3
6b	-	4.3	n/a	4.1	5.0	-	4.4
6c	-	3.7	5.0	3.5	5.0	-	4.3
7a	-	4.7	5.0	4.0	4.4	-	4.3
7b	-	4.3	n/a	4.2	5.0	-	4.4
7c	-	4.0	5.0	3.9	5.0	-	4.3
8	-	4.6	4.0	4.5	4.6	-	4.3
9	-	4.9	5.0	4.4	4.8	-	4.2
10a	-	5.0	n/a	4.6	4.6	-	4.6
10b	-	4.7	5.0	3.9	5.0	-	4.4
11	-	4.6	5.0	4.4	4.8	-	4.4
12	-	4.0	4.0	4.0	4.2	-	3.8
13a	-	3.2	4.0	3.5	3.8	-	3.4
13b	-	3.4	4.0	3.6	4.5	-	3.6
14	-	4.4	5.0	4.4	4.8	-	4.4

3. 1997 SFRP & GSRP EVALUATION RESPONSES

The summarized results listed below are from the 257 SFRP/GSRP evaluations received.

Associates were asked to rate the following questions on a scale from 1 (below average) to 5 (above average) - by Air Force base results and over-all results of the 1997 evaluations are listed after the questions.

1. The match between the laboratories research and your field:
2. Your working relationship with your LFP:
3. Enhancement of your academic qualifications:
4. Enhancement of your research qualifications:
5. Lab readiness for you: LFP, task, plan:
6. Lab readiness for you: equipment, supplies, facilities:
7. Lab resources:
8. Lab research and administrative support:
9. Adequacy of brochure and associate handbook:
10. RDL communications with you:
11. Overall payment procedures:
12. Overall assessment of the SRP:
13. a. Would you apply again?
    b. Will you continue this or related research?
14. Was length of your tour satisfactory?
15. Percentage of associates who experienced difficulties in finding housing:
16. Where did you stay during your SRP tour?
    a. At Home:
    b. With Friend:
    c. On Local Economy:
    d. Base Quarters:
17. Value of orientation visit:
    a. Essential:
    b. Convenient:
    c. Not Worth Cost:
    d. Not Used:

SFRP and GSRP associate's responses are listed in tabular format on the following page.

Table B-4. 1997 SFRP & GSRP Associate Responses to SRP Evaluation

	Arnold	Brooks	Edwards	Eglin	Griffiss	Hanscom	Kelly	Kirtland	Lackland	Robins	Tyndall	WPAFB	average
# res	6	48	6	14	31	19	3	32	1	2	10	85	257
1	4.8	4.4	4.6	4.7	4.4	4.9	4.6	4.6	5.0	5.0	4.0	4.7	4.6
2	5.0	4.6	4.1	4.9	4.7	4.7	5.0	4.7	5.0	5.0	4.6	4.8	4.7
3	4.5	4.4	4.0	4.6	4.3	4.2	4.3	4.4	5.0	5.0	4.5	4.3	4.4
4	4.3	4.5	3.8	4.6	4.4	4.4	4.3	4.6	5.0	4.0	4.4	4.5	4.5
5	4.5	4.3	3.3	4.8	4.4	4.5	4.3	4.2	5.0	5.0	3.9	4.4	4.4
6	4.3	4.3	3.7	4.7	4.4	4.5	4.0	3.8	5.0	5.0	3.8	4.2	4.2
7	4.5	4.4	4.2	4.8	4.5	4.3	4.3	4.1	5.0	5.0	4.3	4.3	4.4
8	4.5	4.6	3.0	4.9	4.4	4.3	4.3	4.5	5.0	5.0	4.7	4.5	4.5
9	4.7	4.5	4.7	4.5	4.3	4.5	4.7	4.3	5.0	5.0	4.1	4.5	4.5
10	4.2	4.4	4.7	4.4	4.1	4.1	4.0	4.2	5.0	4.5	3.6	4.4	4.3
11	3.8	4.1	4.5	4.0	3.9	4.1	4.0	4.0	3.0	4.0	3.7	4.0	4.0
12	5.7	4.7	4.3	4.9	4.5	4.9	4.7	4.6	5.0	4.5	4.6	4.5	4.6
Numbers below are percentages													
13a	83	90	83	93	87	75	100	81	100	100	100	86	87
13b	100	89	83	100	94	98	100	94	100	100	100	94	93
14	83	96	100	90	87	80	100	92	100	100	70	84	88
15	17	6	0	33	20	76	33	25	0	100	20	8	39
16a	-	26	17	9	38	23	33	4	-	-	-	30	
16b	100	33	-	40	-	8	-	-	-	-	36	2	
16c	-	41	83	40	62	69	67	96	100	100	64	68	
16d	-	-	-	-	-	-	-	-	-	-	-	0	
17a	-	33	100	17	50	14	67	39	-	50	40	31	35
17b	-	21	-	17	10	14	-	24	-	50	20	16	16
17c	-	-	-	-	10	7	-	-	-	-	-	2	3
17d	100	46	-	66	30	69	33	37	100	-	40	51	46

4. 1997 USAF LABORATORY HSAP MENTOR EVALUATION RESPONSES

Not enough evaluations received (5 total) from Mentors to do useful summary.

5. 1997 HSAP EVALUATION RESPONSES

The summarized results listed below are from the 113 HSAP evaluations received.

HSAP apprentices were asked to rate the following questions on a scale from 1 (below average) to 5 (above average)

1. Your influence on selection of topic/type of work.
2. Working relationship with mentor, other lab scientists.
3. Enhancement of your academic qualifications.
4. Technically challenging work.
5. Lab readiness for you: mentor, task, work plan, equipment.
6. Influence on your career.
7. Increased interest in math/science.
8. Lab research & administrative support.
9. Adequacy of RDL's Apprentice Handbook and administrative materials.
10. Responsiveness of RDL communications.
11. Overall payment procedures.
12. Overall assessment of SRP value to you.
13. Would you apply again next year? Yes (92 %)
14. Will you pursue future studies related to this research? Yes (68 %)
15. Was Tour length satisfactory? Yes (82 %)

	Arnold	Brooks	Edwards	Eglin	Griffiss	Hanscom	Kirtland	Tyndall	WPAFB	Totals
# resp	5	19	7	15	13	2	7	5	40	113
1	2.8	3.3	3.4	3.5	3.4	4.0	3.2	3.6	3.6	3.4
2	4.4	4.6	4.5	4.8	4.6	4.0	4.4	4.0	4.6	4.6
3	4.0	4.2	4.1	4.3	4.5	5.0	4.3	4.6	4.4	4.4
4	3.6	3.9	4.0	4.5	4.2	5.0	4.6	3.8	4.3	4.2
5	4.4	4.1	3.7	4.5	4.1	3.0	3.9	3.6	3.9	4.0
6	3.2	3.6	3.6	4.1	3.8	5.0	3.3	3.8	3.6	3.7
7	2.8	4.1	4.0	3.9	3.9	5.0	3.6	4.0	4.0	3.9
8	3.8	4.1	4.0	4.3	4.0	4.0	4.3	3.8	4.3	4.2
9	4.4	3.6	4.1	4.1	3.5	4.0	3.9	4.0	3.7	3.8
10	4.0	3.8	4.1	3.7	4.1	4.0	3.9	2.4	3.8	3.8
11	4.2	4.2	3.7	3.9	3.8	3.0	3.7	2.6	3.7	3.8
12	4.0	4.5	4.9	4.6	4.6	5.0	4.6	4.2	4.3	4.5
Numbers below are percentages										
13	60%	95%	100%	100%	85%	100%	100%	100%	90%	92%
14	20%	80%	71%	80%	54%	100%	71%	80%	65%	68%
15	100%	70%	71%	100%	100%	50%	86%	60%	80%	82%

A STUDY OF ELECTRONICS DESIGN ENVIRONMENTS IN TERMS OF COMPUTER AIDED DESIGN: A PSYCHOLOGICAL PERSPECTIVE

Janae N. Lockett
Graduate Student
Department of Experimental Psychology

University of Toledo
2801 W. Bancroft
Toledo, OH 43606

Final Report for:
Graduate Student Research Program
Wright Laboratory

Sponsored by:
Air Force Office of Scientific Research
Bolling Air Force Base, DC

and

Wright Laboratory

August 1997

A STUDY OF ELECTRONICS DESIGN ENVIRONMENTS IN TERMS OF COMPUTER AIDED DESIGN: A PSYCHOLOGICAL PERSPECTIVE

Janae N. Lockett
Graduate Student
Department of Experimental Psychology
University of Toledo

Abstract

The Electronics Design Environment in terms of Computer Aided Design was studied. In order to design an effective user interface, a program which displays a sequence of words, followed by the word stems of the previously presented word was written in Java in order to assess how much information the user can process before information overload occurs. The user will be asked to complete the word stem based on the given instructions of inclusion (consciously using one of the previous words to complete the word stem) or exclusion (consciously not using one of the previously presented words to complete the word stem). If an individual, under exclusion instructions, uses the previously presented words to complete the word stems this will provide evidence that their response was not due to conscious control. Jacoby (1991) coined this procedure as the Process Dissociation Model. To test whether or not unconscious processing has occurred due to information overload, the appropriate statistical measure will be used.

A STUDY OF ELECTRONICS DESIGN ENVIRONMENTS IN TERMS OF COMPUTER AIDED DESIGN: A PSYCHOLOGICAL PERSPECTIVE

Janae N. Lockett

Introduction

Cognitive Psychology can be applied to the real world in many different ways. Whether it be through human factors, computer simulation, or the simple application of learning techniques, this field embodies the many aspects of information processing.

One of the major areas in this field is attention—the amount of cognitive resources that an individual allocates to a particular event. Everyday we are constantly bombarded with outside stimuli that more often than not tend to occur simultaneously. It would be impossible to process all of this information at once. Thus, in order to avoid information overload, we consciously process information which has been attenuated. This in turn generates a response. However, we also process unconscious information—information which has not been attenuated. This raises a very important issue: the effects of unconscious processing on behavior. Do unconscious processes effect behavior, and if so, in what way?

This research may be applied to areas such as Learning and Memory, both as a function of conscious and unconscious control. As well as these areas, this research may also be applied to Electronics Design Environments. These Design Environments, in terms of Computer Aided Design (CAD), need effective, practical, and proficient user interface. In order to achieve this requirement, Cognitive Psychology has been incorporated to effectively design this user environment. We need to know how much to design as well as how much an individual can process. Thus, it is important to know how much information a person can handle before information overload becomes an issue. The key approach with this research is to reduce the information overload that the user may experience during the design cycle. To assess whether or not information overload has occurred, basic tests must be conducted.

Methodology

The following method was used to create the source code involved in the implementation of the user interface:

Pseudocode: Conscious/Unconscious Information Processing

1--create a file with words containing only 6 letters.
2--use a data input stream.
3--get data from the file.
4--display word1 (50/500ms).
5--erase word1.
6--display word2 (50/500ms).
7--erase word2.
8--display word3 (50/500ms).
9--erase word3.
10--display word stem.
11--user must input the stem completion via the keyboard.
12--input must be stored.
13--repeat steps 4-12 until subject/user has completed 30 trials.

```
/*This program (Janae.java) will create a file containing six-letter-words.  This program
 *will read the words from a larger file containing over 25,000 words of various lengths.
 */


import java.io.*;


class Janae {

  public static void main (String [] args) throws java.io.IOException {

    DataInputStream f1=new DataInnputStream(new FileInputStream("words.txt"));
    DataOutputStream f2=new DataOutputStream(new FileOutputStream("myFile6.txt"));

    String  s;

    while ((s = f1.readLine()) ! = null) {
          if  (s.length() = = 6) {
                f2.writeBytes (s + "\r\n");
          }
    }

    f1.close();
    f2.close();
    }
}
```

```
/*This program (JanaeII.java) will display three six-letter-words sequentially, and then will
 *present a word stem (of one of the previously presented words). The user must then
 *complete the word stem in order for the next sequence of words to appear. The
 *completed word stem will be written to a new file.
 */

import java.io.*;

class JanaeII {

  public static void main (String [] args) throws java.io.IOException,
                                                   StringIndexOutofBoundsException {

    DataInputStream f2=new DataInputStream(new  FileInputStream("myFile6.txt"));
    DataOutputStream f3=new DataOutputStream(new  FileOutPutStream("stemCompletion.txt"));
    DataInputStream inn=new  DataInputStream(System.in);

    String   s, wordstem, stemcompletion;

    s = f2.readLine();

    while (s ! = null) {
            wordstem=s.substring(0,3);

            for (int counter=0; counter<3; counter++) {
                    System.out.println(s);
                    try{Thread.sleep(1000);} catch (Exception e) {}
                    for (int i=0; i<30; i++) {
                        System.out.println("");
                    }
                    s = f2.readLine();
            }
            System.out.print(wordstem);
            System.out.flush();
            stemcompletion=inn.readLine();
            // System.out.println("READ: " + wordstem = stemcompletion);
            f3.writeBytes(wordstem + stemcompletion + "\r\n");
    }
    f2.close();
    f3.close();
    inn.close();
  }
}
```

Results

Two programs were created. The first program generated a list of six-letter-words from a previously existing word pool. The second program was based on the cognitive theory of attention in an attempt to employ the Process Dissociation Model (Jacoby 1991) of conscious and unconscious processing in order to design an effective environment for the user. The words were presented at a rate which allows conscious processing to occur. Thus, the user is not faced with information overload and can effectively interact with the computer when it is time to complete the word stem. If I were to decrease the time in which the words (stimuli) were presented to the user, conscious processing would be less likely to occur. This would interfere with the interaction between the user and the computer—it would be less effective. The actual results of the study will be assessed at a later date, once the study is completed. Once the study is completed the results will be analyzed appropriately.

Conclusion

I found that once I had completed my training period I had a fairly good understanding of the basic code in which Java script is written. Thus, with outside assistance, it was fairly easy to design this user environment. Having a background in Cognitive Psychology proved to be very useful because it allowed me to incorporate my knowledge about human information processing into the design of an effective user interface. This program can be enhanced by incorporating Graphical User Interface (GUI) components known as layout managers. A layout manager informs the Abstract Window Toolkit (AWT) where to place one component in relation to another. There are five different types of layout managers: flowlayout, borderlayout, gridlayout, cardlayout, and gridbaglayout. These are the different user interfaces available. For the second program, two layout managers should be implemented: the flowlayout and borderlayout managers. The flowlayout manager will be used to arrange the components (i.e., words & word stems) from left to right on the computer screen. The borderlayout manager will be used to place the components in the center of the screen. These are the two most appropriate managers to use because the user will need to view the components in the center of the screen, from the left to the right.

This research will be beneficial in an academic, government, as well as industrial setting. Various learning techniques, as well as the design and implementation of technology is dependent upon the limits of human information processing. Thus it is important that the information overflow that the individual may experience is reduced during the design cycle so that he/she may perform more effectively.

Appendix

I.) JAVA COMMANDS (summary)

this appendix will present a summary of the commands involved in the ArcTest and Blink programs. explaining these programs served as part of my training of Java script.

a.) programs: ArcTest.java
Blink.java

1a.) ArcTest.java

this program utilizes two of the methods (Graphics.drawArc and Graphics.fillArc) of the Graphics class interactively.

.import java.awt.*; import java.applet.*;

these import statements load the classes belonging to the awt and applet packages that are necessary for compiling this program.

.public class ArcTest extends Applet

the keyword public enables the browser to create and execute the applet. the keyword class introduces a class definition. in this case, ArcTest is known as the subclass because it inherits the attributes of Applet, the superclass.

.variable initializations and declarations

.add ()

the add method places GUI components on the applet so that the user can interact with them. in this case this method is inherited from the Applet class when defining the ArcTest class.

.public void start ()

start is a public method that returns no information after it has completed its task. the start method of the Applet class is called by the browser/applet viewer to inform this applet that it should start its execution.

.public void stop ()

stop is a public method that returns no information after it has completed its task. the stop method of the Applet class is called by the browser/applet viewer to inform this applet that it should stop its execution.

.public boolean handleEvent (Event e)

handleEvent is a public method that returns a boolean value when it completes its task. the handleEvent method receives an event argument which is used to determine what event occurred.

.if (e.id==Event.Window_Destroy) {
System.exit(0);
}

this if statement tests to see if the Event object "e" is equal to the window destroy event type. if it is then the exit method will become activated (this will exit the system). "id" is a variable of the Event class.

.public static void main (String args [])

method main must always begin with this first line—if it does not then the java interpreter will not be able to execute the program. main is a public method. a browser will automatically call this method, that returns no information once it completes its task. the method's parameter list indicates that it will use string arguments to complete its task. the keyword static indicates that the data is class-wide and that only one copy of a particular variable should be shared by all objects in a class.

.Frame f = new Frame ("ArcTest");

this statement creates a Frame object using the new operator and assigns the result to "f" (which is declared as a Frame). the value in parenthesis is used to initialize the object created.

.ArcTest arcTest = new ArcTest ();

this statement creates an ArcTest object using the new operator and assigns the result to "arcTest" (which is declared as an object of ArcTest). there is no value in parenthesis given to initialize the object created.

.arcTest.init (); arcTest.start ();

the init method initializes a variable. the start method is called by the browser/applet viewer to inform the applet that it should start its execution.

.f.add(); f.resize(); f.show();

if" is the name of the frame object. the add method places GUI components on the applet so the user can interact with them (this will add the frame to the applet). the resize method requests that the applet (frame) be resized. the show method requests that the argument string be displayed

.class ArcCanvas extends Canvas

the keyword class introduces a class definition. in this case ArcCanvas, is known as the subclass because it inherits the attributes of Canvas, the superclass.

.variable declarations and initializations

.public void paint (Graphics g)

paint is a public method that returns no information upon completing its task. the method's parameter list indicates that the paint method requires a Graphics object "g" to complete its task.

.variable declarations and initializations (defined in the method section).

.g.setColor (Color.pink)

the setColor method sets this graphics context's current color to the specified color (pink).

```
.for  (int i = 1;  i <= hlines; i++ )  {
     g.drawLine (0, i  *  10, r.width, i  *  10);
}
for  (int i = 1;  i <= vlines; i++ )  {
     g.drawLine  (i  * 10, 0, i  *  10, r.height);
}
```

the first section of the for statement initializes the control variable, the second section consists of the loop continuation condition, and the third section increments the control variable. the Graphics object "g" instructs the computer to perform an action to use the drawLine method to draw a line, using the current color, between the points (x1, y1) and (x2, y2) in this graphics context's coordinate system.

.g.setColor (Color.red)

the setColor method sets this graphics context's current color to the specified color (red).

```
.if  (filled) {;
        g.fillArc (0, 0, r.width - 1, r.height - 1, startAngle, endAngle);
} else  {
        g.drawArc (0, 0, r.width - 1, r.height - 1, startAngle, endAngle);
}
```

the first if statement tests if user requests that the arc be filled. if he/she does then the fillArc method fills a circular or elliptical arc covering the specified rectangle (specified coordinates). if this does not occur (else) the drawArc method will draw the outline of a circular or elliptical arc covering the specified rectangle (specified coordinates).

.g.setColor (Color.black)

the setColor method sets this graphics context's current color to the specified color (black).

.g.setFont (font)

the setFont method sets this graphics context's current font to the specified font (font).

.g.drawLine

these series of drawLine commands will draw a line, using the current color, between the points (x1, y1) and (x2, y2) in this graphics context's coordinate system.

.int sx = 10; int sy = r.height - 28;

variable sx and sy are being declared and initialized in these two statements. they are declared as type integer and are initialized to the numerical value to the right of the assignment operator.

.g.drawString ("S = " + startAngle, sx, sy);

.g.drawString ("E = " + endAngle, sx, sy + 14);

the drawString method of the Graphics object "g" draws the string of characters contained between the quotation marks. the "+" operator is used for string concatenation (not addition). it combines the values of start/endAngle to the strings "S=" and"E=".

.public void redraw (boolean filled, int start, int end) {;

redraw is a public method that returns no information upon completion of its task. within the method parameter, the arguments boolean filled, int start, and int end are used to enable the redraw method to complete its task as to where to redraw the arc.

.this.filled = filled; this.startAngle = start; this.endAngle = end;

this is a special reference value which is used inside of any method to refer to the current object. the value "this" refers to the object's (filled, startAngle, and endAngle) which the current method has been called on.

.repaint ();

} the repaint method forces your applet to repaint. calling repaint in turn calls update, which erases any information on the applet, calling the paint method shortly thereafter.

.class ArcControls extends Panel {

the class keyword introduces a class definition. in this case, ArcControls is known as the subclass because it inherits the attributes of Panel, the superclass.

.TextField s; TextField e, ArcCanvas canvas;

these are all variable declarations.

.public ArcControl (ArcCanvas canvas) {

the keyword public indicates that the interface of this ArcControl class represents everything that the external users of the class need to know (i.e., this information may be accessed by external users). the arguments (ArcCanvas canvas) within the class parameter indicate that these are defined as objects and instance variables of this particular class.

.this.canvas = canvas;

this is a special reference value that is used inside of any method to refer to the current object (canvas).

.add (s = new TextField ("0", 4));

a TextField object is created using the new operator. the result is assigned to the variable "s". the value in parenthesis is used to initialize the object created. the add method places the GUI component "s" on the applet so that the user can interact with it.

.add (e = new TextField ("45", 4));

a second TextField object is created using the new operator. the result is assigned to the variable "e". the value in parenthesis is used to initialize the object created. the add method places the GUI component "e" on the applet so that the user can interact with it.

.add (new Button ("Fill"));

.add (new Button ("Draw"));

this statement creates a Button object using the new operator. the values in parenthesis are used to initialize the new object created. the add method places the GUI component (Button) on the applet so that the user can interact with it.

.public boolean action (Event ev, Object arg) {

action is a public method that returns a boolean (true/false) value upon completion of its task. the action method processes interactions between the user and the GUI component.

.if (ev.target instanceof Button) {

String label = (String) arg;
canvas.redraw (label.equals ("Fill"),
Integer.parseInt (s.getText () .trim ()),
Integer.parseInt (e.getText () .trim ()));
return true;

}

return false;

}

instanceof is a keyword. this if statement tests whether or not the Button object is referenced by the method target. if the "if" statement is true, then a label (of type String) will be set to the value of a string argument. the equal method is then used to compare the label to the string "Fill" for equality. the label is then redrawn to the canvas via the redraw method. as the label is being redrawn to the canvas, the Integer.parseInt method converts the string argument into an integer using the getText method to retrieve text from a specified text field (s and e). the trim method removes the white space from both ends of the string. once this task is complete a boolean value of true is returned. if the "if" statement is false from the start, the program will never enter the body of the "if" statement and a boolean value of false will be returned.

2a.) Blink.java

this program focus' on Java's StringTokenizer class (from package java.util) which breaks a string into its component tokens.

.import java.awt.*; import java.util.StringTokenizer;

these import statements load the classes belonging to the awt and util packages that are necessary for compiling this program.

.public class Blink extends java.applet.Applet implements Runnable {

the keyword public enables the browser to create and execute the applet. the keyword class introduces a class definition. in this case, Blink is known as the subclass because it inherits the attributes of Applet, the superclass. Runnable is an interface which the Applet class implements. this interface is designed to provide a common protocol for objects that wish to execute code while they are active. being active simply means that a thread has been started and has not yet been stopped. in addition, Runnable provides the means for a class to be active while not subclassing Thread .

.variable declarations

.public void init() {

init is a public method that returns no information after it has completed its task.

.font = new java.awt.Font("TimesRoman", Font.PLAIN, 24);

this statement creates a new java.awt.Font object using the new operator and assigns the result to "font". the value inside the parenthesis is used to initialize the object created.

.String att = getParameter("speed");

the getParameter method gets the value of a specified parameter "speed". this value is then assigned to string "att".

.speed = (att == null) ? 400 : (1000 / Integer.valueOf(att).intValue());

this statement utilizes the ternary if-then-else operator to test some value to select which expression to evaluate. if the result is true, then statement1 is executed, otherwise, statement2 is executed. both statements are required to return the same type. thus, if att equals a null value, then 400 is evaluated and used as the value of the entire expression. if att does not equal a null value, then 1000 is divided by the integer value of att and this result will be used for the value of the entire expression, which is then assigned to the variable on the left-hand side of the assignment operator (speed).

.att = getParameter("lbl");

the getParameter method gets the parameter "lbl", and this value is assigned to the string att.

.lbl = (att == null) ? "Blink" : att;

if att equals a null value, then "Blink" is evaluated and used as the value of the entire expression. if att does not equal a null value, then att is evaluated and used as the value of the entire expression, which is then assigned to the variable on the left-hand side of the assignment operator (lbl). (in java it is possible to evaluate the value of characters because each character --both upper and lower case--has an integer value).

.public void paint(Graphics g) {

paint is a public method that returns no information after it completes its task. the method's parameter list indicates that the paint method requires a Graphics object "g" to complete its task.

.int x = 0, y = font.getSize(), space;

these are variable declarations (of type integer) and initializations within the method section. the font.getSize command gets the point size of the font this value is assigned to the variable "y".

.int red = (int) (Math.random() * 50);

this statement uses the random method to generate a random number between 0.0 and 1.0. this number is multiplied by 50 and the result is assigned to the variable red (which is being declared as an integer).

.int green = (int) (Math.random() * 50);

this statement uses the random method to generate a random number between 0.0 and 1.0. this number is multiplied by 50 and the result is assigned to the variable green (which is being declared as an integer).

.int blue = (int) (Math.random() * 256);

this statement uses the random method to generate a random number between 0.0 and 1.0. this number is then multiplied by 256 and the result is assigned to the variable blue (which is being declared as an integer).

.Dimension d = size();

this statement sets the variable "d" equal to the value of size.

.g.setColor(Color.black);

the setColor method sets this graphics context's current color to the specified color (black).

.g.setFont(font);

the setFont method sets this graphics context's current font to the specified font (font).

.FontMetrics fm = g.getFontMetrics();

the getFontMetrics method gets the screen metrics of the font. this value is then assigned to the variable "fm".

.space = fm.stringWidth(" ");

the stringWidth method returns the total advance width for showing the specified string (in this case an empty string) in this font. the width of this empty string is assigned the to the variable space.

.for (StringTokenizer t = new StringTokenizer(lbl) ;
t.hasMoreTokens() ;) {

within this for loop a StringTokenizer object is created using the new operator. the result is assigned to the variable "t". the value in parenthesis is used to initialize the object created. after this new StringTokenizer object is created, the for loop immediately tests if there are more tokens available from this token's string.

. String word = t.nextToken();

in this statement the nextToken method returns the next token from this string tokenizer. this result is assigned to the variable word.

.int w = fm.stringWidth(word) + space;

the stringWidth method returns the total advance width for showing the specified string in the font. this value is added to the value allocated to the space variable. the result is then assigned to variable "w".

.if (x + W > d.width) {

if the sum of x and w are greater than the width of the dimension...

.x = 0;

this statement assigns zero to the variable x.

.y += font.getSize();

the getSize method gets the point size of the font. this value is then added to the value of variable "y".

.if (Math.random() < 0.5) {

this if statements tests whether the random method returns a random value less than 0.5

.g.setColor(new java.awt.Color((red + y * 30) % 256, (green + x / 3)
% 256, blue));

this statement creates a java.awt. Color object using the new operator. this new object is the argument within the method parameter that enables the setColor method to complete its task. the value in parenthesis following the new object is used to initialize the object created.

.else {
g.setColor(getBackground());

the setColor method sets this graphics context's current color to the specified color (the getBackground method gets the background color for this component).

.g.drawString(word, x, y);

the drawString method draws the text given by the specified string, using this graphics context's current font and color. the argument within the method's parameter will enable this method to complete its task—variable "word" represents the string, and the "x" and "y" variables represent the size of the font and dimension of the string.

.x += w;

this statement adds the value of "w" to the variable "x".

.public void start() {

start is a public method that returns no information upon completion of its task. the start method is called by the browser/applet viewer to inform this applet that it should start its execution.

.blinker = new Thread(this);

this statement creates a Thread object using the new operator and assigns the result to "blinker". the value in parenthesis is used to initialize the object created. "this" is a special reference value which is used inside of any method (start) to refer to the current object (Thread).

.blinker.start();

the start method is called by the browser/applet viewer to inform this applet that it should start its execution. "blinker" is the object that performs this method.

.public void stop() {

stop is a public method that returns no information upon completion of its task. the stop method of the Applet class is called by the browser/applet viewer to inform this applet that it should stop its execution.

.blinker.stop();

the stop method is called by the browser/applet viewer to inform this applet that it should stop its execution. "blinker" is the object that performs this method.

.public void run() {

run is a public method that returns no information upon completion of its task. the run method initiates the execution phase.

```
.while (true) {
   try {Thread.currentThread().sleep(speed); } catch
   (InterruptedException e) {}
   repaint();
 }
```

the try keyword can be used to specify a block of code that should be guarded against all exceptions. the currentThread method returns the currently executing thread object. the sleep method causes the currently executing thread to sleep (temporarily ceasing execution) for the specified (speed) number of milliseconds. the catch clause specifies the exception type you wish to catch. in this case the specific exception type is the "InterruptedException e". the repaint method forces your applet to repaint. calling repaint in turn calls update, which erases any information on the applet, calling the paint method shortly thereafter.

II.) JAVA PROGRAMS

this portion of the appendix will display a program (InputOutput.java) written in Java script.

```
/*This program receives information from the keyboard until a 12-byte buffer is
 *is filled. Then the information is output to the screen. This program is
 *referenced from The Java Handbook (Naughton, 277).
 */

import java.io.*;

class FileOutputStreams {
    public static byte getInput()[] throws Exception {
          byte buffer[] = new byte[12];
          for (int i=0; i<12; i++) {
          buffer[i] = system.in.read();
      }
          return buffer;
}

    public static void main(String args[]) throws Exception {
        byte buf[] = getInput();
        OutputStream f0 = new FileOutputStream("file1.txt");
        OutputStream f1 = new FileOutputStream("file2.txt");
        OutputStream f2 = new FileOutputStream("file3.txt");
        for (int i=0; i<12; i += 2) {
            f0.write(buf[i]);
        }
        f0.close();
        f1.write(buf);
        f1.close();
        f2.write(buf,12/4,12/2);
        f2.close();

    }
}
```

Reference

Jacoby, Larry L. A process dissociation framework: Separating automatic from intentional uses of memory. Journal of Memory & Language, vol 30 513-541, Oct. 1991.

FATIGUE CRACK GROWTH BEHAVIOR OF Ti-22Al-23Nb

Stephanie Luetjering
Graduate Student
Department of Materials Engineering

University of Dayton
300 College Park
Dayton, OH 45469-0240

Final Report for:
Graduate Student Research Program
Wright Laboratory

Sponsored by:
Air Force Office of Scientific Research
Bolling Air Force Base, DC
and
Wright Laboratory

August 97

FATIGUE CRACK GROWTH BEHAVIOR OF Ti-22Al-23Nb

Stephanie Luetjering
Graduate Student
Department of Materials Engineering
University of Dayton

Abstract

The fatigue crack growth (FCG) behavior of an orthorhombic titanium aluminide alloy has been investigated for two microstructural conditions: a duplex microstructure consisting of 5 vol.% globular α_2 phase within a two phase mixture of orthorhombic platelets in a continuous β_0 matrix, and a fully transformed microstructure containing only the orthorhombic and the β_0 phases. FCG tests were conducted at room and elevated temperature in lab air. Results indicate no significant difference between the two microstructural conditions with regard to their da/dN-ΔK behavior for both 20°C and 540°C testing in lab air, except for the cyclic fracture toughness values, which are higher for the duplex microstructure. Initial results of vacuum FCG testing at room temperature show that the da/dN-ΔK curve is shifted to the right in the threshold regime as compared to the equivalent curve obtained in lab air, indicating an environmental effect. Furthermore, the fatigue crack propagation behavior at 540°C is superior to the room temperature behavior over most of the ΔK range investigated. Fractographic analysis indicates a predominantly transgranular failure mode for both microstructures, with a more brittle appearance at room temperature than at 540°C.

Introduction

In aerospace industry one major goal is to steadily improve the efficiency of the aircraft by increasing the thrust-to-weight ratio of the turbine engine. The demand for low density structural materials with high temperature strength has lead to great interest in titanium aluminide intermetallics, based on TiAl, Ti_3Al and most recently on Ti_2AlNb. Titanium aluminide alloys based on the Ti_2AlNb composition contain a significant amount of the ordered orthorhombic phase. These alloys have been found to be very promising as potential material for aerospace applications, both in monolithic form and as matrix material for composites. The benefits of these Ti_2AlNb based alloys, as compared to Ti_3Al based alloys are higher specific strength at elevated temperatures, improved creep resistance, improved fracture resistance and reduced fiber/matrix reaction, /1 - 7/.

A strong dependency of mechanical properties on microstructural features such as phase constituency, grain size and morphology was determined for various alloy compositions based on the Ti_2AlNb compound, /2, 3, 8/. Primary interest in improving the creep properties focused recent research efforts in this area. The cyclic properties have not been studied in any detail with respect to the material's microstructure. The main objective of this study therefore is to investigate the effect of microstructural changes on the fatigue crack growth behavior of the orthorhombic alloy Ti-22Al-23Nb (at.%).

Material and Experimental Procedure

The starting material was a plasma hearth melted Ti-22Al-23Nb (at.%) ingot, which was forged above the beta transus and then subtransus pack cross rolled down to 0.5 mm sheet. Bulk chemistry of the alloy indicates that the actual composition is closer to Ti-21Al-22Nb (at.%), Table 1.

Ti [at.%]	Al [at.%]	Nb [at.%]	N [wt.%]	O [wt.%]
bal	20.8	22.2	0.010	0.087

Table 1: Chemical analysis of bulk material

The beta-transus temperature of 1075°C was determined by the disappearing phase technique. This result is consistent with studies by /9/, where the dependency of the beta transus temperature on the material's oxygen content was investigated. Two microstructures, a duplex and a fully transformed one, were developed by solutionizing coupons, wrapped in Ta foil, in a vacuum furnace (10^{-4} torr) at different temperatures above and below the beta-transus, followed by direct cooling to 815°C where the specimens were aged. Previous studies by Smith /10/ had shown that heat treatments just below the beta transus temperature resulted in the best combination of tensile and creep properties, whereas the heat treatment above the beta transus temperature gave the best creep resistance, but a reduced tensile ductility. Cooling rates of 50°C/min were chosen over slower cooling rates to prevent growth of orthorhombic platelets at preferred sites such as grain boundaries. The two applied heat treatments are:

1055°C for 2 hr \ cool @ 50 °C/min \ 815°C for 8 hr \ furnace cool (duplex)

1095°C for 30 min \ cool @ 50 °C/min \ 815°C for 8 hr \ furnace cool (fully transformed)

Dog bone specimens for tensile testing and straight sided single edge notched (SEN) specimens for FCG testing were wire electrodischarge machined (EDM) according to Figure 1. A servohydrolic horizontal test system equipped with quartz lamp heating elements, which provided a uniform temperature distribution throughout the gage section of the specimens, was used for tensile and fatigue crack growth testing. The system is described in detail by Hartman and Buchanan /11/ and Hartman and Russ /12/. Tensile testing was performed with a constant cross head speed of 0.0084 mm/s. Fatigue crack propagation tests were carried out using SEN specimens with clamped ends, allowing no longitudinal rotation or transverse displacement, as described by Blatt *et al.* /13/. According to ASTM Designation E647-91 /14/ specimens were precracked applying the K-decreasing test procedure. To obtain crack growth data decreasing K_{max} tests and constant load tests were carried out. A stress ratio of 0.1 and a frequency of 10 Hz were applied. Crack advance was monitored using the compliance method. Additionally, to verify the accuracy of this technique, optical measurements were taken using traveling microscopes. All tests were conducted under two temperature conditions, 20°C and 540°C, in laboratory air and in vacuum (better than 2×10^{-6} torr).

Materials characterization included bulk chemical analysis and microstructural analysis. Metallographic samples, etched with Kroll's reagent, were studied using a Leica 360 FE scanning electron microscope (SEM), which has a spatial resolution of 2 nm at 25 kV. Quantitative phase analysis was accomplished by applying an NIH image analysis program to digitally stored backscattered electron SEM micrographs. After testing fracture surfaces were examined using the SEM to correlate fatigue crack paths to microstructural features.

Results and Discussion

Microstructure

The solutionizing heat treatment in the single beta phase field results in a fully transformed microstructural condition, with the ordered orthorhombic (O) phase precipitating out upon cooling down to the aging temperature of 815°C. The final microstructure consists of O platelets of an average size of approximately 5 μm, within an ordered beta matrix (β_0), Figure 2. A continuous layer of orthorhombic phase is also present along the prior beta grain boundaries. The beta grain size is about 300 μm in diameter. The duplex microstructure, Figure 3, is formed by a solutionizing treatment in the $\alpha_2 + \beta_0$ two phase field at 20°C below the beta transus temperature. The controlled cooling results in precipitation of the orthorhombic platelets of comparable size and distribution to the ones in the fully transformed microstructure. The duplex microstructure consists of an α_2 phase content of 5 vol.%, present mainly in globular form but also as thin semi-continuous layer along the beta grain boundaries. The flat beta grains have an average diameter of 150 μm in the plane of the cross-rolled sheet and 75 μm in the short transverse direction. This fairly large prior beta grain size can be attributed to the sheet's processing history.

Tensile Properties

Tensile properties for the two microstructural conditions at room temperature and at 540°C in air and vacuum, all average values of at least two tests, are listed in Table 2. The duplex microstructure exhibits better overall properties, especially with regard to the ductility, than the fully transformed condition. Fracture characteristics are different between the two microstructures. Whereas the duplex fracture surface shows mostly ductile transgranular failure with only small areas of intergranular fracture at the crack initiation sites, the fully transformed condition predominantly fails intergranularly. Similar to previous observations obtained on neat Ti-22Al-23Nb /16/ an expected drop in strength and a slight increase in ductility is exhibited at 540°C as compared to 20°C. Tensile testing at 20°C in vacuum gives comparable properties to those received in lab air, whereas at 540°C vacuum testing results in ductility values almost twice as high as the ones in air, indicating a strong effect of environment at this elevated temperature.

Microstructural Condition	Test Condition	0.2% Yield [MPa]	UTS [MPa]	Elongation [%]	Modulus [GPa]
FT	20°C, lab air	920	1095	2.9	112
FT	20°C, vacuum	1000	1100	3.1	121
duplex	20°C, lab air	975	1150	7.8	112
duplex	20°C, vacuum	1010	1175	7.1	120
FT	540°C, lab air	740	965	4.6	109
FT	540°C, vacuum	780	965	6.3	107
duplex	540°C, lab air	750	960	7.5	101
duplex	540°C, vacuum	795	965	15.4	107

Table 2: Tensile properties of Ti-22Al-23Nb for the duplex and fully transformed (FT) microstructures

Fatigue Crack Growth

Fatigue crack growth rate curves for the two investigated microstructures at 20°C and 540°C are shown in Figures 4 and 5 respectively. The room temperature curves represent a conventional da/dN-ΔK behavior with a constant slope starting at a near threshold value of 5 MPa$\sqrt{m}$ and approaching a cyclic fracture toughness value of approximately 20 MPa$\sqrt{m}$ for the fully transformed condition and 25 MPa$\sqrt{m}$ for the duplex microstructure. At 540°C the crack growth behavior is similar for both microstructures. The fully transformed condition has slightly lower threshold values than the duplex structure. Both elevated temperature curves show a very steep slope in the threshold region up to crack growth rates of $5x10^{-8}$ m/cycle (ΔK = 10 MPa$\sqrt{m}$). Then a plateau with only little increase in crack growth rate is exhibited in the ΔK range from 10 - 30 MPa$\sqrt{m}$, before cyclic fracture toughness values of 60 MPa$\sqrt{m}$ are reached. Similarly shaped elevated temperature curves like these have been observed for conventional titanium alloys under equivalent test conditions.

In a study which compares fatigue crack propagation behavior of Ti-6242 at 500°C in air with tests conducted in high vacuum (< $5x10^{-4}$ Pa) and in humidified argon, Lesterlin *et al.* /17/ showed that this plateau was attributed to an embrittling effect of water vapor. Vacuum testing has so far only been performed for the duplex microstructure at room temperature. Results are presented in Figure 6, and the difference in the crack growth rates near the threshold region for the two conditions indicates a detrimental effect of environment at room temperature. Further FCG testing in vacuum and in environments with controlled partial pressures of water vapor at room and elevated temperature will be necessary to evaluate possible environmental effects and identify the role of oxygen and water vapor in this process. When plotting the crack growth curves obtained at room temperature and elevated temperature for the fully transformed microstructure in the same plot, Figure 7, it is interesting to note that at 540°C lower fatigue crack growth rates are observed for most of the ΔK regime investigated.

Crack propagation for both microstructures at room and elevated temperatures is dominated by a transgranular mode with regard to the prior beta grains, although occasional intergranular fracture is observed. Representative fractographs of the duplex microstructural condition tested at 20°C and 540°C are shown in Figures 8 and 9 for fatigue crack growth rates of $6x10^{-7}$ and $2x10^{-7}$ m/cycles, which correspond to ΔK values of 20 MPa$\sqrt{m}$. Crack growth appears to depend on the underlying microstructure. Fatigue surfaces show distinct regions of flat transgranular fracture. The mean size of these cleavage facets (5 μm) corresponds well with the primary α_2 particles. Besides these areas, irregular stepped growth is revealing orthorhombic platelet structure. At elevated temperature striations are visible in some cases even within α_2 particles, indicating a more ductile failure mode. Measurements of the striation spacing, in case of the area in Figure 9 it is 0.2 μm, show a very good agreement with the crack growth rates obtained by the compliance method. Specimens subjected to 540°C environment show evidence of high density microcracking in the appearance of cracked striations.

Summary

Sheet-material of the nominal composition Ti-22Al-23Nb (at.%) was used to investigate the effect of microstructure on its cyclic behavior. Two microstructures were selected, a duplex microstructure consisting of 5 vol.% globular α_2 phase within a two phase mixture of β_0 and orthorhombic, and a fully transformed structure, containing only orthorhombic platelets in a β_0 matrix. The only significant difference observed in the FCG behavior between the two microstructures is the cyclic fracture toughness behavior at room temperature, which is 5 MPa$\sqrt{m}$ higher for the duplex condition. Room temperature vacuum testing indicates an environmental effect on the near threshold FCG behavior. To evaluate the environmental effect in greater detail, fatigue crack growth testing in controlled environmental conditions is necessary. Of further interest is, that both microstructures exhibit better crack growth behavior at 540°C than at 20°C over most of the ΔK range. Fatigue failure modes at room temperature are more brittle than at elevated temperature, predominantly transgranular failure is observed for both temperatures investigated.

References

/1/ *D. Banerjee, A. K. Gogia, T. K. Nandi and V. A. Joshi:* " A new ordered orthorhombic phase in Ti_3Al-Nb alloy", Acta. Met. , vol 36, pp 871-882, (1988)

/2/ *R. G. Rowe:* " Recent developments in TiAlNb titanium aluminide alloys", High Temperature Aluminides and Intermetallics, eds. S. H. Whang, C. T. Liu, D. P. Pope and J. O. Stiegler, TMS, pp 375-401, (1990)

/3/ *R. G. Rowe:* " The mechanical properties of titanium aluminides near Ti-25Al-25Nb", in Microstructure/Property Relationship in Titanium Aluminides and Alloys, eds. Y.-W. Kim and R. R. Boyer, TMS, pp 387 - 398, (1991)

/4/ *P. R. Smith, J. A. Graves and C. G. Rhodes:* " Comparison of orthorhombic and alpha-two titanium aluminides as matrices for continuous SiC-reinforced composites", Met. Trans., A., vol 25A, pp 1267-1283, (1994)

/5/ *R. G. Rowe:* " Ti_2AlNb-based alloys outperform conventional titanium aluminides", Adv. Mater. Processes, vol 141, pp 33-35, (1992)

/6/ *R. G. Rowe:* " The mechanical properties of ternary and quarternary Ti_2NbAl-based titanium aluminide alloys", in Titanium '92 Science and Technology, eds. F. H. Froes and I. Caplan, TMS, pp 343 - 350, (1993)

/7/ *R. G. Rowe:* " Tensile and creep behavior of ordered orthorhombic Ti_2AlNb-based alloys", Mat. Res. Soc. Symp. Proc., 213, pp 703 - 708, (1991)

/8/ *J. A. Graves, P. R. Smith and C. G. Rhodes:* " Evaluation of a Ti-22Al-23Nb orthorhombic alloy for use as the matrix in a high temperature Ti-based composite", in Intermetallic Matrix Composites II, eds. D. Miracle et al., MRS, pp 31 - 42, (1992)

/9/ *C. G. Rhodes, J. A. Graves, P. R. Smith and M. R. James:* " Characterization of orthorhombic titanium aluminide alloys", Structural Intermetallics, eds. R. Darolia, J. J. Lewandowski, C. T. Liu, P. L. Martin, D. B. Miracle and M. V. Nathal, TMS, (1993)

/10/ *P. R. Smith, W. J. Porter, W. J. Kralik and J. A. Graves:* " The effect of heat treatment on tensile and creep response of "neat" Ti-22Al-23Nb", Proc. ICCM-10 Conference, eds. A. Poursartip and K. N. Street, Vol II Metal Matrix Composites, pp 731 - 738, (1995)

/11/ *G. A. Hartman and D. J. Buchanan:* " Methodologies for thermal and mechanical testing of TMC material", Characterization of fiber reinforced titanium matrix composites, AGARD Report 796, pp 12-1 - 12-9, (1994)

/12/ *G. A. Hartman and S. M. Russ:* " Techniques for mechanical and thermal testing of Ti_3Al /SCS-6 metal matrix composites", Metal Matrix Composites: Testing, Analysis and Failure Modes, ASTM STP 1032, ed. W. J. Johnson, pp 43-53, (1989)

/13/ *D. Blatt, R. John and D. Coker:* "Stress intensity factor and compliance solutions for a single edge notched specimen with clamped ends", Eng. Frac. Mech., vol 47, no 4, pp 521 - 532, (1994)

/14/ "ASTM E647-91, Standard test method for measurement of fatigue crack growth rates", Annual book of ASTM Standards, Section 3, vol 03.01., ASTM, (1991)

/15/ *P. R. Smith, J. A. Graves and C. G. Rhodes*: " Evaluation of a Ti-22Al-23Nb orthorhombic alloy for use as the matrix in a high temperature Ti-based composite", Mat. Res. Soc. Symp. Proc., 273. pp. 31-42, (1992)

/16/ *S. Luetjering, P. R. Smith, S. M. Russ and D. Eylon:* "The Effect of Post Consolidation Heat Treatments on the Isothermal Fatigue of Ti-22Al-23Nb in Neat Matrix Form", FATIGUE '96, Proc. of the Sixth International Fatigue Congress, pp 1767 - 1772, (1996)

/17/ *S. Lesterlin, C. Sarrazin-Baudoux andJ. Petit:* "Temperature-environment interactions and fatigue behavior inTi6242 alloy", Titanium '95, Proc. of the 8th World Conf. on Titanium, eds. P. A. Blenkinsop, W. J. Evans and H. M. Flower, pp 1211 - 1218, (1996)

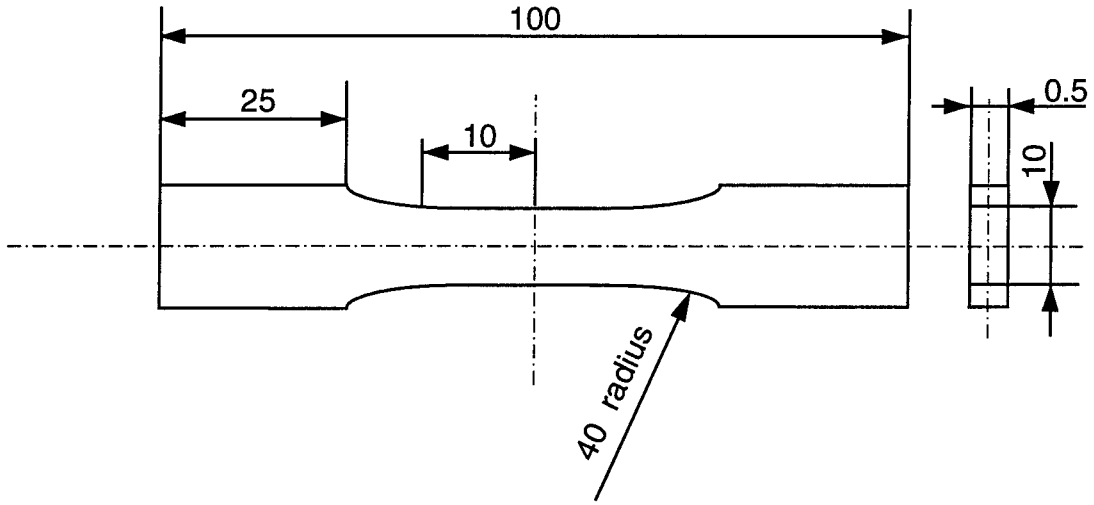

a

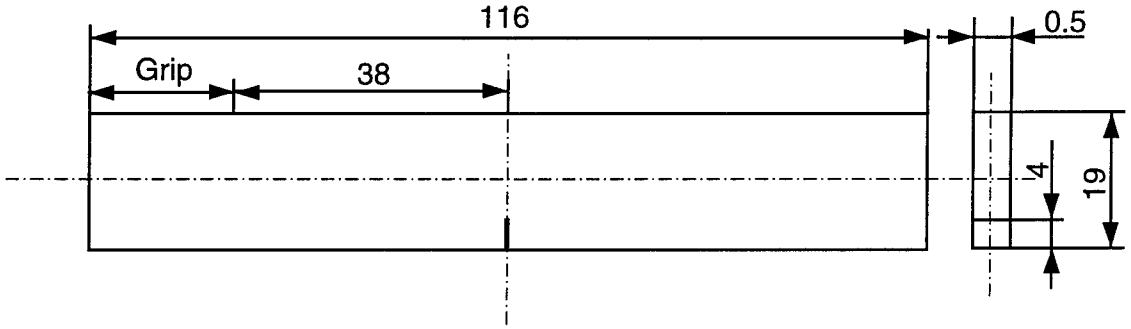

b

Figure 1: Schematic drawing of a) dogbone specimen used for tensile testing and b) straight sided single edge notched (SEN) specimen used for fatigue crack growth testing

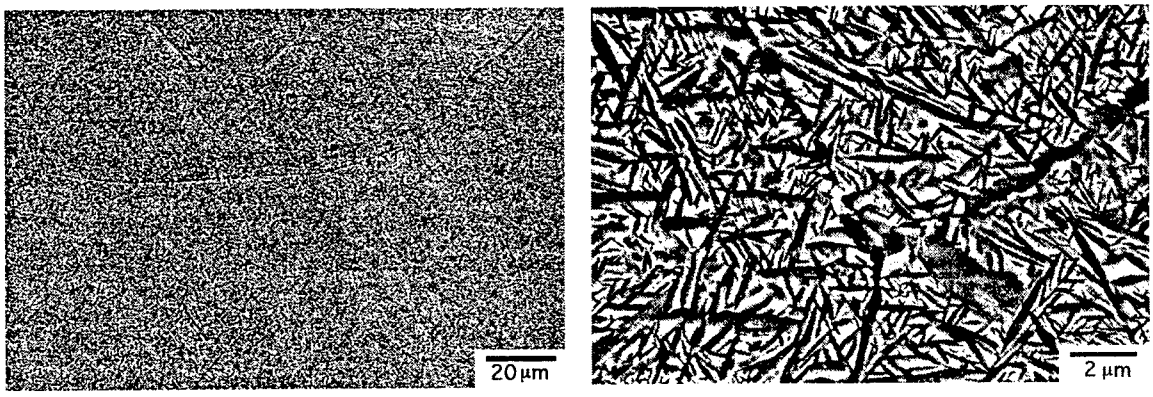

Figure 2: SEM micrographs of the fully transformed microstructure

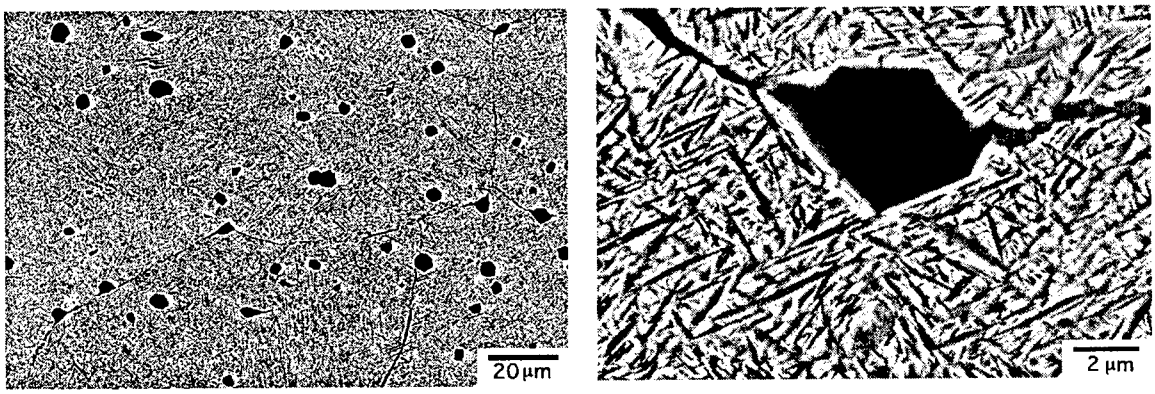

Figure 3: SEM micrographs of the duplex microstructure

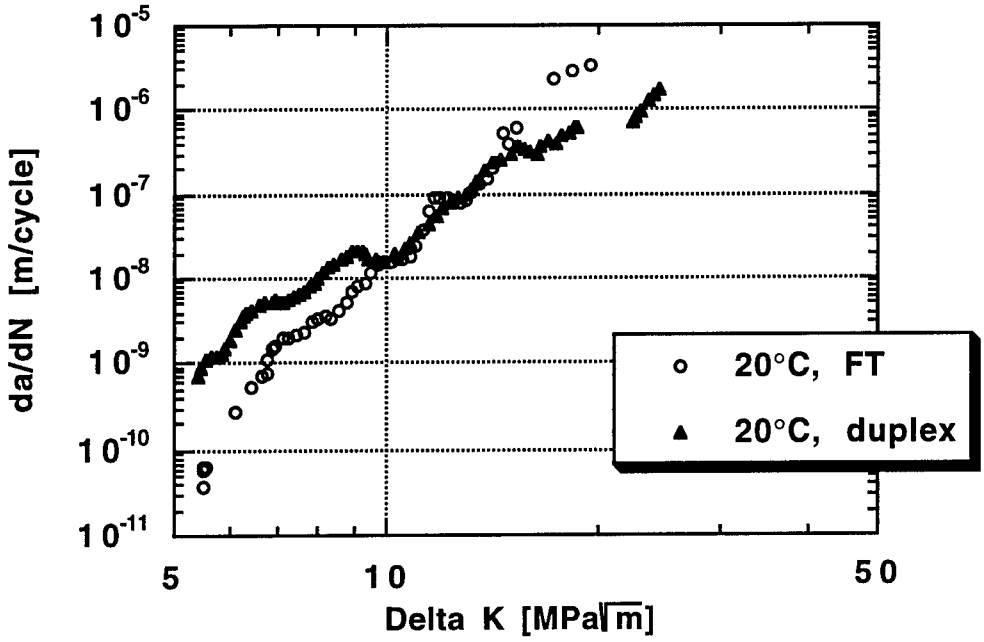

Figure 4: da/dN-ΔK curves for the fully transformed and duplex microstructure tested at 20°C in lab air

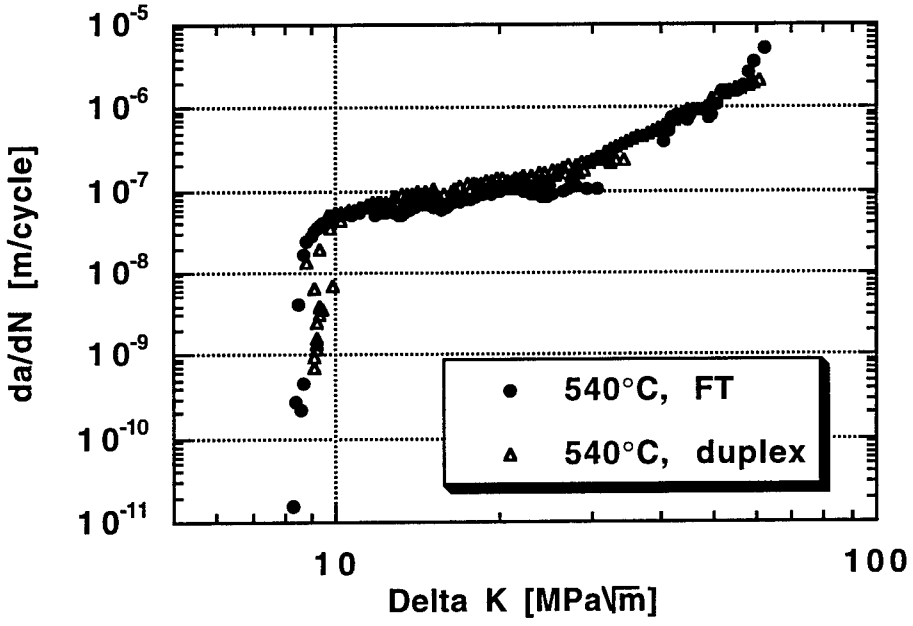

Figure 5: da/dN-ΔK curves for the fully transformed and duplex microstructure tested at 540°C in lab air

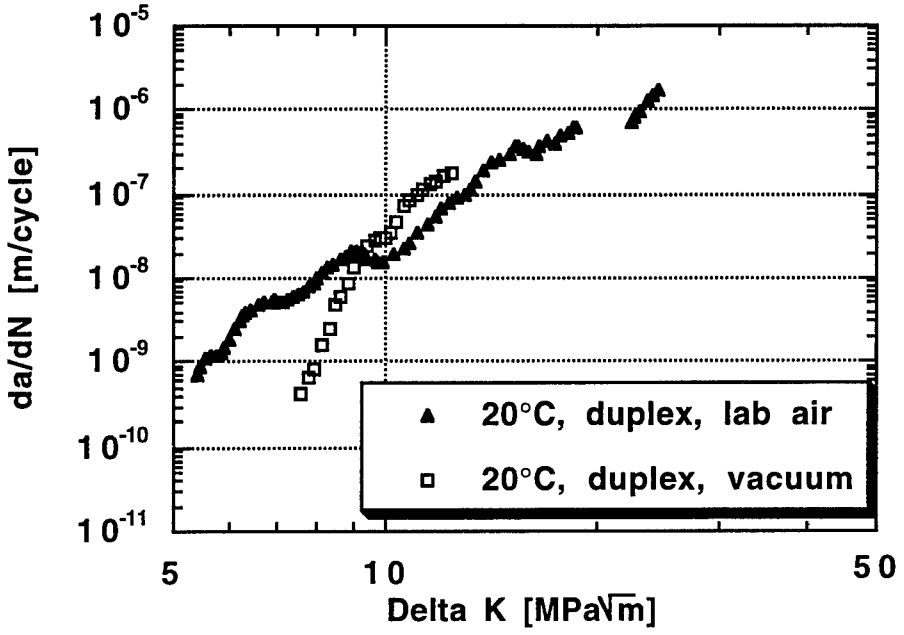

Figure 6: da/dN-ΔK curves for the duplex microstructure tested at 20°C in lab air and in vacuum

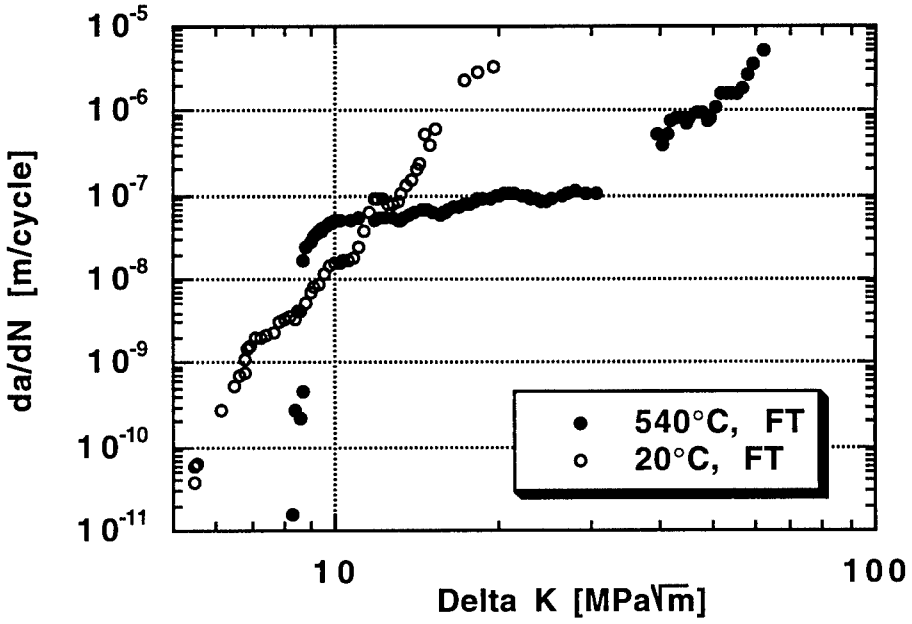

Figure 7: da/dN-ΔK curves for the fully transformed microstructure tested at 20°C and 540°C in lab air

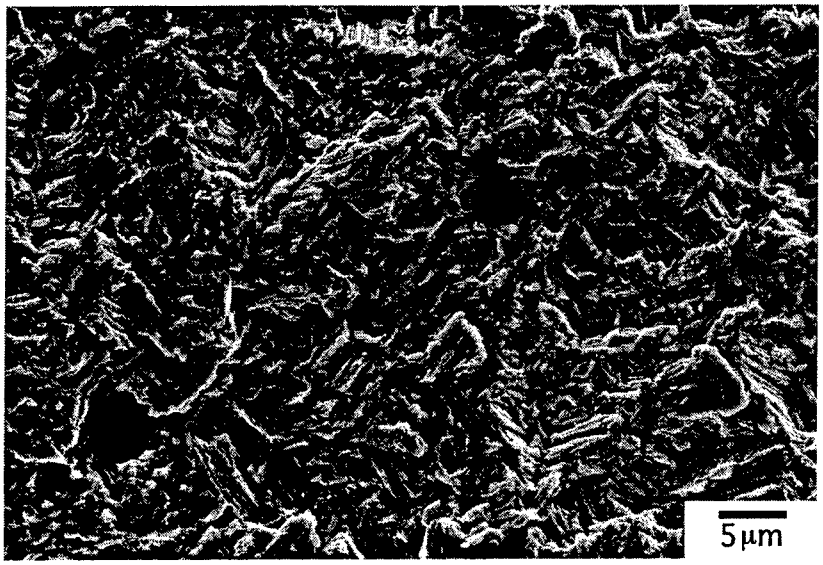

Figure 8: Fracture surface of a FCG specimen (duplex microstructure) tested at 20°C in lab air. Fatigue crack growth rates of 6×10^{-7} m/cycle ($\Delta K = 20$ MPa$\sqrt{m}$)

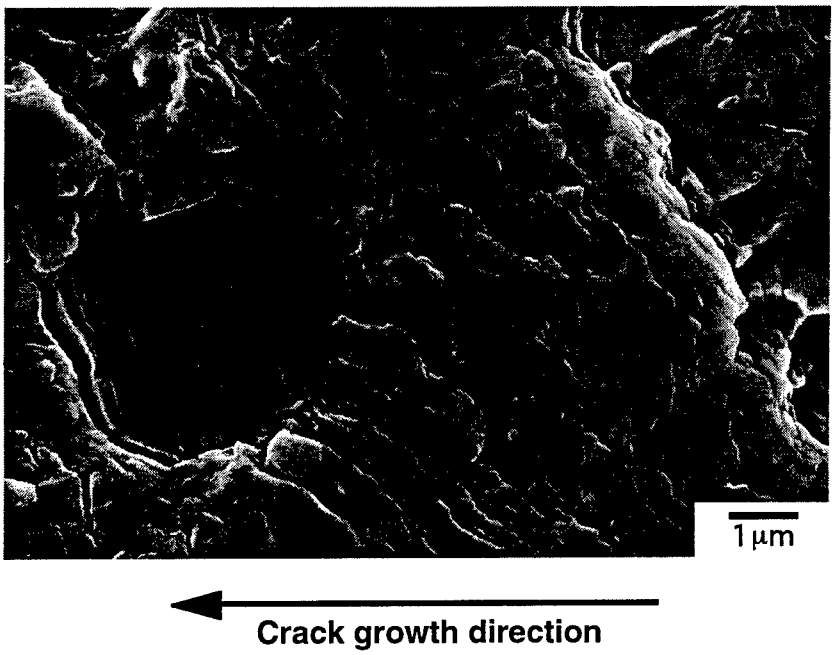

Figure 9: Fracture surface of a FCG specimen (duplex microstructure) tested at 540°C in lab air. Fatigue crack growth rates of 2×10^{-7} m/cycle ($\Delta K = 20$ MPa$\sqrt{m}$)

COMPARISON OF SELF-ASSEMBLED MONOLAYERS AND CHITOSAN AS FUNCTIONAL SUBSTRATES FOR DEPOSITION OF ULTRATHIN PHOTORESPONSIVE FILMS.

John L. Hazel
Graduate Student
Department of Construction Materials and Industrial Design

Western Michigan University
1057 Kohrman Hall
Kalamazoo, MI 49008

Final Report for Summer Graduate Student Research Program

Sponsored by:
Air Force Office of Scientific Research
Bolling Air Force Base, DC

and

Wright Laboratory
MLPJ

August 1997

COMPARISON OF SELF-ASSEMBLED MONOLAYERS AND CHITOSAN AS FUNCTIONAL SUBSTRATES FOR DEPOSITION OF ULTRATHIN PHOTORESPONSIVE FILMS.

John L. Hazel
Graduate Student
Department of Construction Materials and Industrial Design
Western Michigan University

Abstract

Chitosan, an extract from the exoskeleton of arthropoda is compared to a traditionally prepared self-assembled monolayer (SAM) for its suitability as a functional substrate in constructing multilayers of C60-Porphyrin. Measurement of topography, friction, chemical composition, mechanical stiffness and stability of the surface was performed by adaptation of recently developed atomic force microscope (AFM) procedures. While the SAM has a theoretically superior surface character as a substrate for multilayer photoresponsive films, the chitosan was found to be superior in qualities critical for adsorption and mechanical stability. This is due to the different distribution and mechanical stabilization of surface functional amine groups controlled by the helical intramolecular structure of chitosan macromolecules.

COMPARISON OF SELF-ASSEMBLED MONOLAYERS AND CHITOSAN AS FUNCTIONAL SUBSTRATES FOR DEPOSITION OF ULTRATHIN PHOTORESPONSIVE FILMS.

John L. Hazel

Introduction

Siloxane based self-assembled monolayers (SAM) anchored to hydroxyl bearing surfaces were introduced in 1983[1] and are now considered a well established tool for use in surface modification. A typical Siloxane based SAM consists of a Siloxane group for chemically binding the molecule onto the surface and a functional group that has the desired character for the final surface. The two groups are typically connected by a chain of carbon atoms (Fig. 1). The concept of having a majority of the binding groups on the solid substrate and most of the functional groups on the outermost plane of the surface layer is generally accepted. However, in recent work by Hao at WL/MLPJ a comparison of NH_2 terminated silane SAM with chitosan adsorption substrates showed that sulphonated C_{60} was adsorbed several times greater on the chitosan surface (Fig. 2). The difference in adsorption continued through subsequent electrostatic self-assembly[1] of C_{60}-porphyrin bilayers (Fig 3). These bilayers were of interest for their synergistic enhancement of optical florescence vs. the expected simple arithmetic sum when the two are combined (Fig 4). The greater adsorption on the chitosan is in contradiction with the theoretical density of NH_2 groups on the SAM, $5x10^{14}/cm^2$, being about 3 times greater. One possible cause of this contradiction is a non-ideal structure in the SAM.

As mentioned earlier, many investigators have demonstrated SAMs. However, reported successful building of well ordered SAMs with functional terminal groups has been rare. A review of the literature reveals several other troublesome observations about

functionalized SAMs that can easily be explained by assuming that the SAM is really a disordered ultrathin layer with only sparse chemical bonding to the substrate: easier mechanical scratching of films deposited on SAMs vs. bare silicon when there is an expected stronger attraction of the film,[2] little change in composition with respect to XPS takeoff angle,[3] smaller than expected water contact angles,[4] irreversible distortion (wear) of the silane SAM by AFM tips under conditions that do not damage alkanethiol SAMs on gold,[5] large hysteresis in advancing and retracting contact angle measurements.[6] In fact, direct report of the difficulty in forming SAMs from silanes having functional termination of NH_2 has been made and an alternative approach of adding the NH_2 after silane and carbon chain surface attachment was proposed and attempted.[7,8] An additional alternative for the production of gold-alkanethilol directed SAMs involving ultraflat template stripped epoxy surfaces resulting in NH_2 terminated substrates that are transparent enough for optical microscopy has been demonstrated.[9]

Methodology

Surface preparation. NH_2 terminated SAM was produced at MLPJ on glass microscope slides (Fisher finest). 3-aminopropyltriethoxysilane ($C_9H_{23}NO_3Si$) was added to 95% ethanol 5% milli-Q water for a final concentration of 2% 3-aminopropyltriethoxysilane. This solution was allowed to stand for 15 minutes for hydrolysis of the silanol after which the substrates were immersed in the solution for 30 minutes. The substrates were then removed from the solution and rinsed with ethanol twice and kept overnight in a dry N_2 atmosphere. Before application of C_{60}-porphyrin bilayers the silanized surfaces were protonated by immersion in .01N HCl for 10 minutes.

The chitosan substrates were spin coated onto glass slides. A 2% weight solution of chitosan in water was spin coated at 800 RPM. The samples were then dried overnight in a vacuum oven at 50 degrees C. The resulting films had thickness of about 0.5 μm as measured by AFM across intentional scratches.

Measurements. Surface roughness was measured in contact mode with a Digital Instruments Nanoscope using Digital Instruments "short narrow" V-shaped tips. Scans of 1 μm square were collected at 2-4 Hz scanning rates. Contact forces were minimized during topography scans to avoid damaging the surface being measured. Calculation of roughness was done both on the full 1 μm scan and a smaller area of about 200 nm square as a rapid test of the effect of scale on measured roughness. Friction maps were simultaneously collected with all topography images. Tips were changed when artifacts appeared in the collected images.

Variation of contact forces was exploited to test the mechanical stability of the silane and chitosan layers. A high force contact was established and then several complete scans were made at 20 Hz in an attempt to scratch or plow away the surface layer. The scan force was then reduced and the scan size increased to reveal any damage caused by the previous high rate, high force, scanning.

Tip-surface adhesion was measured by locating the AFM tip out of contact and then extending the piezo tube until contact was detected by deflection of the tip. The piezo tube was then retracted until the spring force of the cantilever pulled the tip off the surface. The maximum negative deflection of the cantilever in this process then indicates surface-tip adhesion. Chemically modified cantilevers produced at WMU[10] with NH_2 functionalized contact points were used to assess the surface chemical and electrostatic

interaction of bare glass, silanized glass and chitosan surfaces. This was used as an indicator of surface coverage by chemically active or charged molecular groups.

The approach-retract cycling of the AFM tip was also employed to assess the mechanical stability of the C_{60}-Porphyrin bilayers. The initial cantilever deflection is smaller on soft samples that allow some penetration of the tip into the surface.[11] This method was modified by performing the surface probing under water. The strong capillary attractive forces were thereby eliminated allowing detection of penetration at the initial stages of tip-surface contact. There is a definite difference in the stability or hardness of the bilayers when they are examined this way. Testing mechanical stability of the C_{60}-porphyrin layers by the AFM scratching test mentioned above was not feasible due to the tip destroying abrasiveness of C_{60}. This nanoindentation under fluid was therefore an important technique for mechanical analysis.

Results and Discussion

The bare glass slides showed smooth 100x100 nm areas of about 0.7 nm rms with ~5 nm wide pits and bumps spaced about 100 nm which brought the rms roughness for a 1 μm scan size to 1.2 nm (Fig. 4). Silanized glass showed some smoothing of the bare glass surface with the overall roughness reduced to 0.4 nm rms at the 1 μm scale (Fig 5). The spin coated chitosan surface showed a fine (lateral periodicity ~5 nm) grainy texture with calculated 1 μm rms roughness of 0.9 nm, the 200 nm scale roughness was 0.8 nm (Fig. 6). Neither the silanized glass nor the chitosan surface roughness was significantly changed by the adsorption of the sulphonated C_{60}. This indicates that the C_{60} layer was not composed of aggregates but was actually adsorption of individual C_{60}.

An AFM wear resistance test on the silanized and chitosan surfaces was performed using the method described above. This test done in air produced similar results for both samples. The high force scanning areas showed only slight changes in topography and friction. However, when this test was repeated with the scanning done under water, the results were dramatically different between the two surfaces. The chitosan showed little damage in the topography image with friction being generally reduced in the high force area (Fig. 7). This large change in friction paired with the small change in topography indicates a slight reordering of the surface layer but no actual displacement of material during the high force scanning. Chitosan has the advantage of being a polymer, so nearly all monomers of this material have their position maintained by at least two chemical bonds. Conversely, the silane layer was completely removed by the high force scanning under water (Fig 8). This is confirmed by the higher friction in the worn area where the tip is in contact with the substrate. This increased susceptibility to wear under water indicates that the water is able to soften or loosen the silanes. However a chemically attached silane would not change its wear resistance so much under fluid. Also of interest are the domains shown in the friction image which are only faintly reflected in the topography. This might be an effect of changes in the surface layer ordering in the silanes.

The adhesive force measurements for an unmodified tip on the two surfaces showed nearly identical values (Fig 9). With an AFM tip having NH_2 terminated surface modification, the adhesive forces are much smaller on the chitosan surface which indicates that the surface density of NH_2 groups is much greater than the silanized surface or that the contact area is much larger (Fig 10). Note that the scales in each figure are

identical but the scale of figure 10 is not identical to that of figure 11 due to uncertainty of spring constant in the AFM cantilevers.

In tests using a stiff cantilever, the relative hardness of the chitosan-porphryn bilayers were tested as the number of bilayers were added. Note the point where the tip makes contact in the one bilayer force curve for each surface (Fig 11,12). The chitosan surface shows a larger penetration by the AFM tip in the initial contact. This can be seen by the large radius of the "corner" formed as the tip deflection begins during initial contact of the chitosan surface. This result is expected since the chitosan layer is much thicker than the silane. Note also the presence of a "jump to contact" evident in the silane layer. Moving to the force curves for 3 bilayers, the radius of the initial contact is much smaller on the chitosan surface. In fact the change is very sharp indicating almost no penetration by the AFM tip. In contrast, tip penetration of the 3 and 5 bilayers on silane samples is apparent. This indicates that chitosan adsorbs the bilayers and packs them closely enough that they support each other at or before the 3rd set of bilayers are deposited. Bilayers on the silane substrate do not display this until after more than five bilayers are applied. The force curve for the 10 bilayer sample of the silanized substrate indicates the surface penetration is minimal so there is some self reinforcement of the adsorbed material before the tenth bilayer. These comparative results are consistent with the adsorption data provided by Hao at WL/MLPJ. Suface hardness increases with the number of bilayers much more quickly in samples with chitosan substrates.

Conclusion

If the SAM studied in this work is indeed a disordered layer then the explanation for lower adsorption of sulphonated C_{60} is fairly straightforward. Most of the NH_2 groups are buried inside the SAM and therefore less likely to attract a C_{60}. Many of the NH_2 that are exposed at the surface will be part of silane groups that have not made a chemical attachment to the surface. Each C_{60} that adsorbs to the surface could then draw nearby NH2 terminated molecules. This would further reduce available adsorption sites and also mask some or all of the SO_2 sites on the adsorbed C_{60} inhibiting attachments of the subsequent porphyrin molecules. This reduction in adsorption and the masking of C_{60} sulphonates explains the propagation of the reduced adsorption to subsequent bilayers.

The obvious solution to these problems is to expose more NH_2 groups at the surface and keep them from moving around. Chitosan is a good candidate for achieving this solution. The chitosan used here is a polymer with a helical backbone and molecular weight of about 70,000. The helical backbone is beneficial in this situation because it insures that some NH_2 is exposed at the surface. The backbone of the polymer also provides a relatively regular spacing and orientation of the active groups thus insuring that a fairly homogeneous distribution of favorably oriented NH_2 appears at the surface. This spacing is enforced by the bonds along the chitosan polymer. When the sulphonated C_{60} is adsorbed the chitosan polymer bonds prevent adjacent NH_2 groups from migrating to it. The NH_2 is then available to attract sulphonated C_{60} and is also keeping active adsorption sites on already deposited C_{60} available for adsorbing porphryn in the next step of the electrostatic assembly process. The stable location of the NH_2 then adsorbs the C_{60} in a more tightly packed layer which also contributes to the mechanical stability.

Data from the application of various atomic force microscope (AFM) techniques such as chemical force microscopy (CFM), friction force microscopy (FFM) to this problem indicate that the most straightforward explanation for the discrepancy is that the SAMs used in these experiments are very disordered ultrathin coatings. Additionally the chitosan substrate showed a superior tendency to stabilize bilayers of C_{60}-porphyrin.

References

1. Netzer L., Sagiv J.; J. Am. Chem. Soc. 105 674 (1983)
2. Lvov Y. M., and Decher G.; Crystallography Reports 39 696 (1994)
3. Ararwal M., DeGuire M. R., and Heuer A. H.; Appl. Phys. Lett. 71 891 (1997)
4. Trevor J. L., Mencer D. E., Lykke K. R., Pellin M. J. and Hanley L.; Anal. Chem. 69 4331 (1997)
5. Laibinis P. E. and Whitesides G. M.; J. Am. Chem. Soc. 114 1990 (1992)
6. Xiao X, Hu J. Charych, and Salmeron M.; Langmuir 12 235 (1996)
7. Wasserman S. R., Tao Y., Whitesides G. M.; Langmuir 5 1047 (1989)
8. Balachander N. and Sukenik C. N.; Langmuir 6 1621 (1990)
9. Wagner P., Hegner M., Guntherodt H., Semenza G.; Langmuir 11 3867 (1995)
10. Tsukruk V. V. and Bliznyuk V. N.; Langmuir accepted.
11. Vanlandingham M. R., McNight S. H., Palmese G. R., Elings J. R., Huang X. Bogetti T. A., Eduljee R. F., and Gillespie J. W. Jr.; J. Adhesion 64, 31 (1997)

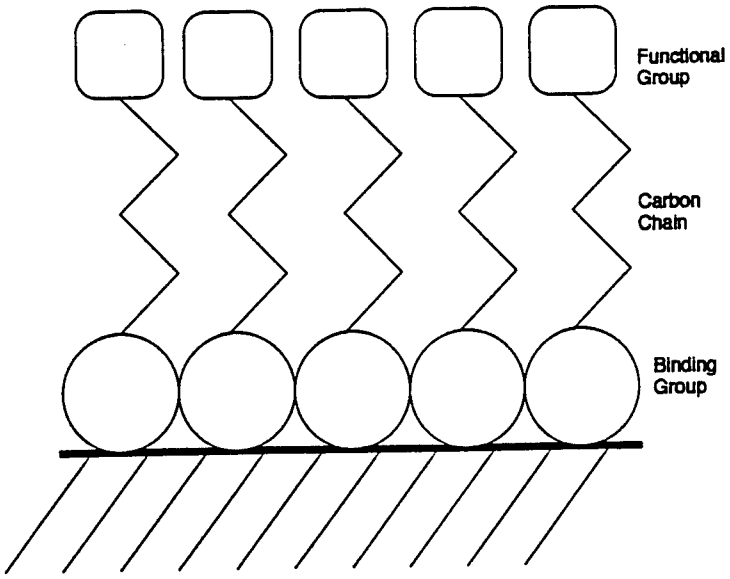

Figure 1 Typical SAM conceptual illustration.

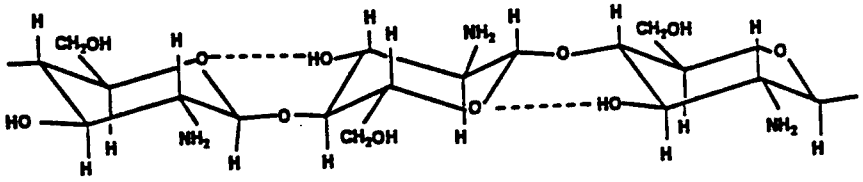

CHITOSAN

Figure 2

Supplied by Hao

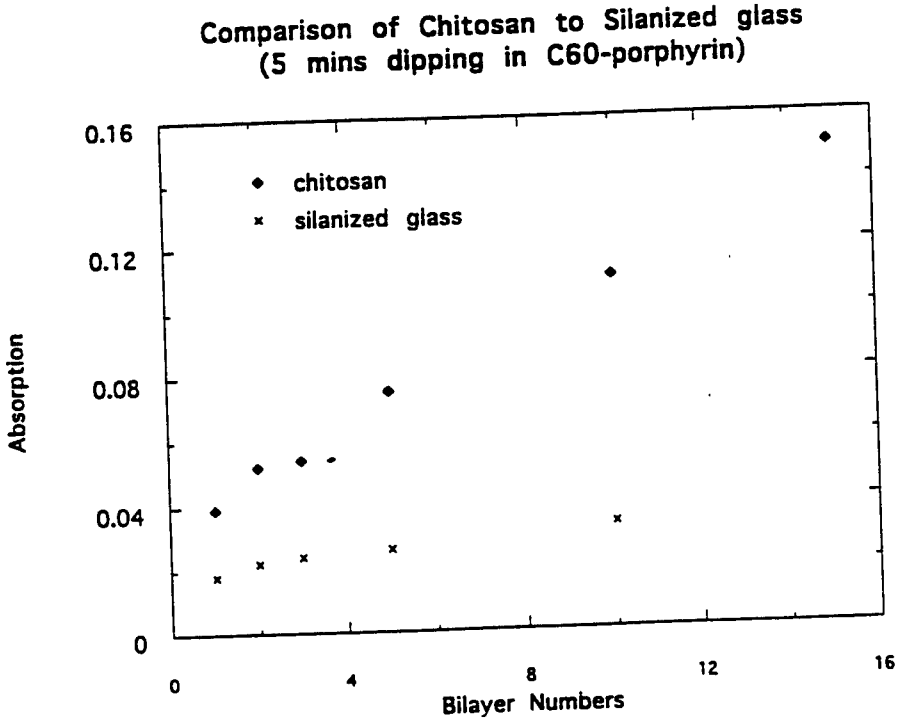

Figure 3

Supplied by Hao

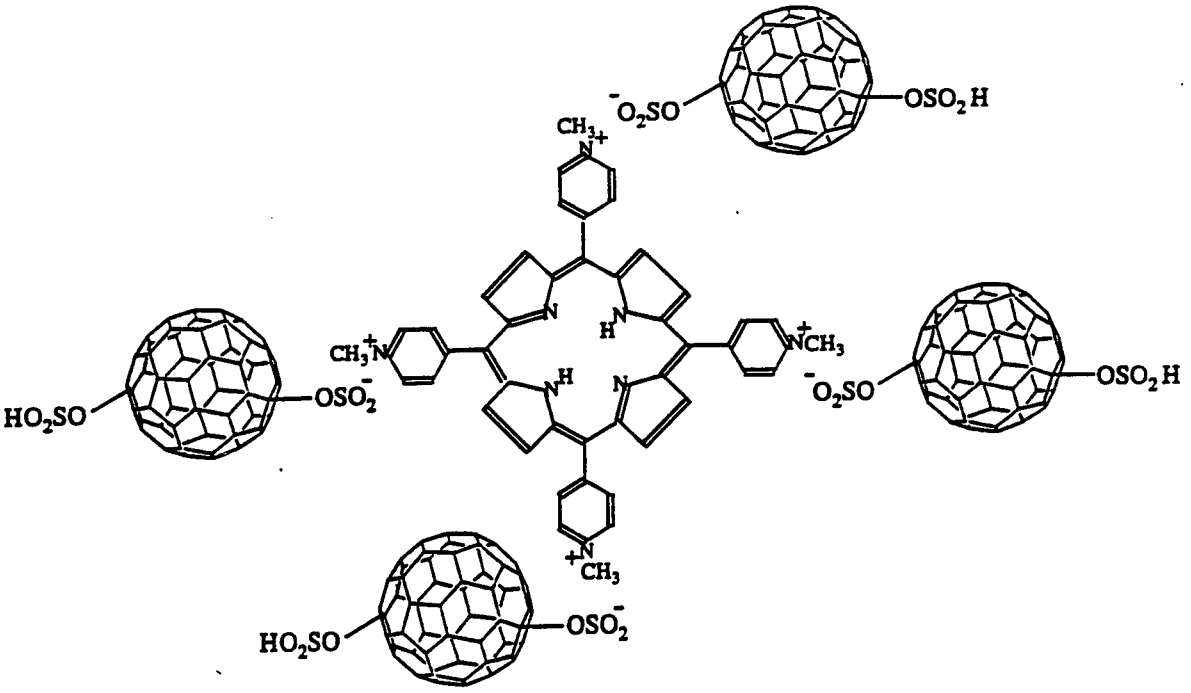

Supplied by Hao

Figure 4

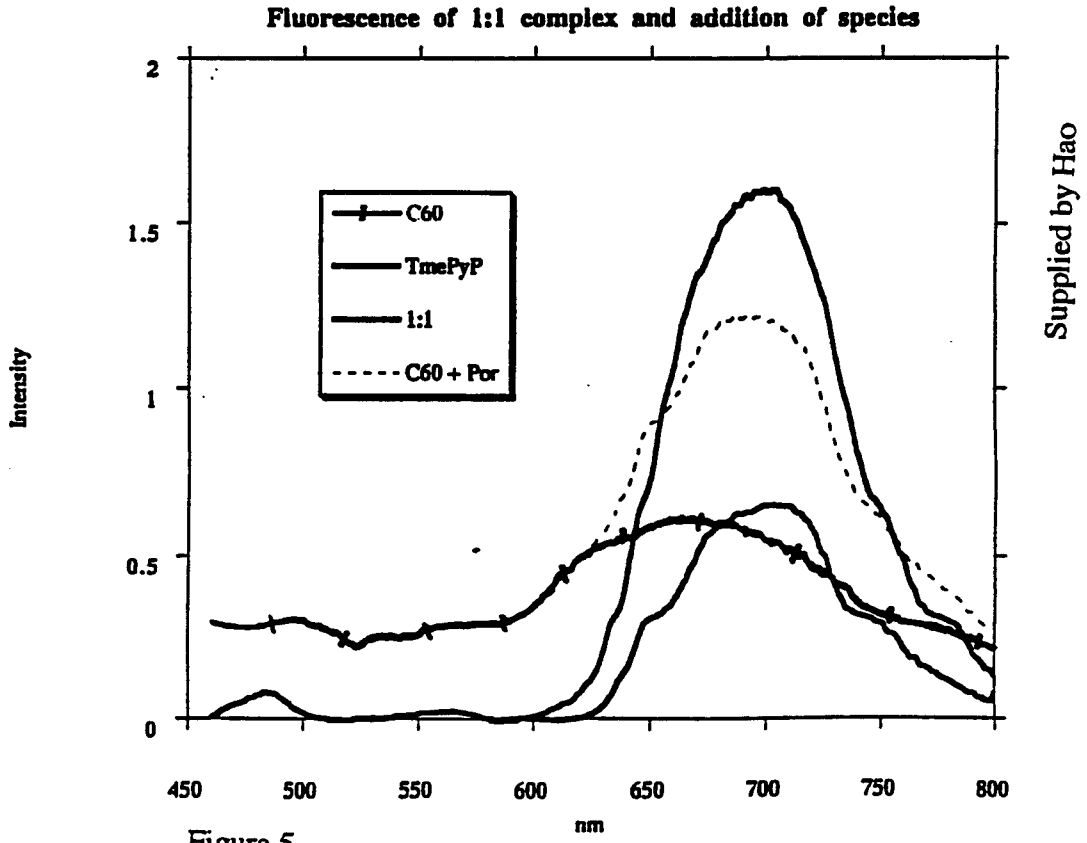

Supplied by Hao

Figure 5

Peak Surface Area Summit Zero Crossing Stopband Execute Clear

Roughness Analysis

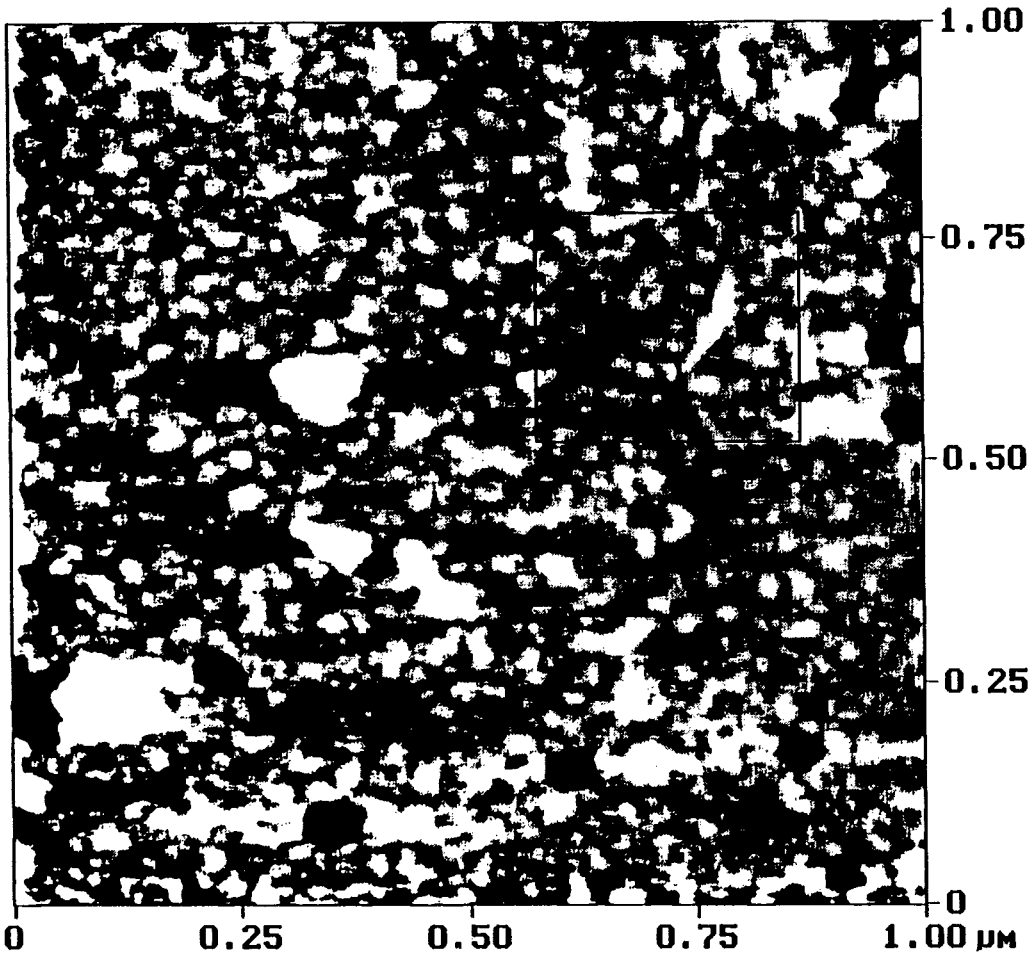

glasn.016

Image Statistics

Img. Z range	17.946 nm
Img. Mean	-0.000000 nm
Img. Raw mean	7.486 nm
Img. Rms (Rq)	1.171 nm
Img. Ra	0.731 nm

Box Statistics

Z range	8.298 nm
Mean	-0.085 nm
Raw mean	3.605 nm
Rms (Rq)	0.687 nm
Mean roughness (Ra)	0.478 nm
Box x dimension	290.20 nm
Box y dimension	258.82 nm

Peak off Area off Summit off Zero Cross off

Figure 6

Peak Surface Area Summit Zero Crossing Stopband Execute Clear

Roughness Analysis

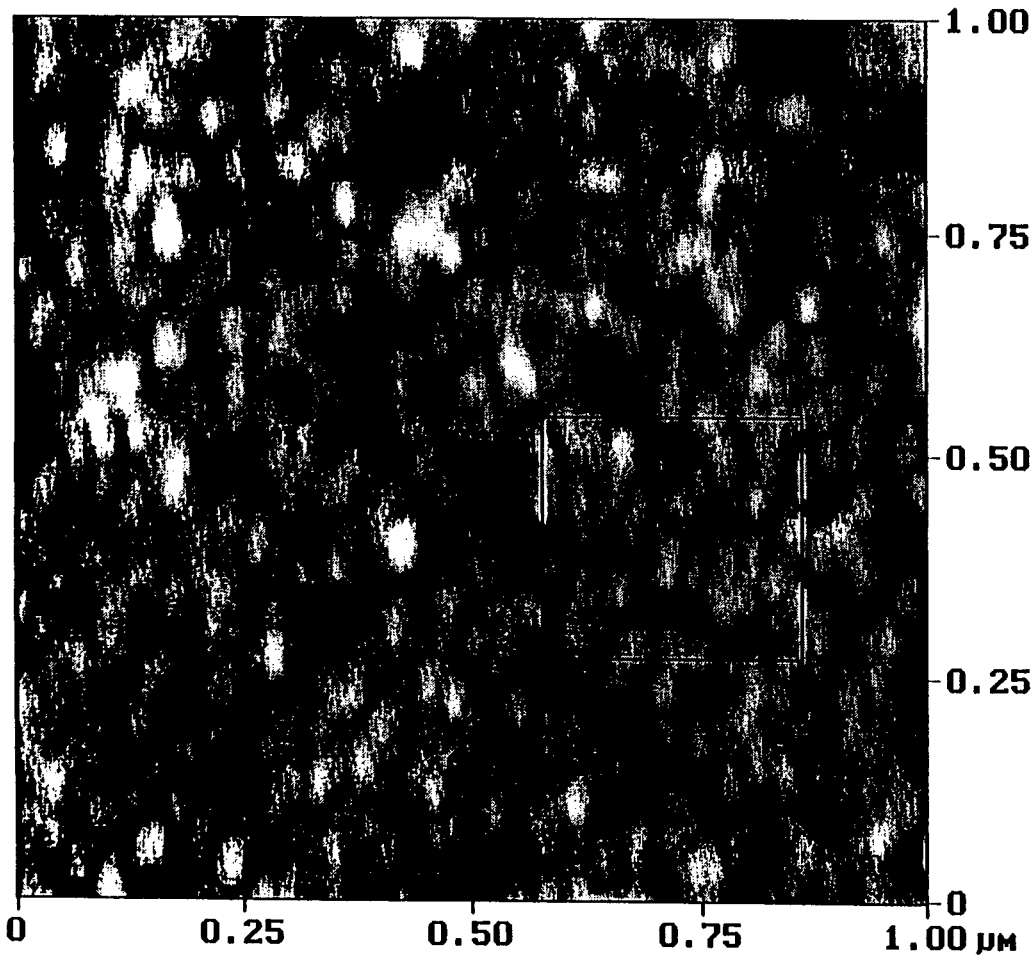

siglasn.010

Image Statistics

Img. Z range	4.316 nm
Img. Mean	-0.000000 nm
Img. Raw mean	0.860 nm
Img. Rms (Rq)	0.404 nm
Img. Ra	0.303 nm

Box Statistics

Z range	2.375 nm
Mean	0.063 nm
Raw mean	2.663 nm
Rms (Rq)	0.324 nm
Mean roughness (Ra)	0.244 nm
Box x dimension	286.27 nm
Box y dimension	274.51 nm

Peak off Area off Summit off Zero Cross off

Figure 7

Peak Surface Area Summit Zero Crossing Stopband Execute Clear

Roughness Analysis

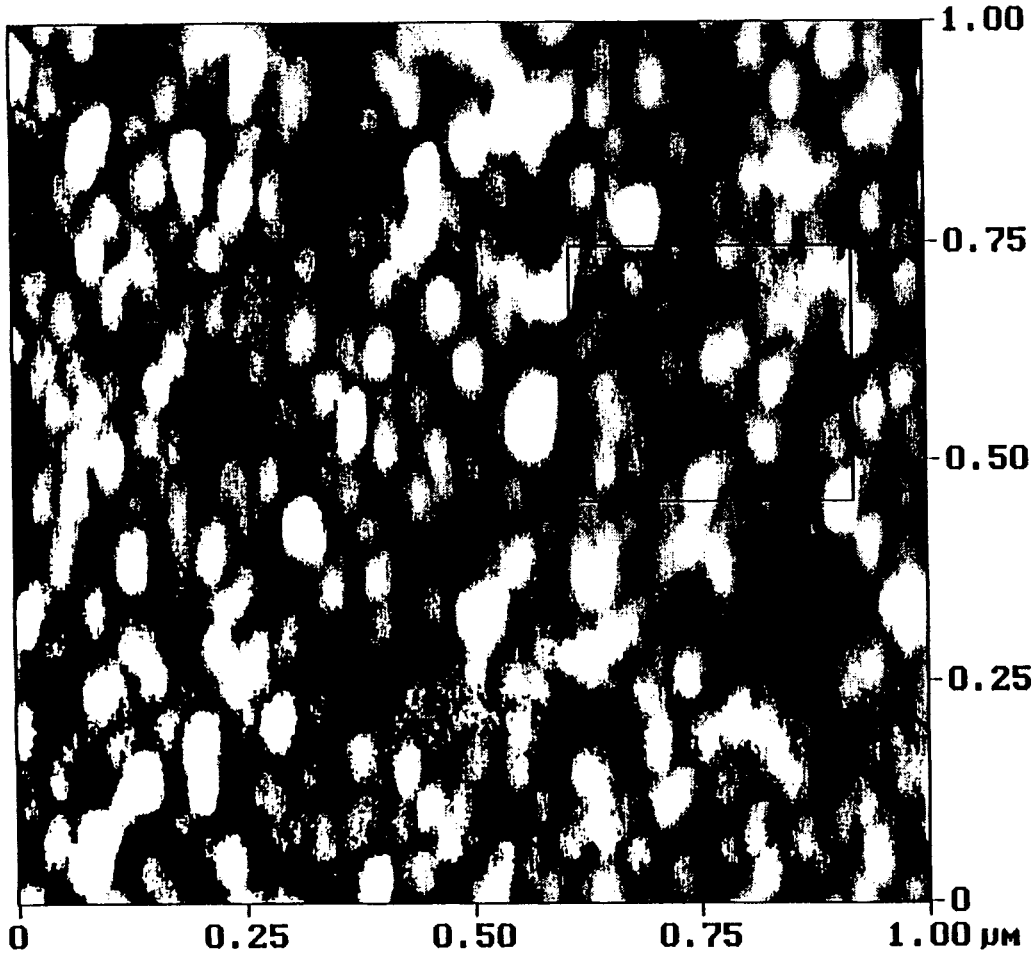

chiton.004

Image Statistics

Img. Z range	6.456 nm
Img. Mean	0.000000 nm
Img. Raw mean	0.396 nm
Img. Rms (Rq)	0.882 nm
Img. Ra	0.705 nm

Box Statistics

Z range	4.510 nm
Mean	-0.091 nm
Raw mean	8.446 nm
Rms (Rq)	0.788 nm
Mean roughness (Ra)	0.639 nm
Box x dimension	309.80 nm
Box y dimension	294.12 nm

Peak off Area off Summit off Zero Cross off

Figure 8

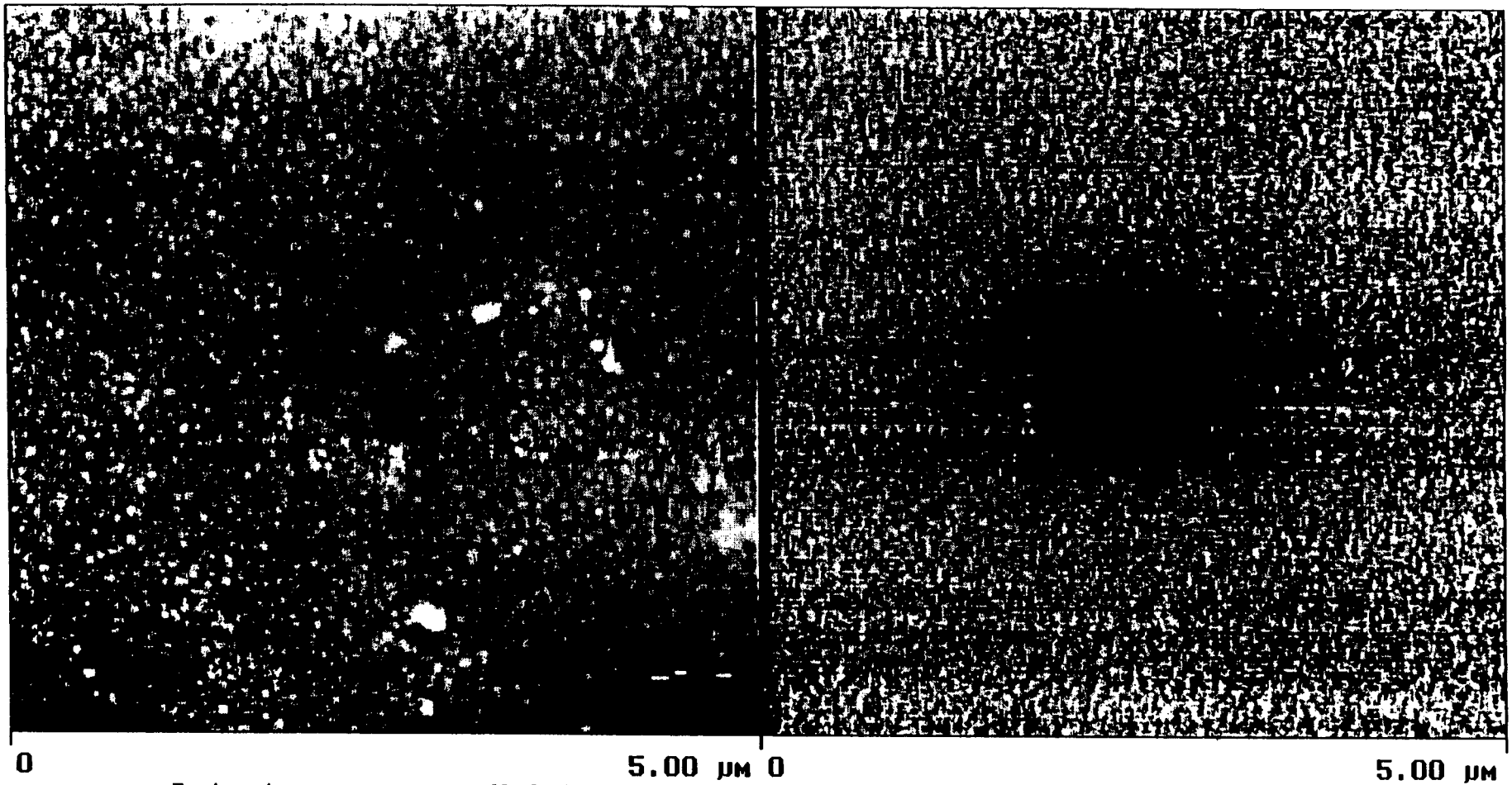
0
5.00 µm 0
5.00 µm
Data type
Height
Z range
25.0 nm
Data type
Friction
Z range
0.500 V
c60low11.008

Figure 9

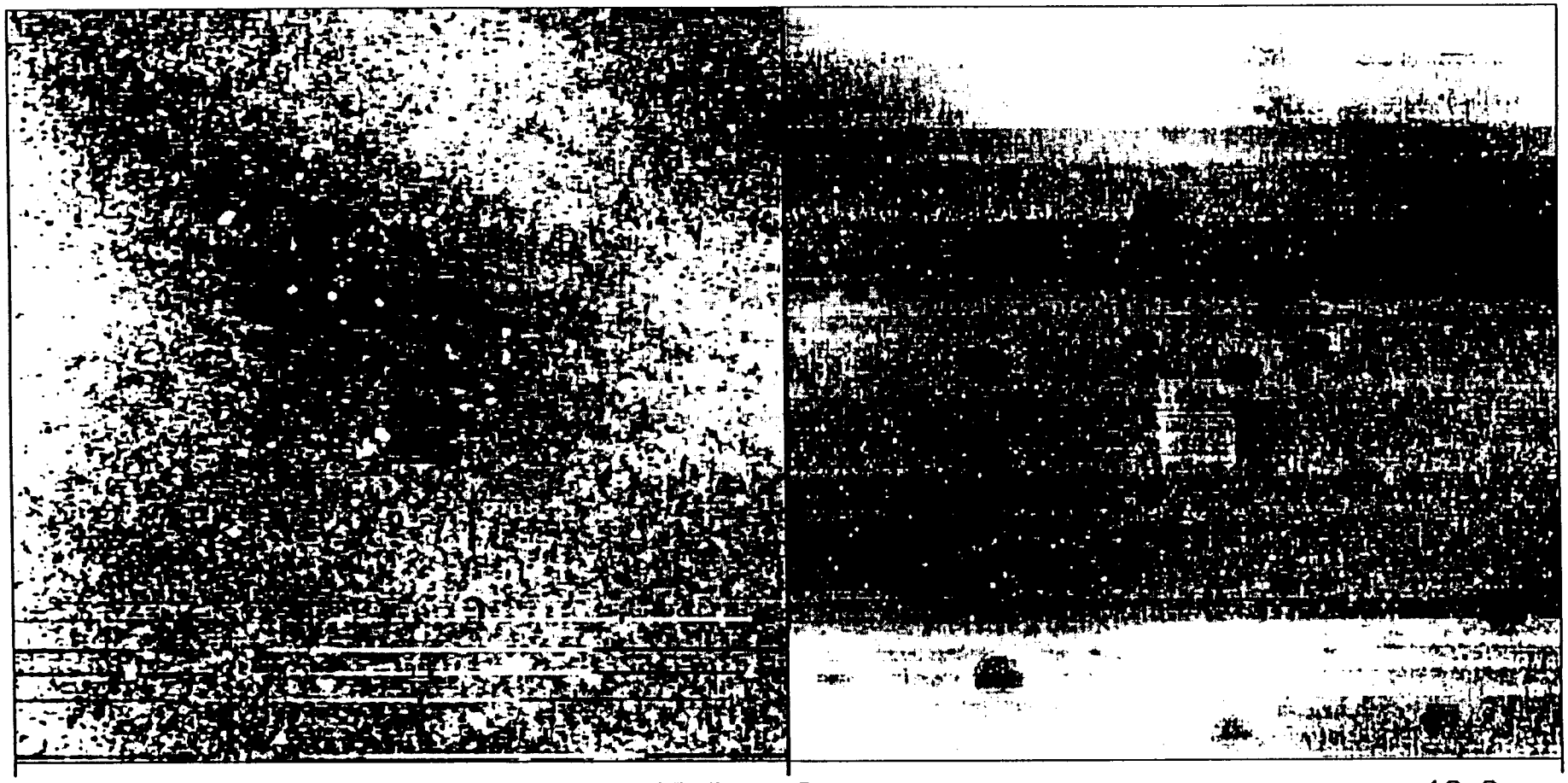

si.009

Figure 10

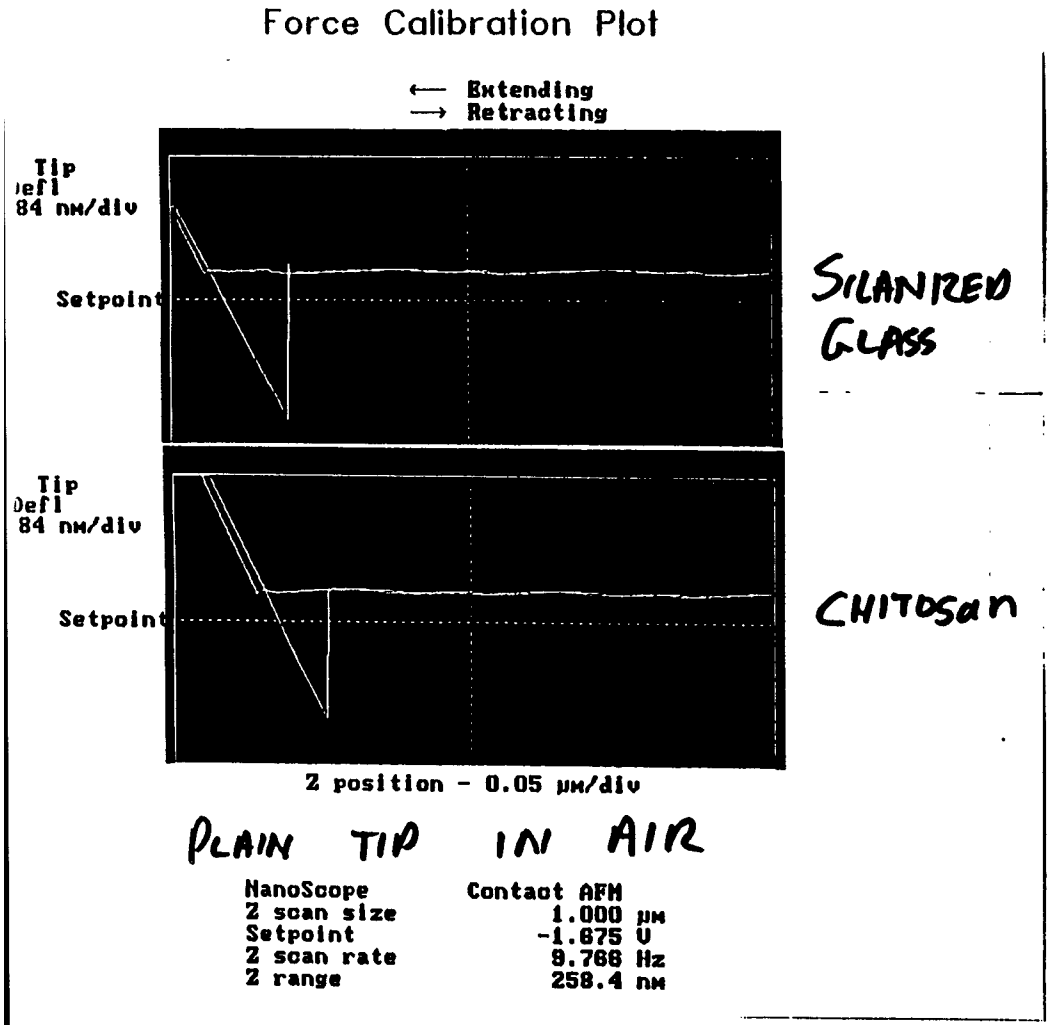

Figure 11

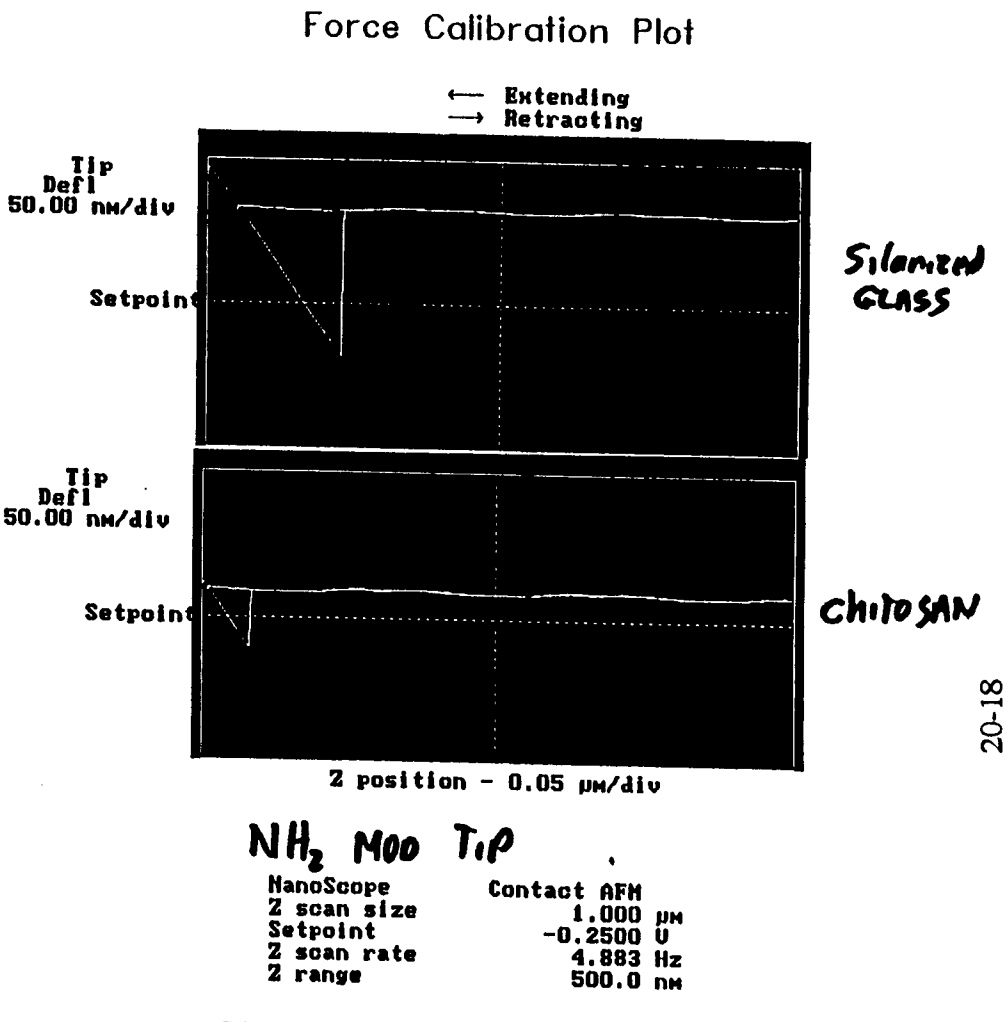

Figure 12

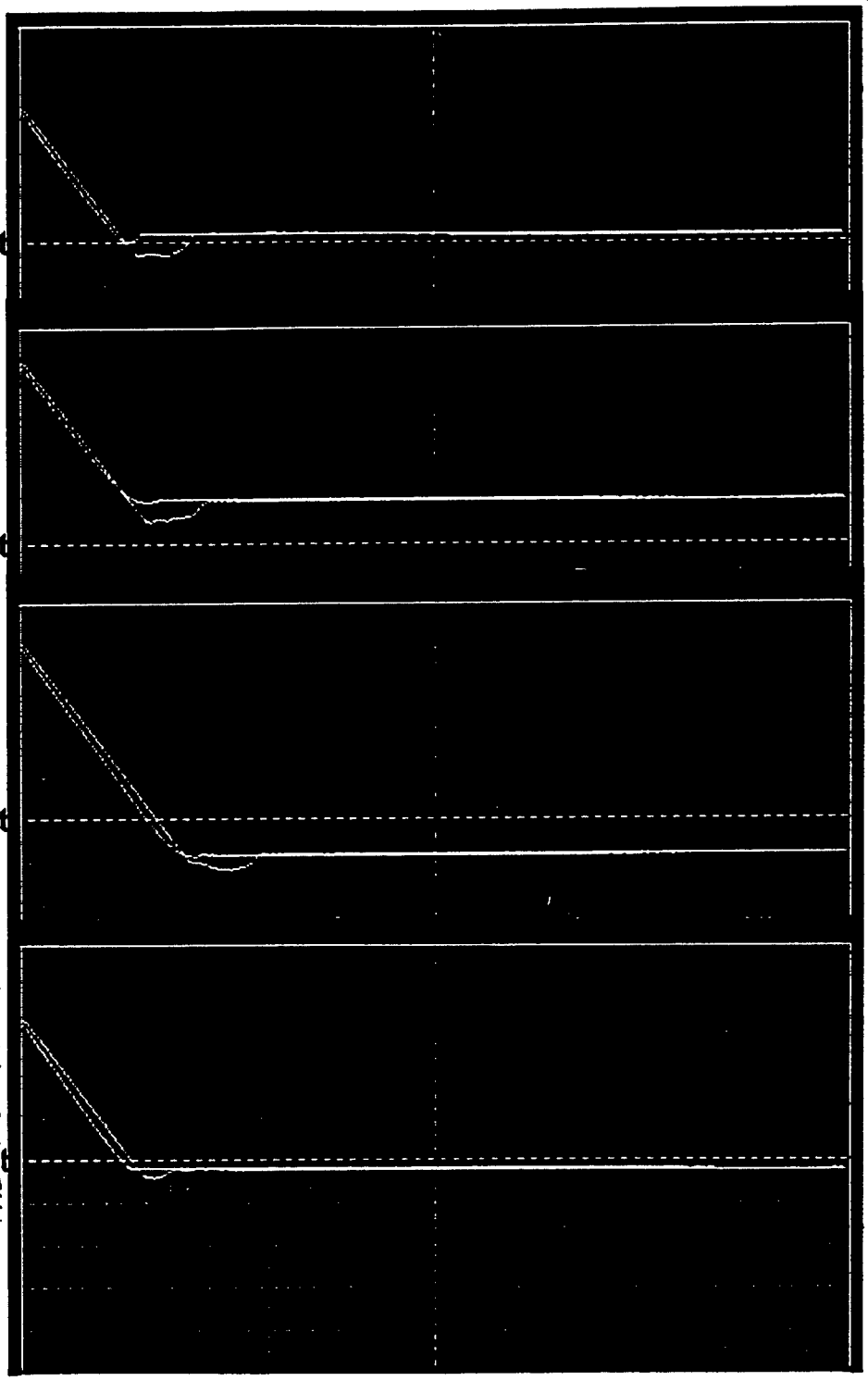

Figure 13

SCAN IN H_2O

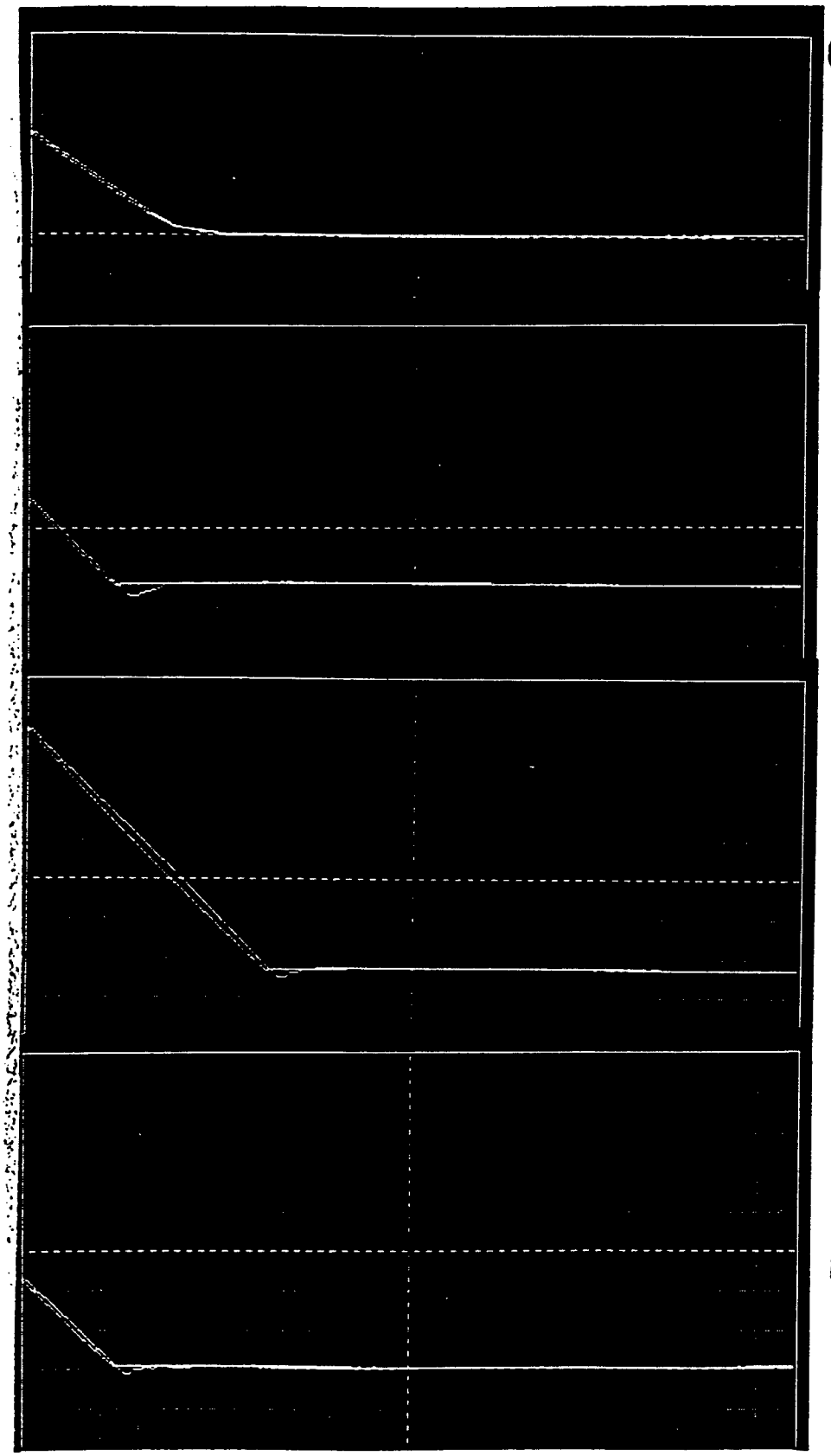

Figure 14

SCAN IN H_2O

Electrical and Mathematical Characterization of the Semiconductor Bridge Ignitor

Alfred LaShawn Malone

Research Assistant

Department of Electrical Engineering

Auburn University

200 Broun Hall

Auburn, AL 36849-5201

Final Report for:

Summer Faculty Research Program

Wright Laboratory

Sponsored by:

Wright Laboratory, Eglin AFB, FL

August 97

Alfred LaShawn Malone

Research Assistant

Department of Electrical Engineering

Auburn University

Abstract

Semiconductor bridge ignitors (SCB) were characterized electrically and mathematically. The voltage and current measurements of the devices were analyzed during excitation by high currents. From these measurements, the resistance, energy and specific action versus time were determined. A mathematical model of the resistance versus energy was then developed. In the near future a more depth analysis will be done on the SCB.

Introduction

Semiconductor bridge ignitors are electro-explosive devices that are used in pyro-igniters and explosive detonators. These devices consist of a heavily doped polysilicon bridge processed on a silicon wafer and aluminum lands used for wire bonding to the detonator header. The SCB has also been used to ignite secondary explosives, such as PETN and HNS.

Typically the ignitor is excited using current generated by a capacitor discharge unit. As the capacitor discharges, the potential across the SCB induces the flow of current through the device and this causes ohmic heating. The bridge vaporizes as the temperature of the Si exceeds its evaporation point which in turn produces an ionized plasma that ignites the pyrotechnic compound. In order to further understand and enhance the use of the device the electrical characteristics must be determined and a mathematical model constructed. This can be achieved by examining the time, current, energy and resistance at burst, and modeling the resistance versus energy. Several SCBs were fired at various voltages while the current and voltage were monitored in order to attain the electrical characteristics. The resistance versus energy curves were then determined and modeled.

Methodology

The devices were fired using a standard fireset with a 0.07 μF capacitor. To simulate a range of possible real life voltages several shots were taken at voltages ranging from 250V to 600 V. This was done to make sure the data was complete and reproducible.

The SCB was mounted on the fireset, and a high voltage pulse was produced to fire the device. The pulse was generated by a pulse generator and a high voltage source. When the pulse generator was triggered, a high voltage potential was placed across the SCB thus allowing current to flow and functioning the device. The current was measured using a current viewing resistor. The voltage was acquired using a standard Hewlett Packard voltage probe. The data was acquired by a Hewlett Packard HP 54542A digital oscilloscope. The data was saved using LabView. LabView is a graphical software package, that saves the data from the oscilloscope in a format that is easily imported into a data analysis software package. The data was then imported into a data analysis software package called VuPoint to get analyzed. A mathematical model of the resistance versus energy was constructed using Table Curve. TableCurve is a software package that fits mathematical functions to the data after analysis.

Results

The SCB active area consists of a heavily doped polysilicon layer. The device is processed on a silicon wafer. A picture was taken of the device before and after firing, shown in Figure 1a and b. In the first photo the narrow region in the middle is the polysilicon bridge and the areas to either side consist the lands and wire bonds. The second photo of the SCB shows the aftermath of the explosive plasma arc. This showed that the firing of the device not only destroys the bridge but part of the silicon substrate also. The actual current was found by using current viewing resistor (CVR), where the measured voltage was divided by the resistance of the CVR, 0.010347 Ω. The current trace shown in Figure 2 depicts the amount of current flowing through the device as a

function of time. The current trace increased over the first 250 ns and decreased over the next 250 ns. This supported the initial hypothesis that the current should pass the burst point because even though the bridge was blown while the current was still increasing, the current still had a path to flow due to the plasma plume that was present. The decrease in current was due to the decay of the conducting plasma plume, the changing resistance of the plasma arc and the RLC time constant of the circuit, which dampens the current waveform.

Figure 3 illustrates the voltage across the SCB as a function of time during firing. The resistance curve shows the resistance of the bridge as a function of time. The resistance shown in Figure 4 was found by dividing the voltage by the current. The resistance decreases as the voltage is applied to the device. As the device explodes the resistance decreases. As the plasma plume decayed the resistance increased. A graph of the energy absorbed by the device versus time, shown in Figure 5 was developed. This was done by multiplying the voltage and the current, and integrating with respect to time.

A mathematical model of the resistance versus energy absorbed was then constructed to model the SCB. A plot of the resistance versus energy absorbed is shown in Figure 6. TableCurve was used to model the raw data with a mathematical function. In order to develop the best model, every data set was model using TableCurve. After a function was found that model each data sufficiently, the best fit for each data set was found using that function. Then, the coefficients of the function were averaged to give one equation. The function that was used to model the SCB is as follows:

$$Y = (a/(1+\exp(-X-b+c/2)/d)))(1-1/(1+\exp(-(x-b-c/2)/e)))$$

where: Y is the resistance

X is the energy absorbed

a = 7.1447

b = 0.0003

c = 0

d = 0.0002

e = 0.00003.

A plot of the mathematical model is shown in Figure 7.

Conclusions

The test data of the SCB was analyzed. A mathematical model of the resistance versus energy absorbed was constructed. This allows for the device to be model using Pspice. Pspice can simulate and test circuit designs without having to build the actual hardware. This will be useful for the Air Force when designing any circuitry for testing the SCB in the future.

Acknowledgments

Special thanks to Dr. Keith Thomas, Lt. Jeff McGuirk, Lt. Dan Steve Smith, Joey Jarriel, Mark Adams and all the personnel at the Fuzes Branch, WL-MN/MF for their hospitality and for the use of their facilities.

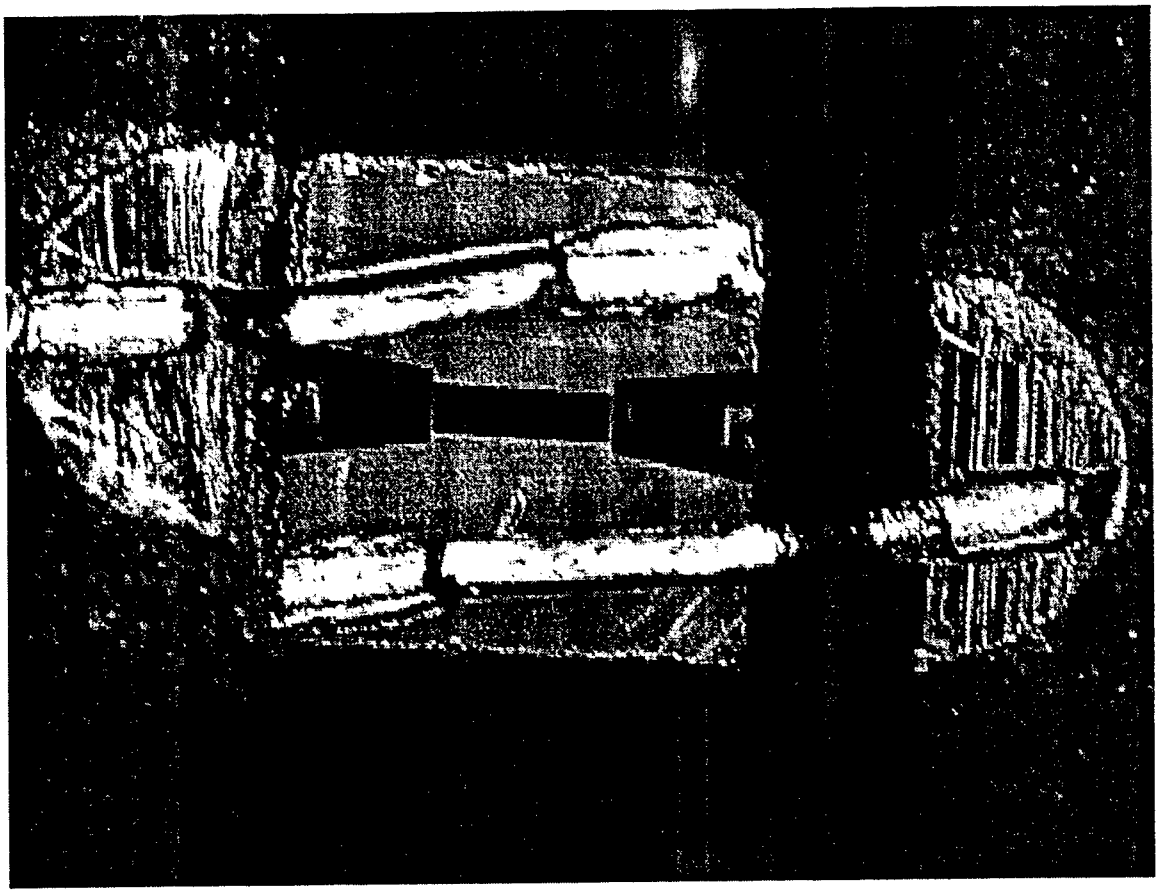

Figure 1a : Semiconductor Bridge Ignitor (Pre-Fire)

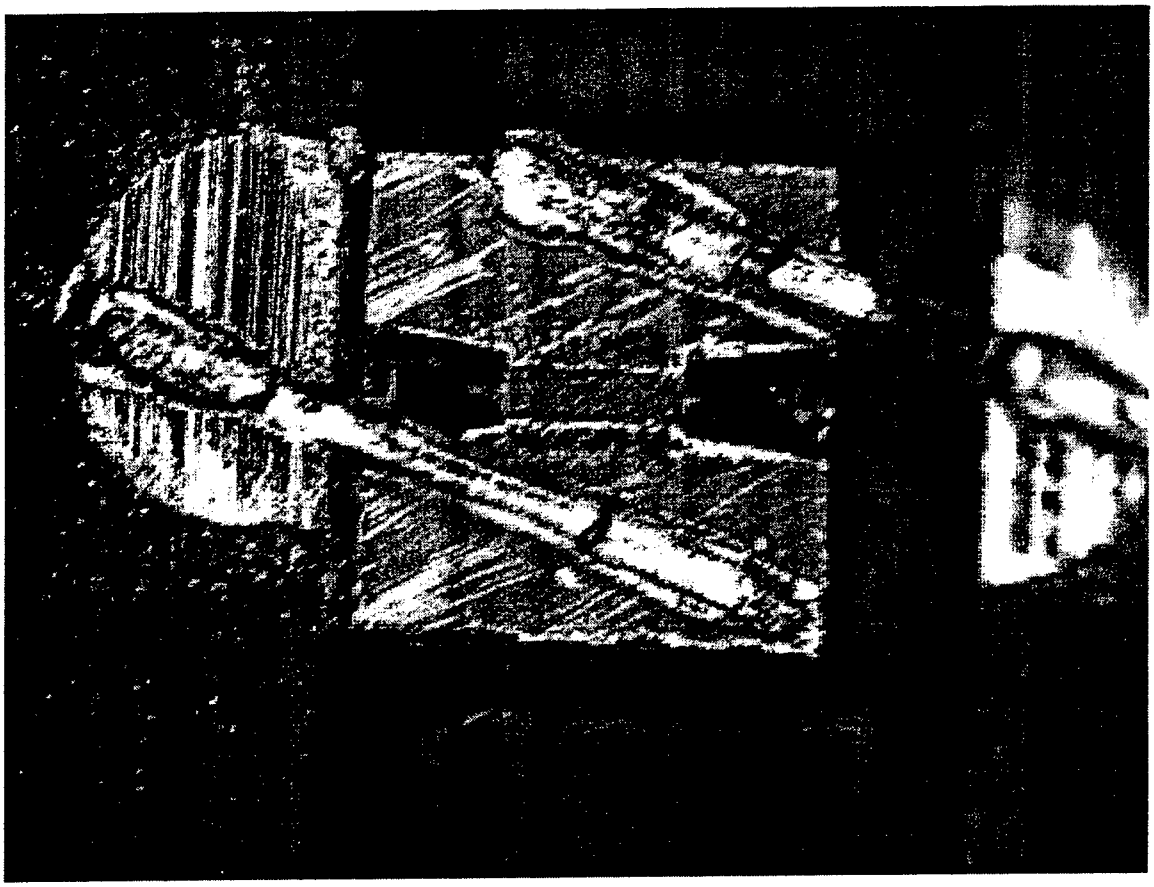

Figure 1b : Semiconductor Bridge Ignitor (Post-Burst)

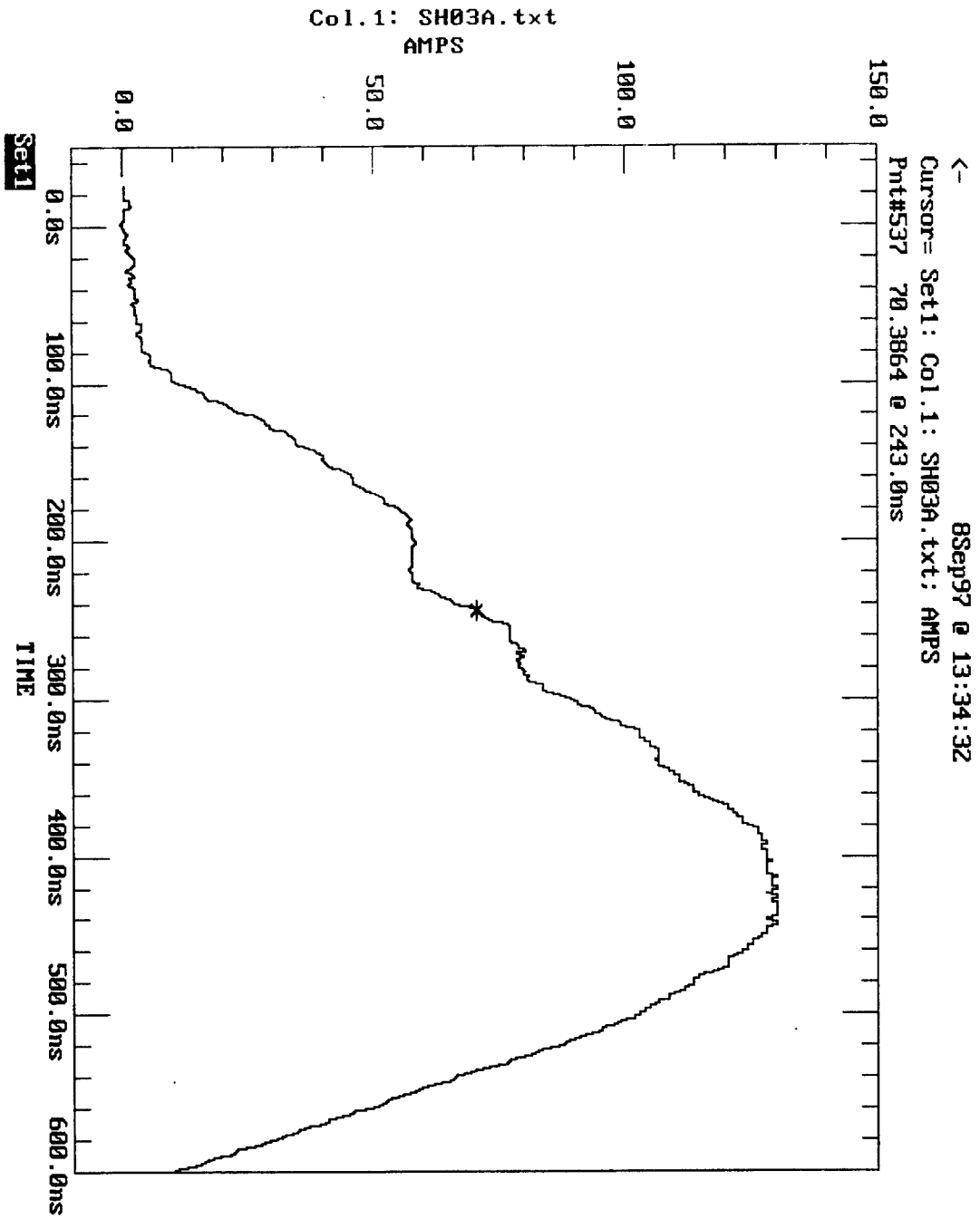

Figure 2 : Current Versus Time

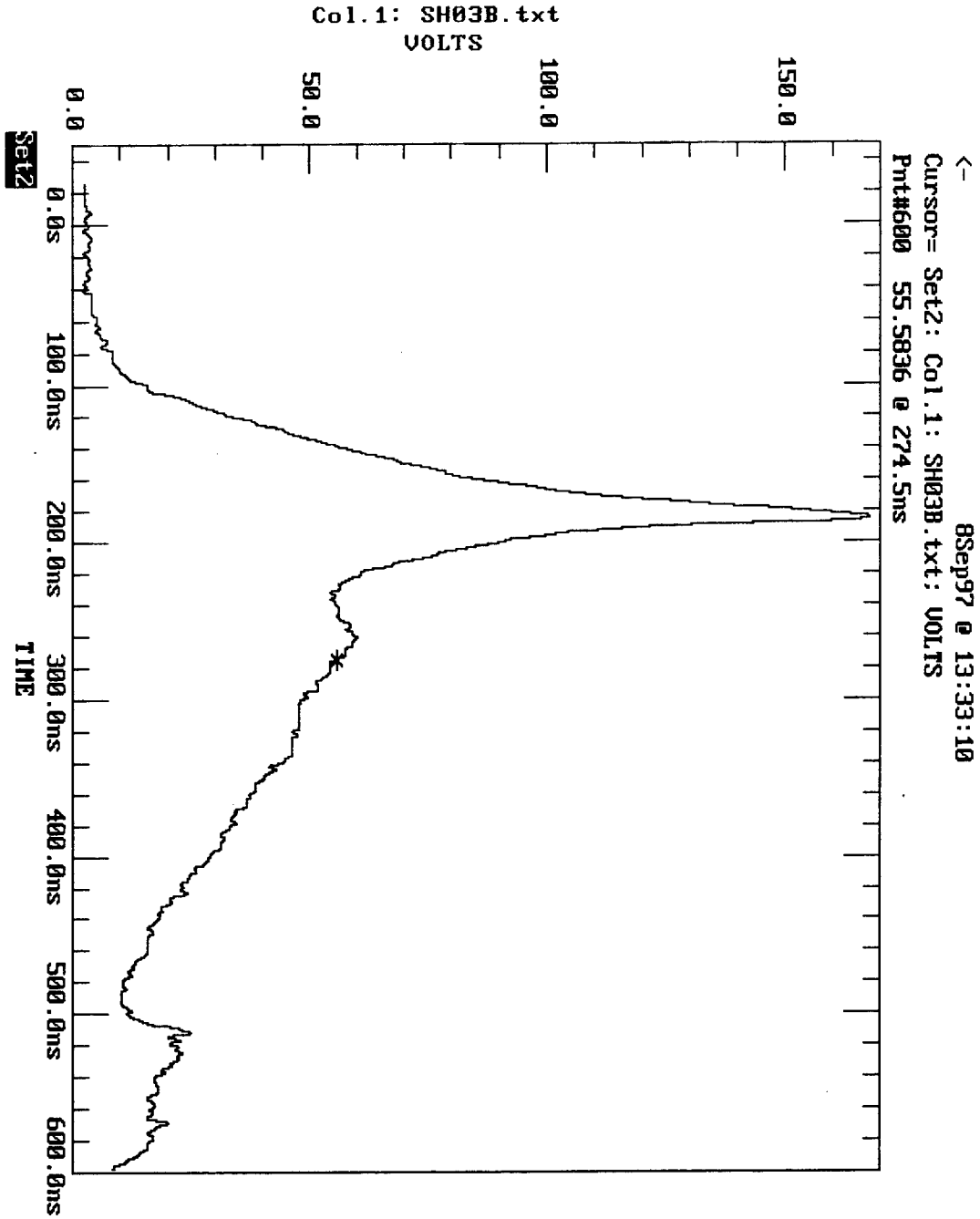

Figure 3 : Voltage Versus Time

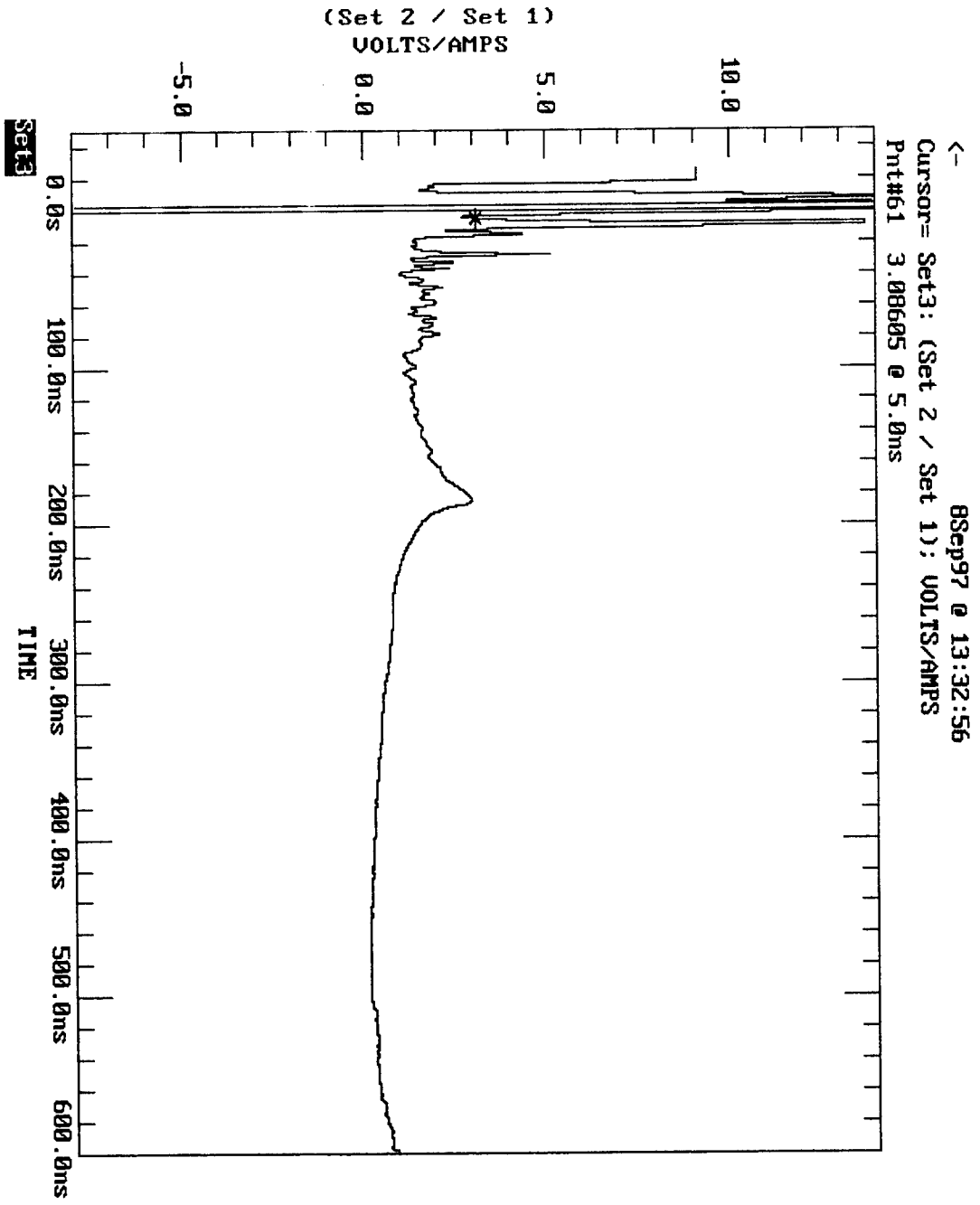

Figure 4 : Resistance Versus Time

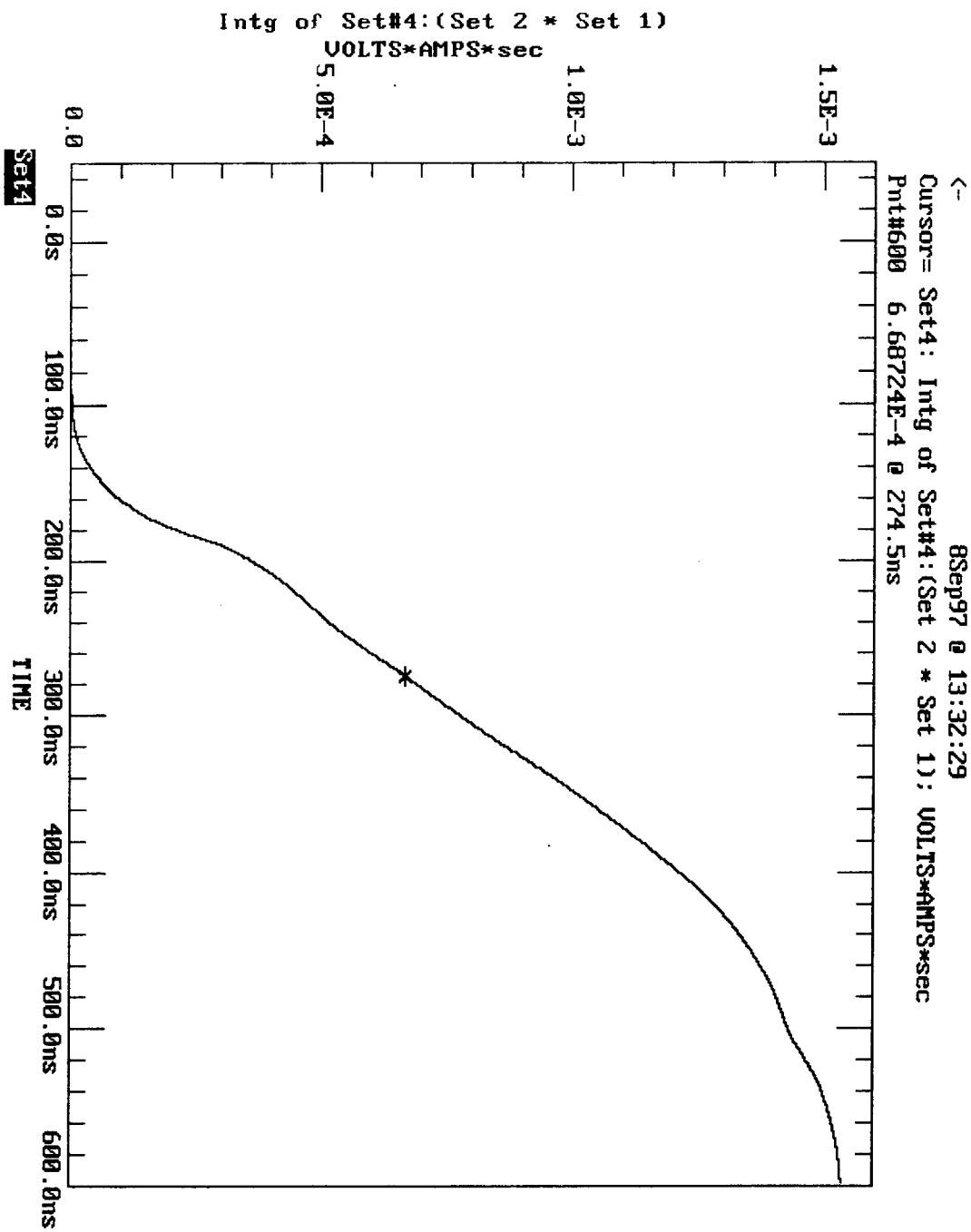

Figure 5 : Energy Versus Time

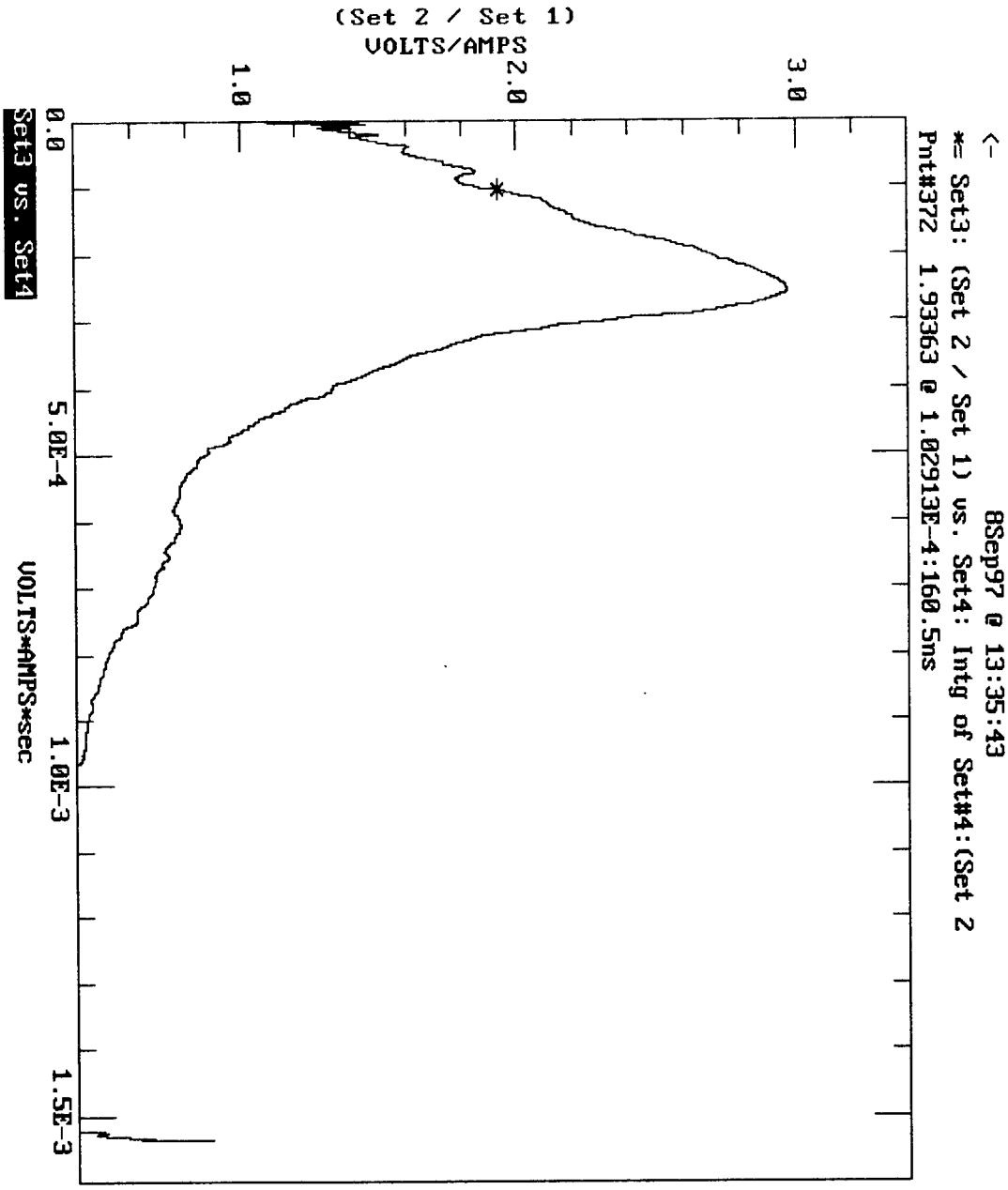

Figure 6 : Resistance Versus Energy

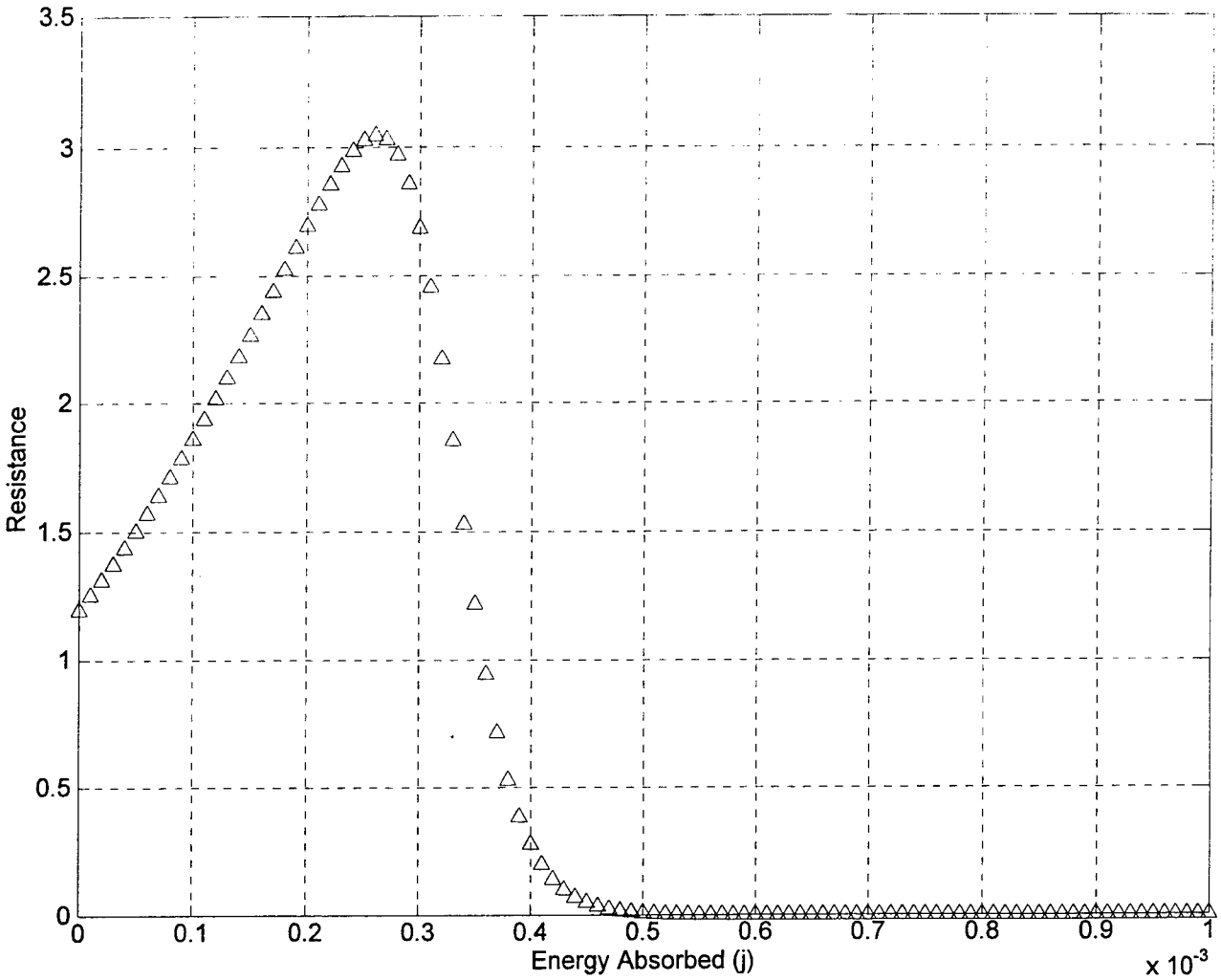

Figure 7 : Mathematical Model of Resistance Versus Time

Associate did not participate in program.

ORGANICALLY MODIFIED SILICATE FILMS AS CORROSION RESISTANT TREATMENTS FOR 2024-T3 ALUMINUM ALLOY

Robert Parkhill
Candidate for the degree of Ph.D., Chemistry
Department of Chemistry

Oklahoma State University
Physical Science I, Room 205
Stillwater, OK 74078

Final Report for:
Summer Graduate Research Program
Wright Patterson Air Force Base

Sponsored by:
Air Force Office of Scientific Research
Bolling Air Force Base, DC
and
Wright Patterson Air Force Base

September 1997

ORGANICALLY MODIFIED SILICATE FILMS AS CORROSION RESISTANT TREATMENTS FOR 2024-T3 ALUMINUM ALLOY

Robert L. Parkhill
Candidate for the degree of Ph.D., Chemistry
Department of Chemistry
Oklahoma State University

Abstract

Organically modified silicates (ormosils) sol-gel films coated on aluminum alloy 2024-T3 coupons were investigated for the purpose of developing an environmentally-compliant replacement for chromate-based surface treatments. The effect of surfactants, hybrid organic content, and alkoxide size effects on resultant films were evaluated for corrosion protection in comparison to Alodine-1200 type surface treatments. Results indicate that pinhole surface defects were present in most films; these limit the ultimate performance of sol-gel treatments. Even with pinhole defects, however, 4 orders of magnitude improvement in corrosion protection was demonstrated for sol-gel treated coupons with respect to Alodine 1200 surface treatments. Selected single-layer sol-gel compositions were found to rival the performance of the chromate-laden paint system (e.g., Alodine/primer/topcoat) currently used by the Air Force.

ORGANICALLY MODIFIED SILICATE FILMS AS CORROSION RESISTANT TREATMENTS FOR 2024-T3 ALUMINUM ALLOY

Robert L. Parkhill

I. Introduction

Recently, the Air Force has identified corrosion of aluminum-skinned aircraft and the development of improved environmentally-compliant surface treatments of aluminum alloys to be high priority topics. Changing federal regulations dictate the use of fundamentally new coating systems which are capable of meeting more strict environmental standards [1]. Coating processes which rely on the use of chromate-based passivating agents, such as strontium chromate (e.g., Alodine 1200-type treatments) will no longer be approved for use. The issue becomes more problematic as the service lifetimes of aging weapons systems such as the C/KC-135 are now projected to be 80 years and longer. Replacement coating systems must be capable of satisfying the substantial need for dramatically extended lifetimes, must be compatible with present and future environmental requirements, and must be easily integrated into the current primer/topcoat paint systems.

Recent research has been directed the toward the development of a new coating process based on the sol-gel process. Preliminary investigations indicate that the one of the most promising approaches involve a sol-gel coating system doped with corrosion-inhibiting additives [2-5]. The studies described herein suggest that selected sol-gel compositions may provide a fundamentally new protective barrier capable of meeting both environmental and corrosion-protection performance goals.

II. Approach

Over the past two summers, researchers from Oklahoma State University (Parkhill and Knobbe) have investigated the use of organically modified silicate (ormosil) films as potential replacement treatments for the passivation of aluminum alloys (AAs). Ormosils

provide a route to the preparation of hybrid organic-inorganic materials composed of intimately mixed network polymer systems. Sol-gel films prepared using ormosil precursors are of particular interest, because they blend the mechanical and chemical characteristics from both network types. The ceramic hybrid component may be optimized to provide improved film adhesion to AA substrates and impart greater hardness, while the organic hybrid network component contributes to increased film density, flexibility, and functional compatibility with organic polymer paint systems. Hybrid films may be tailored to have exceptional durability and adhesion, while still providing a dense, flexible barrier to permeation of water and corrosion initiators such as $Cl^-_{(aq)}$.

Last year's studies showed that alcohol based sol gel films possessed superior corrosion protection compared to standard chromate treatments such as Alodine 1200 [6]. Ormosil coatings were found to exhibit substantial improvement, by up to six orders of magnitude, in corrosion resistance with respect to chromate-based conversion coatings. Thus, sol-gel films demonstrated much promise for the development of environmentally-compliant replacements to chromated surface treatments.

In addition to chromate elimination, viable replacement systems must have low or zero component volatile organic compounds (VOCs). Thus, it is desirable to investigate entirely or largely water-based processes. This aspect introduces several new problems for sol gel materials and processes, including high solution surface tension (and resultant poor surface wetting), precursor solubility, and sol stability. Very few published studies have successfully employed water based sol gel solutions for coating systems. However, research results described herein provide a basis for developing dramatically improved, water-based sol gel coatings capable of meeting the future need for low VOC formulations.

III. Background

In general terms, the sol-gel method consists of hydrolysis and condensation reactions in which alkoxy-silanes react with water to form a polymeric network of nanoporous material. The sol-gel process is extensively described in the work by Brinker and Scherer [7]. Organically-modified silicate hybrid materials consist of a comparable reaction sequence with the addition of organic functionality which can be blended into the hybrid system to tailor material properties for the desired functionality. In such systems the influences of organic groups and cross-linking agents, water content, and alkoxide precursors have been shown to have profound effects on the chemical reaction kinetics and upon the resultant hybrid.

III.a Water Based Systems

Under conditions of excess water (i.e., more than that needed for complete alkoxide hydrolysis), the hydrolysis and condensation reaction rates are significantly altered. Aelien *et al.* found the acid-catalyzed hydrolysis of TEOS to be first order with respect to H_2O concentrations [7,8]. Increased water concentrations result in more rapid and complete hydrolysis of alkoxide species. Since water is a by-product of the condensation step, elevated water levels slow condensation and polymerization. Increased water content tends to stabilize the sol phase, resulting in the development of more branched colloidal structures. Sols composed of highly branched particles tend to yield films having increased porosity and lower film density. Conversely, more linear particles tend to yield denser, harder films. Thus, it is clear that the water/alkoxide ratio can substantially influence reaction kinetics in a way which impacts film porosity and hardness characteristics.

In addition to perturbing reaction kinetics, water content also effects solution viscosity and surface tension. Unlike typical sol-gel derived solution's used for thin film coatings, which generally rely on the use of organic co-solvents, water-based systems tend to have substantially greater surface tensions and viscosities. Methanol, for example, has a surface tension (23 dynes/cm^2) which is only one third that of water (72 dynes/cm^2) [9].

Solutions having large surface tensions can result in poor substrate surface wetting characteristics; they also tend toward slow evaporation rates of volatile compounds subsequent to film formation. It is known that sol viscosity increases as a function of particle growth and reduced alcohol content. Ultimately, water content substantially impacts film thicknesses and sol stability. In order to develop an understanding of chemical effect (i.e., precursor alkoxide group, wear content, hydrolysis rate, surface tension, viscosity, dilution, *etc.*) on film morphology, an integrated series of studies on related parameters was performed. One of the goals of the summer project was to improve film quality and corrosion protection characteristics through the development of dense films having improved surface wetting characteristics compared with films prepared during the '96 summer program.

III.b. Surfactants

Surfactant use in coating systems has been shown to be one of the primary mechanisms for improving film quality. Research by Murakata, T. ect. al has shown that various salt additives and ionic surfactants can profoundly alter the surface area and pore diameters of silica samples [10]. Other studies have utilized surfactants to aid in surface wetting of high energy surfaces [11,12]. Currently, many industrial sources offer surfactants which can be tailored to a particular system for reducing surface tensions and improving wetting. By introducing various surfactants, the morphology of film coatings can be optimized for improved corrosion protection.

In this study, a dual surfactant system was investigated to improve wetting behavior on clean AA surfaces. Surfactants were chosen on the basis of reducing surface tension in aqueous solution. Vender-supplied literature indicates surface tension reduction in aqueous media may be decreased from 72 dynes/cm^2 to 22 dynes/cm^2 through the use of selected surfactants. Surface tension effects on wetting, overall film quality, and corrosion

protection have been investigated, and the impact of surfactant use on corrosion protection has been quantified

III.c. Precursor Use

Alkoxide precursors can largely effect hydrolysis and condensation reaction kinetics through steric bulk and electron donating (or withdrawing) characteristics. Short chain alkoxides react much faster than large chain alkoxides due to a lower degree of steric hindrance and less stability due to electron donation characteristic [7]. Precursor sols incorporating small alkoxide side groups, such as tetramethoxy silane (TMOS), hydrolyze more readily than those incorporating larger alkoxide side groups (i.e., tetraethoxy silanes, (TEOS), tetrapropoxy silane, (TPOS), *etc.*), resulting in a more chemically reactive solution. Thus, precursor alkoxide side chains can be utilized to control reaction kinetics and/or the stability of a sol system. Ormosils prepared using TMOS, TEOS, and organically modified silicate precursors were coated onto AA substrates. The impact of alkoxy side group size on film morphology and corrosion protection have been assessed.

The presence of organic functional side chains in a hybrid silica system can effect film wetting and surface compositions. Research has shown that organic content can change the chemical nature of colloidal surfaces in sol-gel systems [12-15]. In the case of low organic content in the sol-gel derived network polymer, the organic functional groups have been shown to be more or less evenly dispersed throughout the ormosil composition. With elevated organic concentration, however, the functionalities have been found to segregate, yielding organic-rich regions which are preferentially positioned at surface sites. Thus, film characteristics can be dramatically altered by varying the relative amount of polymer components. Elevated organic content tends to produce surfaces with a hydrophobic surface character.

4. Experimental Methods

4.1. Materials and Reagents

Substrates consisted of aluminum 2024-T3 coupons which were polished with 300 and 600 grit silicon carbide sand paper followed by cleaning in an ultrasonic bath using isopropanol and hexane solvents. Alkoxide reagents (i.e., TEOS, TMOS, and ormosil) reagents were used as received from Aldrich. Surfactants were incorporated by direct dissolution into the aqueous sol phase. Spectroscopic grade isopropanol and hexane were used as received from Aldrich. Nitric acid was used to catalyze the hydrolysis reaction.

4.2. Sol-gel Preparations

Preparation of the ormosil solutions was performed as follows: 25.0 ml of TEOS was placed in a beaker with 18.7 ml of acidified water. The resultant two-phase solution was vigorously stirred to induce mixing and initiate hydrolysis. The bi-phasic solution became a clear single phase sol approximately 2 hours after initial mixing. Once the solution cleared, organically modified precursors were added and thoroughly mixed. One hour later, additional water and surfactants additives were added in a drop-wise manner until the desired concentrations were obtained. The final solution was stirred continuously in a closed container held at room temperature until its use in dip-coating. Immediately prior to coating, the sol was transferred to a teflon cells into which the AA substrate were dipped.

4.3. Coating and Curing Methods

Aluminum 2024-T3 substrates were dipped into precursor sols using a Chematic Technology Inc. model 201 dip-coater. The sol gel coatings were applied using a single dip step. 30 ml of sol were transferred to the teflon dipping cell. Dip-coating was done using a dwell time of 10 seconds in the coating sol. The withdrawal speed was 10 cm/s into RT air. After dipping, samples were cured using selected time/temperature conditions.

Curing temperatures included room temperature, 60°C, 100°C, and 150°C. Cure times at these temperatures ranged from 1 to 24 hours. After heat treatment, samples were removed from the ovens and allowed to cool to room temperature before characterization and analysis.

4.4. Characterization

Film morphologies were characterized using an OPTIPHOT-POL Nikon polarizing microscope equipped with a 5.0X microscope objectives. Film thickness was determined using a Sloan Dektak IIA profilometer.

The corrosion potentials were determined from potentiodynamic polarization curves using a Gamry potentiostat. Sweep potentials were varied from -1.0V to 0.2V vs. SCE after coated samples were immersed in a 3% NaCl solution. Specimens were maintained in the 3% NaCl for 1 hour prior to potentiodynamic polarization measurement, except in cases where the effects of longer term immersion are noted. Data were analyzed using CMS100 software.

5. Results and Discussion

Film performance and morphology were characterized as functions of surfactant addition, organic content, and chemical nature of alkoxide precursors used. Compositional parameters were varied in order to develop optimal corrosion protection. Film protection characteristics were determined in relation to one of three protection standard specimens: untreated 2024-T3 aluminum alloy, Alodine 1200 treated 2024-T3, or a "standard" complete paint system (i.e., Alodine surface treatment/chromated primer/topcoat) applied to a 2024-T3 coupon. Preliminary assessments of protection afforded by sol-gel surface treatments were made on the basis of film morphology, thickness, and screening potentiodynamic polarization measurements.

5.1. Corrosion Protection as a Function of Surfactants Addition.

Table I represents profilometer measurements from 2 sets of ormosil coatings. Films were prepared using water/alkoxide molar ratios concentrations as indicated in Table I. In each specimen set, film thicknesses were found to increase as water ratios were reduced. Surfactant addition caused film thickness to increase for a given water/alkoxide ratio.

Table I. Thickness Variation in Ormosil Coatings due to Surfactant Addition.

Sample	Water:Alkoxide Ratio	Surfactant	Thickness
1	2:1	no	1.8 μm
2	2:1	yes	2.2 μm
3	4:1	no	0.8 μm
4	4:1	yes	1.5 μm

Thickness reduction due to increased water content is expected as a result of simple dilution effects. However, surfactant-induced film thickness increases are not so easily explained. Surfactant addition caused the sol to become observably more viscous. The mechanism which leads to such a substantial viscosity increase is not well understood or documented in the literature. Upon dipping into the more viscous, surfactant-containing sol, the deposited layer entrained substantially more liquid. Gelatin of this thick viscous layer resulted in a substantially thicker coating as indicated in Table I..

Figure 1 shows optical micrographs of samples 1 and 2. At 50X, micrographic images revealed the significance of surfactant addition. Sample 1 (containing no surfactant) had a large areal pinhole number (# pinholes/area). Pinhole sizes generally ranged form 10 to 80 μm. Sample 2, which contained surfactant additives, was found to have two types of pinholes. Small pinholes were estimated to have diameters of less than 10 μm, with an

areal number of 45 holes/mm^2. Larger pinholes were randomly positioned with estimated diameters between 20 and 50 μm and an areal number of 3 pinholes/mm^2.

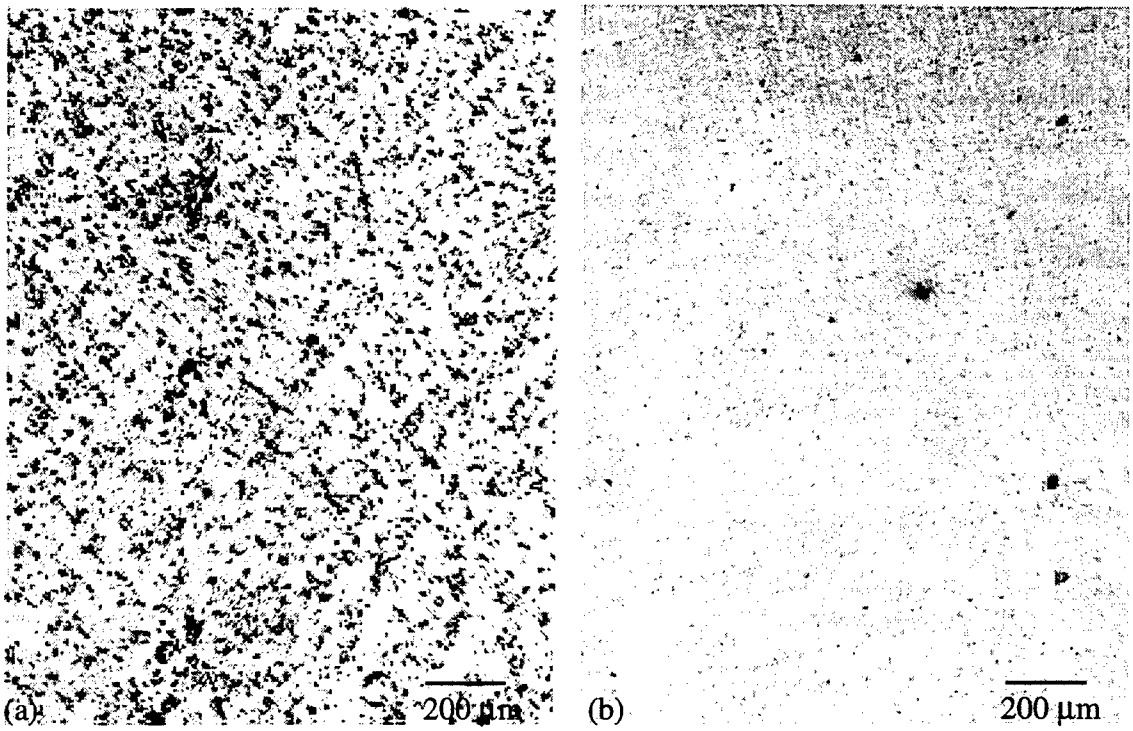

Figure 1 : Aluminum 2024-T3 substrates coated with an ormosil coating with a water : alkoxide ratio of 4:1: (a) No surfactant sample 1 (b) Surfactant sample 2.

The development of extensive pinholes in the ormosil films is postulated to occur as a result of the high surface tension found in water-based sols. As water evaporates during film formation, large capillary forces cause the free energy of the solid-liquid interface to increase. In order to compensate, the remaining sol can minimizes the interfacial energy by decreasing the liquid-solid interface. As water continues to evaporate, the sol begins to bead on the AA surface, leaving voids at the interface (Figure 2a). With surfactant addition, the surface tension of the sol was estimated to be reduced by as much as two thirds. Reduced surface tension lowers the capillary forces, which permits the sol to spread more uniformly across the substrate (Figure 2b). It is clear from examination of Figures 1(a) and

(b) that pinhole formation was significantly reduced through the use of appropriate surfactant additives.

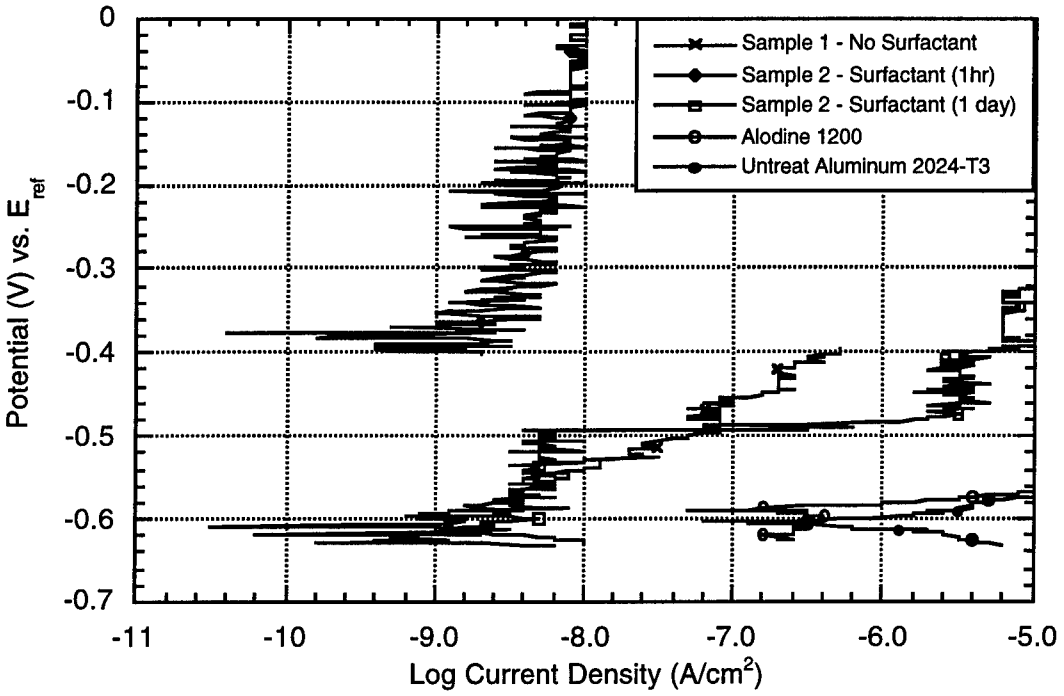

Figure 2: Anodic behaviors for a non surfactant ormosil film, ormosil film with surfactant, Alodine 1200-treated, and untreated aluminum 2024-T3 coupons.

Electrochemical evaluation of Samples 1 and 2 demonstrated the excellent corrosion resistance imparted by the surfactant system. Figure 2 represents an anodic electrochemical polarization spectroscopy measurements used to assess ormosil corrosion protection (with and without surfactant addition) compared to Alodine 1200-treated and untreated aluminum 2024-T3 substrates. Untreated 2024-T3 coupons had a corrosion potential (E_{oc}) of -610mV and did not exhibit a passive region before pitting. Alodine 1200 had an E_{oc} of -580mV and showed a small (0.04V) passive zone prior to pitting. Sample 1 (no surfactant) had an (E_{oc}) of -610mV with little observable pre-pitting passivation. Sample 2 (surfactants added) had an E_{oc} of -380mV and showed a passive zone of 0.4V without measurable

pitting after a 1 hour soak in 3% NaCl solution. After 24 hours of immersion, Sample 2 showed a E_{oc} of -620mV and a small passive zone of 0.13V before the onset of pitting. Comparison of the passivation current densities indicate that surfactant-enhanced ormosil coatings have a 4 order of magnitude improvement in field-induced corrosion rate when compared to the Alodine 1200 surface treatment.

These results clearly indicate that surfactant addition provides dramatically-improved corrosion protection. The evidence is consistent with the dominant corrosion failure mechanism proposed for in the ormosil films; i.e., pinhole defects. The rapid failure of sample 1 indicates incomplete barrier protection, consistent with the large areal pinhole number found for such specimens. However, the comparatively small current density at elevated potentials implies that the corrosion rates for such specimen is slow. It is postulated that the gradual increase in current density as a function of applied field (above the corrosion potential) was due to pinhole enlargement from dissolution of aluminum at local defect sites. The pitting observed in sample 2 was attributed to catastrophic film failure (i.e. localized coating delamination and/or cracking). As water permeates through film defects, interfacial stresses develop leading to film failure. The rapid increase in current density suggests the onset of pitting, resulting from an instantaneous change in the exposed AA surface. Post electrochemical test examination of the films revealed significant cracking near and around pinholes, which is consistent with the proposed failure mechanism. Thus, the overall improvement in corrosion protection associated with surfactant addition is presumed to be a direct result of significant reduction in areal defect number.

5.2. Organic Composition:

Table II represents profilometer measurements from 3 sets of ormosil coatings as a function of organic component. Film compositions are presented as water:alkoxide molar ratios. In each set, film thickness was shown to decrease with elevated water content. The

thickness differences found to exist between 20 and 33 percent organic composition gels were not significant (within experimental measurement error).

Table II Thickness results of ormosil films with variable dilutions and organic content

Sample	Water:Alkoxide Ratio	Organics	Thickness
O1	2:1	20%	1.7 μm
O2	2:1	33%	1.5 μm
O3	4:1	20%	0.9 μm
O4	4:1	33%	1.0 μm
O5	6:1	20%	0.7 μm
O6	6:1	33%	0.8 μm

Variations in organic content (i.e., 20% vs. 33%) resulted in minimal observable surface morphology variation. Figure 4 represents two ormosil films typical of the 20% and 33% organic components (specimen O3 and O4). Ormosils with 33% organics were found to have two types of pinholes. Small pinholes were estimated to have diameters of less than 10 μm with an areal number of 45 holes/mm^2. Larger pinholes were randomly positioned with diameters of 20 to 50 μm and areal number of 3 holes/mm^2. Ormosils containing 20% organics were shown to have similar pinhole types, with areal pinhole numbers of 25 holes/mm^2 and 2 holes/mm^2 for small and large pinholes, respectively.

These results suggest that ormosil films containing 20% organic components have moderately improved wetting characteristics. The lower areal pinhole number indicates that reduced surface tensions may have occurred as a result of lowered organic content (increased surface tensions are associated with poorer sol wetting behavior).

The electrochemical evaluation for the organic component (20% and 33%) ormosil films and a complete paint system on aluminum 2024-T3 substrates are presented in Figure 5. The 33% organic ormosil had an E_{oc} of -630mV a passive zone of nearly 0.14V after 1

day of immersion in 3% NaCl solution. The 20% organic film showed an E_{oc} of -460mV and a passive zone of 0.45V after 1 day of exposure to 3% NaCl solution (no pitting).

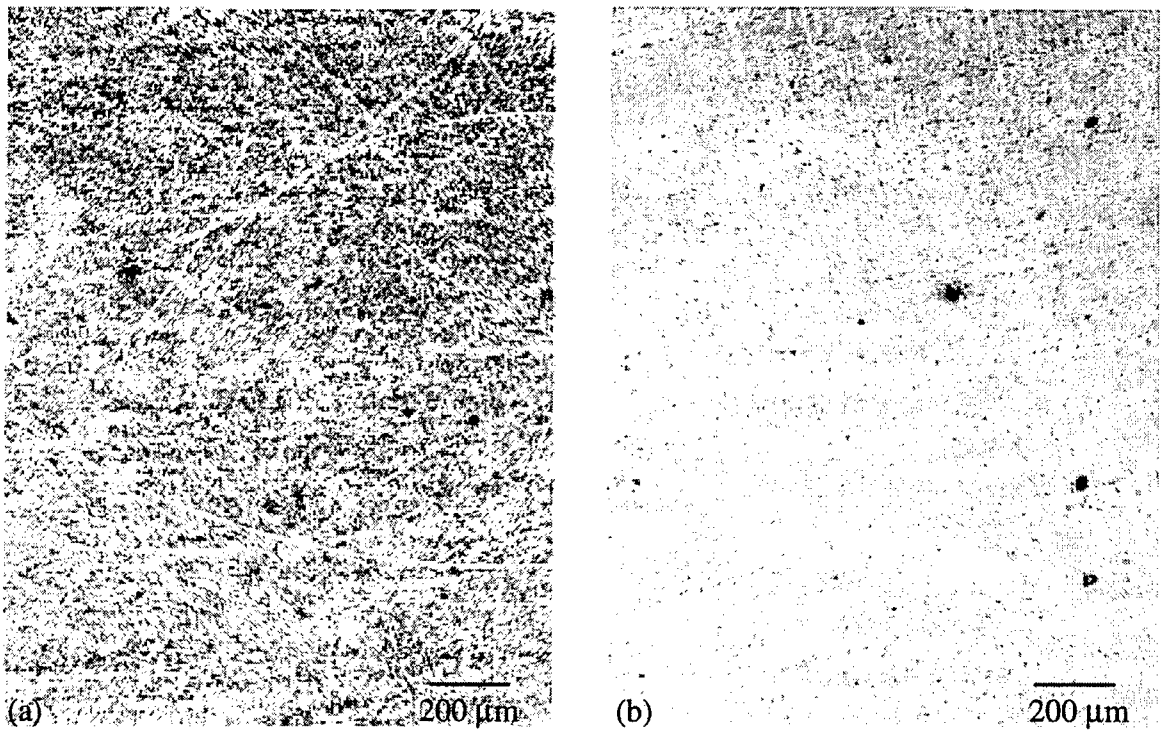

Figure 4: Aluminum 2024-T3 substrates coated with ormosil films containing different concentrations of organic material (a) 20% (b) 33 %.

The film eventually failed after 3 days of immersion in the salt water solution; at that time these films exhibited an E_{oc} of -620mV and a reduced passive zone (0.08V). These films are shown in Figure 3 compared to the performance of a complete paint system (CPS; i.e., Alodine surface treatment/chromated epoxy primer/polyurethane topcoat). The CPS exhibited an E_{oc} value of -300mV after 3 days immersion in 3% NaCl solution, with a passive zone of 0.3V. Direct comparison of the anodic polarization behavior of these specimens clearly shows that the single layer, chromate-free 20% organic ormosil coating offers a level of corrosion protection which is very similar to that afforded by a chromate-laden CPS.

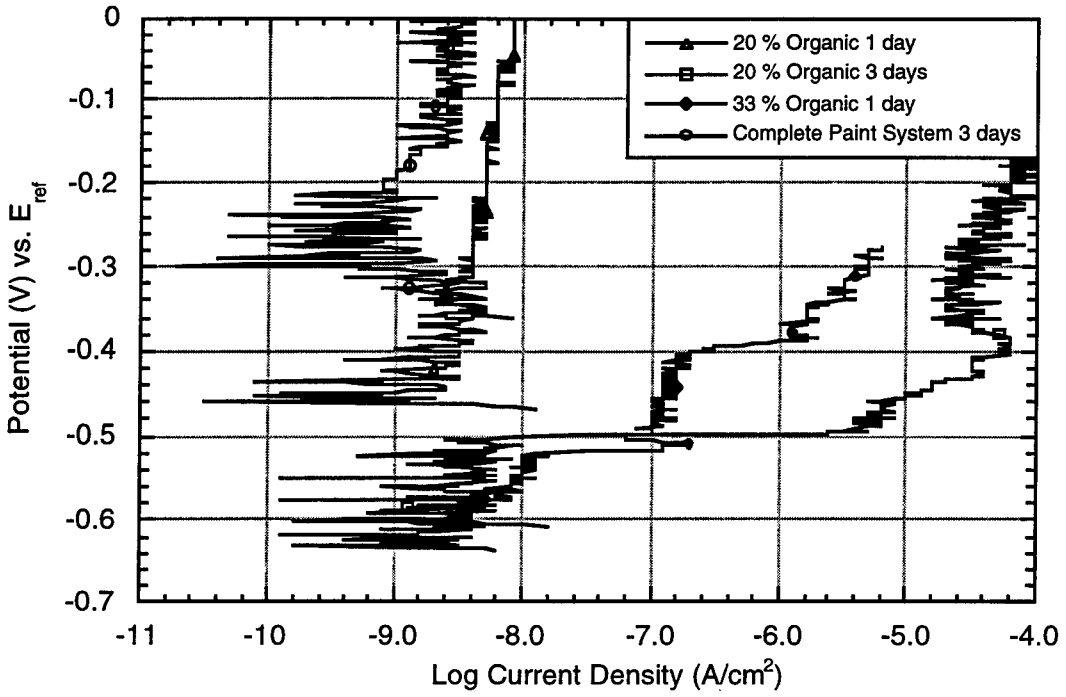

Figure 5: Polarization behaviors for 20% organic ormosil, 33 % organic ormosil, and complete paint system coated on aluminum 2024-T3 coupons.

The electrochemical evaluation showed greatly improved corrosion resistance for the 20% organic ormosil film compared to the 33% organic film. In both systems, the pitting initiation appear to be caused by localized film fracture induced at defect sites by internal stresses. Thus, the extended protection provided by the lower organic content ormosil can be attributed to both a reduction in pinhole density and lower water/$Cl^-_{(aq)}$ permeability through such films.

5.3 Silica Precursor:

Table III represents profilometer measurements from 3 sets of ormosil coatings with different silicon alkoxide precursors. The films are presented as water:alkoxide molar

ratios. In each set, film thickness was shown to decrease as water ratios increased. The thickness differences between alkoxide precursors was negligible.

Table III

Sample	Water:Alkoxide Ratio	Precursor	Thickness
M1	4:1	TMOS	1.4 μm
E1	4:1	TEOS	1.7 μm
M2	6:1	TMOS	0.8 μm
E2	6:1	TEOS	0.9 μm
M3	8:1	TMOS	0.5 μm
E3	8:1	TEOS	0.7 μm
M4	10:1	TMOS	0.3 μm
E4	10:1	TEOS	0.4 μm

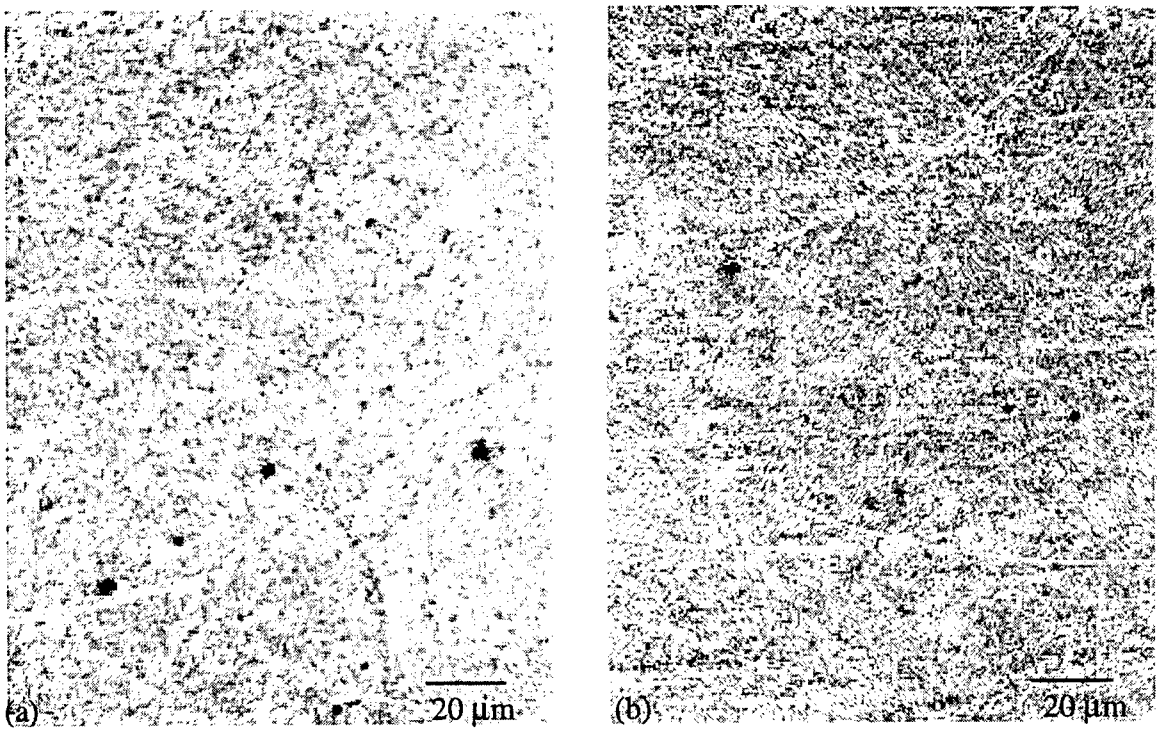

Figure 6. Optical micrographs of two ormosil films with different silica alkoxide precursors. (a) TMOS (b) TEOS

The small variation in film thickness can be attributed to the nature of the alcoholic by-products of the hydrolysis reaction for TMOS (methanol-generating alkoxide) precursor

versus the TEOS (ethanol-generating alkoxide) precursor. The two system are primarily composed of water, but alcohol by-products can influence the viscosity of the sol.

The use of different alkoxide precursors showed only small variation in surface morphology. Figure 6 represents optical micrographs of two typical ormosil films derived from TMOS and TEOS alkoxide precursors. The TMOS ormosil film was found to have two types of pinholes. Small pinholes were estimated to have diameters of less than 10 μm and an areal pinhole number of 35 holes/mm^2. Larger pinholes were randomly scattered with diameters between 50 and 100 μm and an areal pinhole number of 4 holes/mm^2. The TEOS ormosil film was shown to have similar population densities, but pore diameters of less than 10 μm for small pinholes and between 20 and 50 μm for large pinholes.

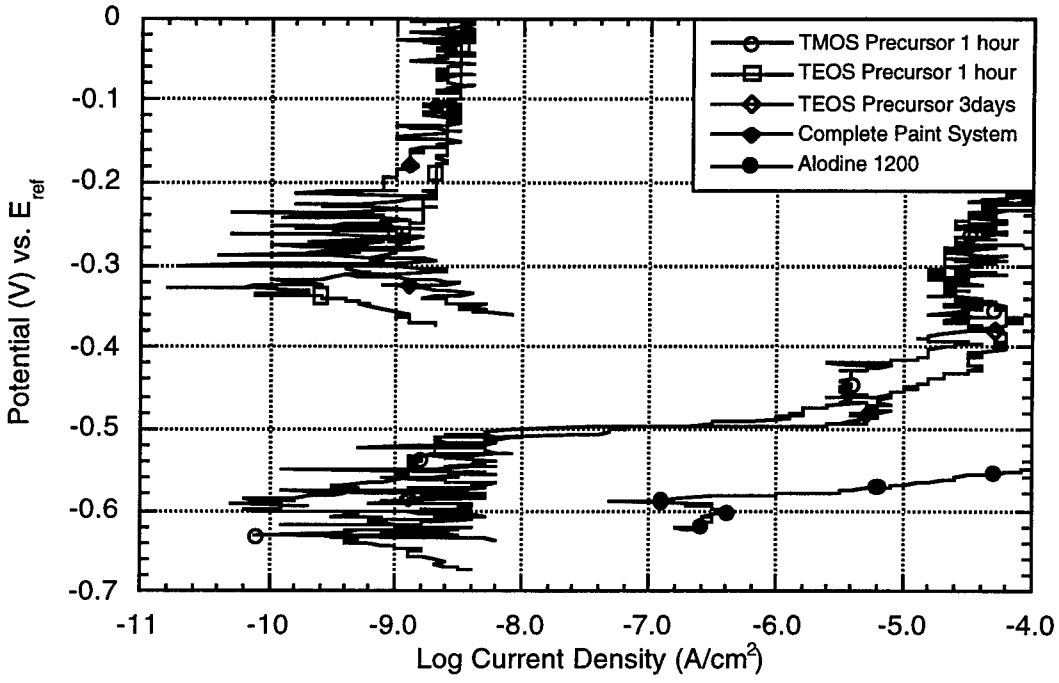

Figure 7. Anodic polarization behavior of silica precursors, Alodine 1200, and a complete paint system .

Figure 7 represents electrochemical analysis for a TEOS ormosil film, TMOS ormosil film, Alodine 1200, and complete paint system on aluminum 2024-T3 substrates. The TMOS ormosil film had an E_{oc} of -630mV and a passive zone of 0.13 after 1 hour of immersion in 3% NaCl solution. The TEOS ormosil film had an E_{oc} of -330mV and a passive zone of 0.35V after 1 hour of immersion in 3% NaCl solution. The film failed only after 3 days of continuous immersion in salt water and showed an E_{oc} of -590mV and a passive zone of 0.09V. The complete paint system showed an E_{oc} of -300mV and a passive zone of 0.3V after 3 day of immersion in 3% NaCl solution.

TEOS derived films were shown to provide superior corrosion protection compared to TMOS derived films. In both cases, the mechanism of failure is postulated to be film cracking. The comparatively early failure of TMOS-derived ormosils suggests that such films are (a) more porous and/or (b) more highly strained. The TMOS-derived sol is believed to have resulted in the development of more branched particulate structures during the colloidal particle growth phase due to the more reactive nature of the methoxy precursor. A higher degree of branching could lead to more porous film structures with a subsequent lowering of film integrity. Thus, less reactive silicon alkoxide precursors appear to yield films having improved corrosion protection due to the denser gel network which results.

6. Summary and Conclusion

The corrosion resistance of aluminum alloy 2024-T3 substrates coated with water based ormosil film preparations were investigated. Corrosion performance and surface morphology were assessed as a function of surfactant addition, organic content, and silicon alkoxide precursors. Films were characterized by profilometry, optical spectroscopy, and electrochemical impedance spectroscopy analysis.

Results of the summer term project showed that water based sol-gel coatings provided corrosion protection values which were several orders of magnitude better than

the current Alodine 1200 treatments on aluminum 2024-T3 coupons, and equivalent to the alcohol based sol-gel systems previously investigated. Optimization of surfactant addition, organic content, and silicon alkoxide group selection results in substantial reduction in the pinhole defect areal number. Chromate-free ormosil films provide corrosion protection of up to ten thousand times that of conventional chromate-based surface treatments. Selected single-layer compositions yielded corrosion protection values which equaled or exceeded that afforded by chromate-laden complete paint systems. Thus, water-based sol-gel coatings were found to exhibit great potential for the replacement of chromate based conversion coatings presently used in the passivation of aircraft aluminum alloys.

7. References

1 Private Communication, Dr. Michael Donley, Coating Research Program POC, Wright Laboratory , Wright Patterson Air Force Base, Dayton OH.

2. K. Kato, *J. Mater. Sci.*, **28**(1993) p4033.

3. F.M. Seon, *J. Less-Comm. Metals*, **148**(1989) p73.

4. S. Roure, F. Czerwinski, and A. Petric, *Oxid. Met.*, **42**(1994) p75.

5 V.A.C. Haanappel, T. Fransen, B. Geerdink, and P.J. Gellings, *Oxid. Met.*, **30**(1988) p201.

6. R. Parkhill and E.T. Knobbe, AFOSR 1996 summer report.

7. C.J Brinker and G.W. Scherer, Sol-gel Science, Academic Press, San Deigo, (1990)

8. R. Aelion, A. Loebel, and F. Eirich, *J.Am.Chem.Soc.*, **72**(1950) p5705.

9. D. R. Lide, CRC Handbook of Chemistry and Physics, CRC Press, Boston, (1991).

10. T. Murakata, S. Sato, T. Ohgawara, T. Watanabe, and T. Suzuki, *J.Mater.Sci.*, **27**(1992) p1567.

11. D. Quere, A. de Ryck, and O. Ou Ramidane, *Europhysics Lett.*, **37**(1997) p305.

12. D.R. Karsa, Additives for Water-Based Coatings, Royal Society of Chemistry, Great Brittan, (1990)

13. J. Mackenquie, Q. Huang, T. Iwamotot, *J.Sol.Sci.&Tech.*, **7** (1996) p151.

14. B.M. De Witte, D. Commers, and J.B. Uytterhoeven, *J. Non-Cryst. Solids*, **202**(1996) p35.

15. C. Della Volpe, S. Dire, and E. Pagani, *J.Non-Cryst. Solids*, **209**(1997) p51.

COST-BASED RISK PREDICTION AND IDENTIFICATION OF PROJECT COST DRIVERS USING ARTIFICIAL NEURAL NETWORKS

Annie R. Pearce
Ph.D. Candidate
Construction Engineering and Management Division

School of Civil and Environmental Engineering
Georgia Institute of Technology
Atlanta, GA 30332

Final Report for:
Graduate Student Research Program
Tyndall AFB
Wright Laboratory

Sponsored by:
Air Force Office of Scientific Research
Bolling Air Force Base, Washington, DC

And

Wright Laboratory

August 1997

COST-BASED RISK PREDICTION AND IDENTIFICATION OF PROJECT COST DRIVERS USING ARTIFICIAL NEURAL NETWORKS

Annie R. Pearce
Ph.D. Candidate
Construction Engineering and Management Division
School of Civil and Environmental Engineering
Georgia Institute of Technology

ABSTRACT

This research investigated the effectiveness of using Artificial Neural Networks (ANNs) to predict risks related to final project costs and to identify potentially significant cost drivers relating to construction projects. Several ANN models were developed which related potential project costs to a variety of input factors typically used to perform conceptual cost estimating. Using the intrinsic feature representation properties of ANNs, cost drivers were identified which should be managed for projects to reduce the risks of cost growth. Results of the research indicate that ANNs can serve as a robust tool for cost estimation and approximated multivariate regression analysis.

COST-BASED RISK PREDICTION AND IDENTIFICATION OF PROJECT COST DRIVERS USING ARTIFICIAL NEURAL NETWORKS

Annie R. Pearce

INTRODUCTION

As budgets for the construction of new facilities and the maintenance, decommissioning, or rehabilitation of existing facilities become more limited, stakeholders responsible for funding these activities are seeking better ways to increase the accuracy of their project cost estimates, especially in the early phases of project planning and design. Being able to predict how much a project will cost is important not only to set sufficient funds aside to complete a project, but also to ensure that the project is not over-budgeted, potentially encouraging cost overruns or preventing other deserving projects from receiving adequate funding.

Alternative methods for cost prediction are especially important in the early planning or conceptual design phases of projects, before enough detail is known to allow a traditional quantity takeoff estimate to be performed. Since much of the budgeting process often takes place during these early phases of a project, an accurate estimate is essential to ensure that projects are allocated a sufficient budget so that functional requirements are met. At the same time, an accurate project estimate can help to avoid over-budgeting that may encourage gold-plating during design, or remove efficiency and performance constraints during construction.

Accurate project cost predictions or estimates early in the planning and design processes can also serve as a cost-control measure to assist in managing the design process. With an understanding of the most significant factors affecting final project cost, i.e., cost drivers, project owners and managers can proactively make cost-effective choices during design, rather than after construction begins and budgeted dollars begin to fall short of requirements.

In this paper, we examine the potential of Artificial Neural Networks (ANNs) as a tool to support the tasks of cost prediction, cost driver identification, and risk management during the planning and design phases of the project life cycle. ANNs are a modeling tool based

loosely on the computational paradigm of the human brain, and have proven to be robust and reliable for tasks of prediction, ranking, classification, and interpretation or processing of data. We begin by examining the problem of project cost prediction in more detail, followed by the objectives of the research and a description of the methodology followed. The results of the research and a discussion of their implications form the primary contribution of this work. The paper concludes with a look at future research and applications that can stem from this proof of concept.

PROBLEM STATEMENT

As a point of departure for the research described in this report, we first needed to establish the nature, parameters, and objectives of the problem of project cost management before developing a strategy for approaching the research. The following sections describe the background to the problem and objectives guiding the research.

Background to the Problem of Project Cost Management

The problem of managing project costs is not new. The whole procurement paradigm of Project Management was created as a response to the need to ensure that projects are completed on time and within budget, to an acceptable standard of quality (Figure 24-1). However, this paradigm is typically most influential during the construction phase of a project life, whereas the greatest impact with the least effort can be had on final project cost much earlier in the life cycle, namely in the planning and design phases (Figure 24-2). In fact, most of the critical decisions affecting the total cost of a project are made during the project planning phase, before designers, project managers, and contractors typically join the project team (Burns 1997).

In today's cost-conscious project environment, project owners and planners need a way to predict how their early decisions will ultimately impact the final cost of a project. While this need has traditionally been addressed by heuristic or "rule-of-thumb" knowledge (e.g., "the larger the building perimeter, the greater the cost of exterior enclosure"), no quantitative method currently exists for understanding how planning choices affect final project costs.

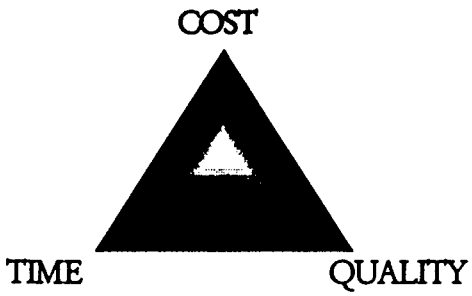

Figure 24-1: Traditional Concerns in Managing a Construction Project

This lack of quantitative method is due primarily to the complexity of analyzing the multiple factors influencing final cost. With the multitude of interacting variables that potentially affect cost even in the early planning stages of projects, performing a rigorous multivariate nonlinear regression to determine the relative importance of those variables is a nontrivial computational task.

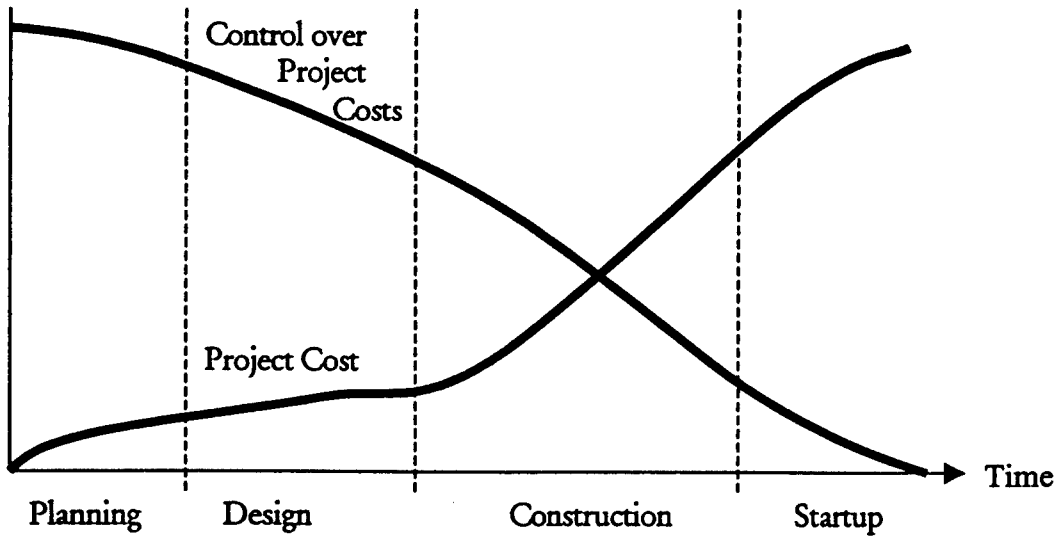

Figure 24-2: Cost and Control vs. Time for a Construction Project

Artificial Neural Networks (ANNs) offer an alternative to traditional methods of cost prediction based on parametric or quantity takeoff techniques. With their capacity to learn from examples and to generalize that knowledge to novel cases, ANNs provide the ability to undertake rapid modeling of systems in which the interaction between input and output variables is unknown but where representative examples of inputs and outputs exist. ANN modeling of the process of project cost prediction potentially provides important clues to

the relationships between initial planning-phase project variables and final cost. ANN models were used in this research as a quantitative approach to identifying cost drivers and risk factors that can be used to manage project planning and design.

Research Objectives

The objectives of this research were twofold:

- To develop a quantitative methodology for identifying and ranking significant project cost drivers.
- To develop a prototype cost prediction model useful for generating range estimates of final project costs with limited knowledge of project details.

These objectives were addressed to meet the needs of project owners during the planning phase of construction projects for guidance on which factors should be most closely managed to result in projects that meet functional requirements while remaining within budget. The range estimating capability of the model enables project planners to identify the potential for cost variation by the end of the project, thus facilitating the budgeting process.

METHODOLOGY AND RESULTS

The methodology undertaken to achieve the project objectives is presented in Figure 24-3. The following sections describe each of the primary phases of the research, along with the key results obtained at each phase.

Research Scoping

The first phase of the research involved scoping the work to narrow the population of construction projects to be considered in developing the ANN model. In order to demonstrate proof of concept, we sought to minimize the number of input variables considered, while still maintaining a sufficient degree of problem complexity to keep the relationships between inputs and outputs unpredictable using traditional regression techniques. Scoping was also based on the availability of simulation tools to generate scenarios or examples to be used to train the ANN model.

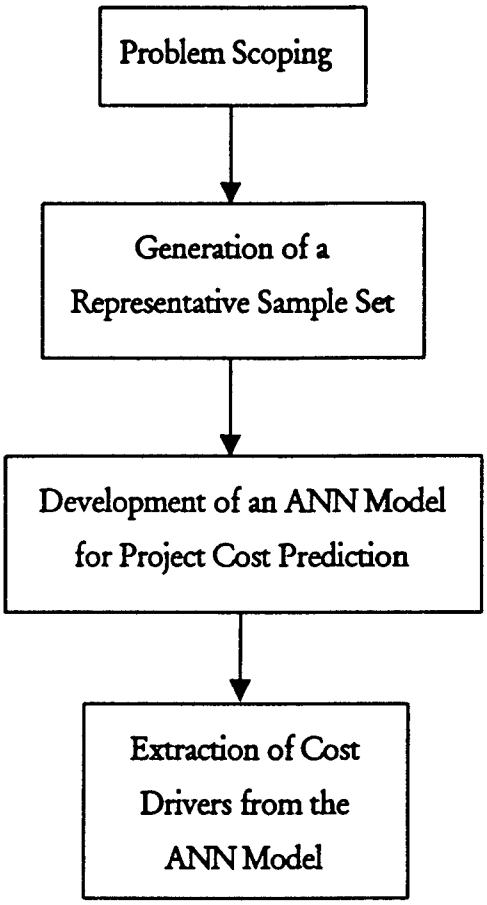

Figure 24-3: Research Methodology

We elected to limit our attention to vertical construction, since we had a Parametric Cost Engineering System (PACES) model to use for scenario simulation (see Williams 1997). This cost estimating tool provides the capability to model total project costs for a variety of typical commercial building types, ranging from communication centers to medical facilities to living quarters (Williams 1997). Within each category of building types in PACES, various models are included to estimate costs for specific building configurations and functional capabilities. We selected a specific facility type and functional model based on the availability of an existing database of real project data to be used for validation. The type of facility we selected was dormitories, and the specific model we chose to simulate was for enlisted personnel dormitories in a "1+1" configuration, i.e., suites of two rooms, each housing one enlisted person, with shared bath and living areas. This type of dormitory comprises the

majority of new military enlisted dormitory construction (Burns 1997), and thus has strong potential for initial research results to have an impact on future construction practice. The military enlisted "1+1" dormitory model provided in PACES is comparable to many dormitory designs also used in civilian commercial construction, such as the dormitories constructed for university campuses.

To further scope the problem, we chose to investigate various facility configurations for a constant number of inhabitants. In the PACES model, number of inhabitants drives the total floor area of the facility. By keeping the number of inhabitants constant, we limited the scope of variability to two main classes of variables (geometric variables and architectural variables), while keeping factors constant that are typically fixed early in the planning process. The parameters that were fixed over the sample set are shown in Table 24-1.

Table 24-1: Parameters Fixed for Problem Scoping

Parameter	Value	Comments
[redacted]	Dormitory	Selected due to availability of real cases for validation.
[redacted]	Enlisted "1+1"	Greatest number of empirical cases; generalizability to civilian construction.
[redacted]	156	Fixed to maintain constant building square footage; typically known early in the planning phase. This is the default number of persons for the PACES Dormitory model.
[redacted]	Atlanta, GA	The index city for the cost database. Fixed since location is typically known early in the planning phase. Affects seismic and foundation conditions, and heating and cooling loads.

Generation of a Representative Sample Set

After the parameters discussed in the previous section were fixed, the next task of the research was to generate a set of samples by varying the remaining input variables in a way that is representative of the range of possible design and construction practices. All data sets for this research were simulated using the PACES cost estimating tool. Simulated data were

selected for model development instead of real data due to the field-demonstrated accuracy of the PACES model (Burns 1997).

Despite the relative savings in labor due to using simulated data instead of empirical data, developing cases using PACES is still quite labor-intensive. Thus, finding a modeling technique that works with representative rather than comprehensive data sets was an important consideration in selecting ANNs to model project costs. Due to the massively interconnected and parallel nature of ANNs, a well-trained ANN model has the ability to generalize, i.e., provide reasonable outputs given a set of inputs to which it has not previously been exposed. This quality implies inversely that ANN models can be trained using sample sets which are not comprehensive but are instead representative, thus saving significant time and effort in simulating training cases.

Determining what cases should be simulated to generate a representative sample set was itself a nontrivial task, given the relatively large number of input variables, the large number of potential values for each variable, and the nonlinear interactions between input configurations. For this initial proof of concept, only selected PACES input variables were manipulated, namely those which were hypothesized to have the most influence on final project cost. Table 24-2 shows selected input variables, which could be manipulated to generate the sample set used in this research, along with possible values for each variable. While many of the input variables in isolation had a linear relationship to total project cost, in combination the variables interacted to result in a complex nonlinear cost function. Thus, significant effort was required to determine what values should be used for each variable to generate a representative sample set, while at the same time minimizing the number of scenarios that had to be generated using the PACES model.

As can be seen by inspecting Table 24-2, the number of possible permutations in a comprehensive data set is quite large, especially depending on the increments of sampling for continuous variables such as building perimeter or floor to floor height. Thus, determining a sampling strategy that would minimize the number of cases to be simulated was an extremely important task. The final set of parameters used to generate the representative sample set for model development is shown in Table 24-3.

Table 24-2: Selected PACES Parameters and Possible Values

Parameter	Possible Values
	0 – 10
	50 – 5,000 Sq. Ft.
	0 – 50 Ft.
	0 – 50 Ft.
	Low, Average, High
	Concrete Frame Steel Frame with Reinforced Concrete Deck Steel Frame with Metal Joists/Steel Deck/Concrete Fill Load Bearing Walls with Metal Joists/Steel Deck/Concrete Fill Load Bearing Walls with Wood Joists/Wood Deck Load Bearing Walls with Precast/Prestressed Floors
	Small, Average, Large
	Single Membrane Built-Up Shingle Standing Seam Metal Clay Tile Metal (Typical Metal Building)
	Brick Veneer 4" Split Rib Masonry Veneer 8" Split Rib Masonry 8" Masonry Block Tilt-up Concrete Exposed Aggregate Precast 12" CIP Concrete with Exposed Aggregate Finish Metal Sandwich Panel Stucco E.I.F.S. (Dryvit)

Varying the input parameters shown in Table 24-3 resulted in a total of 46 training cases, as indicated by X's in the matrix. Five additional randomly selected cases were developed to serve as test cases for assessing the model's performance with novel inputs. These cases are indicted by Ts in Table 24-3.

Table 24-3: Parameter Values Used in Sample Set

Floors Above Grade		1	2	3	4	5	6	7	8	9	10
	Default	X	X	X	X	X	X	X	X	X	X
	2000 LF	X	X	X							
	3000 LF	X	X	X			T				
	4000 LF	X	X	X							
	8 FT	X	X	X	X		X		X		
	10 FT			X				T			
	12 FT	X	X	X	X		X		X		
	14 FT	T		X							
	16 FT	X	X	X	X		X		X		T
	18 FT			X		T					
	20 FT	X	X	X	X		X		X		

Development of an ANN Model for Project Cost Prediction

One of the first tasks in developing an ANN model was to determine an acceptable threshold for error in output. An ANN model can be manipulated in many ways to improve its performance, including varying its internal architecture, learning paradigm or parameters, or modifying the data set used to "train" it. Given the large number of possible network configurations, selecting an acceptable level of error is important to scoping the process of network experimentation. Upon developing a network that performs within an acceptable level of error, further experimentation to improve accuracy is unnecessary. To select a threshold of acceptable error for the cost estimation problem, we used a range of acceptability of {+25%, -10%}. The upper limit was based on the cost variation authorized by the U.S. Congress for military construction projects (USC 1995), while the lower limit was based on standard industry practice for vertical construction projects (Rast 1997, Gregory 1997). Thus, an ANN model which could predict direct project costs within {+25%, -10%} was considered acceptable for the purposes of this research.

The next steps in developing an ANN model to predict project costs were to select a network paradigm, and to transform the data from the PACES simulations into a form that could be fed to the network. The back-propagation paradigm of ANNs was selected, due to its demonstrated accuracy in problems of prediction and the transparency of logic underlying the theory of back-propagation neural networks. Transformation of data from the PACES

simulations involved "squashing" each value for input and output variables to lie between {0, 1}. Each value was squashed using a linear compression formula:

$$X_{squashed} = (X_{original} - X_{min}) / (X_{max} - X_{min})$$

where $X_{squashed}$ = squashed value for variable X
$X_{original}$ = original value for variable X
X_{min} = minimum value over all instances of variable X
X_{max} = maximum value over all instances of variable X

In addition to the input variables shown in Table 24-3, the PACES simulator automatically varied other quantitative parameters based on initial input values. The total set of twelve variables used as input to the model is shown in Table 24-4.

Table 24-4: Input Variables for the ANN Model

Input Variable	Unit	Minimum Value	Maximum Value
	EA	1	10
	LF	604	4000
	SF	6313	62316
	SF	6682	65961
	LF	8	20
	SF	16308	129744
	SF	1201	9557
	EA	4	41
	EA	0	4
	EA	0	2
	MBH	649	1137
	Tons	77.62	123.91

Two different configurations of outputs were considered: a single total direct cost output, and a direct cost split by Uniformat building system categories. The second configuration was selected, resulting in an initial set of data with 15 outputs per case – one for each Uniformat category (see Table 24-5). Eight of these initial variables were excluded from the transformed data, since they did not vary as a result of manipulating input variables. The seven output variables used to train the network are indicated in Table 24-4.

Table 24-5: Output Variables for the ANN Model

Uniformat Category	Used in Model?
	yes
	yes
	yes
	yes
	yes
	no
	yes
	no
	yes
	no
	no
	no
	no
	no
	no

After configuring the 46 training cases to serve as network input, the next step was to begin experimentation with back-propagation ANN models to obtain the required level of accuracy in predicting project direct costs. The aforementioned error thresholds were used to evaluate network performance by summing the outputs of all Uniformat subsystems and comparing the total to the PACES predicted total cost for these subsystems.

Despite many advances in the theory of ANNs, choosing an appropriate network paradigm and architecture is still largely art rather than science. Various configurations of numbers of processing elements and hidden layers were tried in the general class of back-propagation ANNs. After initial experimentation, the Delta learning rule was selected to govern the ANN training, since it seemed to provide the best performance. Back-propagation is one paradigm for network learning that involves changing connection weights between hidden units based on the contribution each has made toward generating an erroneous output during training (see Wasserman 1989, NeuralWorks 1996 for more explanation). In addition to experimentation by trial and error with various network architectures, the cascade correlation algorithm (Feldman & Lebiere 1993) for developing ANN architectures was used to guide the trial and error, using the Predict expert system ANN shell by NeuralWorks.

Various ANN architectures were tried, ranging from one hidden layer consisting of 0 processing elements to three hidden layers consisting of a total of 21 processing elements.

The tested architectures, along with various error metrics, are shown in Table 24-6 and illustrated graphically in Figure 24-4.

Table 24-6: Network Architectures and Errors

Network Architecture (input-hidden-output)	Maximum % Error (% of predicted total cost)	Average Error (% of predicted total cost)
	-10.31%	-5.21%
	-13.72%	-6.18%
	-10.60%	-5.31%
	-7.16%	-4.15%
	-7.22%	-3.79%
	-8.67%	-4.11%
	-10.56%	-4.90%
	-13.74%	-6.21%
	-9.19%	-4.27%
	-11.26%	-4.94%
	-10.59%	-5.17%
	-10.19%	-5.17%
	-10.55%	-5.49%
	-9.41%	-4.20%
	-10.86%	-5.18%
	-7.28%	-3.96%
	-9.78%	-4.43%
	-9.13%	-4.20%
	-11.00%	-4.85%

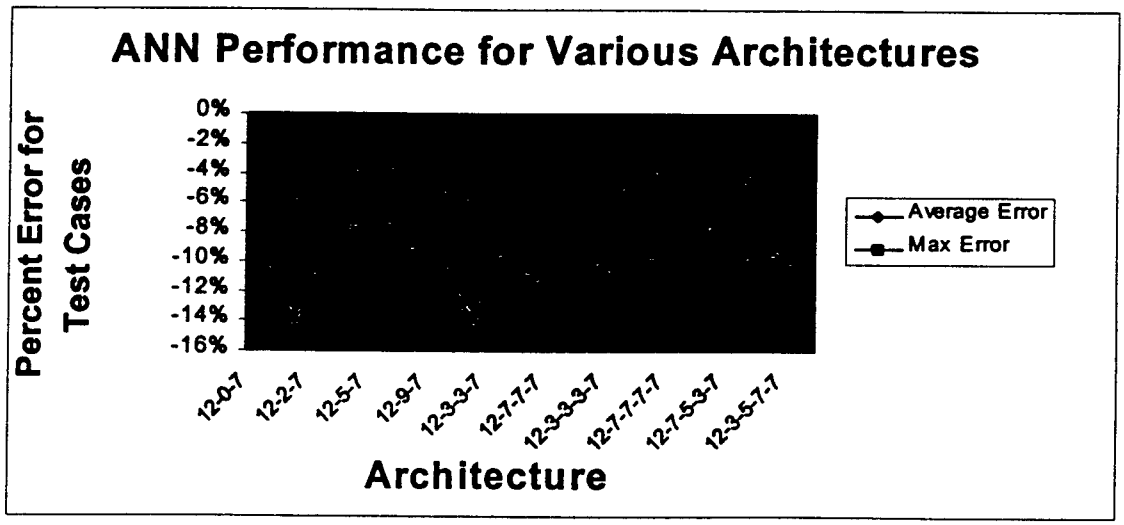

Figure 24-4: ANN Architectures vs. Error

Networks were trained for 50,000 passes of the training set, and used a learning coefficient of 0.3 with a sigmoid transfer function. The best performing network had an architecture of 12 input units, 7 output units, and one hidden layer with five processing elements. This network had an average error of -3.79%, and a maximum error of -7.22% of in predicting total direct project costs over the test set.

While all ANN models seemed inclined to underestimate total direct costs on average, in fact many of the test cases resulted in slight overestimation by the models. The negative average error resulted in many cases from the fact that the models had difficulty in extrapolating to outlying cases, of which there was one in the test set. Despite this difficulty, even the worst-performing network had a maximum error of -13.74%, which is not far from the maximum industry-accepted threshold of -10%. Additional training and manipulation of ANN parameters is likely to improve even the worst-performing network to acceptable levels of performance.

Extraction of Cost Drivers from the ANN Cost Model

The primary rationale for using ANNs to model the cost estimating process is their ability to internally represent complex, non-linear relationships between input and output variables. Given a sufficiently large number of input variables, performing a traditional regression analysis becomes computationally prohibitive when nonlinear relationships are present.

An advantage of using ANNs is their capacity to approximate non-linear relationships between inputs and output variables with relatively little computational effort. During the training process, an ANN model continually refines its internal architecture to produce more accurate outputs by comparing its initial output to the desired or target output provided by the trainer and adjusting its connection weights to increase the accuracy of its output. ANNs with at least one hidden layer approximate nonlinear regression (NeuralWare 1996), and therefore have the capability to model complex relationships among large numbers of variables, a feat which is typically computationally prohibitive using traditional regression techniques. After training, an ANN model can be manipulated to extract information about the relative importance of input variables in predicting output variables, which was the second objective of this research.

In order to utilize the ANN model as a source of information for cost drivers, the best-performing ANN model was exposed to an identity matrix as a means for extracting composite weights influenced by each input over the full network architecture. The identity matrix served as a "recall" set of cases, in which only one input neuron was activated at a time. The output for each identity case was an approximation of the relative importance of the input variable activated for that case. The set of outputs for the recall set was "unsquashed" to restore cost proportions, summed, and sorted in ascending order to provide a prioritized list of input variables in terms of their importance in driving final project cost. The resulting list is shown in Figure 24-5. Influence of each variable on system costs and total direct cost is shown using shading.

Figure 24-5: Prioritized List of Input Variables Representing Project Cost Drivers

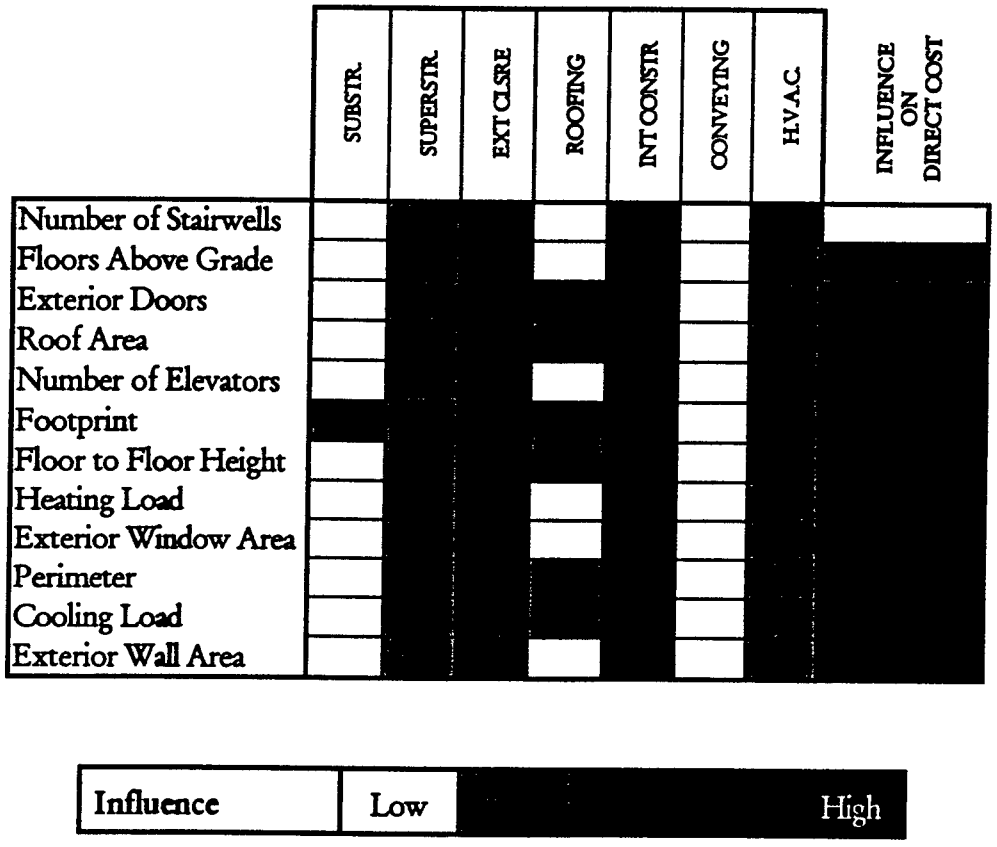

According to the influences derived from the trained ANN model, the three most influential variables driving total direct cost were building perimeter, cooling load, and exterior wall area. In the PACES model, the cooling load and exterior wall area variables are also dependent on the number of floors above grade, building perimeter, and floor to floor height. While the ANN model did not learn the dependencies between these variables, it did predict the most influential variables in terms of total direct cost.

DISCUSSION AND CONCLUSIONS

Potential Impacts of Cost Management Information on the A/E/C Industry

The ability to extract information about the primary factors driving project cost holds promise for improved management of the planning and design processes. The knowledge of these factors will enable project owners to make informed decisions when specifying initial design parameters, and to prevent design decisions from being made casually when those decisions have the potential to strongly impact final project costs. With an awareness of the potential impacts of early design information, information from future projects can be compiled to provide real case data to develop improved ANN models.

Applicability and Validity of the Cost Driver Extraction Methodology

While longitudinal field validation of the results of this research was outside the scope of this research, initial heuristic validation of the research outcomes supports the methodology underlying the process of cost driver extraction. Although this proof of concept was limited in scope to one specific type of vertically-constructed facility within the entire range of construction projects, the methodology demonstrated in this work is anticipated to be extensible to other types of construction projects within the sector of vertical construction, as well as to other project sectors.

FUTURE RESEARCH

Three areas of additional work can stem from this research, including continued refinement of ANN performance beyond that achieved in this proof of concept, generalization of the

cost driver extraction methodology to other types of construction projects, and the development of a project-specific methodology for identifying and prioritizing cost drivers.

Continued Refinement of ANN Performance

The first area of future research is to continue to experiment with additional configurations of ANN parameters and architecture, along with additional research into developing representative sample sets using clean, simulated data. While the purpose of this research was to demonstrate the concept of cost driver prediction using ANNs, additional refinement and development of theory could lend substantial benefit to this work. Future research will also include testing and validation of ANN models and cost driver extraction techniques using real data.

Generalization of Approach to Other Project Types

More research is needed to test the ANN approach to cost driver prediction in other project types besides military administration buildings and dormitories. Although significant differences are not anticipated for similar commercial type buildings, examples from other fields of construction such as industrial plants may pose a challenge due to the uniqueness of each facility.

Development of Project-Specific Cost Driver Identification Tool

One promising application of the ANN concept to project risk management is the potential for prediction of specific cost drivers for projects at the pre-design phase of work. While many project managers rely on years of expert experience to know what to watch for, the development of knowledge-based systems for these applications has been unexplored. Using ANNs to undertake identification of project-specific cost drivers is a promising application for ANNs, extending the capabilities of generalized feature recognition for generic construction projects exploited in this research.

ACKNOWLEDGEMENTS

This research was sponsored by the U.S. Air Force Office of Scientific Research under a Graduate Student Summer Research Grant. Grateful acknowledgement for technical and facilities support is given to Delta Technologies Group, Inc., owner of the commercial license for PACES software. Thanks also to the Georgia Tech Research Institute for their financial support of this research, and to NeuralWare, Inc., owner of the commercial license for the NeuralWorks Professional II software used in this research.

REFERENCES

Burns, T. J. (1997). Deputy Director, Construction Cost Management, HQ AFCESA/DC, Tyndall AFB. Informal interview. July 16.

Feldman, S.E., and Lebiere, C. (1988). "The Cascade-Correlation Learning Architecture," Advances in Neural Information Processing Systems, v. 2, Morgan Kaufmann, ed.

Gregory, R.A. (1997). Assistant Professor of Civil & Environmental Engineering, Georgia Institute of Technology. Informal interview. July 31

NeuralWare. (1996). *Neural Computing*. NeuralWare Technical Publications Group, Pittsburgh, PA.

Rast, R.R. (1997). CEO, Delta Technologies Group, Inc. Informal interview, July 31.

USC. (1995). 104th Congress, 1st Session, No. 2, Title 10, *USCode Armed Forces* as amended through 12/31/94. Committee on National Security, HoR, March 1995. Page 1047, Section 2853, Authorized cost variations. Ch 169 - Military Construction and Military Family Housing.

Wasserman, P.D. (1989). *Neural Computing: Theory and Practice*. Van Nostrand Reinhold, New York.

Williams, L.E. (1997). "Data Simulation Supporting Range Estimating for Researching and Developing Alternatives". USAFOSR Graduate Student Summer Research Report.

A Study of Intra-Class Variability in ATR Systems

Raj Bhatnagar, Associate Professor
Dax Pitts, Graduate Student

ECECS Department

University of Cincinnati
Cincinnati, OH 45221

Final Report for:
Summer Faculty Research Program
Wright Laboratory

Sponsored by:

Air Force Office of Scientific Research
Bolling Air Force Base, DC

and

Wright Laboratory
Wright Patterson Air Force Base, Dayton, OH

September 1997

A Study of Intra-Class Variability in ATR Systems

Raj Bhatnagar, Associate Professor
Dax Pitts, Graduate Student
ECECS Department, University of Cincinnati
Cincinnati, OH 45221

Abstract

In this report we describe the results of our investigation into the intra-class variability of a vehicle class from the perspective of an automatic target recognition system. We examine the relevance of synthesized vehicle models for ATR systems and conclude that these models fall within the bounds of the vehicle class set by the intra-class variability of the vehicle. We also demonstrate the relevance of the mean-square-error between an image chip and a template when used as a measure of distance between the physical vehicles. We also show that it is feasible to intelligently merge chips from different vehicles of a class and construct classifiers that perform better than those designed with any individual member of the vehicle class.

A Study of Intra-Class Variability in ATR Systems

Raj Bhatnagar, Associate Professor
Dax Pitts, Graduate Student
ECECS Department, University of Cincinnati
Cincinnati, OH 45221

1 Introduction

An automatic target recognition system is usually trained completely with measured data obtained from target vehicles. However, such an effort, if done correctly, is extremely expensive from the perspective of computational resources. Collection of the templates requires an exhaustive data collection across all of the operating conditions of the ATR scenario. Storage of the templates would require extremely large amounts of storage space, and an algorithm based on comparisons with the numerous templates would require prohibitively large processing time. Such an effort would need to account for various possible articulations of target vehicles and the large intra-class variability of every vehicle class.

One solution for handling the above problems lies in using synthesized models of target vehicles and a model based ATR system. DARPA's MSTAR program, agented by the Wright Laboratory, WPAFB, Dayton, Ohio, follows this philosophy to a large degree. The performance of such a system depends on how well the synthesized vehicle-signatures match the actual measured signatures.

The objective of the research described in this paper is to examine the extent and consequences of variability within the class of T72 tanks from the perspective of MSTAR system developed by the Wright Laboratory in Dayton Ohio. In the context of this intra-class variability we then examine the closeness with which synthetic data identifies various instances of the T72 class.

The scope of our study includes the following tests with the measured and the synthetic data.

1. The performance of a classifier trained on a single member of the T72 class in discriminating the members of *T72-class* from the members of *confuser-vehicles* class. The problem is formulated as a two-class discrimination problem. An image chip from a target vehicle is sought to be classified as belonging to either the *T72* class or the *confuser-vehicles*

class.

2. The performance of a classifier trained on the synthetic signatures generated by DEMACO's XPATCH radar system prediction code and its comparison to the classifiers trained on the measured data.

3. Relevance of Mean-Square-Error distance measure between templates and test chips to physical features and articulations of the target vehicles.

2 The Data Set

Our study has been performed with data from the DARPA's MSTAR program. The measured data corresponds to 1ft. X-band SAR imagery. We have used the measured data for the following vehicles from the MSTAR collections:

Collection-1 T72s: T72-132, T72-812, and T72-s7. For each tank, the data from 31 and 32 degree elevations has been used.

Collection-2 T72s: T72-A04, T72-A05, T72-A07, T72-A10, T72-A32, T72-A62, T72-A63, and T72-A64. For each tank, the data from 30 and 31 degree elevations has been used.

Confuser Vehicles: M109, M110, BMP2, M2, M1. For these vehicles, data from 31 and 32 degree elevations has been used.

Confuser Vehicles M113, M35, and BTR70. For these vehicles, data from 31 degree elevation has been used.

In addition to this measured data, we used the synthetic data generated by DEMACO's XPATCH radar signature prediction code. The synthetic data models the same vehicle and articulation as has been measured for the T72-812 configuration mentioned above.

3 The Test Runs

Our target recognition tests consisted of a number of runs, each one of which contained the following main steps:

1. **Template Construction:** We constructed 72 templates of 5-degree width for each of the eleven measured T72s and also for the synthetic data from the XPATCH system.

We take all the available image chips from within the angular boundaries of a template and generate a mean template, and a mask. The mask is formed by thresholding the mean template and thus corresponds to the target's bright region. The mask specifies the pixels over which the distance computations are made during comparison with an unknown image chip. Each chip, used for constructing the templates, was typically of size 128 X 128 pixels. The number of image chips available for an elevation angle for any one vehicle ranged between 270 and 320. The image chips from two different elevation angles, as mentioned above, were included in the templates. A set of templates thus formed constituted one classifier for our study.

2. **ATR Tests:** We used a standard MSE classifier for comparing image chips from a target to the templates from a classifier. The classifier compensates for the unknown scale factor on the image chip and also for the unknown location of the target on the chip. Each test consisted of the following steps:

   (a) Select one vehicle as the *Target* vehicle and one T72 as the *classifier*. Obtain all image chips from the selected *Target* and all templates from the selected *classifier*.

   (b) Compare each image chip from the *target* to each template from the *classifier* and determine the template closest to each chip. The *mean-square-error* between each chip and its closest template is also recorded.

   The output of a test is a list containing the closest matching template for each chip, the *mean-square-error* distance between the chip and the template, and the scale factor used with the chip. We have used eleven measured and one synthetic T72s as classifiers and there are nineteen different possible target vehicles; 11 T72s and 8 confusers. The number of test runs, therefore, was 228; one for each target-classifier combination.

4 Intra-Class Variability

A number of observations are made by examining the distributions of the MSE distances for each test. The following diagram shows the distributions of MSE values from two of the tests. The two curves in this plot correspond to the histograms for the MSE values from the two tests. The x-axis shows 70 bins for the histogram. Each bin corresponds to 0.005 units of MSE distance as determined by the MSE classifier. For both these tests the classifier templates have been used from the measured data for T72-A10. The solid curve on the left corresponds to the distribution for image chips from T72-A64 and the dotted curve to the right corresponds to the distribution for image chips from the confuser vehicle BMP2.

It can be seen from this plot that most of the MSE values for the T72-A64 are smaller than those for the confuser vehicle BMP2. A ROC plot can be constructed for any such pair of distributions.

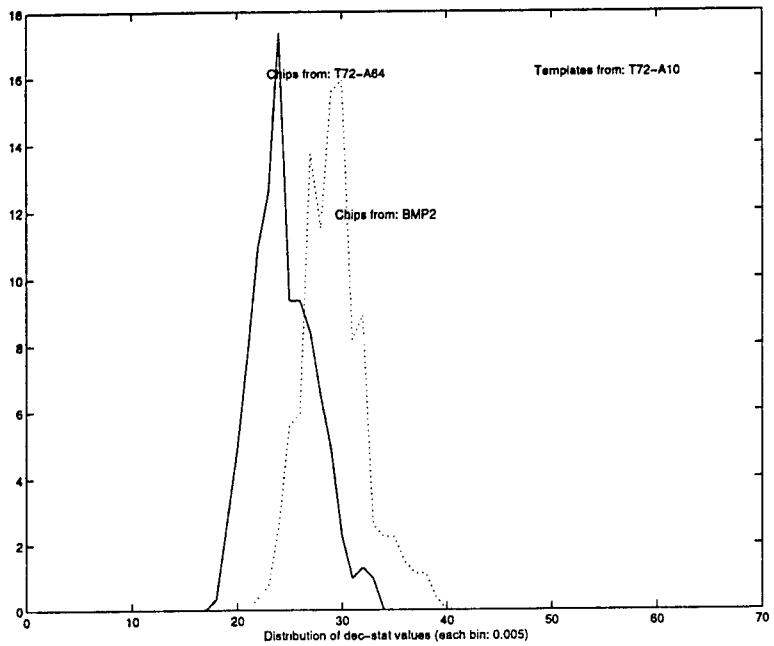

4.1 T72 Class vs. Confusers Class

From our tests we accumulated data in such a way that for each classifier we obtained one distribution curve for the set of T72s and one distribution curve for all the confuser vehicles. When computing the distributions, the T72 being used as the classifier was excluded from the distribution curve for the set of T72 vehicles. This process was repeated for each of the eleven measured T72s acting as classifiers. For each classifier we constructed a ROC curve and the following plot shows all the ROC curves.

It is evident from this set of ROC curves that the performance of a classifier based on an individual member of the T72 class varies very widely with the selected member. According to this set of ROC curves it can be seen that T72-A10 acts as the best classifier and T72-A32 acts as the worst classifier. The difference between these two classifiers is very large. The statistical confidence level in each of the curves is significantly high because the number of chips used for computing each ROC curve is very high. For each curve we have used more than 5,500 image chips from the T72s and more than 4,000 image chips for the confuser vehicles.

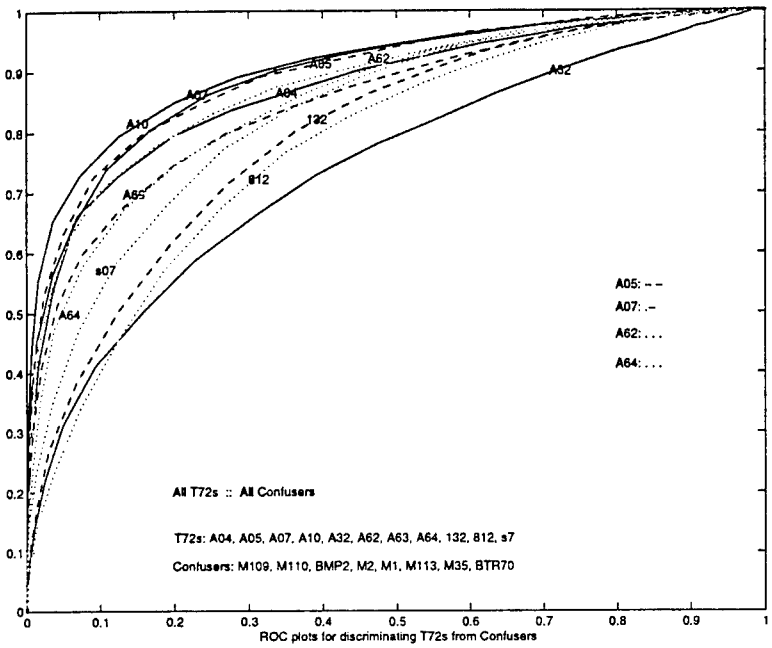

4.2 T72 Class vs. Individual Confusers

Each of the above ROC curves can be examined in its decomposition into ROC curves where each individual confuser has been tested against the set containing all the eleven T72s. The set of ROC plots that decomposes the accumulated ROC plot for T72-A04 classifier is shown below.

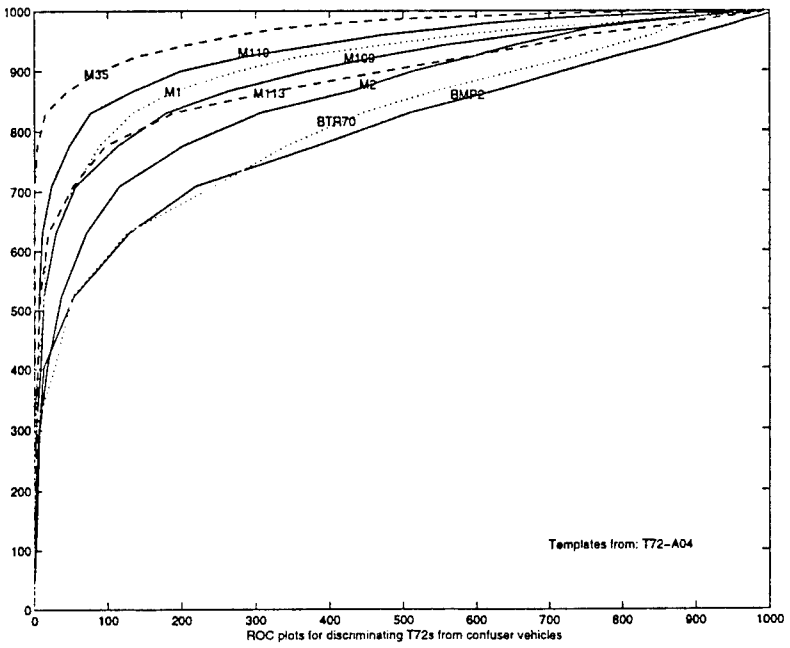

It is evident from the above set of ROC plots that the success of a classifier in discriminating

the T72s from a confuser vehicle varies very significantly with the confuser vehicles.

4.3 Individual T72s vs. Confusers Class

Another way to decompose a ROC curve from those described in Section 4.1 is to examine the performance of the classifier when individual T72s are to be discriminated against the complete set of confuser vehicles. In the following plot we have selected the classifier based on the synthetic T72-812 data and show the ROC plots for discriminating individual T72s from all confusers using this classifier. As expected, the synthetic classifier best discriminates the measured T72-812 from the confusers.

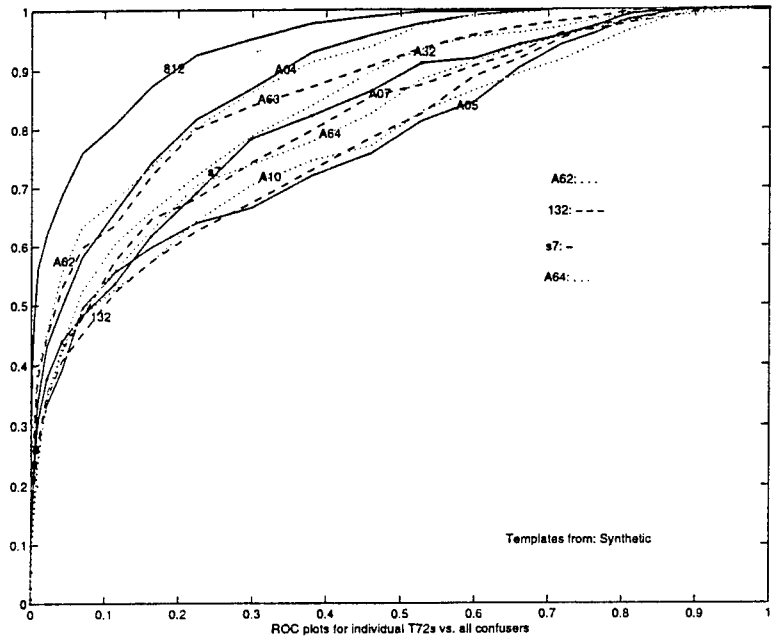

4.4 Individual T72s vs. Individual Confusers

For discriminating an individual T72 from an individual confuser vehicle the performance of various classifiers varies very significantly. This can be inferred from the above sets of ROC plots. We can explicitly pick a particular T72 and confuser and plot the ROC curves using different classifiers. One such set of ROC curves is shown below. Here T72-A04 has been selected as the target vehicle, BMP2 as the confuser vehicle, and ROC curves for five different classifiers have been shown.

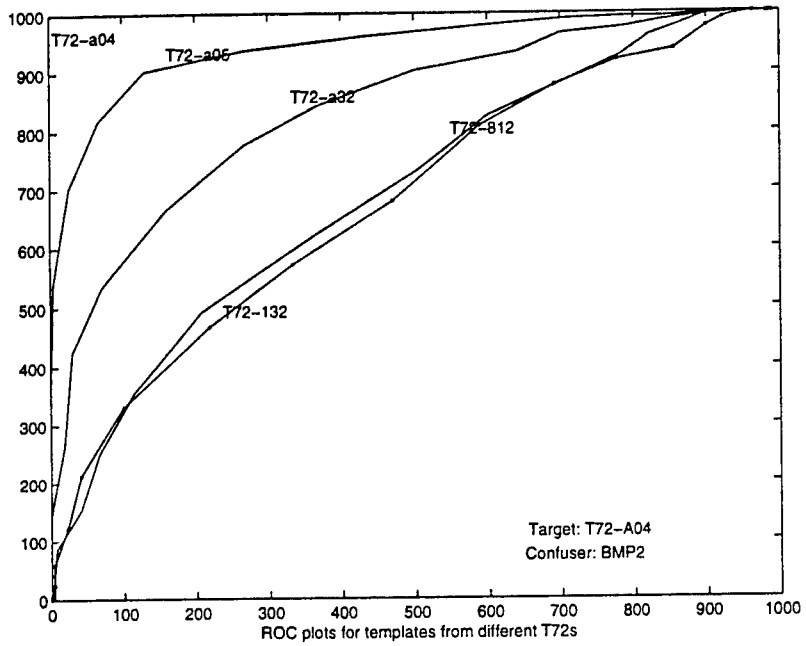

5 Synthetic Data

We now examine the performance of a classifier designed with the synthetic data. As mentioned above, the synthetic data available to us is for the same model and articulation of a T72 as the measured data for the T72-812. We show below the ROC plots for the classifiers designed with the measured and the modeled data for the same T72 vehicle.

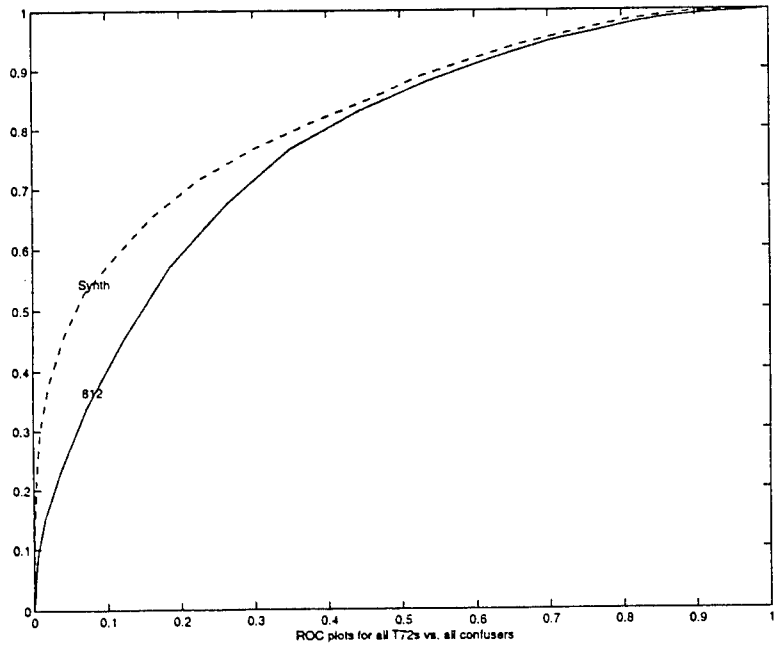

The ROC plots are for discriminating the class of all T72s from the set of all confuser vehicles. Two important conclusions can be derived from this set of plots. First, the classifier based upon the synthetic data has performed consistently better than the classifier based upon the measured data. Second, the ROC plot for the synthetic classifier falls well inside the range of ROC curves shown in Section 4.1 above. Both these observations are very significant from the perspective of usability of synthetic data for ATR systems.

A further comparison between the performance of classifiers based upon synthetic and measured data can be seen in the following two sets of ROC curves. In the first set we have used the classifier based upon the measured data for discriminating the set of all T72s from individual confuser vehicles. The second set of plots shows the same discrimination task being performed by the classifier based upon the synthetic data.

The ROC curves in the second plot show significantly better performance for classification against many confuser vehicles than that shown in the first plot. It is clear that the synthetic model is performing better as a classifier than its measured counterpart in several cases. A deeper analysis of the performance is needed to investigate the reasons for the order of various confuser vehicles not being the same in the two plots. Such an investigation will shed more light on the nature of the synthetic data.

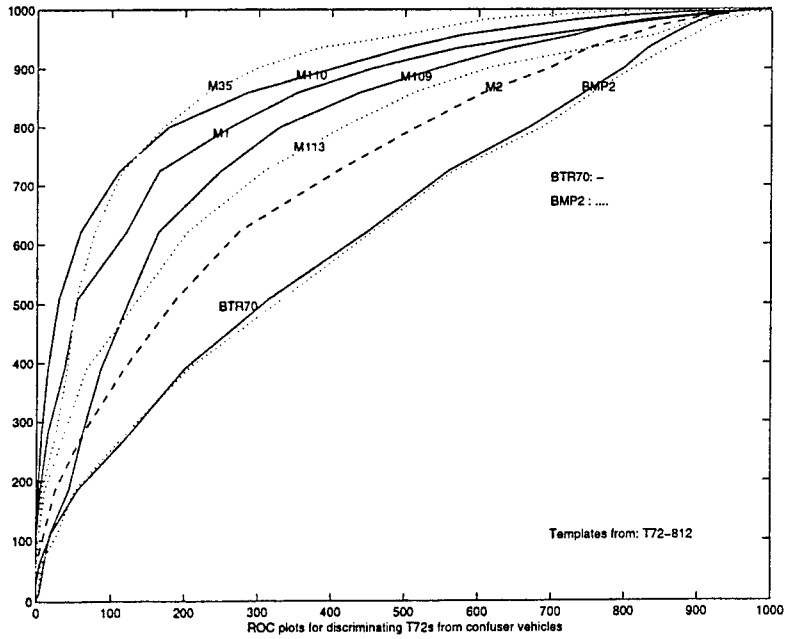

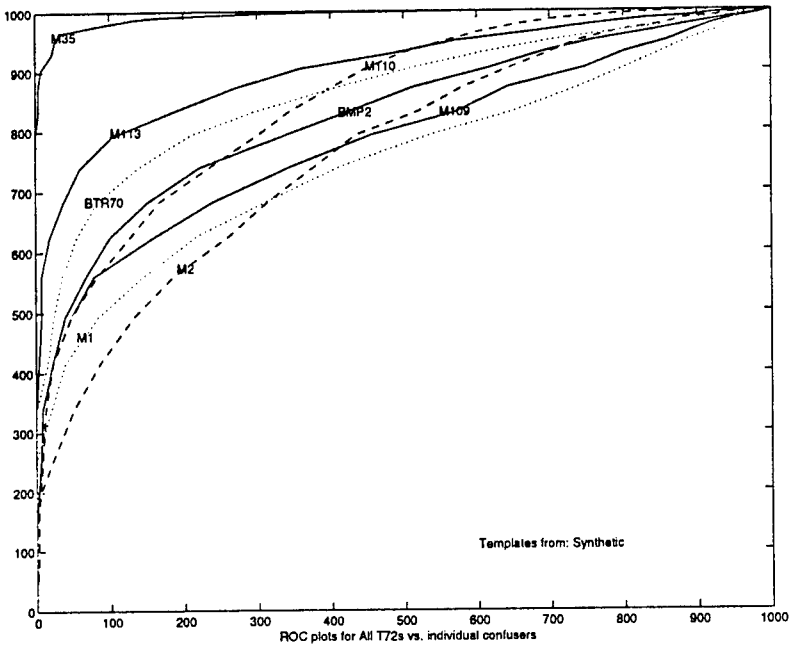

6 A Notion of Separability: Quantified

We developed a notion of *distance* between two vehicles based upon the MSE values computed by the classifiers. For vehicles V_1 and V_2 we measure this distance as follows.

1. For each image chip from V_1, determine the minimum MSE distance from the templates for V_2.
2. For each image chip from V_2, determine the minimum MSE distance from the templates for V_1.
3. Take the average value of all the minimum distances from all the chips for V_1 and V_2. It was observed that typically, average distance from V_1 chips to V_2 templates remains very close in value to the average distance between V_2 chips and V_1 templates.

We use this average value as the distance between the vehicles V_1 and V_2 and call it the *MSE-Distance(1,2)*. We computed the MSE-Distance for every pair of T72s for which measured data is available.

We now seek to represent each T72 vehicle by a point on a 2-dimensional plane in such a way that the distance between points for V_1 and V_2 is as close as possible to the MSE-Distance between V_1 and V_2. If the actual distance on the 2-dimensional plane between points for V_1 and V_2 is $D(1,2)$ then the cumulative error for all the vehicles included on the plot is:

$$Error = \sum_{i=1}^{11} \sum j = i^{11} \ (abs(D(i,j) - MSEDistance(i,j))/MSEDistance(i,j).$$

We used a simple relaxation algorithm to place the points on the MSE distance plane in such a way that the mean square value of the above described error quantity is minimized. The result of placing the points for the eleven measured T72s is shown below.

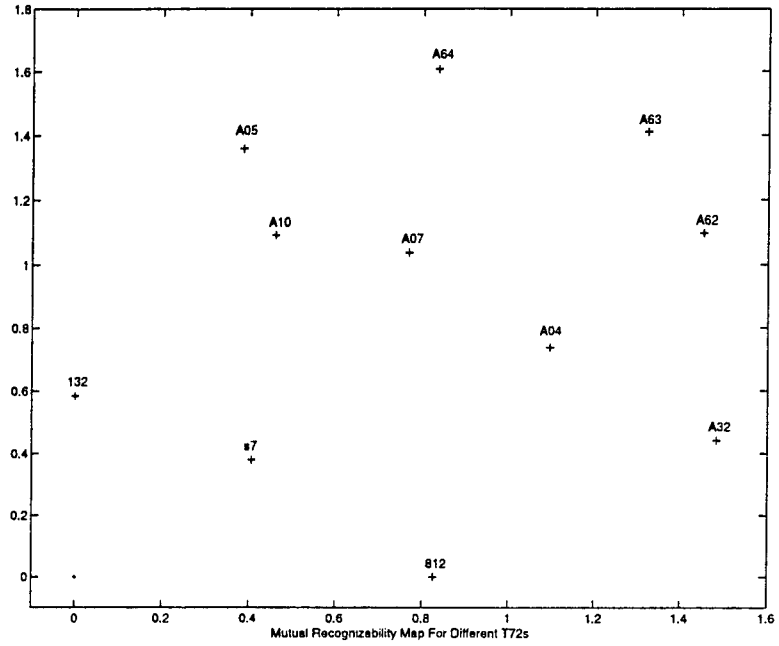

It turns out that in this plot the T72s cluster according to their physical characteristics, articulations, and configurations. This, on one hand revalidates the use of MSE measure for classification purposes, and on the other hand provides a very good tool for visually examining the relative closeness and disparity among the various members of a vehicle class.

We now add to the set of T72s the synthesized model. The resulting plot is shown below.

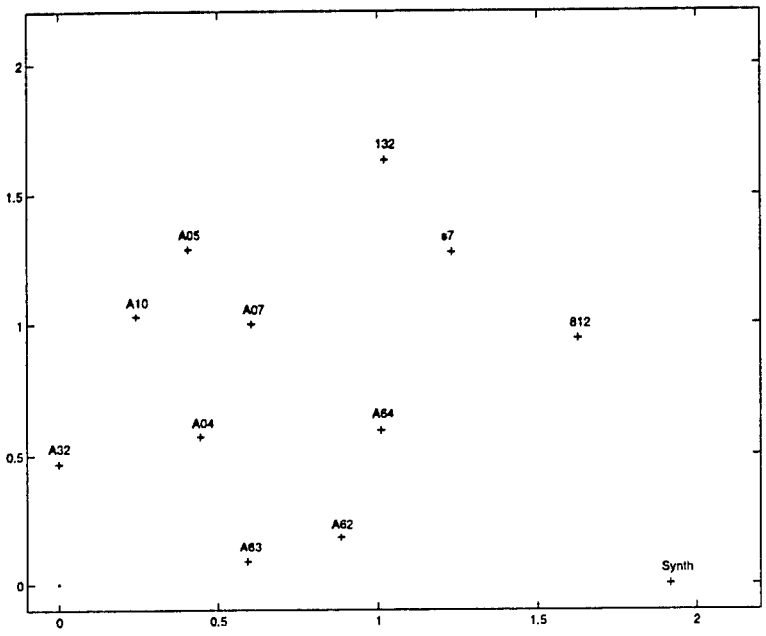

We see in this plot that the synthetic model lies far away from all the other T72s. Ideally, for a model to be a representative of the class of T72s, we would expect it to lie somewhere in the middle of the area populated by the T72s. Since a model emulates a unique T72, we can only expect it to be close to the point corresponding to the measured data for the same T72. In this case the point corresponding to the synthetic data is farther than expected from the point corresponding to the measured T72-812. Determining a synthetic model located at a point closer to the center of the population of T72s is a challenging problem and may involve creative use of chips from a number of T72 vehicles for creation of classifier templates.

The classifier trained on the synthetic model for a T72 performs better than its measured counterpart as evidenced by the ROC curves shown above but it itself appears to be somewhat distant from the measured T72-812 and also from the class of T72s. This requires further investigation and our current work is focused in that direction.

7 Construction Of Mixed Templates

We performed some preliminary tests to determine the feasibility of constructing templates for a classifier by mixing chips from a number of different T72s. An examination of ROC curves presented in Section 4.1 shows that T72-A10 is the best performing classifier and T72-A32 is the worst performing classifier. In our first test, we included chips from both these vehicles to construct a set of templates. We then performed the ATR tests with this new merged classifier.

A comparison of its performance can be seen in the figure below containing the three ROC curves.

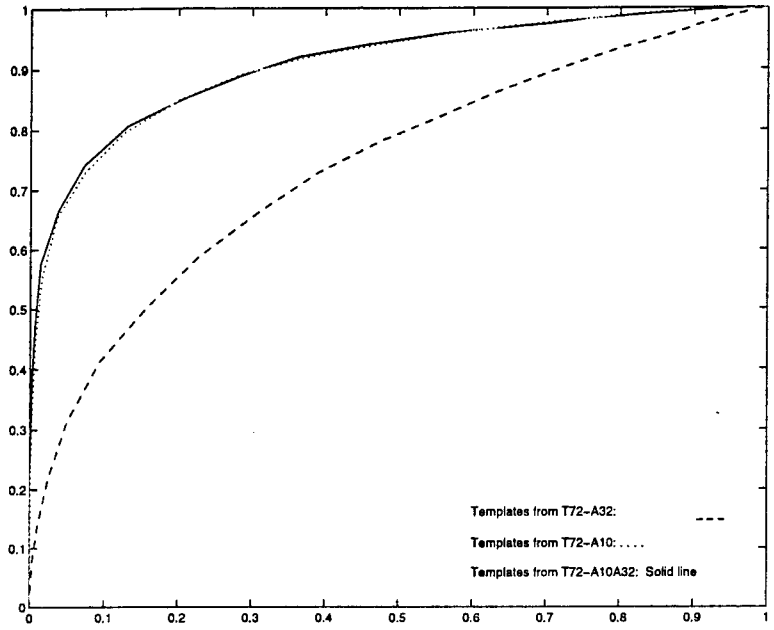

We can see from the above ROC curves that the mixed classifier performs almost as well as the best performing classifier. The chips from T72-A32 haven't made any apparent difference in performance. This is an interesting observation and a deeper investigation is needed to discover the reasons for this behavior. For our second test we looked at the following mutual distance map containing T72s and the M35 confuser vehicle.

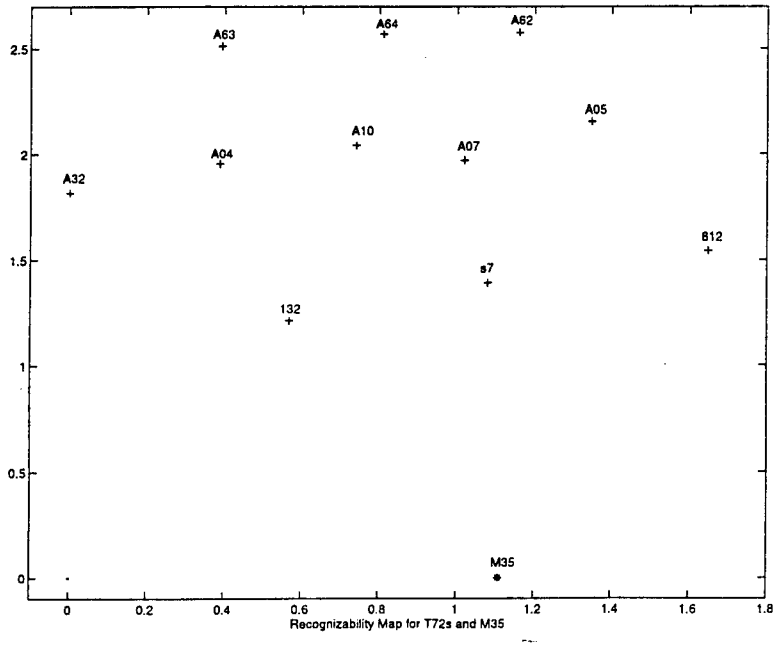

We selected T72-A10 and T72-A62 for merging into a single classifier based on their positions in the above map. They belong to different clusters and are best performers among their respective clusters. (Performance, as discerned from the ROC curves in Section 4.1.) The performance of this mixed classifier, and its comparison with its constituting components, is shown below.

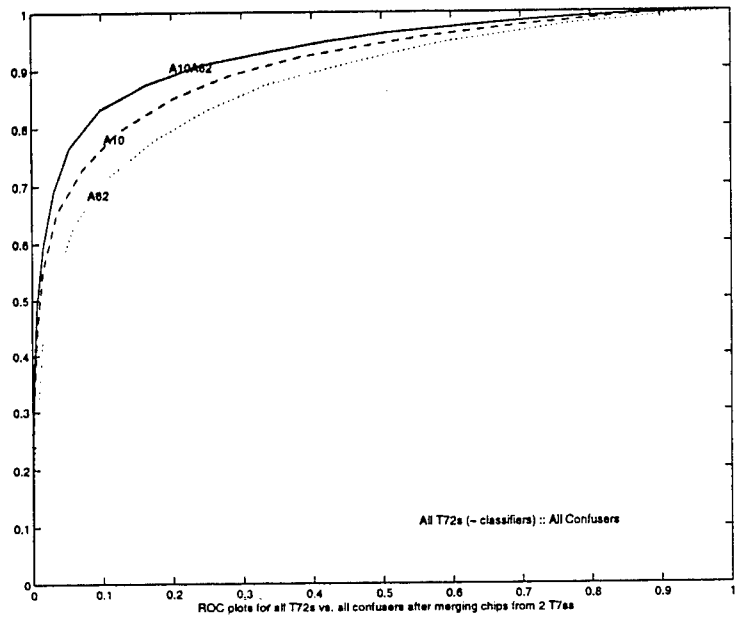

The composite classifier in this case has performed significantly better than its constituting components. This lends credence to the hypothesis that a better performing classifier can be constructed by using and intelligently merging data from different members of a vehicle class. How to select data to be merged is an important question and needs further testing and investigation. as discussed above, the T72s clustered in the MSE-distance map according to their physical features and articulations. The second test, therefore, can be seen to imply in a very general way that a classifier designed from data taken from vehicles with different physical features would perform better than individual members of the vehicle class. This is to be expected from an intuitive perspective.

8 Confusion Matrices

A new perspective on the performance of various classifiers can be obtained by constructing a confusion matrix. We show four different confusion matrices below.

For each image chip in our dataset we determined the template, across all classifiers, that comes closest to the chip. We marked the classifier corresponding to this template as the

selected classifier. However, each T72 almost always "recognizes" its own chips and this is evidenced in the table shown below.

Confusion Matrix for T72s
The **BEST** matching template for each chip.

	TEMPLATES FROM										
	A04	A05	A07	A10	A32	A62	A63	A64	132	812	s7
CHIP											
A04	589	0	0	4	1	0	2	1	1	0	0
A05	1	594	1	2	1	0	0	0	0	0	0
A07	0	3	591	4	0	1	0	0	0	0	0
A10	4	0	1	594	0	0	0	0	0	0	0
A32	0	0	0	0	599	0	0	0	0	0	0
A62	0	0	7	2	0	577	10	3	0	0	0
A63	1	2	0	1	0	1	592	1	0	1	0
A64	0	1	1	2	0	0	0	595	0	0	0
132	0	0	0	0	0	0	0	0	489	0	0
812	0	0	0	0	0	0	0	0	1	483	1
s7	0	0	0	0	0	0	0	0	2	0	474
M109	16	66	42	21	57	20	17	88	67	30	63
BMP2	18	35	59	18	54	23	40	79	66	36	61
M110	12	27	58	33	33	16	21	81	73	70	62
M2	48	34	43	21	34	24	25	75	65	27	87
M1	36	35	31	29	30	15	19	70	54	38	49
M113	24	32	56	30	40	32	32	66	118	32	78
M35	20	16	30	28	14	8	8	30	138	124	124
BTR70	42	28	42	24	52	14	18	72	74	56	86

In order to determine the T72 that is closest to a chip and is different from the T72 from which the chip emanates, we selected the second best template match for each image chip and considered its classifier as being the *2nd closest* to the chip. A confusion matrix based on this criterion is shown below.

Confusion Matrix for T72s
The **2nd BEST** matching template for each chip.

	TEMPLATES FROM										
	A04	A05	A07	A10	A32	A62	A63	A64	132	812	s7
CHIP											
A04	7	88	152	144	43	48	60	36	4	2	14
A05	51	4	133	256	13	22	30	65	11	2	12
A07	61	154	7	256	6	24	27	45	9	1	9
A10	69	199	206	1	9	35	23	36	8	3	10
A32	189	67	83	99	0	53	26	37	17	12	16
A62	46	30	52	48	3	16	270	112	1	10	11
A63	47	34	36	34	0	295	4	130	3	1	15
A64	23	97	76	91	4	132	110	3	20	1	42

132	24	42	71	35	6	5	7	9	0	85	205
812	46	35	20	22	15	33	13	17	165	2	117
s7	27	24	36	51	5	32	35	61	161	42	2
M109	17	58	44	31	52	30	27	59	79	37	53
BMP2	31	34	57	35	39	26	41	80	56	30	60
M110	24	63	47	29	31	22	24	60	74	43	69
M2	20	42	45	35	34	28	33	65	68	43	70
M1	25	38	50	32	45	17	16	35	57	34	57
M113	30	46	50	42	58	18	40	56	82	32	86
M35	50	20	34	20	26	12	22	50	106	78	122
BTR70	34	56	64	28	56	24	28	54	62	46	56

The above confusion matrix shows some patterns of affinity among subsets of T72s. Each T72 "looks" more like some other T72s and less like some others. This pattern is very similar to the one observed in the MSE-distance maps discussed above.

We further modified the structure of the confusion matrices by including the two mixed classifiers whose design has been discussed above, and the synthetic classifier designed with the XPATCH data. A repeat of the above two confusion matrices with this change resulted in the following two matrices.

Confusion Matrix for T72s+Mixed Classifiers
The best matching template for each chip.

	TEMPLATES FROM													
	A04	A05	A07	A10	A32	A62	A63	A64	132	812	s7	Syn	mx1	mx2
CHIP														
A04	585	0	0	2	0	0	2	1	1	0	0	0	4	3
A05	1	590	1	2	0	0	0	0	0	0	0	0	2	3
A07	0	3	587	3	0	0	0	0	0	0	0	0	1	5
A10	4	0	0	518	0	0	0	0	0	0	0	0	27	50
A32	0	0	0	0	565	0	0	0	0	0	0	0	34	0
A62	0	0	6	1	0	510	4	3	0	0	0	0	0	75
A63	0	2	0	1	0	1	590	1	0	1	0	0	1	2
A64	0	1	1	1	0	0	0	591	0	0	0	0	1	4
132	0	0	0	0	0	0	0	0	489	0	0	0	0	0
812	0	0	0	0	0	0	0	0	1	483	1	0	0	0
s7	0	0	0	0	0	0	0	0	2	0	474	0	0	0
M109	15	56	32	9	42	13	12	71	58	28	47	2	77	25
BMP2	17	27	54	12	43	18	30	69	58	30	55	0	42	34
M110	10	22	57	25	26	11	21	75	68	68	61	1	29	12
M2	45	32	37	15	26	22	21	69	58	26	77	0	33	22
M1	27	33	23	19	22	10	14	68	48	34	47	1	39	21
M113	18	26	48	20	24	28	30	60	112	32	76	2	52	12
M35	20	16	30	24	14	8	8	28	136	124	120	2	10	0
BTR70	38	24	38	14	38	12	18	72	66	54	72	2	40	20

1. *mx1* templates are formed by mixing chips from T72-A10 and T72-A32.
2. *mx2* templates are formed by mixing chips from T72-A10 and T72-A62.

Confusion Matrix for T72s+Mixed Classifiers
The **2nd BEST** matching template for each chip.

	TEMPLATES FROM													
	A04	A05	A07	A10	A32	A62	A63	A64	132	812	s7	Syn	mx1	mx2
CHIP														
A04	7	47	79	47	12	18	36	23	3	1	9	0	147	169
A05	19	7	96	116	1	6	16	38	9	0	4	0	108	179
A07	25	74	9	93	0	9	11	17	4	1	4	0	111	241
A10	2	12	24	63	1	0	1	1	1	0	0	0	200	294
A32	9	6	2	2	34	0	0	2	1	1	0	0	541	1
A62	5	0	4	0	0	72	52	7	0	0	0	0	2	457
A63	24	19	20	3	0	147	4	91	3	1	8	0	12	267
A64	10	62	39	19	1	30	56	6	12	1	24	2	33	304
132	17	34	59	16	3	3	2	7	0	78	186	2	56	26
812	35	29	14	10	13	17	5	8	143	2	103	27	36	43
s7	23	14	19	15	0	15	20	36	139	35	2	2	30	126
M109	10	37	35	17	38	23	18	57	57	29	48	3	69	46
BMP2	23	28	45	24	35	16	35	59	50	28	52	0	55	39
M110	17	52	39	27	28	21	15	52	69	37	54	0	37	38
M2	19	33	41	27	28	19	27	49	64	41	61	4	41	29
M1	24	24	38	25	34	15	10	24	45	26	41	6	69	25
M113	36	38	50	24	60	18	36	48	74	28	74	0	34	20
M35	42	16	30	18	20	12	20	52	94	78	120	2	20	16
BTR7 0	28	48	42	18	50	16	26	44	56	42	54	4	54	26

1. *mx1* templates are formed by mixing chips from T72-A10 and T72-A32.
2. *mx2* templates are formed by mixing chips from T72-A10 and T72-A62.

A number of interesting observations can be made from the above two matrices. The first is that a chip's affinity to its own classifier is very significant and is larger than that for the mixed classifiers. The second confusion matrix, however, reveals that the mixed classifiers are preferred overwhelmingly as the second choice by all the T72 vehicles in our set. This is a very interesting observation. When two good representatives of the class are merged to construct a classifier, even those T72s that are not part of the classifier prefer it over any other individual T72. This demonstrates that it is possible to capture features from multiple T72s into a single classifier and these classifiers then attract other T72s that may have affinity to any combination of features in the merged classifier. This is an interesting line of investigation and our results are only very primitive. A detailed investigation along this line is bound to result in deeper insight into the design of more representative classifiers for classes with large intra-class variability.

Another interesting observation that can be made from the last matrix is that the image chips from the measured T72-812 did not choose the synthetic classifier even as their second preference. This is a surprising observation. Synthetic classifier is designed for the same vehicle as represented by the T72-812. However, we have seen above that the synthetic classifier has performed better than its measured counterpart in all classification tasks. There is, therefore, need to investigate further the character of synthetic data, the reasons for its superior performance, and reasons for its greater-than-expected distance from its measured counterpart.

9 Conclusion

The main conclusions of the research described above can be summarized as follows.

1. There is a very significant amount of variability within the class of T-72 vehicles. A classifier designed with any one member of this class may perform very well for some members and very poorly for some other members.
2. The synthetic models of vehicles, generated by the XPATCH system, perform within the bounds of the performance set by the variability within the class of T72 vehicles.
3. The synthetic models of vehicles are not as close to their measured counterparts as expected. They perform better than the measured counterparts because the MSE-distance between synthetic models and confuser vehicles is even larger.
4. It is possible to mix data from two members of the T-72 class to design a classifier that performs better than a classifier designed with the members taken individually.

With the help of various tests we have demonstrated that there exists a large amount of variability within the class of T72s. This difference makes it harder for a classifier designed with any one member of the class to discriminate between the T72s and the confuser vehicles. Also, the classifiers designed based upon any one member of the class of T72s have very widely varying performance. The synthesized model of the T72 performs within the bounds of performance set by various members of the T72 class, but is still significantly different from all the measured T72s in some respects. This is an interesting observation and needs further investigations. Our tests towards designing *class-representative* classifiers by merging image chips from different members of the T72 class have shown very encouraging preliminary results. Further investigation along this line will yield beneficial insights and better performing classifiers.

10 Acknowledgment

We are thankful to Mark Minardi, WL/AACA, for hosting us at the Wright laboratory during the summer of 1997 and providing all the assistance and resources for conducting this study. We are thankful to Ron Dilsavor of Sverdrup Technology and based at Wright Laboratory for providing significant amount of help and assistance during the course of this study.

We express our thanks to the Wright Laboratory, Wright Patterson Air force Base, and Sverdrup Technology, Inc., for making available to us all the data and various pieces of software for making this study possible. We are also thankful to the AFOSR for supporting two authors from the University of Cincinnati during the summer of 1997 for performing this study.

An LPV Controller for a Tailless Fighter Aircraft Simulation

Jonathan M. Protz
Graduate Student
Department of Aeronautics and Astronautics

Massachusetts Institute of Technology
77 Massachusetts Avenue
Cambridge, MA 02139

Final Report for:
Graduate Student Research Program
Wright Laboratory

Sponsored by:
Air Force Office of Scientific Research
Bolling AFB, DC

and

Wright Laboratory August 1997

An LPV Controller for a Tailless Fighter Aircraft Simulation

Jonathan M. Protz
Graduate Student
Department of Aeronautics and Astronautics
Massachusetts Institute of Technology

Abstract

Linear parameter-varying (LPV) controllers were developed for the short-period longitudinal and roll and Dutch-roll lateral-directional dynamics of the McDonnell Douglas Tailless Advanced Fighter Aircraft (TAFA) flight-vehicle simulation. In linearized simulations, the controllers were shown to exhibit Level 1 handling qualities for Mach numbers below 0.7. Controller stability and performance were verified in simple nonlinear simulations.

An LPV Controller for a Tailless Fighter Aircraft Simulation

Jonathan M. Protz

August 22, 1997

1 Introduction

Modern aircraft are expected to maintain stability and deliver desirable handling qualities over a broad range of flight conditions. The dynamics of the aircraft generally depend strongly on the flight condition and, therefore, the control law gains must be scheduled. Traditionally, the scheduling has been done by linearizing the aircraft dynamics at several flight conditions, choosing appropriate gains for each point, and then correlating the gains with flight condition parameters to produce a schedule. Stability and performance are verified through exhaustive simulation.

The approach to gain scheduling described above is both time consuming and difficult to apply to modern multi-variable controller design techniques. An alternate approach is necessary. In recent years, there has been considerable interest in the design of controllers for linear parameter-varying (LPV) dynamics systems. LPV systems can be written as finite-dimensional linear systems with coefficients that depend on one or more time-varying parameters. In the case of aircraft, the nonlinear equations of motion can be linearized and the resulting linearized models parameterized by flight condition. Thus, LPV techniques can be used to produce automatically gain-scheduled multi-variable linear controllers.

This paper considers the application of an LPV synthesis technique to McDonnell Douglas's TAFA simulation, a recently developed high-fidelity model of a tailless aircraft.

2 Linear Parameter-Varying Control

For the purpose of robust control synthesis, LPV dynamic systems can be described by the linear equations:

$$\dot{\mathbf{x}} = \mathbf{A}(\theta)\mathbf{x} + \mathbf{B}_1(\theta)\mathbf{w} + \mathbf{B}_2(\theta)\mathbf{u} \tag{1}$$

$$\mathbf{z} = \mathbf{C}_1(\theta)\mathbf{x} + \mathbf{D}_{12}(\theta)\mathbf{u} \tag{2}$$

$$\mathbf{y} = \mathbf{C}_2(\theta)\mathbf{x} + \mathbf{D}_{21}(\theta)\mathbf{w} \tag{3}$$

where $\mathbf{x}$ is the state of the synthesis plant, $\mathbf{y}$ is the sensed output vector, $\mathbf{z}$ is the auxiliary output vector, $\mathbf{u}$ is the controlled input vector, $\mathbf{w}$ is the disturbance input vector, and θ is a vector of measurable but potentially time-varying parameters.

The goal of the LPV control design problem is to find a control law that depends explicitly on the parameter vector θ and guarantees stability and performance for all allowed values of θ and $\dot{\theta}$. The result is an automatically gain-scheduled linear controller. There are two main approaches to the LPV control design problem. The first approach links the parameters to the plant via a linear fractional transformation (LFT). This results in a fixed state-space controller matrix. The measured parameters enter the controller through a feedback connection. This approach is described in detail in [1] and is applied in [2, 3].

The second approach uses a parameter-dependent quadratic Lyapunov function to guarantee closed-loop stability. A set of Linear Matrix Inequalities (LMIs) is solved to produce a controller that is an explicit function of parameters. A brief summary of the approach is given in Table 1. For a detailed and rigorous explanation, see [4, 5, 6]. For application examples, see [7, 8, 9]. The LMIs must be solved for each θ. Since θ varies over some range of values there are an infinite number of constraining LMIs. To make the problem tractable, the parameter space is gridded and the LMIs are solved only at each grid point. As noted in [5], the gridding approach is an ad-hoc approach that only guarantees stability at the grid points. To verify that the system is stable throughout the envelope, the stability of the closed-loop system is evaluated over a higher-density parameter grid.

3 LPV Plant Models

The LPV synthesis technique requires a parameterized linear model of the plant. The plant used for this paper is the McDonnell Douglas Tailless Advanced Fighter Aircraft (TAFA) model described in [10]. The model is a full six-degree-of-freedom (6-DOF) nonlinear simulation of a tailless fighter aircraft design that includes thrust vectoring and a multitude of aerodynamic surfaces. The aerodynamic data for the model is derived from wind tunnel and propulsion system tests. The nonlinear simulation is implemented in the MATRIXx Xmath package.

The LPV models of the TAFA aircraft were obtained by trimming the simulation for straight-and-level flight at several points around the aircraft's flight envelope. At each point, the aerodynamic derivatives were evaluated and used to construct linearized models. The operating points about which the model was trimmed are presented in Figure 1.

Controllers were developed for the short-period longitudinal dynamics and the roll and Dutch roll lateral-

Table 1: LPV Synthesis Technique

The controller is synthesized by finding two matrices $\mathbf{R}(\theta)$ and $\mathbf{S}(\theta)$ that minimize the controller performance parameter γ subject to the following set of LMIs:

$$\begin{bmatrix} \hat{\mathbf{A}}\mathbf{R} + \mathbf{R}\hat{\mathbf{A}}^T - \sum_i \beta_i \frac{\partial \mathbf{R}}{\partial \theta_i} - \gamma \hat{\mathbf{B}}_2 \hat{\mathbf{B}}_2^T & \mathbf{R}\hat{\mathbf{C}}_1^T & \mathbf{B}_1 \\ \hat{\mathbf{C}}_1 \mathbf{R} & -\gamma \mathbf{I} & 0 \\ \mathbf{B}_1^T & 0 & -\gamma \mathbf{I} \end{bmatrix} < 0 \tag{4}$$

$$\begin{bmatrix} \mathbf{S}\tilde{\mathbf{A}} + \tilde{\mathbf{A}}^T \mathbf{S} + \sum_i \beta_i \frac{\partial \mathbf{S}}{\partial \theta_i} - \gamma \tilde{\mathbf{C}}_2^T \tilde{\mathbf{C}}_2 & \mathbf{S}\tilde{\mathbf{B}}_1 & \mathbf{C}_1^T \\ \tilde{\mathbf{B}}_1^T \mathbf{S} & -\gamma \mathbf{I} & 0 \\ \mathbf{C}_1 & 0 & -\gamma \mathbf{I} \end{bmatrix} < 0 \tag{5}$$

$$\begin{bmatrix} \mathbf{R} & \mathbf{I} \\ \mathbf{I} & \mathbf{S} \end{bmatrix} > 0 \tag{6}$$

If θ is constant, the above LMIs correspond to the H-inf controller design problem. An additional LMI is included to prevent fast controller poles by restricting the poles of the closed loop system to lie to the right of $-\zeta$.

$$\begin{bmatrix} \mathbf{R} & \mathbf{I} \\ \mathbf{I} & \mathbf{S} \end{bmatrix} + \frac{1}{2\zeta}(\Phi + \Phi^T) > 0 \tag{7}$$

The LMIs must be satisfied for all allowed values of θ and β, where θ is the parameter vector and β is a vector of parameter rate limits. The variables used in the LMIs are defined as follows:

$$\hat{\mathbf{A}} = \mathbf{A} - \mathbf{B}_2 \tilde{\mathbf{D}}_{12}^T \mathbf{C}_1 \tag{8}$$

$$\hat{\mathbf{B}}_2 = \mathbf{B}_2 \tilde{\mathbf{D}}_{12}^T \tag{9}$$

$$\hat{\mathbf{C}}_1 = \mathbf{D}_{12\perp}^T \mathbf{C}_1 \tag{10}$$

$$\tilde{\mathbf{A}} = \mathbf{A} - \mathbf{B}_1 \tilde{\mathbf{D}}_{21}^T \mathbf{C}_2 \tag{11}$$

$$\tilde{\mathbf{B}}_1 = \mathbf{B}_1 \mathbf{D}_{21\perp}^T \tag{12}$$

$$\tilde{\mathbf{C}}_1 = \tilde{\mathbf{D}}_{21}^T \mathbf{C}_2 \tag{13}$$

$$\tilde{\mathbf{D}}_{21} = (\mathbf{D}_{21}\mathbf{D}_{21}^T)^{-1}\mathbf{D}_{21} \tag{14}$$

$$\tilde{\mathbf{D}}_{12} = \mathbf{D}_{12}(\mathbf{D}_{12}^T\mathbf{D}_{12})^{-1} \tag{15}$$

$$\Phi = \begin{bmatrix} \hat{\mathbf{A}}\mathbf{R} - \gamma \hat{\mathbf{B}}_2 \hat{\mathbf{B}}_2^T & \hat{\mathbf{B}}_2 \mathbf{C}_1 + \mathbf{B}_1 \tilde{\mathbf{C}}_2 \\ \gamma^{-1}(\hat{\mathbf{C}}^T \hat{\mathbf{C}}_1 \mathbf{R} + \mathbf{S}\tilde{\mathbf{B}}_1 \tilde{\mathbf{B}}_1^T) & \mathbf{S}\tilde{\mathbf{A}} - \gamma \tilde{\mathbf{C}}^T \tilde{\mathbf{C}}_2 \end{bmatrix} \tag{16}$$

The controller is generated from $\mathbf{A}$, $\mathbf{R}$, $\mathbf{S}$, and $\dot{\theta}$. If $\dot{\theta}$ cannot be sensed, then either $\mathbf{R}$ or $\mathbf{S}$ must be chosen to remain constant. The controllers generated for this paper use a constant $\mathbf{S}$ and are given by the following formulas:

$$\begin{aligned} \mathbf{A}_k = & -[\mathbf{A}^T + \mathbf{S}(\mathbf{A} + \mathbf{B}_2\mathbf{F} + \mathbf{L}\mathbf{C}_2)\mathbf{R} \\ & + \gamma^{-1}\mathbf{S}(\mathbf{B}_1 + \mathbf{L}\mathbf{D}_{21})\mathbf{B}_1^T + \gamma^{-1}\mathbf{C}_1^T(\mathbf{C}_1 + \mathbf{D}_{12}\mathbf{F}\mathbf{R})]\mathbf{M}^{-T} \end{aligned} \tag{17}$$

$$\mathbf{B}_k = \mathbf{S}\mathbf{L} \tag{18}$$

$$\mathbf{C}_k = \mathbf{F}\mathbf{R}\mathbf{M}^{-T} \tag{19}$$

$$\mathbf{F} = -\tilde{\mathbf{D}}_{12}^T(\mathbf{C}_1 + \gamma \tilde{\mathbf{D}}_{12}\mathbf{B}_2^T\mathbf{R}^{-1}) \tag{20}$$

$$\mathbf{L} = -(\mathbf{B}_1 + \gamma \mathbf{S}^{-1}\mathbf{C}_2^T\tilde{\mathbf{D}}_{21})\tilde{\mathbf{D}}_{21}^T \tag{21}$$

$$\mathbf{M} = \mathbf{I} - \mathbf{R}\mathbf{S} \tag{22}$$

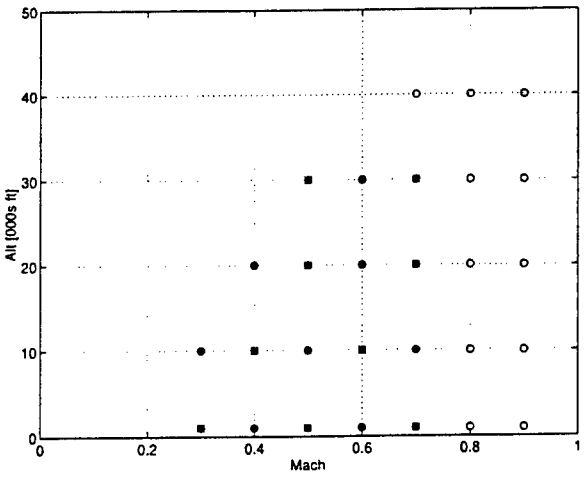

Figure 1: TAFA LPV trim-point grid. Low altitude trim points are at 1000 ft. Legend: 'o' – Point used for $M < 0.9$ design and evaluation, 'x' – Point used for $M < 0.7$ design, '+' – Point used for $M < 0.7$ evaluation

directional dynamics. These dynamics are assumed to be decoupled from each other and from the other aircraft dynamics. The short period longitudinal dynamics are modeled by the equations:

$$\begin{bmatrix} \dot{\alpha} \\ \dot{q} \end{bmatrix} = \begin{bmatrix} Z_\alpha & Z_q \\ M_\alpha & M_q \end{bmatrix} \begin{bmatrix} \alpha \\ q \end{bmatrix} + \begin{bmatrix} 0 \\ u_q \end{bmatrix} \tag{23}$$

The roll and Dutch roll lateral-directional dynamics are modeled by the equations: [1]

$$\begin{bmatrix} \dot{\beta} \\ \dot{p} \\ \dot{r} \end{bmatrix} = \begin{bmatrix} Y_\beta & Y_p & Y_r \\ L_\beta & L_p & L_r \\ N_\beta & N_p & N_r \end{bmatrix} \begin{bmatrix} \beta \\ p \\ r \end{bmatrix} + \begin{bmatrix} 0 \\ u_p \\ u_r \end{bmatrix} \tag{24}$$

The models are written using generalized control moments for pitch (u_q), roll (u_p), and yaw (u_r). Later, these generalized moments are replaced by actual actuator deflections for the nonlinear simulations.

Each aerodynamic derivative in these linear models changes with the trim flight condition. Figures 2 and 3 show the aerodynamic derivatives versus trim dynamic pressure. The figures also show two fits formed using ordinary least-squares regression. In the first case, the data was fit as a linear function of dynamic pressure:

$$\mathbf{A}(\bar{q}) = \mathbf{A}_0 + \mathbf{A}_1 \bar{q} \tag{25}$$

[1] The notation used for equations (23) and (24) is that of [11]. To convert to this notation from the notation typically seen in aerodynamic texts, the following formulas were used: $Z_\alpha = z_\alpha/U$, $Z_q = 1 + z_q/U$, $Y_\beta = y_\beta/U$, $Y_p = \sin(\alpha) + y_p/U$, $Y_r = \cos(\alpha) + y_r/U$.

In the second case, it was fit to the following function of Mach (M) and Altitude (h):

$$\mathbf{A}(M,h) = \mathbf{A}_0 + \mathbf{A}_1 M + \mathbf{A}_2 h + \mathbf{A}_3 M^2 + \mathbf{A}_4 h^2 + \mathbf{A}_5 Mh \tag{26}$$

For some of the elements of the $\mathbf{A}$ matrix (e.g. Z_q), this parameterization is overly complicated. The complication could be reduced by using an element-by-element parameterization instead of a matrix coefficient parameterization. The simplification is useful for the LFT approach to LPV synthesis. However, it is not necessary for the LPV synthesis technique used here.

The data points for some of the aerodynamic derivatives are very scattered. This leads to poor fits, particularly for the dynamic pressure parameterization. Controller robustness is used to address the uncertainty introduced by the poor fits. Also, notice that some of the parameters are very small and, therefore, are unimportant regardless of the accuracy of the fits.

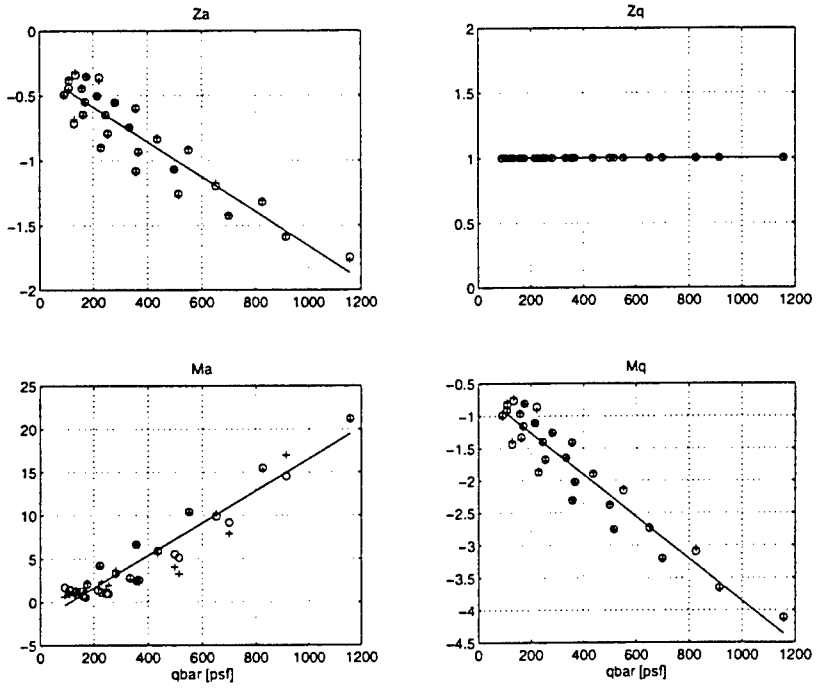

Figure 2: Coefficients for Short-Period Longitudinal Dynamics

4 Longitudinal Controller Synthesis

A gain-scheduled controller for the short-period longitudinal dynamics was designed using the LPV synthesis technique describe above. The controller was designed to deliver Level 1 flying qualities over the broadest

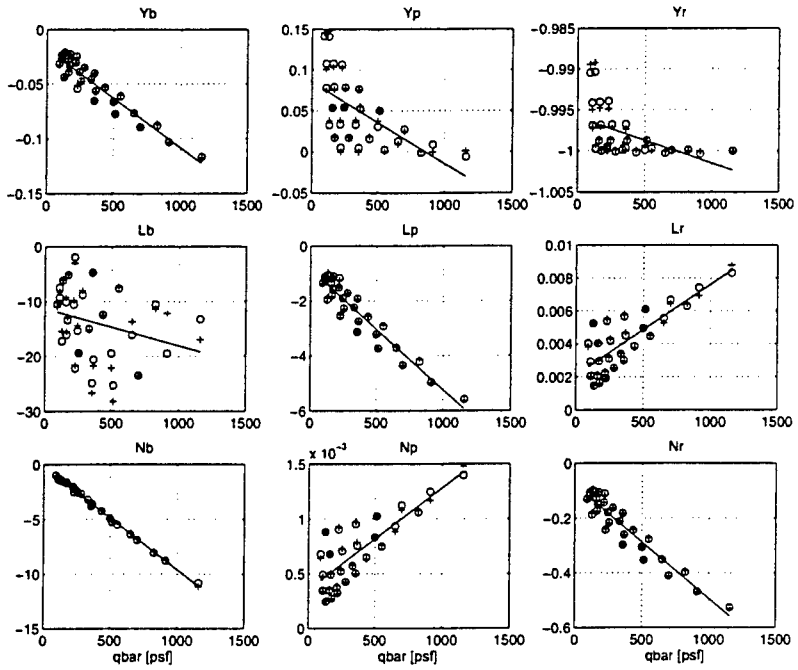

Figure 3: Coefficients for Roll and Dutch Roll Dynamics

possible range of flight conditions while maintaining stability over the entire subsonic envelope. The synthesis procedure involved three steps: (1) problem setup, (2) exploratory design studies, (3) selection and evaluation of the final design.

4.1 Problem Setup

The longitudinal controller synthesis plant is set up using a conventional H-inf framework. Only the vehicle dynamics are parameter varying. Input multiplicative uncertainty is included to account for modeling errors. The input uncertainty weighting is:

$$W_{unc}(s) = \frac{10s + 1}{5s + 10} \tag{27}$$

The control input u_q is weighted with a scaling,

$$W_{act} = \frac{1}{50} \tag{28}$$

A weighting for measurement noise, W_{noise} is included for numerical reasons only. The q and α sensors have weights 0.01 and 0.1 respectively. The closed-loop dynamics are implicitly matched to a fixed reference

model. The model-matching error is weighted by the function:

$$W_{perf}(s) = \frac{4}{s + 0.2} \tag{29}$$

The reference model relates forward-aft stick motion to pitch rate. It is a second order transfer function with relative degree one:

$$\frac{q}{\delta_{pitch}} = \frac{\frac{2}{3}(s + 6)}{s^2 + 2s + 4} \tag{30}$$

This reference model was the result of several design iterations. The zero was positioned to minimize the initial delay. The natural frequency of 2.0 rps was chosen as fast as possible within the constraints imposed by the plant dynamics. A damping of 0.5 was chosen to give desirable settling properties.

4.2 Exploratory Studies

A detailed study of the longitudinal dynamics was executed to determine the best model parameterization. This study was exploratory, and closed-loop flying qualities were not considered. The performance of the closed loop system was first studied for Mach numbers below 0.7. The study was then repeated up to Mach 0.9.

The LPV synthesis technique used here allows separate parameterizations of the plant and the synthesis matrices, $\mathbf{R}(\theta)$ and $\mathbf{S}(\theta)$. The controllers were generated using several different parameterizations. These parameterizations and their achieved values of γ are presented in Table 2. Most designs used a fixed $\mathbf{S}$ matrix and a parameter dependent $\mathbf{R}$ matrix. Designs #8 and #9 did use parameter-varying $\mathbf{S}$ matrices, but no performance benefits were observed. This agrees with the results of [7] where LPV synthesis was applied to a different tailless aircraft model.

The low-mach controllers were all generated on the same coarse grid. They were then tested on a finer grid. The grids are illustrated in Figure 1. The grid tests are important because they are the only way to verify stability and to compare the performance of controllers generated with different plant parameterizations.

The LPV synthesis was considerably more difficult for the high Mach cases than it was for the low Mach cases. Attempts were made to synthesize the controllers using the coarse grids presented in Figure 4. However, both of these grids led to controllers that were unstable for certain points on the dense grid. As a last resort, the entire dense grid was used in the synthesis step. This led to very long computation times. It also precluded testing the controller on a higher-density grid. In the interest of time, only the most promising parameterizations from the low-speed study were used in the high-speed study.

Table 2: Longitudinal Designs

Design Number	Run Number	Sol'n Time (min)	Maximum Mach	Plant Basis	R Basis	S Basis	γ
1	63	3.6	0.70	$1, \bar{q}$	$1, \bar{q}$	1	1.217
2	64	2.1	0.70	(M,h)	1	1	1.736
3	67	4.2	0.70	(M,h)	$1, \bar{q}$	1	1.024
4	65	7.6	0.70	(M,h)	$1, \bar{q}, \bar{q}^2$	1	0.983
5	47	11.1	0.70	(M,h)	$1, \bar{q}, \bar{q}^2, \bar{q}^3$	1	0.983
6	49	4.5	0.70	(M,h)	$1, \frac{1}{\bar{q}}$	1	1.074
7	46	6.5	0.70	(M,h)	$1, \frac{1}{\bar{q}}, \bar{q}$	1	0.981
8	66	7.1	0.70	(M,h)	$1, \bar{q}$	$1, \bar{q}$	1.024
9	48	7.0	0.70	(M,h)	$1, \bar{q}$	$1, \frac{1}{\bar{q}}$	1.025
10	62	50	0.70	(M,h)	(M,h)	1	0.991
11	68	24	0.90	(M,h)	$\bar{q}$	1	2.426
12	69	3h42m	0.90	(M,h)	(M,h)	1	1.549

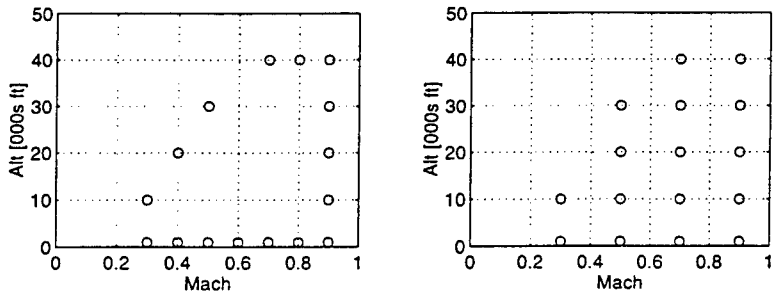

Figure 4: Coarse grids for $M < 0.9$ design. These grids were unsuccessful.

4.3 Selection of Final Design and Performance Evaluation

Two of the designs from Table 2 were chosen as final designs for implementation in the nonlinear sim. Design #3 was chosen at the final low-speed design. Designs #7, #4, and #5 gave slightly better results in term of γ and in terms of performance when applied to the LPV model. However, when the step response was evaluated using the linearized model, design #3 had slightly better performance. Design #12 was chosen as the final high-speed design based on its low value of γ. The closed-loop step responses for these designs were computed using the LPV plant models used for synthesis and using the actual linearized plant models for each grid point. The step responses of designs #3, #12, and, for comparison, #7 are shown in Figure 6.

The flying qualities were determined directly from the step response as in [2, 8]. The step response approach is used here because it is easy to automate and because it can be applied directly to the output of linear and nonlinear simulations. Figure 5 and Table 3 give the step-response requirements for Level 1 and Level 2 aircraft. The specifications are taken from reference [2] and correspond to MIL-STD-1797A, 1990.

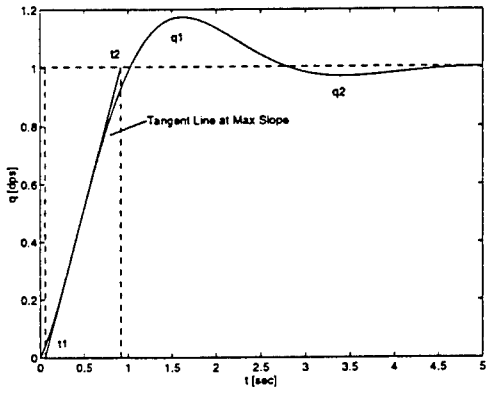

Figure 5: Handling Qualities Parameters. Note $\Delta q_1 = q_1 - q_{ss}$, $\Delta q_2 = q_{ss} - q_2$, and $\Delta t = t_2 - t_1$.

Table 3: Handling Qualities Requirements

Parameter	Level 1	Level 2
Max t_1	0.12	0.17
Max $\Delta q_2/\Delta q_1$	0.30	0.60
Max Δt	$500/V_t$	$1600/V_t$

The achieved performance levels for the low-speed and high-speed pitch controller designs are summarized in Tables 4.3 and 4.3 respectively. As the tables show, both controllers give Level 1 performance for Mach numbers below 0.7. The rise time Δt and the settling measure $\frac{\Delta q_2}{\Delta q_1}$ are both well within Level 1 requirements.

The delay measure, t_1 is marginally Level 1. The low-speed controller is unstable for Mach numbers above 0.7. At these high Mach numbers, the high-speed controller meets Level 1 requirements for altitudes above 10,000 ft and Level 2 requirements below. The low altitude, high Mach trim points correspond to the largest dynamic pressures.

Because this reference model is fixed, it delivers the same rise time regardless of the aircraft's true speed. As Table 3 shows, the performance specifications require faster responses for higher speeds. This issue could be addressed by using a parameter-varying reference model. It could also be addressed by including an appropriate precompensator. The closed loop system would be chosen as above to give the fastest possible step response. The precompensator would then modify the pilot command as necessary to give the desired slower response at low speeds.

Table 4: Low Speed Longitudinal Controller Flying Qualities

Alt. (000 ft)	Mach	$\Delta q_2/\Delta q_1$	t_1 (sec)	Δt (sec)	Level 1 Δt (sec)	Level 2 Δt (sec)
1	0.3	0.23	0.11	0.80	3.89	12.44
1	0.4	0.11	0.12	0.81	2.19	7.00
1	0.5	0.13	0.13	0.81	1.40	4.48
1	0.6	0.30	0.13	0.83	0.97	3.11
10	0.3	0.25	0.10	0.77	5.45	17.45
10	0.4	0.15	0.12	0.79	3.07	9.82
10	0.5	0.15	0.13	0.79	1.96	6.28
10	0.6	0.18	0.13	0.79	1.36	4.36
20	0.4	0.20	0.11	0.77	4.59	14.69
20	0.5	0.19	0.12	0.77	2.94	9.40
20	0.6	0.19	0.13	0.76	2.04	6.53
30	0.5	0.22	0.11	0.75	4.55	14.55
30	0.6	0.22	0.12	0.75	3.16	10.10

5 Lateral-Directional Controller Synthesis

The lateral-directional controller was designed with the same steps used for the longitudinal design. The synthesis plant block diagram has two components that vary. As in the longitudinal synthesis model, the vehicle dynamics are parameter varying. In addition, since the controller is designed for roll about the stability axis rather than the body axis, the command variable $\dot{\mu}$ is a parameter varying mixture of roll rate and yaw rate that depends on the trim angle of attack:

$$\dot{\mu} = p\cos(\alpha) + r\sin(\alpha) \tag{31}$$

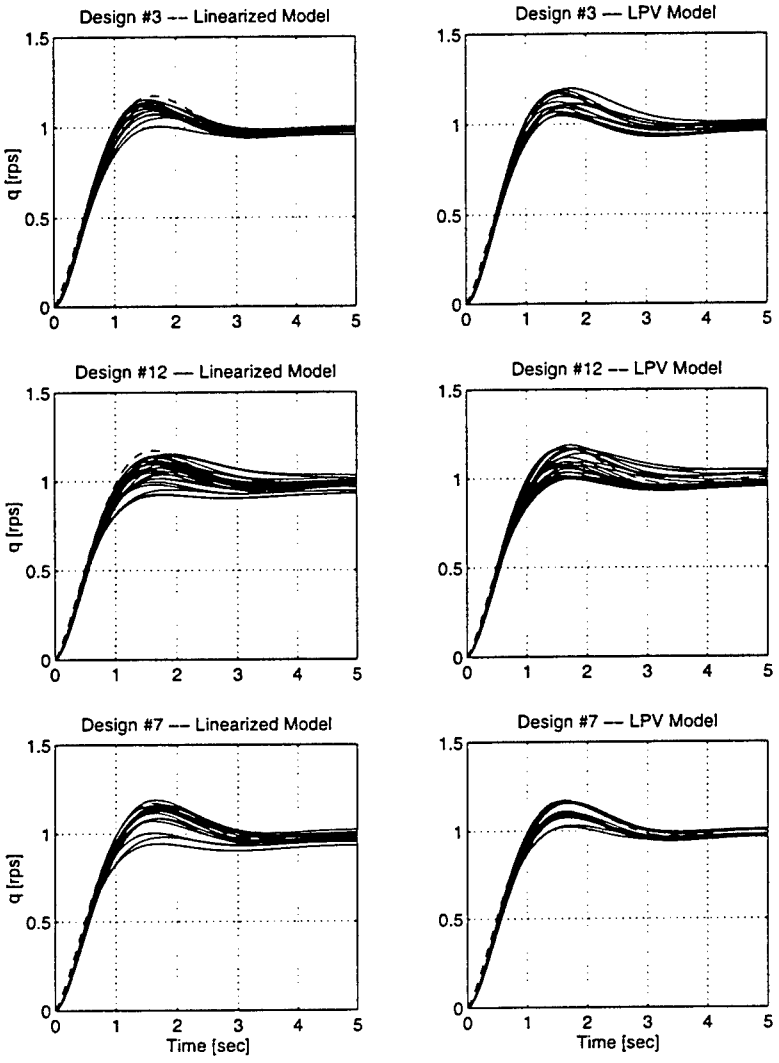

Figure 6: Linear step response of closed-loop longitudinal system. Solid lines indicate simulation results. Dashed lines are the reference model.

Table 5: High Speed Longitudinal Controller Flying Qualities

Alt. (000 ft)	Mach	$\Delta q_2/\Delta q_1$	t_1 (sec)	Δt (sec)	Level 1 Δt (sec)	Level 2 Δt (sec)
1	0.3	0.25	0.11	0.77	3.89	12.44
1	0.4	0.06	0.09	0.81	2.19	7.00
1	0.5	0.23	0.08	0.82	1.40	4.48
1	0.6	-	0.09	0.83	0.97	3.11
1	0.7	-	0.09	0.85	0.71	2.29
1	0.8	0.00	0.07	0.88	0.55	1.75
1	0.9	0.03	0.08	0.89	0.43	1.38
10	0.3	0.22	0.10	0.77	5.45	17.45
10	0.4	0.10	0.10	0.79	3.07	9.82
10	0.5	0.14	0.09	0.80	1.96	6.28
10	0.6	0.66	0.08	0.81	1.36	4.36
10	0.7	-	0.08	0.82	1.00	3.21
10	0.8	0.05	0.07	0.88	0.77	2.45
10	0.9	0.00	0.08	0.93	0.61	1.94
20	0.4	0.14	0.10	0.82	4.59	14.69
20	0.5	0.13	0.10	0.82	2.94	9.40
20	0.6	0.24	0.09	0.81	2.04	6.53
20	0.7	0.46	0.08	0.82	1.50	4.80
20	0.8	0.23	0.08	0.86	1.15	3.67
20	0.9	0.00	0.09	0.92	0.91	2.90
30	0.5	0.17	0.12	0.85	4.55	14.55
30	0.6	0.19	0.11	0.84	3.16	10.10
30	0.7	0.22	0.10	0.83	2.32	7.42
30	0.8	0.13	0.10	0.86	1.78	5.68
30	0.9	0.00	0.10	0.91	1.40	4.49
40	0.7	0.22	0.12	0.85	3.72	11.91
40	0.8	0.18	0.12	0.86	2.85	9.12
40	0.9	0.06	0.11	0.89	2.25	7.20

The remaining blocks in the synthesis plant are time-invariant. They are given as follows:

$$W_{unc}(s) = \frac{10s+1}{5s+10} \tag{32}$$

$$W_{act} = \frac{1}{50} \tag{33}$$

Again, measurement noise, W_{noise}, is included for numerical reasons only. The β, p and r sensors have weights 0.1, 0.01, and 0.01 respectively.

The closed-loop dynamics are implicitly matched to two fixed reference models. The roll transfer function relates side-to-side stick deflections to stability axis roll rate. The directional transfer function relates pedal deflection to sideslip angle. Initial exploratory studies showed a strong coupling between directional command and roll motion in the closed loop system. To suppress this coupling, the $\dot{\mu}$ performance is weighted more heavily than the β performance.

$$W_{perf_{\dot{\mu}}}(s) = \frac{12}{s+0.2} \tag{34}$$

$$W_{perf_{\beta}}(s) = \frac{4}{s+0.2} \tag{35}$$

The reference models for sideslip and roll are first order and second order systems respectively. They are given by the following transfer functions:

$$\frac{\dot{\mu}}{\delta_{roll}} = \frac{1.25}{s+1.25} \tag{36}$$

$$\frac{\beta}{\delta_{roll}} = \frac{2.25}{s^2+2.1s+2.25} \tag{37}$$

These reference models were taken from [7] and correspond to Level 1 flying qualities over the full flight envelope.

The results from the longitudinal study helped direct the design of the lateral controller. As a result fewer parameterizations were considered for the lateral controller designs. As in the longitudinal study, the performance of the closed loop system was first studied for Mach numbers below 0.7. The different parameterizations and their achieved values of γ are presented in Table 5.

Design #14 was chosen as the final lateral-directional design. Figure 7 shows the step responses for this controller. The closed loop system closely matches the reference model for $\dot{\mu}$ and therefore has Level 1 roll handling qualities. The directional control performance of the closed loop system does not match the reference model as well. A Low-Order Equivalent System (LOES) fit or similar analysis of the closed loop system would be necessary to verify Level 1 directional handling qualities.

Table 6: Lateral-Directional Designs

Design Number	Run Number	Sol'n Time (min)	Maximum Mach	Plant Basis	R Basis	S Basis	γ
13	105	13	0.70	(M,h)	$1, \bar{q}$	1	3.18
14	104	26	0.70	(M,h)	$1, \bar{q}, \bar{q}^2$	1	2.62
15	103	38	0.70	(M,h)	$1, \bar{q}, \bar{q}^2, \bar{q}^3$	1	2.57
16	102	1h6m	0.70	(M,h)	$1, \bar{q}$	$1, \bar{q}$	3.17
17	106	36	0.70	(M,h)	1	1	4.56
18	100	5h12m	0.70	(M,h)	(M,h)	1	2.12
19	101	1h50m	0.90	(M,h)	$1, \bar{q}$	1	5.33

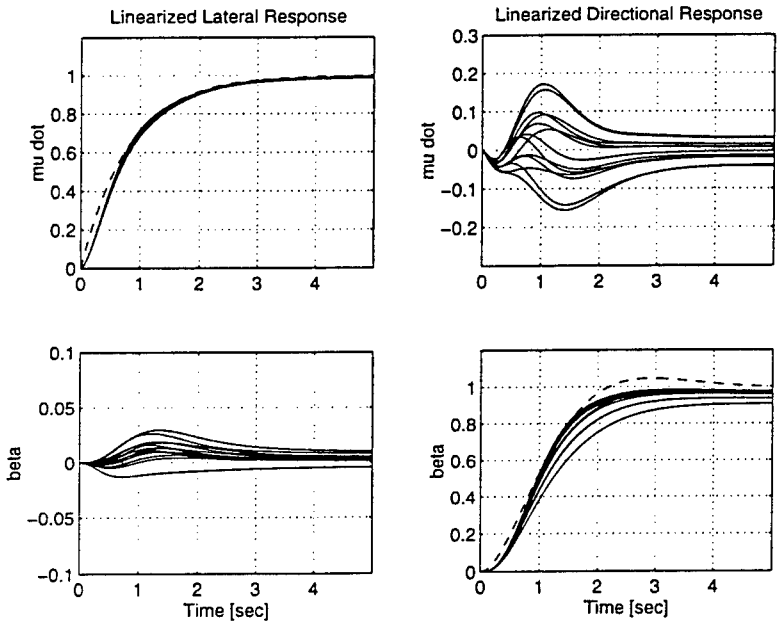

Figure 7: Linear step response of closed-loop lateral-directional system. Solid lines indicate simulation results. Dashed lines are the reference model.

6 Nonlinear Simulations

The finalized longitudinal and lateral-directional controller designs were implemented in the nonlinear MATRIXx TAFA simulation. The simulation was trimmed for straight and level flight at a specific Mach number and altitude. The controller matrices for this trim point were computed off-line and then implemented in the simulation as an LTI state space system. The controller is, therefore, not dynamically parameter varying and large-amplitude maneuvers could not be simulated.

A simple actuator allocation scheme based on engineering judgment was used to convert the generalized commands into surface deflections. Trailing-edge flaps were used as the sole pitch actuator. Trailing-edge flaps, ailerons, and canards were used for roll and yaw control. They were assigned using a weighted pseudo-inverse with a diagonal weighting of $[1.0, 0.2, 0.2]$. See [11] for an explanation of actuator allocation using the pseudo-inverse. The controllers only command the moments generated by the surfaces. The direct force effects of the actuator surfaces were assumed negligible and were ignored in the assignment calculation. The control effectiveness matrix is approximated by the following function of Mach and altitude:

$$\mathbf{B}(M,h) = \mathbf{B}_0 + \mathbf{B}_1 M + \mathbf{B}_2 h + \mathbf{B}_3 M^2 + \mathbf{B}_4 h^2 + \mathbf{B}_5 Mh \tag{38}$$

Further investigation shows that a linear fit to dynamic pressure would also produce suitable results.

Longitudinal step responses from the nonlinear simulation were evaluated at four trim points in the operating envelope. Three of the responses were taken at the corners of the low-speed envelope. The fourth point was taken from the middle of the low-speed envelope. Qualitatively, the simulation gave adequate performance at each point. The trim conditions are presented in Table 7. As an example, Figure 8 illustrates the step responses for each control variable at an altitude of 20,000 ft and a Mach number of 0.5.

Table 7: Nonlinear Sims

NL Sim #	Mach	Alt (000 ft)
1	0.3	1
2	0.7	1
3	0.7	30
4	0.5	20

7 Conclusion and Suggestions for Future Research

The LPV controller presented here represents a promising start for a full-envelope Level 1 flight controller for the TAFA simulation. A complete longitudinal-lateral-directional controller was designed to deliver Level

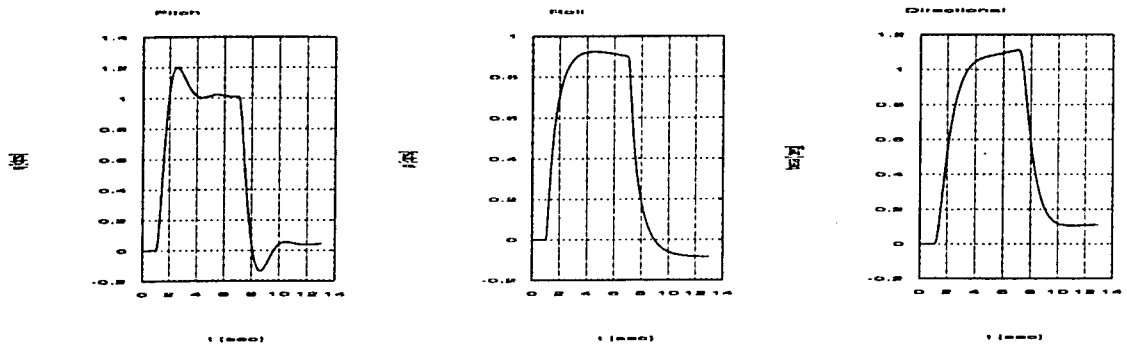

Figure 8: Nonlinear step responses of closed-loop system for pitch, roll, and sideslip at $M = 0.5$, h =20,000 ft.

1 performance for Mach numbers below 0.7. A second longitudinal controller was designed to include the transonic portion of the envelope. The former was tested in a nonlinear simulation using a simple control allocation scheme.

Future research research should focus on generating a complete LPV design for the entire envelope. A complete design should consider the following additional topics:

1. A dynamic implementation of the LPV controller in the nonlinear simulation. This would allow evaluation of large-amplitude maneuvers

2. A parameter-dependent reference model for the longitudinal controller to achieve Level 1 performance for high $\bar{q}$.

3. A detailed flying qualities evaluation of the closed-loop nonlinear simulation to verify Level 1 performance.

4. An extended, full envelope design grid that includes more points near $M = 1$ as well as new points for supersonic and high-α flight.

5. Implementation of a sophisticated control allocation scheme (e.g., the default control allocation scheme provided with the TAFA simulation).

References

[1] P. Apkarian and P. Gahinet, "A convex characterization of gain-scheduled h-inf controllers," *IEEE Transactions on Automatic Control*, vol. 40, pp. 853–864, 1995.

[2] M. Spillman, P. Blue, S. Banda, and L. Lee, "A robust gain-scheduling example using linear parameter varying feedback," *AIAA Guidance, Navigation, and Control Conference*, 1997.

[3] P. A. Blue and S. S. Banda, "D-k iteration with optimal scales for systems with time-varying and time-invariant uncertainties," *ACC*, 1997.

[4] G. Becker and A. Packard, "Robust performance of linear parameterically varying systems using parametrically-dependent linear feedback," *Systems and Control Letters*, vol. 23, pp. 205–215, 1994.

[5] G. Becker, "Additional results on parameter-dependent controllers for lpv systems," *Proceedings of the 13th IFAC World Congress*, pp. 205–215, 1996.

[6] M. Chilali and P. Gahinet, "H-inf design with pole placement constraints: An lmi approach," *IEEE Transactions on Automatic Control*, vol. 40, pp. 358–367, 1996.

[7] A. G. Sparks, "Linear parameter varying control for tailless aircraft," *AIAA Guidance, Navigation, and Control Conference*, 1997.

[8] L. Lee and M. Spillman, "Reduced-order, parameter-varying flight control: Longitudinal and lateral-directional design examples," *AIAA Guidance, Navigation, and Control Conference*, 1996.

[9] P. Apkarian, P. Gahinet, and G. Becker, "Self-scheduled h-inf control of linear parameter-varying systems: A design example," *Automatica*, vol. 31, pp. 1251–1261, 1995.

[10] J. S. Brinker, K. A. Wise, M. Elgersma, A. Calise, and P. Voulgaris, "Restore final report vol ii: Software users manual and programmers manual." Personal communication, 1997.

[11] R. J. Adams, J. M. Buffington, A. G. Sparks, and S. S. Banda, *Robust Multivariable Flight Control*. London: Springer-Verlag, 1994.

Associate did not participate in the program.

ISO-OCTANE AND N-HEPTANE LAMINAR FLAME NUMERICAL STUDY

Thomas Scott
Ph.D Candidate
Department of Mechanical and Aerospace Engineering
and Engineering Mechanics

University of Missouri — Rolla
229 Mechanical Engineering
Rolla, MO 65401

Final Report for:
Graduate Student Research Program
Wright Laboratory

Sponsored by:
Air Force Office of Scientific Research
Bolling Air Force Base, DC

and

Wright Laboratory

August 15, 1997

ISO-OCTANE AND N-HEPTANE LAMINAR FLAME NUMERICAL STUDY

Thomas Scott
Ph.D. Candidate
Department of Mechanical and Aerospace Engineering
and Engineering Mechanics
University of Missouri — Rolla

Abstract

Detailed reaction mechanisms for n-heptane and iso-octane are compared to new experimental data. Disagreement between the extensively investigated and verified n-heptane mechanism and the experimental data are explained by suspected mass balance discrepancies in the experimental data. This hindered evaluation of the proposed iso-octane mechanism. The trends exhibited by the proposed mechanism are not inconsistent with expectations. Primary consumption paths for the proposed iso-octane sub-mechanism are identified and an ad-hoc sensitivity analysis of the iso-octane sub-mechanism is performed.

ISO-OCTANE AND N-HEPTANE LAMINAR FLAME NUMERICAL STUDY

Thomas Scott

Introduction

Detailed combustion kinetic mechanisms for practical fuels continue to be of significant interest given increased awareness of environmental concerns. Recently, Ranzi et al. [1] published a semi-detailed kinetic scheme for iso-octane oxidation featuring comparisons to experimental data comprising intermediate components, heat release, and ignition delay. The experimental data is generally obtained in spatially homogeneous reactors, i.e. a shock tube, a rapid compression machine, a flow stirred reactor and a jet stirred reactor. In an attempt to further the knowledge base of detailed combustion kinetic mechanisms a previously investigated n-heptane mechanism is augmented to consider iso-octane oxidation, and evaluated using the new experimental laminar pre-mixed flame data sets of Bakali [2] and Doute [3]. The present mechanism is previously shown to reproduce species profiles in counterflow diffusion flames and stirred reactors, and laminar burning velocities for n-heptane by Lindstedt and Maurice [4]. The initial goal of the present effort is to evaluate the n-heptane experimental data

and the proposed iso-octane sub-mechanism. Subsequently, the iso-octane experimental data is to be used to refine the proposed iso-octane oxidation sub-mechanism. The disagreement between the experimental data and computational results for n-heptane precluded a thorough investigation of the iso-octane sub-mechanism. Upon further analysis, it is found that the mass balances of the experimental data show large deviations, thus making the data sets suspect, and arguably of limited use.

Methodology

Species profiles are computed using the computer program LAPREM [5], which utilizes a representative temperature profile to solve the species transport equations using an implicit algorithm. The n-heptane mechanism and associated thermo-chemical and physical data can be found in the thesis of Maurice [6], and the iso-octane sub-mechanism, comprising 27 reactions and 7 species, can be found in Table 1. The complete mechanism comprises 808 reactions and 132 species. The computational temperature profile is provided in the form:

$$y = \left(\frac{a_0 + a_1 x + a_2 x^2 + a_3 x^3 + a_4 x^4}{1 + a_5 x + a_6 x^2 + a_7 x^3 + a_8 x^4} \right)$$

No.	reaction			A $m^3 \frac{mole}{sec}$	b	E J/mole	Ref.
772	C8H18	⇔	1C7H15 + CH3	304E+13	0	234.0E+06	adj. [7]
773	C8H18	⇔	1C5H11 + C3H7(I)	608E+13	0	234.0E+06	"
774	C8H18	⇔	PC4H9 + C4H9(S)	608E+13	0	234.0E+06	"
775	C8H18 + H	⇔	1C8H17 + H2	506E+05	2	322.0E+05	est. †
776	C8H18 + H	⇔	2C8H17 + H2	1640E+04	2	209.2E+05	"
777	C8H18 + H	⇔	3C8H17 + H2	1640E+04	2	209.2E+05	"
778	C8H18 + H	⇔	4C8H17 + H2	810E+04	2	209.2E+05	"
779	C8H18 + OH	⇔	1C8H17 + H2O	178E+05	1.8	598.6E+03	"
780	C8H18 + OH	⇔	2C8H17 + H2O	170E+04	1.9	-606.9E+04	"
781	C8H18 + OH	⇔	3C8H17 + H2O	170E+04	1.9	-606.9E+04	"
782	C8H18 + OH	⇔	4C8H17 + H2O	170E+04	1.9	-606.9E+04	"
783	C8H18 + O	⇔	1C8H17 + OH	251E+04	2.4	230.3E+05	"
784	C8H18 + O	⇔	2C8H17 + OH	690E+03	2.6	740.0E+04	"
785	C8H18 + O	⇔	3C8H17 + OH	690E+03	2.6	740.0E+04	"
786	C8H18 + O	⇔	4C8H17 + OH	690E+03	2.6	740.0E+04	"
787	C8H18 + CH3	⇔	1C8H17 + CH4	270E+10	0	485.3E+05	"
788	C8H18 + CH3	⇔	2C8H17 + CH4	144E+10	0	397.5E+05	"
789	C8H18 + CH3	⇔	3C8H17 + CH4	144E+10	0	397.5E+05	"
790	C8H18 + CH3	⇔	4C8H17 + CH4	144E+10	0	397.5E+05	"
791	C8H18 + O2	⇔	1C8H17 + HO2	226E+11	0	219.0E+06	"
792	C8H18 + O2	⇔	2C8H17 + HO2	360E+11	0	204.4E+06	"
793	C8H18 + O2	⇔	3C8H17 + HO2	360E+11	0	204.4E+06	"
794	C8H18 + O2	⇔	4C8H17 + HO2	360E+11	0	204.4E+06	"
795	1C8H17	⇔	1C7H14 + CH3	200E+14	0	970.0E+05	"
796	2C8H17	⇔	1C5H10 + C3H7(I)	200E+14	0	105.0E+06	"
797	3C8H17	⇔	1C4H8 + C4H9(S)	200E+14	0	970.0E+05	"
798	4C8H17	⇔	1C5H11 + C3H6	200E+14	0	900.0E+05	"

Table 1: Iso-octane sub-mechanism.

† Reaction rates are based on analogy to n-heptane reactions [4, 6] with adjustments for molecular size and available reaction sites.

Successful convergence of the code is highly dependent on the polynomial expression being a continuous function at all grid points. This is best achieved by ensuring the polynomial is well behaved over a domain larger than the numerical domain of the code. Temperature profile height is based on the maximum experimental temperature. The flame width coincides with experimental observation. Profiles are smoothed and extrapolated to cover the computational domain in a continuous and physically consistent manner.

To analyze the experimental data the variation of the balances of C, H_2, and O_2 in the reaction zone is examined. Since the experimental data is reported in mole fractions, the following formula is used to compute the total species mole fractions. For H_2 and O_2 the result is divided by two.

$$X_{atoms} = \sum (mole\ fraction) * (number\ of\ atoms\ in\ molecule)$$

The same strategy is applied to the numerical data. It is noted that the base number of moles changes as a result of the combustion process, thus the overall mole fraction is not constant.

Results

Experimental data for comparison with numerical results is obtained from the work of Bakali [2] and Doute [3]. Preliminary investigations show disagreement between computations and the experimental data of Bakali [2] greater than previously observed for similar flames [6]. Therefore, a comparison of the total species mole fraction, computed as outlined above for both the numerical code and the experimental data, is conducted to ensure mass conservation. Figures 1 to 3 show the mole profiles computed for n-heptane at ϕ values of 0.7, 1.5, and 1.7. Scrutiny of the experimental profiles for n-heptane and iso-octane (Figures 4 to 12) indicates that the mole balances obtained from the experimental data do not reflect conservation of mass. The computer code rigidly enforces conservation of mass while the experimental measurements arguably incur errors caused by experimental uncertainties. The prelimary conclusion is that the observed disagreement lies with the experimental data. The data sets for iso-octane are equally problematic. For n-heptane at ϕ=1.0 (Figure 9) the O_2 profile is very stable, while the C and H_2 profiles regrettably continue to exhibit mass fluctuations.

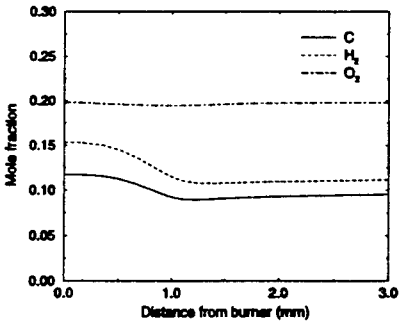

Figure 1: Heptane ϕ=0.7 computational mole balance.

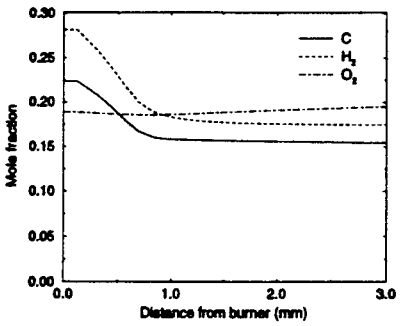

Figure 2: Heptane ϕ=1.5 computational mole balance.

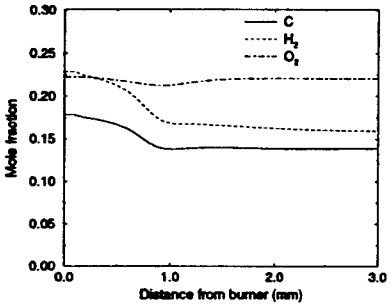

Figure 3: Heptane ϕ=1.7 computational mole balance.

Comparisons between computational and experimental major species profiles for the n-heptane flames are shown in Figures 13 to 42. The maximum reported experimental error for the temperature measurements is $\pm$

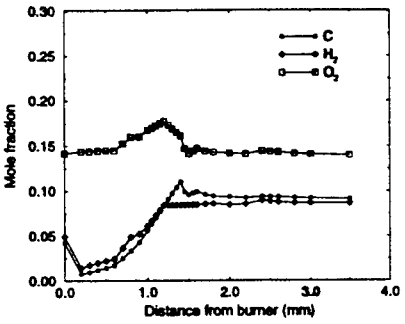

Figure 4: Iso-octane ϕ=1.0 experimental mole balance.

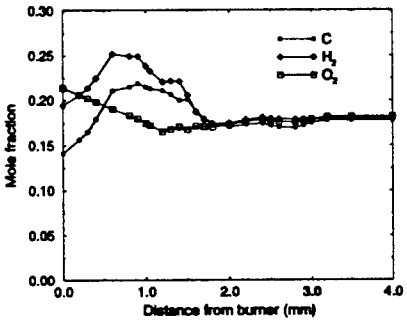

Figure 5: Iso-octane ϕ=1.5 experimental mole balance.

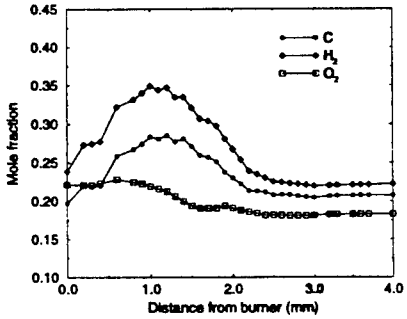

Figure 6: Iso-octane ϕ=1.7 experimental mole balance.

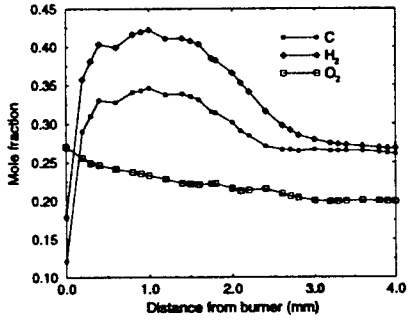

Figure 7: Iso-octane ϕ=1.9 experimental mole balance.

100 K, thus the computational temperature profile is varied across this range to assess the effects of the experimental uncertainties on the predicted species profiles for ϕ=1.0 (Figures 19 to 24).

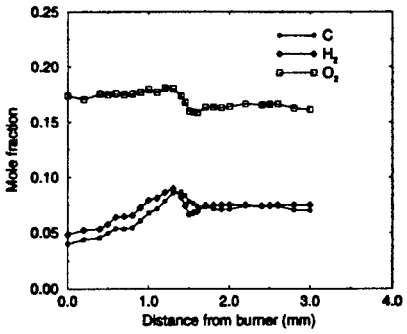

Figure 8: Heptane ϕ=0.7 experimental mole balance.

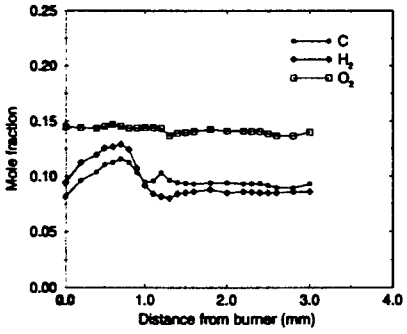

Figure 9: Heptane ϕ=1.0 experimental mole balance.

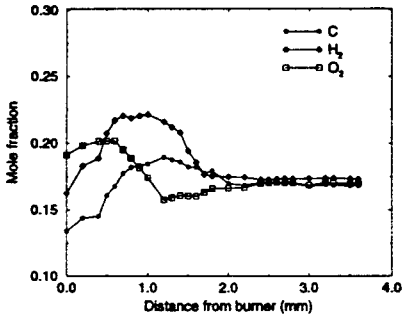

Figure 10: Heptane ϕ=1.5 experimental mole balance.

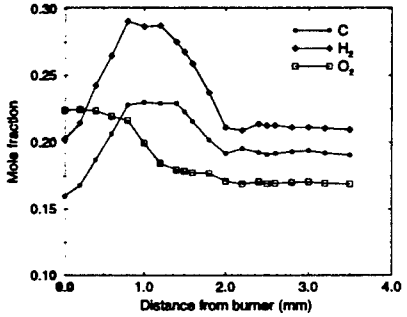

Figure 11: Heptane ϕ=1.7 experimental mole balance.

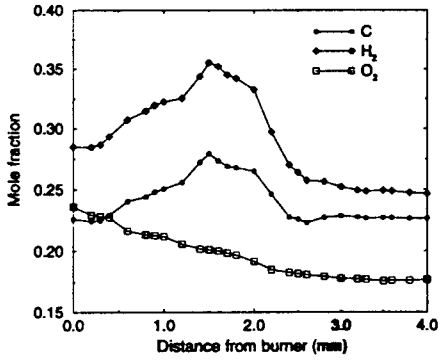

Figure 12: Heptane ϕ=1.9 experimental mole balance.

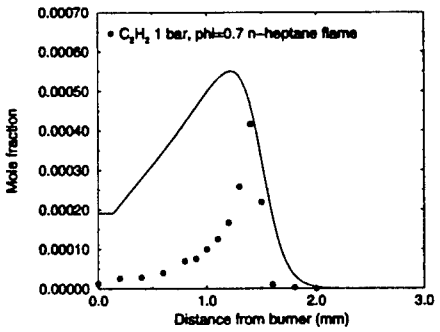

Figure 13: C_2H_2 profile.

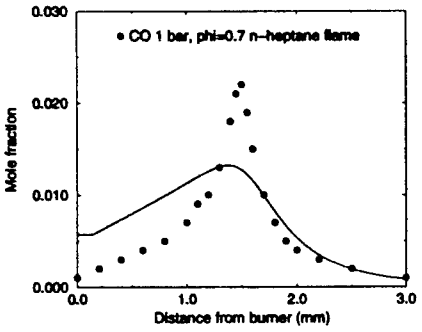

Figure 14: CO profile.

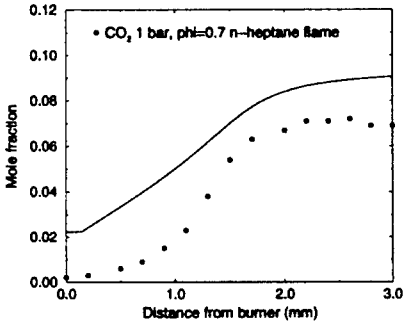

Figure 15: CO_2 profile.

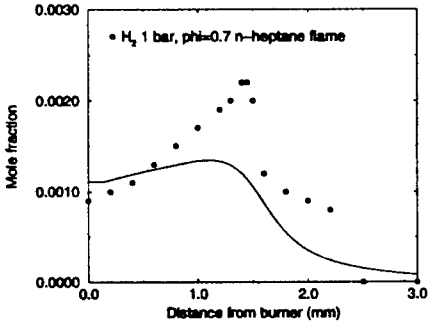

Figure 16: H_2 profile.

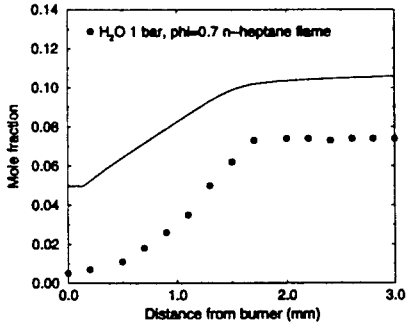

Figure 17: H_2O profile.

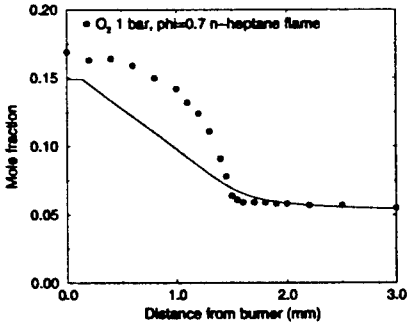

Figure 18: O_2 profile.

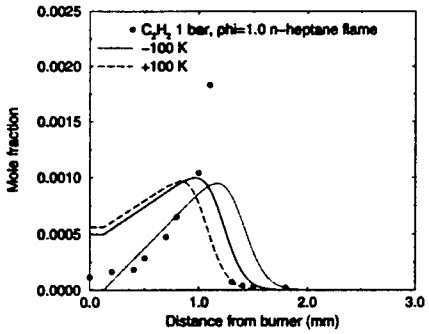

Figure 19: C_2H_2 profile.

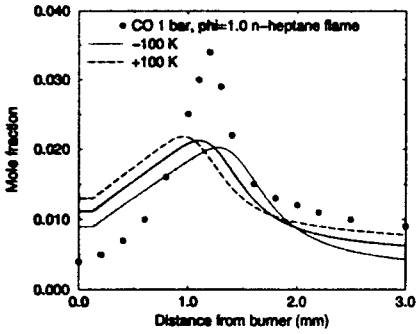

Figure 20: CO profile.

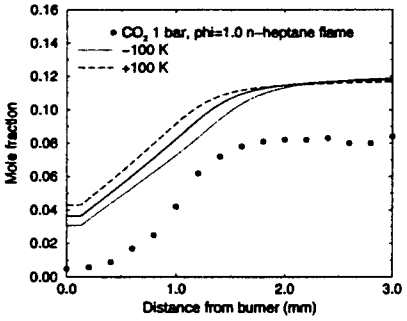

Figure 21: CO_2 profile.

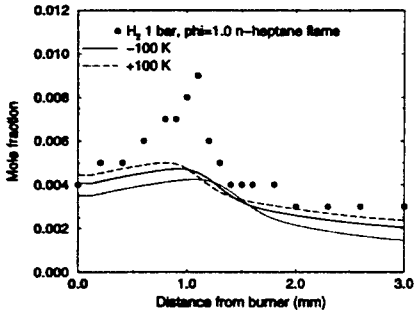

Figure 22: H_2 profile.

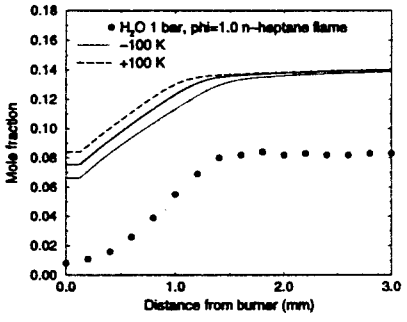

Figure 23: H_2O profile.

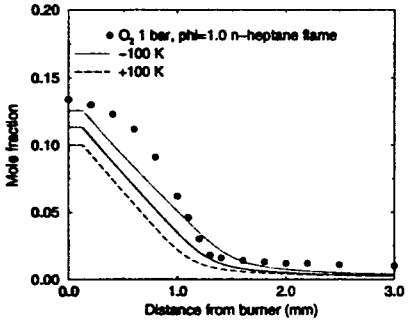

Figure 24: O_2 profile.

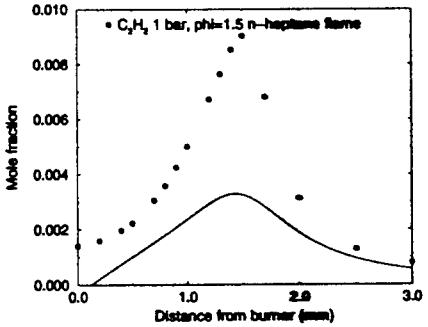

Figure 25: C_2H_2 profile.

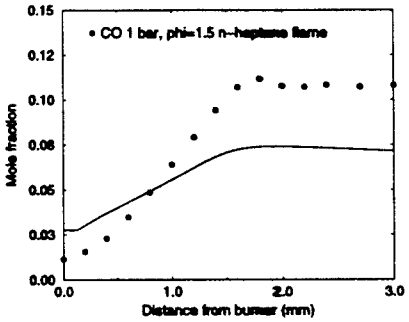

Figure 26: CO profile.

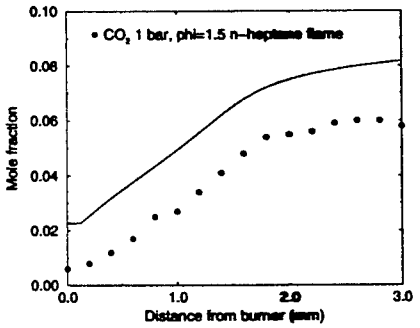

Figure 27: CO_2 profile.

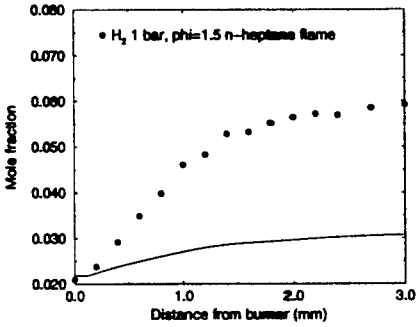

Figure 28: H_2 profile.

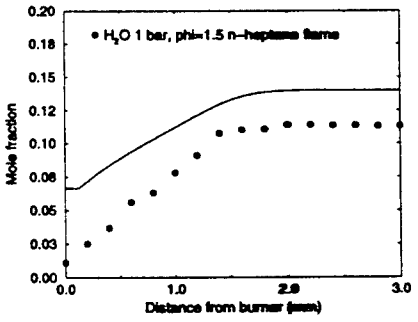

Figure 29: H_2O profile.

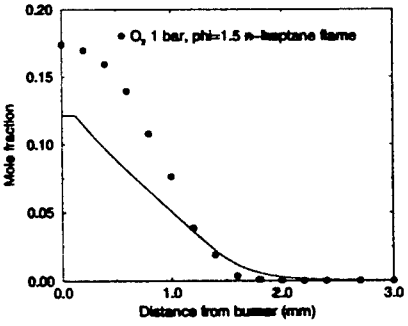

Figure 30: O_2 profile.

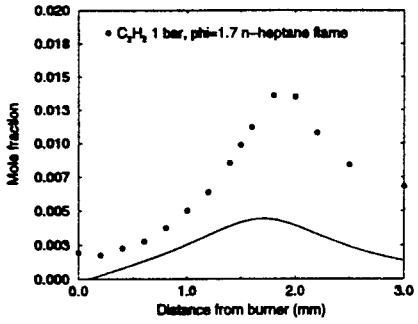

Figure 31: C_2H_2 profile.

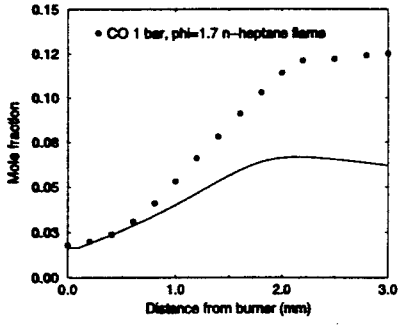

Figure 32: CO profile.

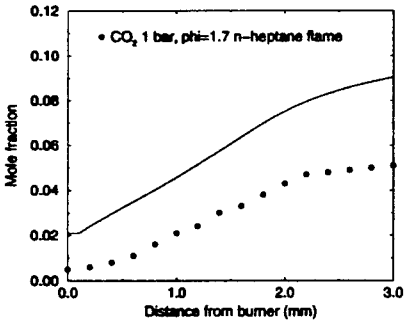

Figure 33: CO_2 profile.

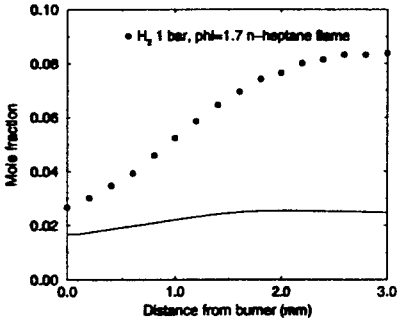

Figure 34: H_2 profile.

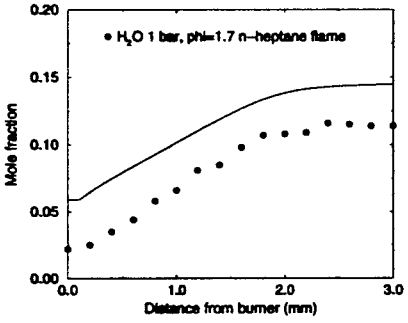

Figure 35: H_2O profile.

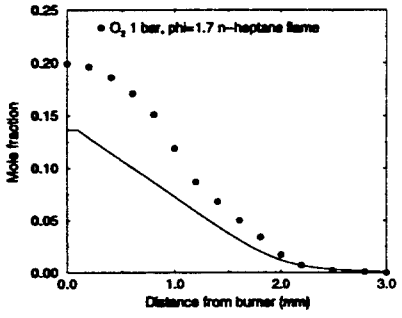

Figure 36: O_2 profile.

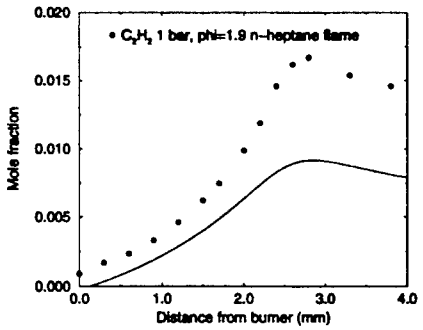

Figure 37: C_2H_2 profile.

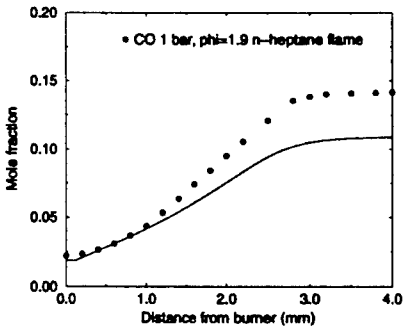

Figure 38: CO profile.

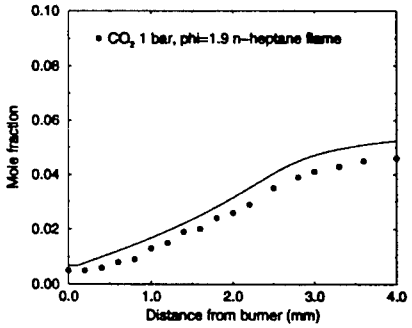

Figure 39: CO_2 profile.

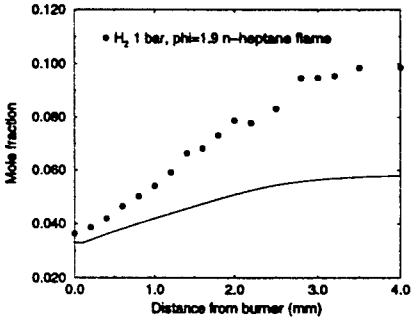

Figure 40: H_2 profile.

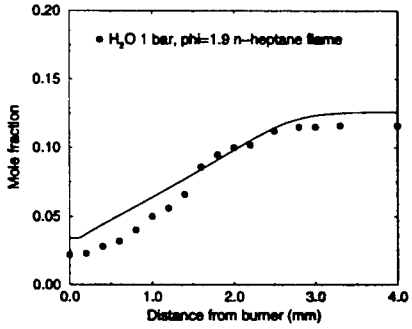

Figure 41: H_2O profile.

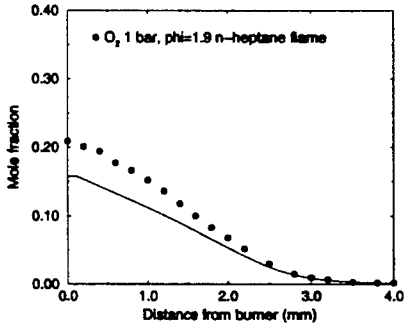

Figure 42: O_2 profile.

The sensitivity of computed species profiles to the primary fuel consumption steps is assessed for iso-octane flames. The ad-hoc sensitivity analysis for a $\phi = 1.7$ flame shows significant effects only in the ethylene, C_2H_4; propene, C_3H_6; and propane, C_3H_8, species profiles (Figures 43 to 45). The analysis is conducted by independently multiplying the pre-exponential factor in the Arrhenius relations by a factor of 5 for each of the thermal decomposition reactions (772,773,774), and each of the abstraction reaction sets yielding the four isomers of the octyl radical, C_8H_{17}, in turn. Thus a total of seven cases is examined. The sensitivity is examined for the predictions of allene, $a - C_3H_4$; propyne, $p - C_3H_4$; acetylene, C_2H_2; ethylene, C_2H_4; propene, C_3H_6; propane, C_3H_8; and benzene, C_6H_6. The effects of the changes are most evident for propane, C_3H_8, as shown in Figure 45. Table 2 translates the graphical data to percentages for cross comparison.

case	pre-exponential factors multiplied by five	percent change in C_2H_4	percent change in C_3H_6	percent change in C_3H_8
L1	772	3.73	0	22.2
L2	773	8.96	11.62	0
L3	774	3.73	9.82	65
L4	775, 779 783,787,791	-1.87	-14.21	5.6
L5	776, 780 784,788, 792	-5.22	21.7	-13.3
L6	777, 781, 785,789, 793	-7.46	12.9	-4.4
L7	778, 782, 786,790, 794	8.96	14.47	-4.4

Table 2: Sensitivity analysis results. Cases refer to lines in Figures 43 to 45.

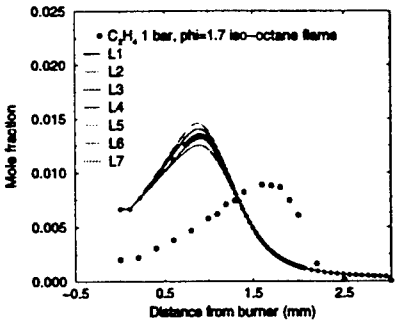

Figure 43: Sensitivities of computed profiles of C_2H_4.

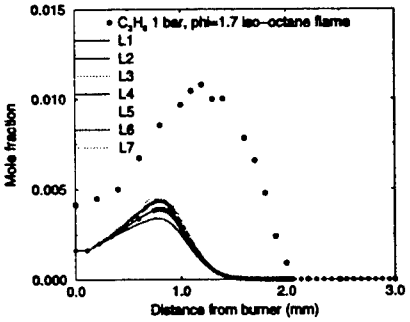

Figure 44: Sensitivities of computed profiles of C_3H_6.

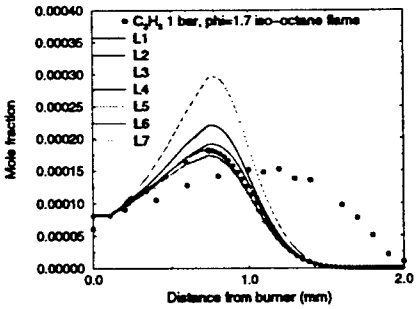

Figure 45: Sensitivities of computed profiles of C_3H_8.

The forward reaction rates are generally dominant and no partial equilibration is noted. The relative importance of the competing pathways is examined by comparing the maximum positive reaction rates of fuel consumption reactions 772-798.

$$pathway\ percentage = \frac{maximum\ path\ reaction\ rate}{\sum maximum\ path\ reaction\ rates}$$

It is fully recognized that reaction paths are strongly dependent on flame stoichiometry. The elementary path analysis for the $\phi = 1.7$ flame is presented here. Computations indicate that C-C scission reactions (773,774) are significant iso-octane consumption steps at fuel rich conditions, contributing about 13 percent. The prevalent H abstraction paths yielding the octyl, C_8H_{17}, isomers are via H atom attack (775-777), contributing about 5 percent.

H atom abstraction yielding the 1-octyl radical, $1-C_8H_{17}$, via OH radical attack (779) contributes about 4 percent. H atom abstraction via O (784-786) and OH (780-782) attack have limited influence, consuming only 1 percent each. H atom abstraction paths via methly radical, CH_3, attack (788-790) also consume about 1 percent each, which is reasonable for fuel rich conditions. Iso-octane consumption via molecular oxygen attack (791-794) are not significant pathways.

Conclusions

The suspected experimental error in the species profiles for the iso-octane and n-heptane laminar flames considered in the present work makes interpretation of the numerical results difficult. The n-heptane mechanism is previously shown to reproduce experimental trends for a variety of devices [4, 6] and is arguably well developed. The goal of the present work is to develop

an iso-octane sub-mechanism capable of predicting major and intermediate species profiles, and benzene growth. At present data of sufficient quality to develop an iso-octane sub-mechanism applicable to flames is arguably lacking. The current iso-octane sub-mechanism produces numerical trends that are consistent with the current understanding of the iso-octane combustion process. Refinement of the proposed mechanism is recommended as additional experimental data becomes available.

It is noted that convergence of the solution is highly dependent on the input temperature profile. The temperature profile is obtained from a curve fitting program and can produce singular disturbances away from input points. The temporary solution is to ensure the curve fit is valid over a larger domain than the code encounters. This tends to force a smoother curve, but there is no guarantee of piecewise continuity. This problem can be addressed with a piecewise continuous curve fit subroutine such as one based on a cubic spline.

References

[1] E. Ranzi, T. Faravelli, P. Gaffuri, A. Sogaro, A. D'Anna, and A. Ciajolo, "A wide-range modeling study of iso-octane oxidation," *Combustion and Flame*, vol. 108, pp. 24–42, 1997.

[2] A. E. Bakali, *Cinetique de Combustion du n-heptane et de l'iso-octane a pression atmospherique.* PhD thesis, l'Uinversite d'Orleans, 1996.

[3] C. Doute, *Cinetique de Combustion d'Hyrocarbures Lourds.* PhD thesis, l'Uinversite d'Orleans, 1995.

[4] R. P. Lindstedt and L. Q. Maurice, "Detailed kinetic modelling of n-heptane combustion," *Combust. Sci. and Tech.*, vol. 107, pp. 317–353, 1995.

[5] R. P. Lindstedt, *LAPREM.* Imperial College. LAPREM is a program developed to compute premixed laminar flames.

[6] L. Q. Maurice, *Detailed Chemical Kinetic Models for Aviation Fuels.* PhD thesis, Imperial College, 1996.

[7] V. Illes, K. Welthern, and I. Pleszkats, "Pyrolysis of liquid hydrocarbons, ii overall decomposition rates for liquid hydrocarbons," *Acta Chim. Acad.*, vol. 78, p. 357, 1973.

A STUDY OF HRR SUPER RESOLUTION ANALYSIS FOR POSSIBLE ATR PERFORMANCE ENHANCEMENT

S. Robert Stanfill
Graduate Student
Department of Electrical Engineering

University of Florida
4th floor NEB
Gainesville, FL 32611-6200

Final Report for:
Summer Graduate Student
Research Program
Wright Laboratory

Sponsored by:
Air Force Office of Scientific Research
Bolling Air Force Base, DC

and

Wright Laboratory

September 1997

A STUDY OF HRR SUPER RESOLUTION ANALYSIS FOR POSSIBLE ATR PERFORMANCE ENHANCEMENT

S. Robert Stanfill
Graduate Student
Department of Electrical Engineering
University of Florida

ABSTRACT

The possible benefit super resolution can provide to High Range Resolution Automatic Target Recognition was studied. Moving and Stationary Target Recognition data was processed to yield target to clutter ratios indicative of moving target High Range Resolution signatures. This data was reduced in resolution and used to generate the parametric model based quantities necessary to simulate resolution enhanced signatures. These simulations were compared to resolution reduced and full resolution signatures to gauge accuracy of estimates and possible Automatic Target Recognition enhancements respectively.

A STUDY OF HRR SUPER RESOLUTION ANALYSIS FOR POSSIBLE ATR PERFORMANCE ENHANCEMENT

S. Robert Stanfill

INTRODUCTION

Automatic Target Recognition (ATR) is an active and important area of research. ATR strives to provide information as to the classification of target captured by the given data acquisition mode. One of the more ambitious goals is to provide real-time target recognition "in-cockpit" to aid pilot targeting decisions and possibly minimize false target kills and eliminate "friendly fire" incidents. To achieve this in a cost efficient manor, the data acquisition mode of choice is simple one dimensional radar data called High Range Resolution (HRR) signatures currently being gathered in the field . This type of data is relatively simple to obtain and minimizes the amount of time that the aircraft must be in the vicinity of the possible target.

The primary goal of this study is to evaluate the performance of resolution enhancement ("super resolution") techniques to see if this added information will boost ATR performance over that achieved using "raw" data. A number of sections will be used to present the results:

- Data Acquisition
- Super Resolution
- Trials
- Results
- Conclusion

Each section will explain in detail the procedure used to complete that portion of the study or give a background tutorial necessary to properly explain the topic.

DATA ACQUISITION

The data was obtained from the Moving and Stationary Target Recognition (MSTAR) collection gathered by Sandia Laboratory and distributed by Veda Inc. Because this collection is two dimensional (2-D) Synthetic Aperture Radar (SAR), some preliminary steps had to be performed to obtain the necessary phase history required for super resolution analysis.

The relationship between SAR and it's phase history can be obtained from a simple 2-D inverse Fourier transform. Because there was some pre-filtering done by Sandia and the target to clutter ratio needed a boost to better represent moving target data, some additional steps had to be done.

Figure 1 shows the process.

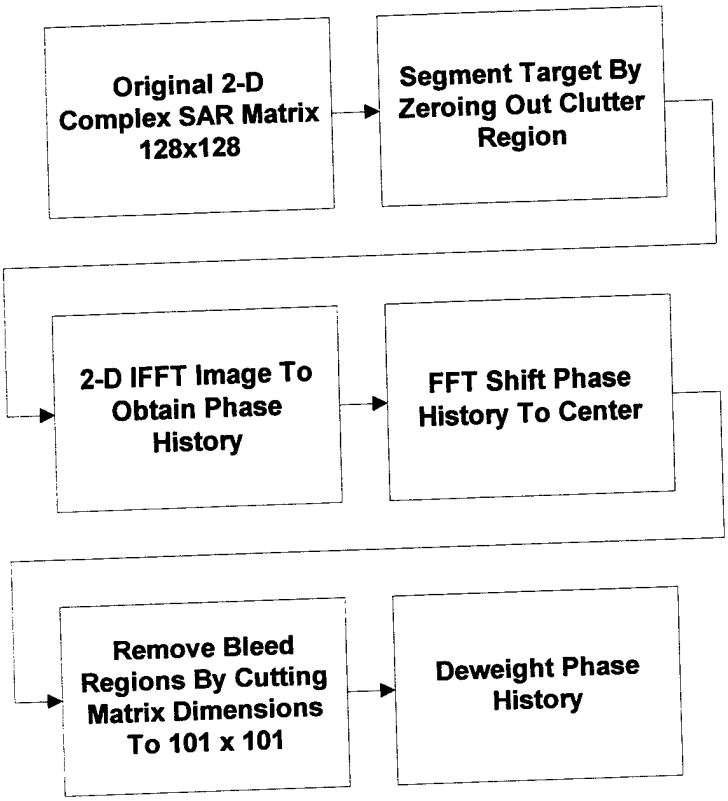

FIGURE 1

First, the original 2-D SAR matrix is obtained from the MSTAR collection, then the clutter is zeroed outside the target region by a segmentation algorithm to provide better target to clutter ratios. A 2-D IFFT is then applied to go from the image domain to the phase history domain. In Sandia's pre-filtering process, the phase history has been shifted and there has been some zero padding placed in the center that provides a bleed region for the filter, therefore, the data is FFT shifted and then the bleed regions are removed. Finally, the phase history is deweighted. The final product, ideally, is a "raw" phase history matrix from which columns are to be inputted into the super resolution algorithm.

Figure 2 shows a typical MSTAR chip going through each step of the data procedure.

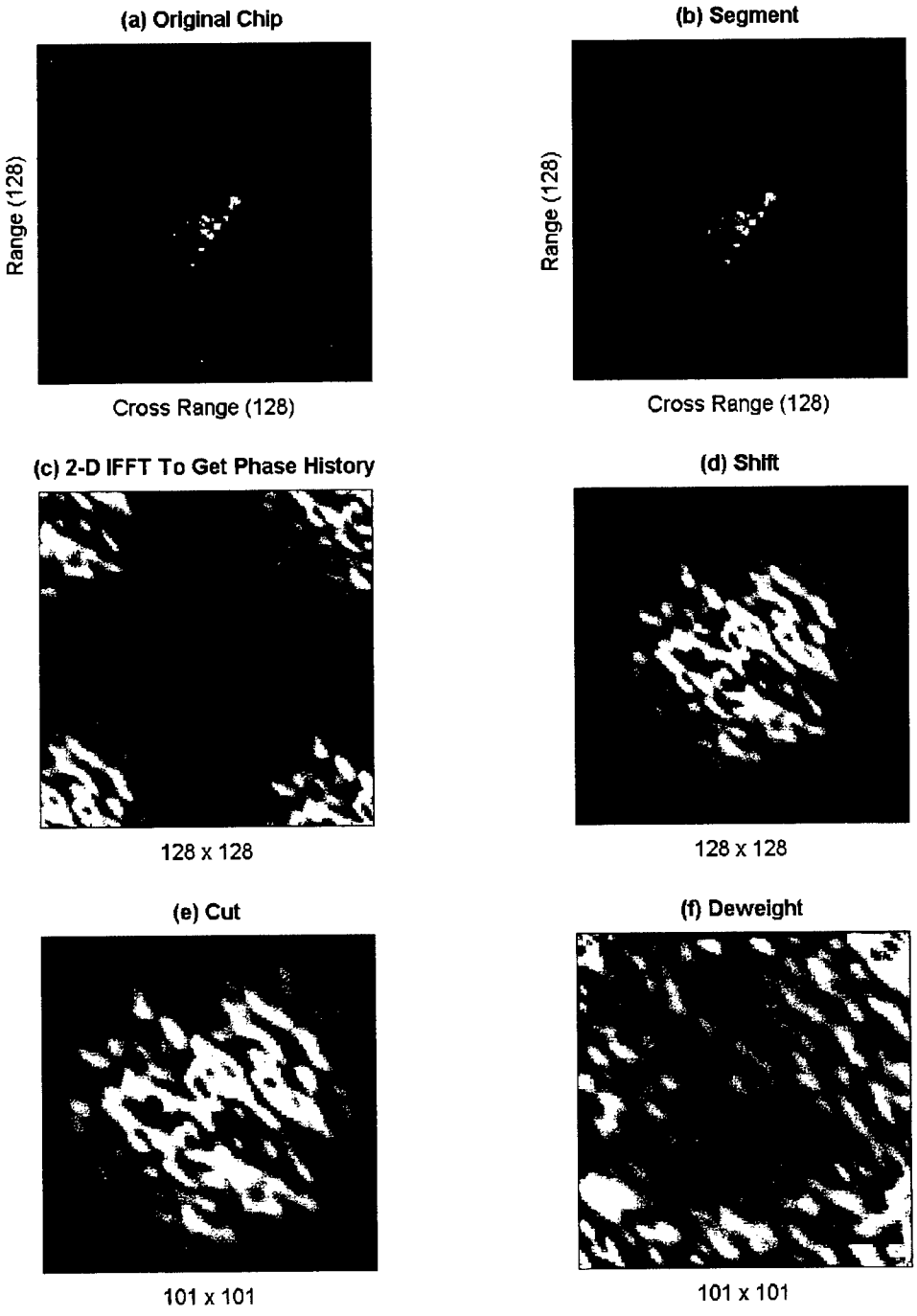
(a) Original Chip
Range (128)
Cross Range (128)
(b) Segment
Range (128)
Cross Range (128)
(c) 2-D IFFT To Get Phase History
128 x 128
(d) Shift
128 x 128
(e) Cut
101 x 101
(f) Deweight
101 x 101

FIGURE 2

A STUDY OF HRR SUPER RESOLUTION ANALYSIS FOR POSSIBLE ATR PERFORMANCE ENHANCEMENT

SUPER RESOLUTION

This past year, working at the Spectral Analysis Laboratory at the University of Florida, I completed a study involving super resolution algorithms applied to synthetic High Range Resolution radar data. Trials were run using the following algorithms:

- RELAX
- Higher Order Yule-Walker (HOYW)
- Method of Direction Estimation (MODE)
- Estimation of Signal Parameters by Rotational Invariance Techniques (ESPRIT)

Each of these methods attempt to estimate the K complex amplitudes (α_i, radar cross sections) and angular frequencies (ω_i, relative ranges) of the data's (p) scatterers using the following phase history parametric model:

$$p_n = \sum_{i=1}^{K} \alpha_i \cdot e^{j \cdot \omega_i \cdot n} + noise$$

Once the estimated parameters are obtained, the above model can be used to generate a data vector of any length.

My results showed that the best algorithms for this type of data were RELAX and ESPRIT.

Each had it's own advantage:

- ESPRIT is especially fast on a computer but is not nearly as robust to the number of scatterers (K) present in the data as RELAX.
- RELAX is very robust to the choice of K but relies on a number of FFT computations and that translates to a heavy flop count. RELAX is also iterative in nature, whereas, ESPRIT is not.

RELAX's robust performance was especially attractive. Given that there is no a priori knowledge of the number of scatterers in the data, it is very important that whatever algorithm is used, has to be able to perform well given different K values. Also, RELAX's heavy flop count can be overcome via FFT hardware implementations. It is for these reasons, I focused all of my attention on RELAX's performance on this type of data.

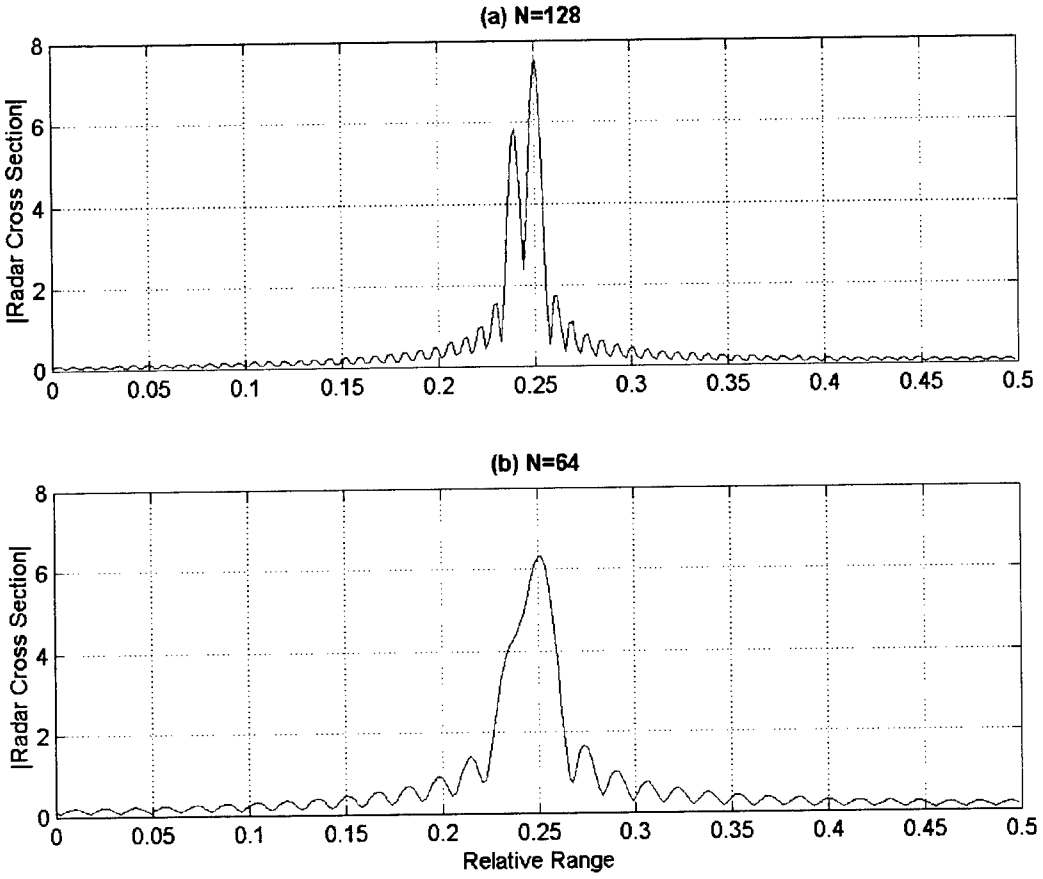

FIGURE 3

All super resolution algorithms are designed to produce a level of resolution that was not apparent before. To gauge the performance of a given super resolution procedure, it is advantageous to de-resolution a typical data set, find the estimates based on the parametric model, and then attempt to simulate it back to the original resolution. This way, a comparison can be made to the actual data and the algorithm's worth can be evaluated. De-resolution is achieved by reducing the number of data points in the phase history domain. The relationship between the number of data points (N) and the resolution is shown in the simulated range signatures of Figure 3.

In part (a), at N = 128 (phase history), there are clearly two peaks representing the returns from two different scatterers spaced closely together in relative range. Part (b) shows the same data but with N = 64. The two peaks have smeared into each other and there is not a very clear distinction as to where these two scatterers might be located. In fact, it isn't even clear if this signature contains one, two, or possibly even more returns. The idea is simple, the higher the resolution, the more information content.

The hope is that after applying RELAX's super resolution capabilities on the HRR data, the additional information it provides will make the ATR decision process easier.... more information, better separability, better ATR performance.

TRIALS

The experiment consists of reducing the resolution of individual signatures, then running them through RELAX with the number of scatterers (K) set to 16. The idea is to take these "de-rezzed" versions and use them to provide the necessary parameter estimates so that a higher resolution set can be simulated. In addition, a simulation to the de-rezzed signature is created to gauge how well RELAX is reproducing the data that is used to base it's estimates.

The data supplied to RELAX is the 101 point individual columns from the raw 2-D phase history. This represents the 1-D phase history of HRR data. The process is depicted in Figure 4.

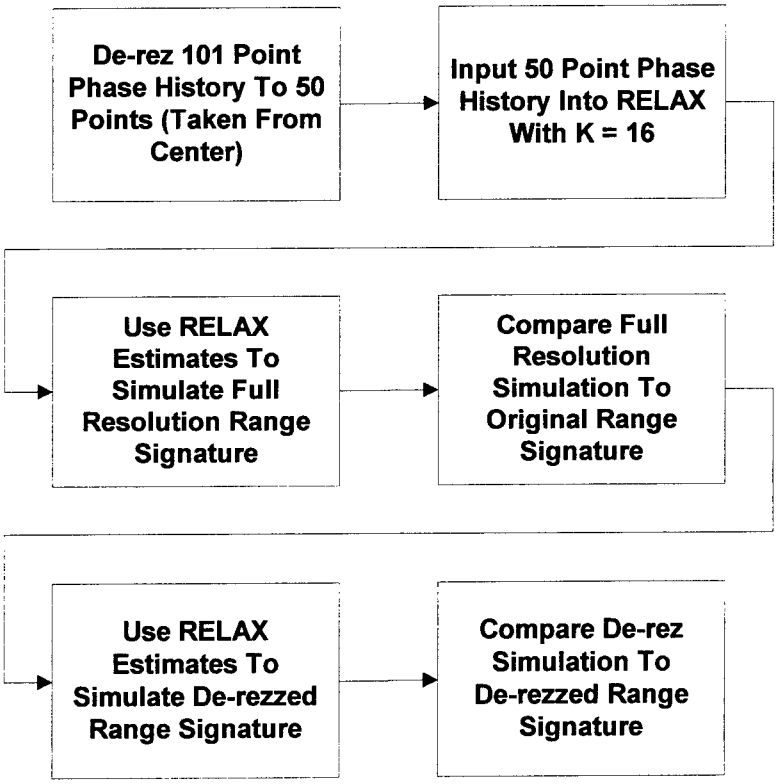

FIGURE 4

RESULTS

Figures 5 -7 show typical results of these trials for three different targets: A T72, BTR, and BMP. Part (a) is the original deweighted range signature. Part (b) is the simulation based on RELAX estimates along with the magnitude and relative range of the parametric estimates themselves (the x's with the dashed vertical lines). Part (c) is the de-rezzed original deweighted range signature with RELAX estimates. Part (d) is the simulation to match the de-rezzed range signature.

By a visual inspection alone, the results look promising. There seems to be a correlation between the original and simulated full resolution graphs. The de-rezzed versions and their matching simulations are near exact! I did a numerical comparison and RELAX can imitate the de-rezzed data to within 1% of a normalized to maximum peak value mean squared error (this is especially encouraging).

A number of trials exactly as those shown were done. There were far to many to include with this report, so a representative graph from each target is given. The total number of columns that need to be processed numbers in the hundreds of thousands. Due to time constraints, I could not complete all necessary trials to gather a complete set for a realistic ATR trial.

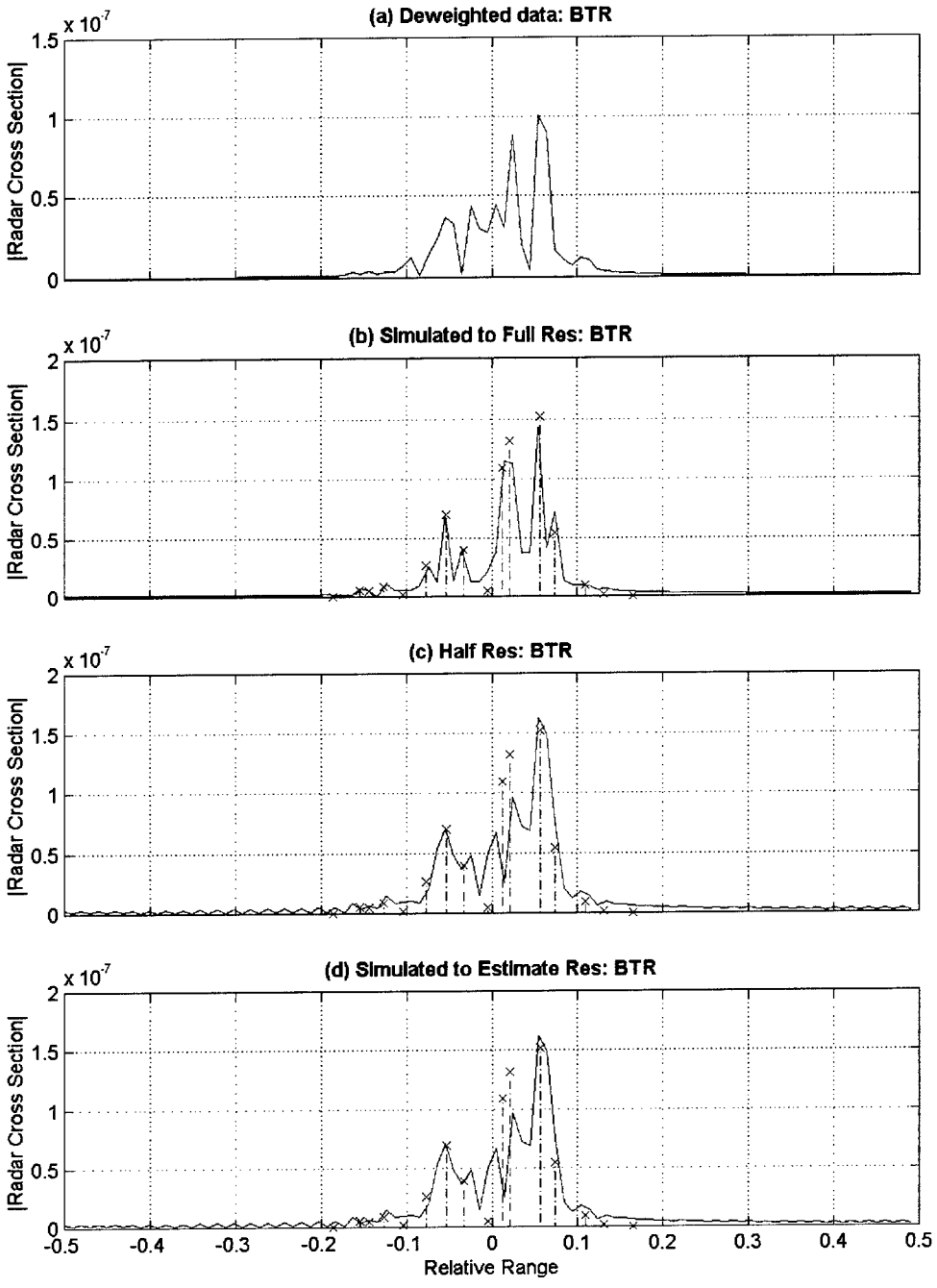
(a) Deweighted data: BTR
x 10^-7
|Radar Cross Section|
(b) Simulated to Full Res: BTR
x 10^-7
|Radar Cross Section|
(c) Half Res: BTR
x 10^-7
|Radar Cross Section|
(d) Simulated to Estimate Res: BTR
x 10^-7
|Radar Cross Section|
-0.5 -0.4 -0.3 -0.2 -0.1 0 0.1 0.2 0.3 0.4 0.5
Relative Range

FIGURE 5

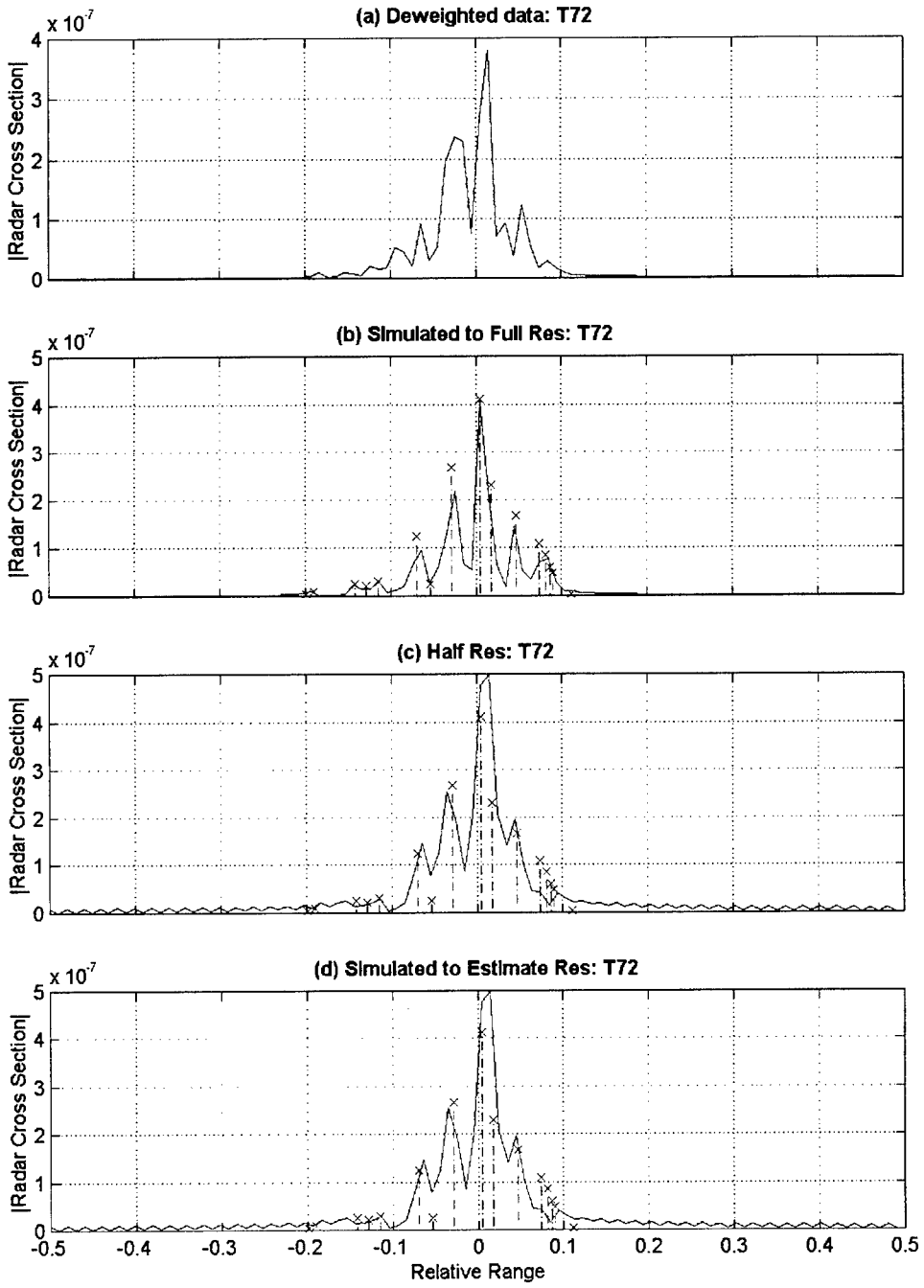
(a) Deweighted data: T72
x 10^-7
|Radar Cross Section|
(b) Simulated to Full Res: T72
x 10^-7
|Radar Cross Section|
(c) Half Res: T72
x 10^-7
|Radar Cross Section|
(d) Simulated to Estimate Res: T72
x 10^-7
|Radar Cross Section|
-0.5 -0.4 -0.3 -0.2 -0.1 0 0.1 0.2 0.3 0.4 0.5
Relative Range

FIGURE 6

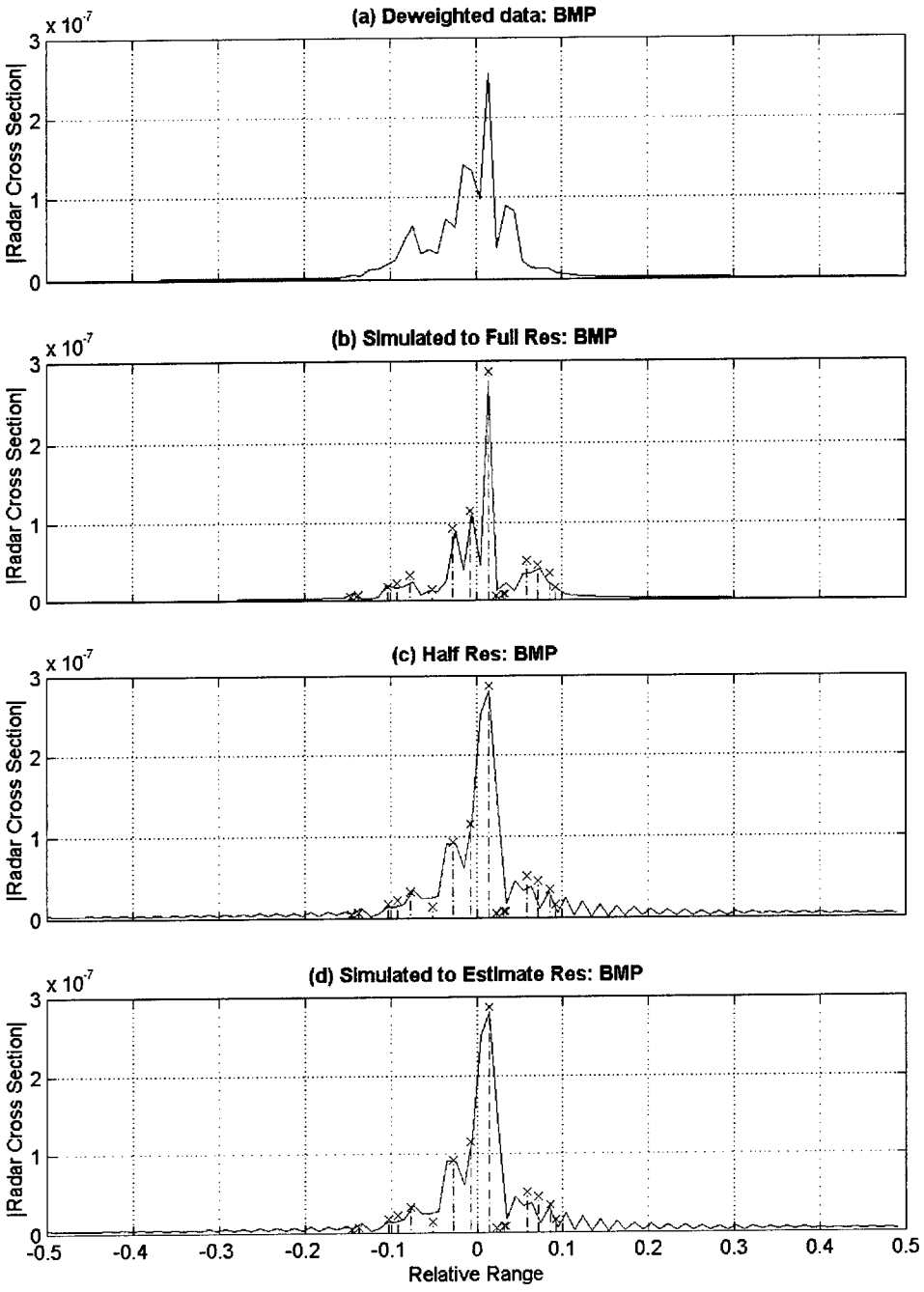
(a) Deweighted data: BMP
(b) Simulated to Full Res: BMP
(c) Half Res: BMP
(d) Simulated to Estimate Res: BMP
x 10^-7
|Radar Cross Section|
0
1
2
3
-0.5
-0.4
-0.3
-0.2
-0.1
0
0.1
0.2
0.3
0.4
0.5
Relative Range

FIGURE 7

CONCLUSION

Super resolution appears to have an important and viable use in the field of High Range Resolution Automatic Target Resolution. Simulations based on RELAX generated estimates can indeed provide a level of resolution that would otherwise not be available using original range signatures. It therefore stands to reason that ATR performance should improve with this added information. To provide the quantitative results necessary to confirm the level of ATR enhancement, an in-depth study needs to be done that includes the hundreds of thousands of trials needed to input into an established ATR program to generate a sound statistic measure of super resolution's worth to this type of research and data.

DETECTION TECHNIQUES USE IN FORWARD-LOOKING RADAR SIGNAL PROCESSING: A LITERATURE REVIEW

Adedokun Sule-Koiki
Graduate Student
Department of Electrical Engineering

Howard University
2600 6th Street, NW
Washington, DC 20059

Final Report for:
Summer Research Program
Wright Laboratory

Sponsored by:
Air Force Office of Scientific Research
Bolling Air Force Base, DC

and

Wright Laboratory

August 1997

Detection techniques use in forward-looking radar signal processing system: A Literature Review

Mohammed. Chouikha
Professor

Adedokun Sule-Koiki
Graduate Student

Department of Electrical Engineering
Howard University

Abstract

(FLAR) Forward-looking airborne radar system, as oppose to (SLAR) side looking airborne radar, allows high target to background contrast, accurate azimuth estimates, day and night operation, and can, to a limited degree, penetrate fog, haze, and dust. On the down side, forward-looking IR radar has range uncertainty, generate false alarm from background clutter, has difficult with occlusion of targets by vegetation and terrain, and is aspect angle dependent. The concept of detection and identification of targets, in nonstationary environment and obscure by inteferences such as clutter, jammer, and noise entails suppressing these inteferences with effective signal processing scheme.

In this report, we will present a comprehensive review of the different STAP algorithms and Neural Network methods, without analytical justification of these algorithms and methods, use for detection of target, obscured by interference such as clutter, Jammer, and noise, applicable to forward-looking airborne radar system.

Detection techniques use in forward-looking radar signal processing system: A Literature Review

Mohammed. Chouikha and Adedokun Sule-Koiki

I. INTRODUCTION

The general approach to detection of target(s) in nonstationary clutter and noise interference attempts to eliminate clutter and noise interference prior to detection by exploiting known differences in the statistical characteristics of target(s) relative to clutter and noise interference. It then performs detection based on statistical models for the remaining residual clutter and noise interference. These models are typically based on experimental data.

It has been demonstrated, in SLAR (side looking airborne radar) applications, space-time adaptive processing can result in weight solution equivalent to those required to perform DPCA. An effective and standard approach to clutter reduction makes use of the differential radial Doppler shift between target and clutter to discriminate against clutter, i.e. perform adaptive MTI processing. A standard MTI approach is only successful in achieve sufficient rejection over full clutter bandwidth at the expense of attenuation of the returns from slow moving targets. In SLAR applications, the DPCA (displaced phased center antenna) technique provide a mechanism for rejecting both mainlobe and sidelobe clutter by compensating directly for the motion of the antenna platform. These two methods mentioned are fully described in [1,2]

Adaptive beamforming is one of the many techniques use in a radar signal processing system. It involves forming multiple beams through applying appropriate delay and weighting elements to signal received by the sensors. The purpose is to suppress unwanted jamming inteferences and to produce the optimal beamformer response which contains minimal contributions due to noise. The most commonly employed technique for deriving the adaptive weights uses a closed loop gradient descent algorithm where the weight updates are derived from estimates of the correlation between the signal in each element and summed output of the array. This processing can be implemented in analog fashion using correlation loops [7] or digitally in the form of the Widrow least mean square (LMS) algorithm [8]. The fundamental limitation for this technique is one of poor convergence for a broad dynamic range signal environment. The limitation was over come through the application of linear constraints to the weights. The basic concept of linearly constrained minimum variance (LCMV) beamforming is to constrain the response of the beamformer such that the desired signals are passed with specified gain and phase. The weights are chosen to minimize output power subject to the response constraint. When the beamformer has unity response in the look direction, the LCMV problem would become the minimum variance distortionless response (MVDR) beamformer problem, which is very general approach employed to control beamformer response. The weights of the beamformer should be updated in real-time in order to respond to rapid time-varying environment.

Meanwhile, the evaluation of weights is computational intensive and can hardly meet the real-time requirement. Systolic implementations of optimum beamformers have been studied to improve the computational speed by a number of investigators. McWhirter and Shepherd [9] showed how a triangular systolic array of the type proposed by Gentleman and Kung [10] can be applied to the problem of linearly constrained minimum variance problem, subject to one or more simultaneously linear equality constraints.

Tank and Hopfield and few other researchers [and subref.] have shown how a class of neural networks with symmetric connections between neurons presets a dynamics that leads to the optimization of a quadratic functional. Chua and Lin and Kennedy and Chua extend the design of Hopfield network and introduce a canonical nonlinear programming circuit, which is able to handle more general optimization problems. Beck et al presented a neural network approach to segmentation of forward-looking infrared and synthetic aperture radar imagery. Chang et al presented a Hopfield-type neural network approach, which is similar to an analog circuit for implementing the real-time adaptive antenna, array. Davis et al in applied a higher-order neural net work to the problem of 2-D target detection in noisy scene. Clark et al presented the use of Gabor representations to generate feature vectors that are robust to variation in rotation, scaling, and translation. They described a prototype system for recognizing target in images by extracting image features, compressing the data, and classifying the targets using a neural network. Hara et al in presented a terrain classification technique to determine terrain classes in polarimetric SAR images, utilizing unsupervised neural networks to provide automatic classification, and employing an iterative algorithm where the SAR image is reclassified using a Maximum likelihood (ML) classifier to improve the performance.

In Section II, a signal model useful for radar signal processing is presented. Section III describes adaptive beamforming. Section IV presents the computational learning methods and it importance to airborne radar. Section VI concluded this report.

II Terminology and Signal model

Suppose it is desired to detect only the target signal in cases where the target Doppler is immersed in clutter/interference and noise and reject the other entire signal referred to as interference. Denote the sample data matrix **X**, N_t x N_s is defined by

$$\mathbf{X} = \left[x_{t1} x_{t2} \cdots\cdots n_{tN_s}\right] = \begin{bmatrix} x_{s1}^T \\ x_{s2}^T \\ \vdots \\ \\ \vdots \\ x_{sN_t}^T \end{bmatrix} \qquad 1$$

T denotes the transpose, and the row vectors of **X**, $x_{sn_t}^T$, $n_t = 1,2,\cdots,N_t$, are the snapshot obtained along

the spatial channels. Under the signal-absence hypothesis H_o, the data matrix **X** consists of

clutter/interference and noise components only, i.e.,

$$\mathbf{X} = \mathbf{C} + \mathbf{N} \qquad 2$$

C and N represent the clutter/interference and noise, respectively, and are assumed to be independent. Under the signal-presence hypothesis H_1, a target signal component also appears in the data matrix, i.e.,

$$\mathbf{X} = \mathbf{AS} + \mathbf{C} + \mathbf{N} \qquad 3$$

A is an unknown complex constant representing the amplitude of the signal and **S** the signal matrix of unknown form. Under the assumptions, the $n_t n_s$ the entry of the signal matrix **S** has the following form:

$$s(n_t, n_s) = \exp\left[i2\pi(n_t - 1)\frac{2v}{\lambda PRF} + i2\pi(n_s - 1)\frac{d\sin\theta}{\lambda} \right], \qquad 4$$

v is the radial velocity of the target. θ is the direction of arrival of the target-return planewave with respect to the broadside of the array and λ the radar wavelength. Denoting

$$f_{st} = \frac{2v}{\lambda PRF} \qquad 5$$

and

$$f_{ss} = \frac{d\sin\theta}{\lambda} \qquad 6$$

f_{st} is the normalized Doppler frequency of the target signal and f_{ss} is the spatial frequency. **S** can be expressed by

$$S = s_s^T \otimes s_t \qquad 7$$

Where $\otimes$ is the Kronecker product, and

$$s_t = \left[1 \quad \exp(i2\pi f_{st}) \quad \ldots \quad \exp\left(i2\pi(N_t - 1)f_{st}\right)\right]^T \qquad 8$$

And

$$s_t = \left[1 \quad \exp(i2\pi f_{ss}) \quad \ldots \quad \exp\left(i2\pi(N_s - 1)f_{ss}\right)\right]^T \qquad 9$$

represent the signals in time and space. To detect signal S in received vector **X** one puts the received vector through a *filter* with weight

$$\mathbf{W} = [w_1, w_2, \ldots\ldots w_n]^T. \qquad 10$$

The output of the filter W is the scalar

$$X = \sum_{k=1}^{n} w_k Z_k = W_T Z \qquad 11$$

T denotes the matrix transpose. For the case of signal noise alone, the expected values as

$$E[X] = \sum_{k=1}^{n} w_k E[z_k] = \sum_{k=1}^{n} w_k s_k = W_T S . \qquad 12$$

Similarly, the noise power or variance of X is

$$\begin{aligned} \sigma^2 &= E\left[|X|^2\right] - |E[X]|^2 \\ &= W_T^* E[N^*] E[N_T] W \\ &= W_T^* M W \end{aligned} \qquad 13$$

Where the asterisk denotes complex conjugate and M is the covariance matrix of the noise process i.e.

$$M = E[N^* N_T] = E[n_j^* n_k] \qquad 14$$

Based on the above concept, determining the weights with linear constraints to the weight vector called the linearly constraint minimum variance beamforming problem, which is usually formulated as

$$\min_{w} \quad \phi(W) = W^H M W \qquad 15$$

$$\text{subject to} \quad W^H S_o = r$$

where H is the complex conjugate transpose of the vector, r is the a complex constant, S_o is the steering vector associated with the look direction and is given by [32]:

$$S_o = \left[1, \exp\left(j\frac{2\pi d}{\lambda_o}\cos\theta_o\right), \ldots, \exp\left(j\frac{2\pi d}{\lambda_o}(L-1)\cos\theta_o\right)\right]^T \qquad 16$$

where d is the element spacing, λ_o is the wave length of the plane wave in free space, and θ_o is the look direction angle (the angle between the axis of the linear array and the direction of the desired signal source). A solution of equation (15), after using method of Lagrange multiplier, is given by:

$$\hat{W} = r\frac{M^{-1}S_o}{S_o^H M^{-1} S_o} \qquad 17$$

The problem in airborne radar signal processing is therefore to detect target while eliminate the unwanted signal returns commonly referred to as clutter, interference and noise.

III. ADAPTIVE BEAMFORMING

The first adaptive system for cancellation of clutter with an unknown Doppler frequency is TACCAR (Time Averaged Clutter Coherent Airborne Radar) [10].

Phase differences between subsequent echoes are used to adjust the COHO (coherent oscillator) frequency so that the mid-Doppler frequency becomes zeros and the clutter spectrum falls into the notch of the two-pulse canceler. The method can adjust for one Doppler frequency only and may fail if there is more than one significant frequency in the clutter spectrum.

A. BeamSpace

Some results on space-time adaptive processing have been presented in [1,2,27]. Earlier work of Reed, Mallet and Brennan (RMB) described an adaptive array procedure for the detection of a signal of known form in the presence of noise (interference) which is assumed to be Gaussian, but whose covariance matrix is totally unknown. They discussed how adaptive array processing is used to achieve optimum detection as applicable to airborne radar signal processing problem The optimum decision criterion for detecting the signal S in the presence of noise begin by formulating the likelihood ratio test given by

$$L = \exp\left[\frac{1}{2\sigma^2}\left(2|S\|X|\cos(\theta-\delta)-|S_1|^2\right)\right] \qquad 18$$

Where $S_1 = W_T S$, $\theta = \arg(X)$; $\delta = \arg(S_1)$

The test is formed by averaging L with respect to θ and by comparing the result with a threshold. That is if

$$\int L(X/\theta)P(\theta)d\theta \geq c > 0 \qquad 19$$

One can then say a signal is detected; if this quantity is less than c, X is said to result from noise alone. L is therefore given by

$$L = \exp\left(\frac{-|S_1|^2}{2\sigma^2}\right) I_0\left(|S_1\|X|\right) \geq c \qquad 20$$

The probability of a false alarm P_F and the probability of detection P_D are given by

$$\begin{aligned} P_F &= prob\{|X| > c|Z = N\} \\ &= \int_c^\infty \int_0^{2\pi} \frac{1}{2\pi\sigma^2}\exp\left(\frac{-r^2}{2\sigma^2}\right) r dr d\theta \\ &= \exp\left(\frac{-c^2}{2\sigma^2}\right) \end{aligned} \qquad 21$$

$$P_D = prob\{|X| > c | Z = S + N\}$$

$$= \int_c^{\infty} \int_0^{2\pi} \exp\left(\frac{-1}{2\sigma^2}\left|re^{j\theta} - ae^{i\delta}\right|\right) \frac{rdrd\theta}{2\pi\sigma^2}$$

$$= \frac{1}{\sigma^2} \int_c^{\infty} I_0\left(\frac{ra}{\sigma^2}\right) \exp\left(\frac{-r^2 + a^2}{2\sigma^2}\right) rdr \qquad 22$$

$$a = |S_1| = |W_T S|; \text{ and } \sigma^2 = W_T^* M W$$

From this, an expression for integrated signal-to-noise ratio α^2 is given by

$$\alpha^2 = \left(\frac{S}{N}\right) = \frac{|W_T S|^2}{W_T^* M W} \qquad 23$$

In Q function, the probability of detection is then expressed as

$$P_D(\alpha) = Q\left(\alpha, \sqrt{2\log\frac{1}{P_F}}\right). \qquad 24$$

The bound on signal-to-noise is obtained to be

$$\max_w \alpha^2 = S_T M^{-1} S^*, \qquad 25$$

If we let

$$W = kM^{-1}S^*, \qquad 26$$

Therefore, the maximum value of probability of detection P_D is given by

$$\max_w P_D = Q\left(\sqrt{S_T^* M^{-1} S^*}, \sqrt{2\log\frac{1}{P_F}}\right). \qquad 27$$

From the above expression, it was explicitly realized that matrix inversions of estimates of M often are not practical in real time. Instead, a recursive relaxation algorithm that simultaneously estimates M and recursively compute W was developed using the method of steepest ascent. The value of the weight W (j+1) is determined by the relationship given by:

$$W(j+1) = W(j) + \frac{1}{2}\mu(j)\tilde{\nabla}F[W(j)] \qquad 28$$

For j=1,2,3... $\tilde{\nabla}F[W(j)]$ is the "complex gradient" and is given by

$$\tilde{\nabla}F = 2\left(\frac{W_T S}{W_T^* M W}\right)\left[S^* - \left(\frac{W_T^* S^*}{W_T^* M W}\right) M W\right] \qquad 29$$

The best choice of $\mu(j)$ is the value of a real variable μ, which maximizes the function

$$F\left[W(j-1)+\mu\tilde{\nabla}F(W(j-1))\right] \qquad 30$$

For j = 1,2,3...

In some adaptive systems, linearization supplies the reduction in computational complexity needed to make the system practical. Therefore, a linearized version of the algorithm is given by

$$W(j-1)=W(j)+\mu a\left[S^{*}-a^{*}M(j)W(j)\right] \qquad 31$$

a is a complex scalar and $M(j)$ is the statistical estimate of the covariance matrix. To determine $M(j)$, the input data is assumed to be the sequence of independent vector $Z(j)$ for j = 0,1,2,

In order to apply this algorithm to airborne radar, the algorithm developed is equivalently expressed as a vector different equation and the form is given by:

$$\frac{d}{dt}W(t)+\frac{\mu}{\Delta}|a|^{2}M(t)W(t)=\frac{\mu}{\Delta}aS^{*} \qquad 32$$

Δ is the radar pulse width for the airborne radar problem.

B. SMI (Sample Matrix Inversion) Algorithm [6]

Reed, Brennan and Mallet described procedure in which the convergence rate, which limits the practical usefulness of adaptive arrays systems, is most severe with a large number of degrees of adaptivity and in situations where the eigenvalues of the noise covariance matrix are widely different. A direct theory of adaptive weight computation based on a sample covariance matrix of the noise field was determined to provide very rapid convergence in all cases i.e. independent of the eigenvalue distribution. The adaptive array filter was achieved by first estimating the covariance matrix M using K samples. Next, this estimate $\hat{M}$ of M is inverted to form finally the filter weight given by:

$$\hat{W}=K\hat{M}^{-1}S. \qquad 33$$

In order to obtain the estimate $\hat{M}$ to substitute for M *above of the optimum filter* W_o, one uses the maximum likelihood principle. The maximum likelihood estimate of M is given by:

$$\hat{M}=\frac{1}{K}\sum_{j=1}^{K}X^{(j)}X^{(j)^{*}}$$

$$=\frac{1}{K}\sum_{j=1}^{K}\left(x_r^{(j)}\bar{x}_s^{(j)}\right) \qquad 34$$

where $x_r^{(j)}\bar{x}_s^{(j)}$ denotes the elements in the rth row and sth column of matrix $X^{(j)}X^{(j)^{*}}$. This result is obtained by maximizing the algorithm of the likelihood function

$$L = P\left(X^{(1)}, X^{(2)}, \ldots\ldots X^{(K)}\right). \qquad 35$$

$\hat{M}$ is called the sample covariance matrix. The output signal-to-noise ratio, conditioned on $\hat{W}$, is given by:

$$\left(S/N \middle| \hat{W}\right)_0 = \left[E\left(\hat{y}\middle|\hat{W}\right)\right]^2 / Var\left(\hat{y}\middle|\hat{W}\right)$$

$$= \left(S^{*}\hat{M}^{-1}S\right)^2 \Big/ \left[\left(S^{*}\hat{M}^{-1}M\hat{M}^{-1}S\right)\right] \qquad 36$$

and the signal-to-clutter ratio [the signal-to-noise ratio] is then given by:

$$S/C = \left|\hat{W}^{*}S\right|^2 / \hat{W}^{*}M\hat{W} \qquad 37$$

Formation of the sample covariance matrix requires $SN\ (N+1)/\ 2$ complex multiplication, where S is the number of samples required for convergence and N is the total number of weights, i.e. antenna elements times pulses for a space time processor. To invert the matrix requires $(N^3/2 + N^2)$ complex multiplication, and to form each set of weights requires another N^2 multiplication. If only one set of weights is required, i.e., no filter banks or multiple beams are needed, then the weights can be found by solving the set of linear equations $W = \hat{M}^{-1}S$, which requires about $N^3/6$ complex computations. Forming a sample covariance matrix and solving for the weights provides a very fast convergence. This rate is dependent only on the number of weights and is independent of the noise and interference environment.

In another paper [14], Brennan *et al* discussed the ability of airborne moving target indication (AMTI) radar to reject clutter is often seriously degraded by the motion of the radar. The AMTI technique adapts the element(s) weights to compensate for the near-field scattering. Array excitation errors due to phase or amplitude differences between channels are sensed and compensated automatically in the adaptive AMTI system. The system has the capability of nulling discrete active interference sources without significantly degrading the AMTI performance.

Three well-known methods of approximating M^{-1} (sample covariance matrix, updated inverse, and adaptive loops) are compared. It was shown that adaptive loops (or gradient techniques) show poor convergence. The updated inverse algorithm is given by

$$\hat{M}^{-1} = \frac{1}{1-\alpha}M^{-1} - \frac{\alpha}{1-\alpha}\frac{\hat{M}_{t-1}^{-1}X_t X_t^H \hat{M}_{t-1}^{-1}}{1-\alpha+\alpha X_t^H \hat{M}_{t-1}^{-1}X_t} \qquad 38$$

The inverse sample covariance matrix is

$$\hat{M}^{-1} = \left(\frac{1}{t_{max}} \sum_{t=1}^{t_{max}} X_t X_t^H \right)^{-1} . \qquad 39$$

It was shown that the inverse sample covariance matrix is slightly better than the updated inverse algorithm. However, the gain maximum is reached in both cases after the same number of iterations (or data vectors X_t). The updated inverse algorithm needs about $(NM)^2$ operations per iteration step, whereas the number of operation required for inverse sample covariance matrix is greater than $(NM)^3$. The important step in using the updated inverse algorithm is the product $Y = M^{-1} X_t$, which is used for updating M^{-1} and is the filter operation at the same time. Y has to be multiplied by a combined beamformer/DOPPLER filter matrix, which can easily be realized by a double FFT (space and time) if a linear array with equidistant sensors and equidistant pulses are used.

C. *Generalized likelihood Processing*

The work of Wang and Cai in [30,41] pointed out that for the cases of limited training-data set the use of localized adaptive processing is almost mandatory, and they showed that localized adaptive processing can actually outperformed fully adaptive processing in nonstationary environments. They studied the problem of achieving the optimum moving target indicator (MTI) detection performance in strong clutter of unknown spectrum when the set of data available to the estimation of clutter statistics is small due to a severely non-homogeneous environment. They proposed an adaptive implementation called Doppler domain localized generalized likelihood processor and its detection performance was studied. They presented a processor refereed to as joint-domain optimum processor and which such as the adaptive algorithms such as the sample-matrix-inversion (SMI) can approach, the generalized likelihood (GLR) and the modified SMI. They picked the GLR because it offers the desirable embedded CFAR feature as well as robustness in non-Gaussian clutter/interference. The $N_l th$ order GLR processor performs adaptive filtering and threshold detection on the N_l bins of the *l*th group (i.e. angle- Doppler bins around the look direction) with the test statistics given by:

$$\eta_{nm}^{(l)} = \frac{\left| Vec\left(S_{nm}^{(l)}\right)^H \hat{R}_l^{-1} Vec(\chi_l) \right|^2}{Vec\left(S_{nm}^{(l)}\right)^H \hat{R}_l^{-1} Vec\left(S_{nm}^{(l)}\right) \left[1 + Vec\left(\chi_l^H\right) \hat{R}_l^{-1} Vec(\chi_l) \right]} \qquad 40$$

$$\hat{R}_l = \sum_{k=1}^{K} Vec(\gamma_{lk}) Vec(\gamma_{lk})^H \qquad 40a$$

and $S_{nm}^{(l)}$, $N_{ll} x N_{so}$, is the signal-steering matrix in the angle-Doppler domain for the *nm*-th bin of the *l*th

GLR. The probability of detection at the *nm*th bin of the *l*th is found to be

$$P_d^{(l)}(n,m) = \int_1^0 P_{d/\rho}^{(l)}(n,m) f_{nm}^{(l)}(\rho) d\rho \qquad 41$$

The probability of false alarm for all bins in the *l*th GLR is given by

$$P_f^{(l)} = \left(1 - \eta_0^{(l)}\right)^{K-N_l+1}. \qquad 42$$

Three facts can be concluded from the GLR approach: 1) The ability to de-couple the degrees of freedom necessary for handling suppression from data dimension was possible through the transformation of data from space-time to angle-Doppler domain, 2) The degrees of freedom necessary for handling clutter suppression at each angle-Doppler bin is much smaller and 3) The clutter components on all angle-Doppler bins can now be correlated, with closer bins having higher correlation in general. Klemm [17,18] in his paper described an adaptive airborne MTI (AMTI) which is based on the principle of two-dimensional radar signal processing. He suggested that the back-scattered echo field have to be sampled in space and time.

Space-Time sampling is necessary because ground clutter echoes are Doppler-colored and depend on two parameters (azimuth and clutter velocity). His method is a generalization of the well-known sidelobe canceled technique to two-dimensional (space-time) sampled field. Before clutter suppression the received echo samples of all sensor outputs are transformed into a vector space of much lower than *NM*. This is done by use of auxiliary channels matched in space and velocity to the clutter returns. Clutter rejection is carried out in the reduced vector space. In another paper [15] he described a technique of adaptive clutter suppression for airborne phased array radar. A statistical model of clutter returns as received by airborne phased array antenna is given. The model consists simply of the space-time covariance matrix samples is given in the literature.

The spatial information is contained in the submatrices $M(\tau)$, whereas the temporal information lies between them. The individual elements of M are given by integrals of the form

$$m'_{ik\tau} = m(\tau) \int_{\phi=0}^{\pi} H^2(\phi) F(\phi,\tau) C_D(\phi,v,\tau) C_s(\phi,\tau) d\phi \qquad 43$$

where C_D is the phase change due to the Doppler effect in the interval τ and C_s is the phase difference due to the relative geometric displacement of target i at time t and element k at time t + τ. Once the clutter covariance matrix is obtained, one may get a first impression of the nature of the clutter echoes by calculating a power spectrum given by:

$$P(v,\phi) = W^H(v,\phi) M W(v,\phi) \qquad 44$$

with $W(\nu,\phi)$ being a space-time steering vector with elements given by:

$$W_{ikn}(\nu,\phi) = \exp(j2\pi\phi_D(\nu)nT)\exp\left[j\frac{2\pi}{\lambda}(x_i\cos\phi\sin\theta + y_k\sin\phi\sin\phi)\right]_{45}$$

where T is the pulse-to-pulse interval. The above expression for power spectrum gives a poor resolution. For a high resolution, the power spectrum is given by:

$$P(\nu,\phi) = \frac{1}{\left|W^H(\nu,\phi)ME\right|^2} \qquad 46$$

with E being a unity vector.

In [22], Short presented a digital realization of an adaptive clutter-locking MTI canceler. The technique proved to be effective in tracking and canceling a unimodal clutter spectrum. The probability of detection was

derived analytically for the adaptive canceler. Averaging this detection probability over all possible target Doppler frequencies, the average probability of detection was found as a function of the input target-to-clutter ratio.

D. Statistical Hypothesis Testing

By using the techniques of statistical hypothesis testing, it was shown that the test exhibits the desirable property that its probability of false alarm (PFA) is independent of the covariance matrix of the actual noise encountered. It was shown that the effect of signal present depends only on the dimensional parameters of the problem and a parameter, which is the same as the *SNR* of a colored noise match filter. It was emphasized that the output of the likelihood ratio algorithm is a decision on signal presence and not a sequence of processed data samples from which the interference component has been nulled and in which actual signal detection remains to be accomplished. For this reason, the direct application of the algorithm to a real radar problem would require the storage of data from an array of inputs (such as adaptive array system), perhaps also sampled to form range-gated outputs for each pulse and collected for a sequence of pulses (such as those forming a coherent processing interval). Under two data sets: 1) primary data which contains the signal and noise interference and 2) secondary data which contain only noise interference, he obtained the likelihood ratio test in the form:

$$\max_b \ell(b) = \frac{\|T_0\|}{\max_b \|T_1\|} > \ell_0 \qquad 47$$

where $T_0 and T_1$ are given in [12] and b is an unknown complex scalar amplitude.

The probability of detection for their test is given by:

$$P_D = 1 - \frac{1}{\ell_0^L} \sum_{k=1}^{L} \binom{L}{k} (\ell_0 - 1)^k H_k\left(\frac{a}{\ell_0}\right). \qquad 48$$

In this formula, the H functions are the expected values of the Gs:

$$H_k(y) = \int_0^1 G_k(ry) f(r) dr, \qquad 49$$

where $G_k and f(r)$ are given in the reference. The performance of the likelihood ratio test depends only on the dimensional integers N and K and the SNR parameter a. The latter is a function of the true signal strength and the intensity and character of the actual noise and interference.

IV. NEURAL NETWORK APPROACH

In real-time, the presence of changing environment such as clutter and uncorrelated noise ensures that W may be invertible. Moreso, the beamforming problem defined in (15) and (16) is indeed a complex-value constraint quadratic problem, which cannot be solved by neural network directly. In order to meet the requirement of neural network-based optimizer, one should convert it into a real-value constrained quadratic programming formulation. A detailed analysis and illustration of this formulation is given in [34]. To allow a beamformer to respond to a rapid time-varying environment, the weights should be adaptively controlled to satisfy (24) in real time. Meanwhile, the evaluation of these weights is computationally intensive and can hardly meet the real-time requirement.

Artificial Neural Networks lend themselves nicely to problem of segmentation of radar images based on the classification of measurements of FLAR as their 'model freedom' and capacity to learn from labeled training data can help overcome the lack of sufficiently accurate statistical models for real world radar measurements. Hence, there has been a number of studies in which ANNs successfully have been applied to the classification radar signals. Backpropagation networks have already been applied successfully to the classification of radar signal, e.g. in [44], [43]. Learning vector quantization (LVQ) networks have also been applied to target classification from radar backscatter measurements [45]. Adaptive neural network have been applied to for radar detection and classification [39].

A. Back-Propagation Algorithm

Clark et al described [37] a prototype system for recognizing targets in radar images by extracting target features, compressing the data, and classifying the target using neural network. This requires a training phase and a recognition phase. Two key issues in ATR are the following :1) Making the recognition process robust with respect to image and target variations, including orientation/position, scale/size, perspective,

occlusion, contrast, background, and noise. 2) Minimizing the computational complexity of the process via data compression, so that real-time operation can be approached. The Gabor transform was used to create feature vectors for the neural network. A two-dimensional Gabor filter is the product of a Gaussian-shaped window and a complex exponential term:

$$\psi(x,y,\sigma,k_x,k_y)=\left\{\exp\frac{-(k_x^2+k_y^2)}{2\sigma^2}(x^2+y^2)\right\}\exp\left(j(k_x x+k_y y)\right). \qquad 50$$

where *(x,y)* are the variables representing position in spatial domain, (k_x,k_y) are the wavenumber, corresponding to spatial frequencies, and σ is the Gaussian window parameter. The Gabor transform $G(x,y)$ of the radar image $\mathrm{I}(x,y)$ is then defined as the convolution of a Gabor filter $\psi(x,y)$ with $\mathrm{I}(x,y)$:

$$G(x,y)=\psi(x,y)**\mathrm{I}(x,y). \qquad 51$$

where ** denotes two-dimensional linear convolution. The resultant image is a complex image. However, only the magnitude of the transform was used because any extra information in the phase- appears to be not worth the storage costs required to save it. Next, a data block was formed by using an ensemble of Gabor transforms. Then, feature vectors were created by selecting a column from the data block. In this application, Artificial Neural Network of backpropagation was used. The feature vectors were then used as inputs .

A neural network approach [33] to segmentation of forward-looking infrared (FLIR) and SAR imagery is reported. This approach integrates three stages of processing. First, a wavelet transform of the image is performed by projection of the image onto a set of 2-D Gabor functions. This results in multiple-resolution decomposition of the image into oriented, spatial frequency channels. Second, a neural network optimization procedure, which is based on gradient descent, is used to estimate the wavelet transform coefficients. The third stage involves a segmentation technique which is accomplished by first projecting the image onto a set of vectors, which decompose the images based on the localized orientation and spatial frequency properties of the projection vectors. The resulting coefficients are sufficient for image reconstruction and region characterization. Finally, the amplitude of the vector responses in the multiple resolution reconstruction and the density of those amplitudes are use to segment the radar image using neural network.

Haykin et al [40] constructed a neural network classifier to successfully distinguish between major classes of radar returns including weather, birds, and aircraft. This classifier incorporates both preprocessing and postprocessing approach. They presented result of an experimental studies aimed at the classification of radar clutter as experienced in air traffic control environment, described a neural network clutter classifier simulated on a Warp systolic computer. The neural network is trained with a modified version of the backpropagation algorithm. In the modified back-propagation algorithm, the weight and learning rate

updating rules are summarized as follows:

$$w_{ij}(n+1) = w_{ij}(n) + \eta_{ij}(n+1)\sum_{b=1}^{P} \delta_{bj}(n) y_{bi}(n) + \alpha \Delta w_{ij}(n-1) \quad 52$$

$$\eta_{ij}(n+1) = \eta_{ij}(n) + \Delta \eta_{ij}(n) \quad 53$$

$$\Delta \eta_{ij}(n) = \begin{cases} \beta \ldots\ldots\ldots\ldots\ldots\ldots S(n-1)D(n) > 0 \\ -\phi \eta_{ij}(n) \ldots\ldots\ldots\ldots\ldots S(n-1)D(n) > 0 \\ 0 \ldots\ldots\ldots\ldots\ldots\ldots\ldots otherwise \end{cases} \quad 54$$

$$D(n) = \sum_{b=1}^{P} \frac{\partial E_b(n)}{\partial w_{ij}(n)} \quad 55$$

$$S(n) = (1-\theta)D(n) + \theta S(n-1). \quad 56$$

The detailed description and implementation of this algorithm is in [40].

B. Self-Adaptive Recurrent Algorithm [38]

Ziemke presented an approach to segmentation and integration of radar images using a second-order recurrent artificial neural network architecture, which consisted of two subnetwork: a function that classifies radar measurement into different categories of objects in sea environment, and a context network that dynamically computes the function network's input weights. For the purpose of target classification basically three major values/features, reflecting the characteristic of the illuminated object or area, can be extracted from theses radar spectra [43]. These are radial velocity, intensity and spectrum width.

Training of SARN takes place in each time step as follows:

1) propagate input forward through the function network to calculate output vector,
2) compare output vector to target vector,
3) backpropagate the error (difference between actual and desired output) through the function network to update W and input weights,
4) use new input weights as target output for the context network, i.e. backpropagate error (difference between update and previous weights) through the context network to update,
5) propagate state unit values forward through the context to calculate next time step's input weights.

V. CONCLUSION

The objective of this report has been to perform literature review and put into perspective the existing methods of detection and identification of target(s) signal in a nonstationary environment with interference background use in forward-looking airborne radar signal processing. In such an environment, the origin of the measurements can be uncertain: they could have come from the target(s) of interest or clutter or false alarm or be due to the background. Particular attention is paid to the existing method(s) and it's use in and applicable

to FLIR airborne radar signal processing problems.

VI. FUTURE WORK

Analysis of candidate methods using synthetic data will be performed by computer simulation. Understanding will follow this; preprocessing and reformatting of real data which will take us into an extensive simulation of learning methods using real data.

REFERENCES

1. Skolnik, M., "Radar Handbook" *(McGraw-Hill, 1970), pp. 18.1-18.16*
2. W. Tam and D. Faubert, "Displaced phased center antenna clutter suppression in space based radar applications," *Proceedings of Radar '87, IEE conference publication 281, pp. 385-389*
3. Brennan and I S. Reed, "Theory of adaptive radar" *IEEE Trans. on Aerospace and Electronic Systems, vol. AES-9, March, 1973*
4. Reed, J. D Mallett, I. E. Brennan , " Rapid Convergence rate in adaptive arrays" *IEEE Trans. on Aerospace and Electronic Systems, vol. AES-10, No 6, March, 1974*
5. S. P. Applebaum, "Adaptive array," *IEEE Trans. Antennas Propagate. vol. AP-24, pp. 585-598, Sept. 1976.*
6. B. Widrow and S. Stearns, *Adaptive Signal processing. Englewood Cliff, NJ: Prentice-Hall; 1985*
7. J. G. McWhirter and T. J. Shepherd, "Systolic array processor for MVDR beamforming," *Proc. Inst. Elec. Eng., vol. 136, pt. F, no. 2, Apr. 1989*
8. W. M. Gentleman and H. T. Kung, "Matrix triangularisation by systolic array," *Proc. SPIE, Real time signal processing IV, 1981, p.298*
9. Andrews, G. A., "Radar pattern design for platform motion compensation", *IEEE Trans., 1978, AP-26, pp. 566-571*
10. Zeger, A. E, and Burgess, L. R., "A adaptive AMTI radar antenna array". *NAECON 74 record, pp. 126-133*
11. Chapman, "Adaptive Arrays and Side-lobe Cancellers: A Perspective," Microwave J., Aug. 1977
12. Brennan, J. D. Mallet, I. S. Reed, "Adaptive Arrays in Airborne MTI Radar". *IEEE Trans. On Antenna and Propagation, vol. AP-24, No. 5 September 1976*
13. Boroson, "Sample Size Consideration for Adaptive Arrays". *IEEE Trans. on Aerospace and Electronic Systems, vol. AES-16, No. 4, July, 1980*
14. R. Klemn, Dr. Ing, "Adaptive clutter suppression for airborne phased array radar", *IEE Proc., vol. 130, Pts. F and H, no. 1,* February *1983*

15. R. Klemn, Dr. Ing, "Adaptive Airborne MTI: an auxiliary channel approach", *IEE Proc., vol. 134, Pts. F, no. 3,* June *1987*

16. J. Ender and R. Klemn, Dr. Ing, "Airborne MTI via digital filtering", *IEE Proc., vol. 136, Pts. F, no. 1,* February *1988*

17. Kelly, "An Adaptive Detection Algorithm", *IEEE Trans. on Aerospace and Electronic Systems, vol. AES-22,No. 1, March, 1986*

18. Short, R. D., "An Adaptive MTI for Weather Clutter suppression", *IEEE Trans. on Aerospace and Electronic Systems, vol. AES-18, No 5, September, 1982*

19. Kelly, "Performance of an Adaptive Detection Algorithm; Rejection of Unwanted Signals", *IEEE Trans. on Aerospace and Electronic Systems, vol. AES-25, No 2, March, 1989*

20. Dickey, M Labitt, F. M. Staudaher, "Development of Airborne Moving Target Radar for Long Range Surveillance", *IEEE Trans. on Aerospace and Electronic Systems, vol. AES-27, No 6, November 1991.*

21. Kalson, "An Adaptive Array detector with Mismatched Signal Rejection" *IEEE Trans. on Aerospace and Electronic Systems, vol. AES-28, No 6, No. 1 January. 1992.*

22. Feldman, L J. Griffiths, " A Projection Approach for Robust Adaptive Beamforming", *IEEE Trans. On Signal Processing, vol. 42, No. 4 April 1994*

23. Addio, M. Di Bisceglie, S. Bottalico, "Detection of Moving Objects with airborne SAR", *Signal Processing 36 (1994) 149-162*

24. Wang H., L. CAI, "On Adaptive Spatial-Temporal Processing for Airborne Surveillance Radar Systems", *IEEE Trans. on Aerospace and Electronic Systems, vol. AES-30, No. 3 July. 1994*

25. Barile. R.L. Fante. J. A. Torres. "Some Limitation on the Effectiveness of Airborne Adaptive Radar" *IEEE Trans. on Aerospace and Electronic Systems, vol. AES-28, No 28, October. 1992*

26. Wang. L. CAI. "On Adaptive Spatial-Temporal Processing for Airborne Surveillance Radar System". *IEEE Trans. on Aerospace and Electronic Systems, vol. AES-28, No 30, July. 1994*

27. P G Richardson "Analysis of the Adaptive Space Time Processing Technique for airborne radar", *IEE Proc.-Radar, Sonar, Navig, vol. 141, No. 4, August 1994*

28. J. Ward, "Space-Time Adaptive Processing for airborne radar," MIT, Technical Report 1015, DEC 1994

29. D. W. Tank and J. J. Hopfield, "*Simple 'neural' optimization network: An A/D converter, signal decision circuit, and a linear programming circuit," IEEE Trans. Circuit Syst., vol. CAS-33, pp. 533-541, May 1986*

30. L. O. Chua and G. N. Lin. "Nonlinear programming without computation," *IEEE Trans. Circuit Syst., vol. CAS-31, PP 182-188, Feb. 1984.*

31. M. P. Kennedy and L. O. Chua, "Unifying the Tank and Hopfield linear programming network and the canonical nonlinear programming circuit of Chua and Lin," *IEEE Trans. Circuit Syst., vol. CAS-34, pp. 210-214, Feb. 1987.*

32. —, "Neural network for nonlinear programming," *IEEE Trans. Circuit Syst., vol. 35, pp. 554-562, May 1988.*

33. H. Beck, D. Bergondy, J. Brown and H. Sari-Sarraf, " Multiresolution Segmentation of Forward Looking IR and SAR Imagery Using Neural Networks," *NASA/CCDS AV SPI, WNN-AIND 91.*

34. Po-Rong Chang, Wen-Hao, and Kuan-Kin Chan, "A Neural Network Approach to MVDR Beamforming Problem," *IEEE Trans. on Ant. and Propagate., vol. 40 no. 30, March 1992*

35. Jon. P. Davis and W. A Schmidt, " Use of Partial Templates with Higher-Order Neural Nets for 2-D Target Detection., *NASA 'CCDS AV SPI, WNN-AIND 91*

36. Y. Hara, R. G. Atkins, S. H. Yueh, R. T. Shin, and J. A. Kong. "Application of Neural Networks to Radar Image Classification," *NASA 'CCDS AV SPI, WNN-AIND 91.*

37. G. A. Clark, J. E Hermandez, B. S Lawver and R. J. Sherwood, " Gabor Transform and Neural Network for Automatic Target Recognition," NASA/CCDS AV SPI WNN-AIND 91

38. T. Ziemke, "Radar Image Segmentation using Self-Adapting Recurrent Network," University of Skovde, Skovde, Sweden

39. S. Haykin and T. K Bhattacharya, 1992 "Adaptive radar detection using supervised learning networks," *Computational Neuroscience Symposium, pp. 35-51, Indiana University-Purdue University at Indianapolis*

40. S. Haykin and C. Deng, 1991. "Classification of radar clutter using neural network," *IEEE Trans. on Neural Networks 2, 589-600.*

41. J. A Anderson, M. T. Gately, P. P. Andrew, and D. R. Collin, "Radar Signal Categorization Using a Neural Network," *Proceeding of IEEE, 78(10), 1646-1657*

42. B. Kosko (1992) "Neural Network for signal processing," *Prentice Hall, Englewood Cliffs*

43. M. Madrid, Juan., Casar Corredera, Jose. R., and de Miguel Vela, G (1992), "A Neural Network approach to Doppler-based target classification," *IEEE International Radar Conference 'RADAR 92'. 450-453*

44. S. C. Ahalt, F. D. Garner, I. Jouny, A. K. Krishnamurthy "Performance of Synthetic Neural Network Classification of Noisy Radar Signals," *D. S. Touretzky (ed) Advances in neutral information processing systems I, Morgan Kauffmann, San Mateo, 281-288, 1989.*

45. O. R. Hager, "Object detection in clutter with learning maps," *SPIE Synthetic Aperture Radar, vol. 1620, 170-186, 1992*

RAPID MODELING FOR AIRCRAFT DESIGN SYNTHESIS

Robert M. Taylor
Graduate Student
Department of Mechanical Engineering

Purdue University
1288 Mechanical Engineering Bldg
West Lafayette, IN 47906

Final Report for:
Graduate Student Research Program
Wright Laboratory

Sponsored by:
Air Force Office of Scientific Research
Bolling Air Force Base, DC
and
Wright Laboratory

July 1997

RAPID MODELING FOR AIRCRAFT DESIGN SYNTHESIS

Robert M. Taylor
Graduate Student
Department of Mechanical Engineering
Purdue University

Abstract

A method for rapid structural analysis was developed and implemented within an aircraft design synthesis environment. The design environment is comprised of aircraft design objects built from an object-oriented knowledge-based modeling environment. In order to provide a useful and usable design environment, it was desirable to develop methods to rapidly evaluate and resize concepts. This paper focuses on the implementation of the structural model for the design environment. This model utilizes a parametric deformation function to relate global and local displacements.

RAPID MODELING FOR AIRCRAFT DESIGN SYNTHESIS

Robert M. Taylor

Introduction

Current practices for sizing an aircraft design concept require either the use of historical data to predict values or time-consuming and expensive exploration of systems. Exploration of new designs proceeds on conservative guesswork and conventional wisdom. A design environment that allows the designer to depart from conventional designs while providing reliable evaluation of concepts would be a valuable tool. An example of the need for such a design environment can be found in the current interest in uninhabited combat air vehicles (UCAV).

Current historical design models are based on piloted vehicles. Without a human on board, the design constraints change completely. Loads are limited entirely by the structure, not human tolerance. Layout does not revolve around a cockpit, allowing unconventional placement of fuel, ducts, or weapons. Top and bottom of the aircraft can be arbitrarily assigned depending on the current phase of the mission (e.g. an inlet on the top of the aircraft can become an inlet on the bottom of the aircraft).

In order for designs to exploit these departures from convention, the designer needs to have methods and tools that do not depend on historical models. A design environment that enables an aircaft designer to rapidly layout, move, and modify structure, aerodynamic shape, control systems, engine, avionics, payload, fuel, etc. and rapidly optimize and resize could be a valuable tool for exploring configuration concepts. These design objects should be ready-to-use encapsulated objects relevant to the aircraft designer's needs. The implementation of such a design environment is feasible and in process.

Background

The development of this design environment is enabled by a knowledge-based object-oriented modeling environment which feeds information between systems and components.

Knowledge-Based Engineering

Knowledge based engineering denotes the ability of engineering tools to build knowledge about the design they are modeling and make decisions based on this knowledge. Decisions can be made based on rules and

procedures and knowledge can be stored in an object-oriented fashion, associating data with particular objects to which the data belongs.

Object-oriented Programming

An object-oriented programming methodology makes knowledge organization straightforward. In object - oriented programming, code is organized into structured bundles of variables, which maintain state, and related methods, which implement behavior. Characteristics of object-oriented programming include data-abstraction and inheritance. Data-abstraction denotes the encapsulation of objects from other objects. This allows details within the object which are irrelevant to other objects to stay hidden from other objects. Inheritance allows classes to receive all or part of their definition from previously defined classes allowing code to be reused. An object-oriented programming methodology results in a structured, hierarchical model that clearly displays relationships between objects. This provides a natural associativity which is desirable for geometric relationships.

Adaptive Modeling Language

Wright Labs has chosen TechnoSoft Inc.'s Adaptive Modeling Languge (AML) for development of the air-craft design configuration environment envisioned above. AML provides a packaged environment with the following features:

- **Knowledge-Based**

  AML objects can determine and maintain their state as well as change state depending on conditions of other objects.
- **Object-Oriented**

  AML provides a suite of classes, methods, and functions encompassing geometry, user-interface, and many other aspects of geometric and mathematical modeling, as well as supporting user-defined class, method, and function definitions.
- **Demand-Driven Calculations**

  Property values remain unbound until the user or method demands them. This reduces computation time because information that is not needed is not calculated.
- **Dependency Tracking**

  The model tracks properties that drive demanded properties so changes propagate through the model tree with current values.
- **Feature-Based Geometric Model**

  AML objects exist for feature-based modeling of geometry.

These features of AML have proven useful in developing a design system that is fast, modular, and non-restrictive.

Configuration Design Synthesis

Previous Work

The author joined this Configuration Design Synthesis project after it was already underway but still in its early stages. Previous work at Wright Labs included development of objects and methods for aircraft geometry layout configuration. Initial aerodynamic modeling had been performed on AML but not with the objects in this system.

Geometric Model

Within AML, the existing suite of aircraft geometry objects includes the following:

- Weapons Bay
- Engine
- Wing (covers wing, horizontal tail, and vertical tail)
- Duct
- Landing Gear

These objects provide a very basic palette from which to demonstrate the desired capability of the design environment. From these objects, a coarse airplane can emerge as shown below.

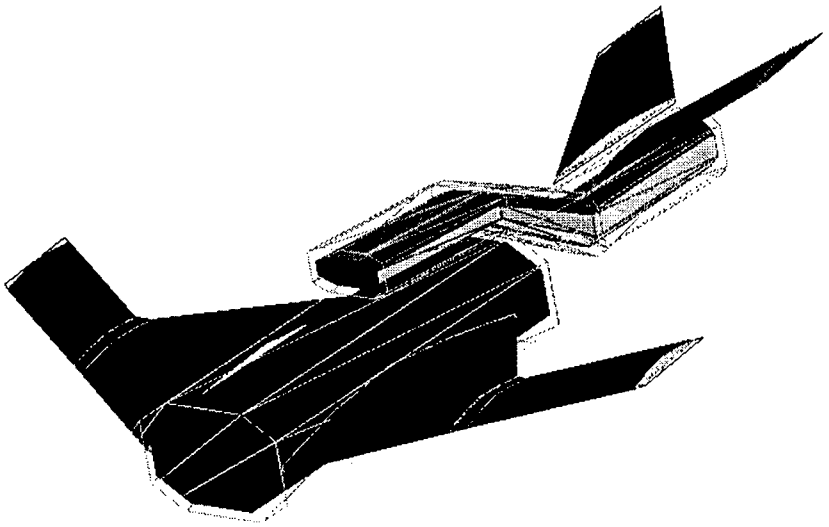

FIGURE 1. UCAV Configuration Using Aircraft Configuration Objects in AML

Faceted geometry provides a linear description of the model, requiring less computation then complex curves and surfaces. When a design is fixed and the designer wants to see a smoothed model, vertices of the faceted model can become control points of complex surfaces.

Present Scope—Structural Model

Geometry is little more than pictures unless it can be used to gain knowledge about the concept it represents. Once a designer has developed a configuration, the proposed system should then use geometric and material information to learn about the validity of the concept. Initially, this should include at least structural and aerodynamic models as well as sizing methods. Eventually, the model should be capable of learning about its manufacturability, cost, and performance.

Wright Labs has chosen to first focus on gaining structural knowledge to be gained from aircraft concepts. This summer, the focus has been development of a stiffness matrix for a wing structure. The method developed for use here is driven by several considerations. It must:

- provide very fast analysis
- preserve modularization of the model components
- allow for novel concepts to be explored

Development of Stiffness Matrix—Theory

The requirements listed above require a departure from traditional finite element analysis. This is necessary for several reasons. First, FEM requires consistent meshing between parts. This takes considerable time, care, and knowledge on the part of the designer. Also, a consistent mesh requires consistent geometric boundaries, which dictates unions or intersections of geometry that can be computationally expensive and require further definition of part relationships.

An alternative to the finite element method can be used. The wing planform can be used as the basis for deformations of structural elements. Shape functions based on a parametric definition of the wing planform surface form a deformation function.

In the chordwise direction define three quadratic shape functions for $0 < \xi < 1$ as follows:

$$f_0(\xi) = 1 - 3\xi + 2\xi^2 \tag{1}$$

$$f_1(\xi) = 4\xi - 4\xi^2 \tag{2}$$

$$f_2(\xi) = 2\xi^2 - \xi \tag{3}$$

These correspond to the deformation at each of the three points, $\xi = (0, 1/2, 1)$

In the spanwise direction define four cubic functions for $0 < \eta < 1$ as follows:

$$g_0(\eta) = -4.5\eta^3 + 9\eta^2 - 5.5\eta + 1 \tag{4}$$

$$g_1(\eta) = 13.5\eta^3 - 22.5\eta^2 + 9\eta \tag{5}$$

$$g_2(\eta) = -13.5\eta^3 + 18\eta^2 - 4.5\eta \tag{6}$$

$$g_3(\eta) = 4.5\eta^3 - 4.5\eta^2 + \eta \tag{7}$$

These correspond to the deformation at each of the four points, $\xi = (0, 1/3, 2/3, 1)$

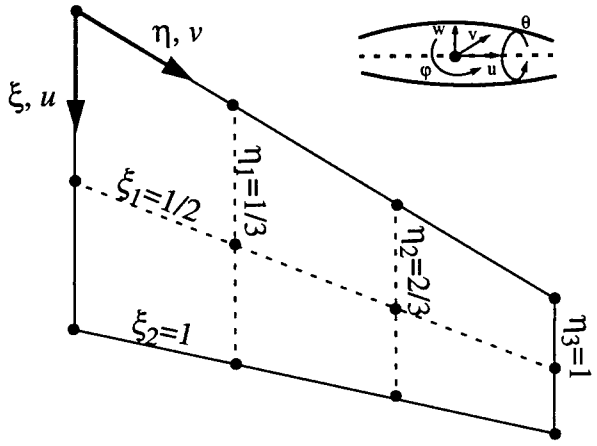

These shape functions can be used in combination to describe in-plane deformation (ξ and η directions), out-of-plane deformation, and rotations about tangents in ξ and η directions (to allow for shear deformations) as follows:

- in-plane deformation (ξ direction):

$$u(\xi, \eta) = \sum_{i=0}^{2} f_i(\xi) \sum_{j=0}^{3} g_j(\eta) u(\xi_i, \eta_j) \tag{8}$$

- in-plane deformation (η direction):

$$v(\xi, \eta) = \sum_{i=0}^{2} f_i(\xi) \sum_{j=0}^{3} g_j(\eta) v(\xi_i, \eta_j) \tag{9}$$

- out-of-plane deformation:

$$w(\xi, \eta) = \sum_{i=0}^{2} f_i(\xi) \sum_{j=0}^{3} g_j(\eta) w(\xi_i, \eta_j) \tag{10}$$

- rotation about tangents in ξ direction:

$$\theta(\xi, \eta) = \sum_{i=0}^{2} f_i(\xi) \sum_{j=0}^{3} g_j(\eta) \theta(\xi_i, \eta_j) \tag{11}$$

- rotation about tangents in η directions:

$$\phi(\xi, \eta) = \sum_{i=0}^{2} f_i(\xi) \sum_{j=0}^{3} g_j(\eta)\phi(\xi_i, \eta_j) \tag{12}$$

This allows deformations in 5 degrees of freedom at 12 control points for a total of 60 degrees-of-freedom. Constrained degrees-of-freedom, such as at the root of the wing are not allowed to deform. For current work, degrees-of-freedom at the root remain fixed, leaving 45 degrees-of-freedom.

These planform deformations describe deformations of wing surface and substructure. Wing structural members are discretized using constant strain (6 local degrees-of-freedom) membrane triangles.

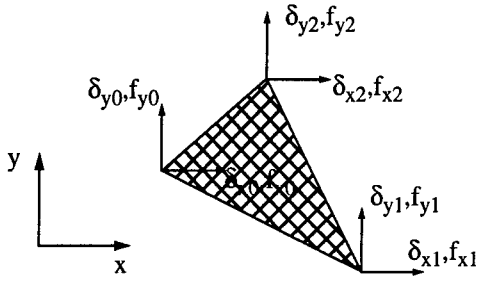

$$\{f\} = [k_M]\{\delta\} \tag{13}$$

Rather than building a patchwork of piecewise continuous local degress-of-freedom, individual stiffness matrices for triangles are formulated and transformed into a global matrix.

$$\{\delta\} = [T]\{q\} \tag{14}$$

The transformation matrix relates global deformation to local deformation. It is formed by looping through *j* possible global deformations using unit displacements. For each global deformation, each triangle has a local displacement at each of three vertices. For each triangle take the dot product of the displacement with each of the two local basis vectors at each corner. This gives six values to be placed in the *j*th column of the transformation matrix. Looping through j allowable deformations, eliminating constrained degrees-of-freedom, produces a 6 x *j* matrix. This transformation matrix then maps a triangle local stiffness matrix to an expanded stiffness matrix.

$$[K] = [T]^T[k_M][T] \tag{15}$$

Summing all triangle expanded stiffness matrices produces a global stiffness matrix for the entire wing.

$$[K_S] = \sum_{n=0}^{m} [K_n] \tag{16}$$

Applied forces are transformed into generalized global forces which we define as follows:

$$\{Q\} = [T]^T\{f\} \tag{17}$$

Finally, the system stiffness equation is as follows:

$$\{Q\} = [K]\{q\} \tag{18}$$

Development of Stiffness Matrix—Implementation

Implementation of this rapid structural modeling technique is straightforward in AML. A wing object class definition already exists from earlier work done for geometric modeling of the aircraft design configuration environment. The wing object is comprised of one or more wing panel objects. Individual wing panel objects have properties such as airfoil, sweep, inboard and outboard chord, twist, dihedral, etc. Wing panel objects also define a list of surfaces which describe the skin geometry. The structural model takes planform corner points and this surface list from the wing panel object to define a mesh object.

Structural Deformation

Using the planform corner points, the mesh object creates a panel which connects these points linearly. This panel has u and v parameters with $0 < u, v < 1$. The panel has a property which drives the number of divisions of the panel in u and v. It then develops grid points in u and v parameter directions. At each grid point the panel computes normals and tangents in u and v directions. It then intersects these normals with the surfaces in the surface list and computes the distance to the top and bottom surface at each point.

The mesh object panel has a deformation function which uses the shape functions presented earlier. Each grid point has u and v coordinates which are input to the deformation function to determine the deformation in each degree of freedom at the given grid point. A grid point translates and its normal vector rotates as calculated by this deformation function. The grid point adjusts its distance to the top and bottom surfaces by dividing the original distance to surface by the cosine of the angle between rotated normal and original normal. The deformed surface point location is this adjusted distance from the translated grid point along the rotated normal vector . Each surface point now has a deformed surface point associated with it. Subtract position vectors of the original surface point from the deformed surface point to obtain the displacement vector at this surface point.

Each grid point now has associated properties as follows:

- original position
- normal vector
- two tangent vectors
- surface point (top and bottom surfaces)
- distance to each surface point (top and bottom surfaces)

- translated position (du,dv,dw)
- rotated normal vector (rot-u, rot-v)
- adjusted distance to surface points (top and bottom surfaces)
- deformed surface points (top and bottom surfaces)
- displacement vector (top and bottom surfaces)

The wing panel can now display any arbitrary deformation input (e.g. a mode shape)

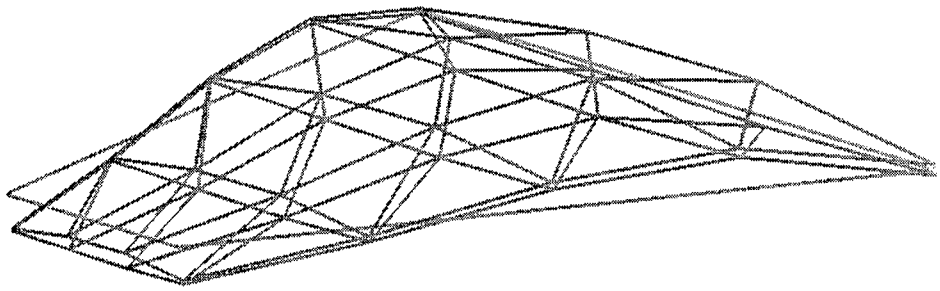

FIGURE 2. Example Mode Shape Deformation

The mesh object can deform substructure using the same procedure. Substructure objects lie in the wing panel object's panel surface. The panel's u and v parameters describe start, end, and intermediate control points. Only one parameter is needed to discretize curvilinear substructure and points along the path can translate like the points in the panel. Normals from points along this structure can intersect wing panel surfaces and rotate just like the grid points in the mesh panel.

Mesh Formulation

Structural objects now define triangles from the grid of surface points and associate previously calculated displacements for each vertex. Each triangle forms a two-dimensional coordinate system in its plane and can construct its own local stiffness matrix at this point from material properties, vertex locations, and this local cordinate system. The stiffness formulation used here is for a constant strain (6 dof) triangle with a plane stress assumption. Each triangle now needs a transformation matrix to relate its local stiffness matrix to the global stiffness matrix.

To formulate transformation matrices, the mesh loops through *j* possible unconstrained deformations. For each vertex *i* of each triangle, it takes the dot product of the displacement at vertex *i* with the two basis vectors that form the local two-dimensional coordinate system. These six values go into the *j*th column of the transformation matrix.

Each triangle now has associated properties as follows:

- 3 vertices
- 3 displacements
- material properties
- 6 x *j* transformation matrix

Stffness Matrix Formulation

Currently, each triangle formulates its local stiffness matrix during formulation of the global stiffness matrix. To formulate the global stiffness, loop through *n* triangles. For triangle *n* calculate a local stiffness matrix, pre- and post-multiply this matrix by the triangle's transformation matrix to expand into the global stiffness matrix, and keep a running sum of all expanded stiffness matrices. This sum is the global stiffness matrix for the wing object.

Future Work

In the near future, Wright Labs plans to increase the modeling capabilities of the Aircraft Design Configuration Environment. Work will continue in structural modeling as the described method is validated and extended to objects in addition to the wing. Aerodynamic modeling will be incorporated through panel or vortex lattice methods. Also, the design environment is expected to connect with concurrent work being done in AML on mission requirements, sizing, and weights. Ultimately, Wright Labs envisions the design environment to provide cost and manufacturability modeling with the ability to optimize for these.

References

[1] Blair, Max, et al, "Rapid Modeling with Innovative Structural Concepts" to be presented at 39th AIAA/ ASME/ASCE/AHS/ASC Structures, Structural Dynamics, and Materials Conference, Long Beach, CA, April 20-23, 1998.

DATA SIMULATION SUPPORTING RANGE ESTIMATING FOR RESEARCH AND DEVELOPMENT ALTERNATIVES

Laura Williams
Undergraduate
School of Civil and Environmental Engineering
Construction Engineering and Management

Georgia Institute of Technology
Atlanta, GA 30332-0335

Final Report for:
Graduate Student Research Program
(97-0416)
Wright Laboratory
Air Base Technology Branch
WL/FIVC-OL

Sponsored by:
Air Force Office of Scientific Research
Bolling Air Force Base, DC

and

Wright Laboratory
Air Base Technology Branch
WL/FIVC-OL

August 25, 1997

DATA SIMULATION SUPPORTING RANGE ESTIMATING FOR RESEARCH AND DEVELOPMENT ALTERNATIVES

Laura Williams
Undergraduate
Department of Civil and Environmental Engineering
Construction Engineering and Management
Georgia Institute of Technology

Abstract

Development of a range estimating methodology using neural nets was attempted this summer. Data needed to compile that would be used by the neural net to determine the sensitivity of model variables in PACES. The procedure for generating direct cost estimates consisted of definition of project and facility, selection of model type, parameter definition, and calculation of quantities ad direct cost. By utilizing these four steps and only varying the parameters of total square footage, floors above and below grade, and the building location, the direct costs varied significantly.

DATA SIMULATION SUPPORTING RANGE ESTIMATING FOR RESEARCH AND DEVELOPMENT ALTERNATIVES

Laura Williams (97-0416)

INTRODUCTION:

One of our summer research goals was to develop a range estimating methodology using neural nets to determine the sensitivity of model variables in PACES with respect to direct costs. Developing this methodology given a "clean" and "safe" data set, we could apply it a complex, multivariant problem such as robot digging unexploded ordnance. To accomplish this objective, a collection of facility estimates needed to be compiled which would serve as inputs for the neural net. For testing the neural net capabilities with respect to our goal, a mini-trial was run using 1200 cost estimates generated by PACES for a general administrative building. These cases were run modifying a few of the varied parameters within the models of PACES and the estimated direct costs were reflective of multi-sized general administrative buildings in all fifty states. The only parameters manipulated that directly affected direct costs were the total square footage, floors above and below grade, and the building location (i.e. state). The process for compiling this data is illustrated in the following section along with the systematic approach PACES uses to generate a direct cost estimate.

PROCEDURE:

Definition of Project and Facility:

In an effort to provide a data set for the neural net, direct cost estimates for twelve thousand facilities were generated using the Air Force Parametric Cost Engineering System. The first step in using PACES is creating a project and then a facility, by entering data into key fields. Key fields in the project addition process include project

description, project location, service branch, and cost file fields. The project description is a reference tool that is used to identify the project at any time, and this description appears on all reports generated by PACES for record-keeping purposes. The project location field identifies where the project is located. This location had a direct effect on the direct cost estimate in terms of applying a location cost modifier. For our research, the state average was chosen for each of the 50 states. The service branch data field is utilized to determine the escalation modifier within the cost estimate. The cost file field tells the user and the software which cost data is being used.

After a project has been added, a facility may then be created under the project. There are several important key fields for adding a facility. They include facility type, model type, and category code. The facility type is similar to the project description in that it is used as a reference tool for future use and it also appears on all reports for the facility generated by PACES. The model type describes the type of construction. PACES has 5 model types: Building models, Sitework and Utilities models, Runway/Taxiway model, Renovation model, and Contractor and Overhead Profit model. For our research, we chose to study a Building model. The category code is used for tracking Congressional appropriations and for accounting purposes.

After the project and facility has been added and defined, construction of the cost estimate can then begin.

Selection of model type:

The next step in the PACES estimating process is selecting a model type. As mentioned above, our data focused on a Building model. Within the Building models is a selection of 78 predefined building models. From this large group, we chose to study a

general administrative facility model from the administrative facilities group. We selected an administrative building because it is a fairly standard model that applies to both the military and commercial industry. An administrative building is also a typical structure being built in today's commercial boom that is flexible with its floors and square footage.

Parameter Definition:

The third step in the estimating process is defining facility parameters. Parameter definition is used to develop quantities of construction material and work items required to construct a facility. Within the PACES models are 7 various parameters including required parameters, secondary parameters, location modifiers, functional space areas, quantity parameters, descriptive parameters, and density parameters by functional space areas. Due to the infinite combinations possible by modifying all 7 parameters, this study only varied the required parameters for each facility. Required parameters include total facility scope, facility full scope, facility half scope, facility total scope, actual full scope, actual half scope, gross floor area, number of stories above grade, and number of stories below grade. These required parameters are the minimum amount of information required for calculate secondary parameters and assembly quantities and are utilized in generating direct costs. The total facility scope parameter is really the only required parameter as the remaining required parameters are defaulted from this user entry. For each of the fifty states in the US, estimates for various sized general administrative buildings were generated. The facility sizes ranged from 50,000 SF increasing increments of 10,000 SF to 100,000 SF. For each size facility in each state, the default floors above and below grade were manipulated to form combinations of 1 or 2 floors

above grade with 0 or 1 floor below grade. By varying the square footage and floors above and below grade for each facility, an array of direct costs was produced.

Consideration was given to the location modifiers defaulted from the project location field in the project definition and unique to each state. These location modifiers include seismic zones, summer dry bulbs, winter dry bulbs, and frost line depth. The seismic zone adjusts the foundation and structure design to accommodate seismic loading; the summer and winter dry bulbs determines the cooling and heating loads required by the building; and the frost line depth adjusts the depth of foundation walls.

Calculation of Quantities and Direct Cost:

The final step of the estimating process is calculating quantities and direct costs. The quantity calculation process is used to develop quantities of construction materials and work items required to construct a facility. These quantity calculations are performed in three steps and correspond to the UNIFORMAT Work Breakdown Structure (WBS). The WBS is a tree-type structure of functional systems used to classify facility components on a level by level basis. The three levels of quantity calculations corresponding to the WBS are the subsystem quantities, the assembly category quantities, and the assembly quantities. The top down approach is employed with each level having an increasing amount of detail. Quantities are calculated based on the facility parameters entered and/or accepted by the user. The models then use the assembly quantities and the M-CACES UPB database to develop the direct costs for the facilities. Direct costs are produced by multiplying the assembly quantity by the unit cost for the assembly in the database multiplied by the area cost factor. Direct costs are cost elements required to perform the actual construction of the project and include on-site construction labor,

materials, and equipment required to build the facility. Unique direct cost estimates were the outputs generated by the various inputs into the system. These direct costs finalized the data set that was to be run through the neural net.

RESULTS:

The data set contained cost estimates ranging from 2.5 million dollars to 12 million dollars. Within each state, an increase in 10,000 square feet corresponded to a rise in direct cost of one million dollars. Large estimates occurred in the 2 states located off the continental USA. These increased costs were due to transporting materials to Hawaii and Alaska and Alaska's extreme weather conditions. There was not a consistent price difference with the variation in floors above and below grade for one state.

CONCLUSIONS

For each state, 24 cases were run with 4 different variables: (1) sizes ranging from 50,000 SF to 100,000 SF in increments of 10,000 SF, (2) either 1 or 2 floors above grade in combination with (3) either 1 or 0 floors below grade, and (4) location modifiers. Cost estimate increases were directly related to increases in square footages. Cost estimates displayed no distinct pattern when adjusting the floors above and below grade for an administrative building in the same state.

BIBLIOGRAPHY

Parametric Cost Engineering System (PACES) User Manual, Version 3.1. Delta Technologies Group, Inc., Englewood, CO, 1997.

ALLYL AND PROPARGYL RESINS

Cornelious W. Williams, Jr.
Graduate Student
Department of Materials Science

University of Cincinnati
495 Rhodes Hall ML 0012
Cincinnati, OH 45221

Final Report for:
Graduate Student Research Program
Wright Laboratory

Sponsored by:
Air Force Office of Scientific Research
Wright-Patterson Air Force Base, Ohio

and

Wright Laboratory

September 1997

ALLYL AND PROPARGYL RESINS

Cornelious W. Williams, Jr.
Graduate Student
Department of Materials Science
University of Cincinnati

Abstract

The synthesis of resins were conducted using various ratios of allyl chloride and propargyl bromide reacted with cyclopentadiene. The formulation of the resins were Allyl Cyclopentadiene (ACP), 3:1 Allyl:Propargyl Cyclopentadiene (3:1 APCP), 1:1 Allyl:Propargyl Cyclopentadiene (1:1 APCP) and Propargyl Cyclopentadiene (PCP). These hydrocarbon resins were compared to existing phenolic resins for thermal stability and mechanical properties. An examination is also given of the optimum method of fiber infiltration with the allyl and propargyl resins. This examination shows that the method of prepregging used in this study is not the method most productive for fiber impregnation. The difficulties of using this impregnation method included resin escaping from the impregnation bath, excess resin dripping from the tow as the drum turned, and prepreg with little or no tack after being removed from the drum. The later of these caused hardships in cutting the prepreg into the desired lay-up angles and an inability to lay-up the plies such that they remained in laminate form. As a result, there were no cured composites which utilized the synthesized resins.

ALLYL AND PROPARGYL RESINS

Cornelious W. Williams, Jr.

Introduction

Epoxy/Carbon composites have been proven to be quite useful in various applications. Their properties, such as, high stiffness, high strength and good specific properties have lead to their uses in various applications. The same may be said of phenolic/carbon composites. Phenolics have the added attributes of good fracture toughness, low thermal expansion coefficient and high thermal emissivity. Both epoxy and phenolic resins are used to form composites with excellent electrical and chemical resistance(2). However, epoxy/carbon composites are susceptible to high water absorption (usually >5%) resulting in poor hot wet physicomechanical properties(1). In addition, when producing carbon-carbon composites, the processing of laminates with these resins often requires several iterations of resin infiltration before a dense material is formed. Consequently, a hydrocarbon resin which shows hydrophobic properties and the ability to be densified with a single resin infiltration along with mechanical properties that are comparable to epoxy and phenolic resins would be quite beneficiary. These are the attributes displayed by allyl and propargyl resins. Preliminary tests have shown that the resins are 90 to 95% carbon. Test also show a 90+% char yield in TGA experiments(3). Their inherent hydrophobicity provides enhanced hot-wet stability and long term resistance to humidity and saline environments(2). The high char yield of these resins will also make them acceptable in high temperature applications.

Experimental

Aldrich Chemical Co. provided the dicyclopentadiene, allyl chloride, propargyl chloride and propargyl bromide. The cyclopentadiene was obtained by cracking the dicyclopentadiene at 175^{o}C and condensing the vapors in a beaker in an ice bath. Solvents were used as received from Spectrum Chemical Manufacturing Corporation. Sulfuric acid was used as received from Corco Chemical Corporation.

AS-4-P-12k fibers from Hercules were used in each laminate. The laminates were made using a prepreg machine that produced a tape 6 feet in length and 1 foot wide. Panels were cut from the tape that were 6 inches by 6 inches. The thickness of the panels varied between .04 and .06 inches.

The cure analysis was conducted on the TA Instruments DSC 2920 modulated DSC. TGA analysis was conducted using TA Instruments TGA 2950 Thermogravimetric analyzer. IR analysis was performed using the Bruker IR IFS 28 Equinox. Interlaminar shear (ILS) and interlaminar tension (ILT) test were conducted on MTS servo-hydraulic mechanical analyzer. The specimen dimensions for ILS were a 4 inch length with one notch on both sides of the specimen. Each notch was .5 inches from the center of the sample. The ILT specimen were 1 inch by 1 inch squares.

Control Panels

Two different resin system were used to produce the control panels. The first was an epoxy resin, 3501-6 from Hercules. The DSC, Rheometrics and TGA of this is resin are pictured in figures 1.1, 1.2 and 1.3 respectively. One panel was produced with this resin system. This panel had dimensions of 12 inches by 12 inches. The purpose of producing this panel was to establish a base line for mechanical properties of a composite using a standard matrix.

The other control resin system utilized in this project was phenolic resin, SC1008 from Borden. Within this group, two different subsets of panels were produced. One set was made with phenolic resin

utilizing methanol as the solvent. The other set of panels was made with phenolic resin and water. The DSC, Rheometrics and TGA are pictured in figures 2.1, 2.2 and 2.3, respectivley. All of the phenolic panels produced were 6 inches by 6 inches. All control panels were cured in an autoclave under previously established cure cycles.

Control Characterization

This began with determining the resin content of the prepreg prior to beginning the cure cycle. This was necessary to determine whether or not a bleeder layer must be added to the vacuum bag lay-up during cure to remove excess resin. The physical measurements of the panels were taken before and after cure to determine the weight loss of the panel during cure. An ultrasonic C-scan was conducted to determine the quality of the panels. Then samples were cut from the panel for both acid digestion and optical microscopy. Acid digestion was used to determine the fiber, resin and void volume of the control panels. This data is given in Table 1. Microscopy evaluation showed the amount of porosity, cracking and compaction of the laminate. Interlaminar tensile (ILT) and interlaminar shear (ILS) test were conducted to establish the mechanical properties of the composites. The results from these mechanical tests are given in Tables 2 and 3, respectively. Scanning Electron Microscope (SEM) pictures were taken of the fracture surfaces of the mechanical test specimen to determine the mode of failure of the test sample.

Synthesis of Allyl Cyclopentadiene(ACP)

The procedure described may be adapted to the synthesis of the various ratios of APCP and PCP. Cyclopentadiene is cooled in an ice water bath. In a three neck round bottom flask, 50% NaOH and a quaternary salt were combined. This combination was stirred and cooled in an ice bath. The cyclopentadiene is added to the three neck flask. Now the allyl chloride is allowed to drip into the flask slowly. This slow dripping should take an hour to complete. This previous description is the point at which the synthesis of the resins varies. Instead of allowing only allyl chloride to drip into the flask, the

allyl chloride/propargyl bromide mix may be added with the appropriate ratio, by formula weight, or the propargyl bromide may be added by itself to produce the APCP or the PCP, respectively. As is the case prior to the addition of the allyl chloride and/or the propargyl bromide, the next steps in the procedure are the same for all of the various formulations of resins (3:1 A:PCP, 1:1 A:PCP, PCP).

Allow the mixture to come to room temperature and continue to stir for 6 hours. When the stirring has been completed, wash the organic phase with dilute HCl. The organic phase will be easily discernible from the aqueous phase. The washing is carried out twice with H_2O and once with a brine solution. Between each washing, allow the phases to clearly separate prior to beginning the next wash.

Composite Processing

The tow was threaded through a resin bath, silicone gasket and dye. The gasket created a flush seal with the bath to prevent the resin from escaping. The dye was used to control the amount of resin which impregnated the fibers. The fibers were wound onto the drum at a controlled rate. The traverse speed and the drum speed were altered, as needed, to prevent gapping in the tape. This method is referred to as prepregging. Once the prepreg tape was removed from the winding drum, the plies were cut from the tape in the desired direction for lay up. All panels were cured in an autoclave after lay-up.

Results and Discussion

Resin Synthesis

The FTIR spectra of the synthesized resin are given in Figure 1. These spectra are similar to those reported by Mathias and coworkers(2). The top trace is for ACP and as described by Mathias and coworkers(2) the cyclopentadiene C-H groups appear at 2976 cm^{-1}. However the peaks at 3076, 3012 , and 1640 cm^{-1} which describe allyl groups C-H stretching, another cyclopentadiene C-H group and C=C stretching, respectively, are not observed. In addition, the peaks at 994 and 908 cm^{-1} which indicate the presence of allyl group C-H out of plane bending are also not observed. The broad peak at 3337 cm^{-1},

which indicates the presence of an alcohol, may be ignored by the reader. An alcohol was used in the preparation of the sample for FTIR. The lower two spectrum are for the 3:1 and 1:1 ratios of the allyl:propargyl resins, respectively. As described by Mathias and coworkers(2) the C-H stretching at 3303 cm^{-1} and the triple bond stretching at 2124 cm^{-1} are observed. The peak at 3303 cm^{-1} is consistent with their description in that it decreased with the increase of the allyl:propargyl ratio from the 1:1 A:PCP to the 3:1 A:PCP.

Cure analysis of synthesized resins

Each of the synthesized resins were evaluated for cure cycle. These were the ACP, 3:1 A:PCP, and the 1:1 A:PCP. Figure 2 shows the DSC of the resins. Figure 2.1 is a DSC of ACP which indicates an exotherm at 152°C followed by an endotherm at 200°C and another exotherm at 220°C. The 3:1 A:PCP exotherms at 235°C, figure 2.2. The 1:1 A:PCP, figure 2.3, indicates that there is a small exotherm at 68°C and another at 220°C. These results were similar to those reported by Mathias and coworkers(2).

Rheometric analysis were also investigated as an indication to the cure cycle of the synthesized resins. The rheometric data for the ACP demonstrates a viscosity increase at 290°C, figure 3.1. The plot of the 3:1 and the 1:1 A:PCP both show viscosity increases near 225°C, figures 3.2 and 3.3 respectively. The ACP rheometric study did not coincide with the expected results for that system. A viscosity increase was anticipated between 150 and 200°C.

Thermogravimetric analysis was the final cure cycle examination made. These results were very different from those anticipated. The ACP plot, figure 4.1, indicates a constant weight loss from the beginning of the test to the end. At 500°C there was only 6% of the beginning product remaining. The 3:1 A:PCP TGA, figure 4.2, showed weight loss from room temperature to 200°C. Then there was a plateau from 200°C to 435°C. This was followed by another weight loss of 20%. There was 7% of the total weight at the end of the test.

Finally, the 1:1 A:PCP plot, figure 4.3, indicates a loss of weight of 80% from room temperature to 200°C. This is followed by a plateau, which last through the end of the test, at 20% of the original weight remaining. The heating rate for each TGA was 10°C/min.

Properties of Composites

The properties of the composites made with the synthesized resins, ACP, 3:1 A:PCP, 1:1 A:PCP and PCP will not be reported. This is due to an inability to impregnate the fibers in a manor which facilitated its lay-up. The infiltration method previously described did not prove to be the optimum method of impregnating the tow with the synthesized resins. This was the case for several reasons. Each of the synthesized resins used to impregnate the fiber in this method had a low viscosity (50 to 150 cps). Several attempts were made to use a dye with an exit diameter of 1.3 mm. These were unsuccessful since the resin merely dripped through the exit hole of the dye which meant that there was an excess getting onto the fiber and waste created with the run off. This created a prepreg which was very wet and had a resin content above the desired range of 30 to 40%. Other attempts were made using a dye which was 1.1 mm in diameter. This dye did not allow a sufficient amount of resin to infiltrate the tow. This created a resin content of 19% which is below the desired range. The tape was not tacky and could not be handled for lay-up.

Conclusion

Synthesis of the hydrocarbon resins was successful. The resins were not as sensitive to air as anticipated. The process of prepregging which takes two hours to complete in air, from winding around the drum to lay-up, did not cause the resin to cure. The DSC data on each resin also shows that the cure cycles may be conducted under relatively low temperatures. This was also confirmed by the Rheometrics experiments. However, the TGA data indicate that the weight loss of the resin is significant. Further study is needed to determine the cause of the weight loss of the resin. These

studies may include various holds and slower ramp rates to determine the condition which causes the least amount of weight loss. In addition, the prepregging impregnation method must be reevaluated as a means of transferring the resin to the fiber. Alternative methods such as resin transfer molding or dip coating may be alternatives to prepregging these low viscosity resins.

Table 1 Fiber, resin and void volume

specimen	%fiber volume	%resin volume	%void volume
cw1a(SC1008/methanol)	64.28	34.04	1.68
cw1b	63.25	34.84	1.91
cw1c	62.81	34.95	2.24
cw2a(SC1008/methanol)	66.58	32.43	0.99
cw2b	68.12	29.61	2.27
cw2c	66.66	31.98	1.36
cw3a(SC1008/methanol)	68.28	29.16	2.56
cw3b	62.16	38.11	-0.26
cw3c	58.33	43.48	-1.81
cw4a(SC1008/H2O)	65.06	32.65	2.29
cw4b	65.57	31.49	2.94
cw4c	63.14	34.42	2.44
cw5a(SC1008/methanol)	72.67	25.96	1.37
cw5b	72.57	25.72	1.71
cw5c	71.31	26.80	1.88
cw6a(SC1008/H2O)	64.04	33.18	2.77
cw6b	61.66	37.63	0.72
cw6c	42.67	62.37	-5.04
ww1(3501-6)	62.61	37.92	-0.53
ww2	63.57	36.37	0.06
ww3	62.89	37.54	-0.42
cw8a(SC1008/H2O)	62.99	33.11	3.90
cw8b	65.64	31.65	2.71

Table 2 ILT data

specimen	ultimate strength(lb./in.^{2})
CW1	727
CW2	939
CW3	1001
CW4	837
CW5	827
WW**	1775

- CW series are phenolic matrix composites
- WW series are epoxy matrix composites;

** samples did not fail

Table 3 ILS data

specimen	ultimate strength(lb./in.^{2})
CW2	776
CW3	536
CW4	547
WW	1224

Figure 3 FTIR of synthesized resins; ACP (top), 3:1 A:PCP (middle), 1:1 A:PCP (bottom)

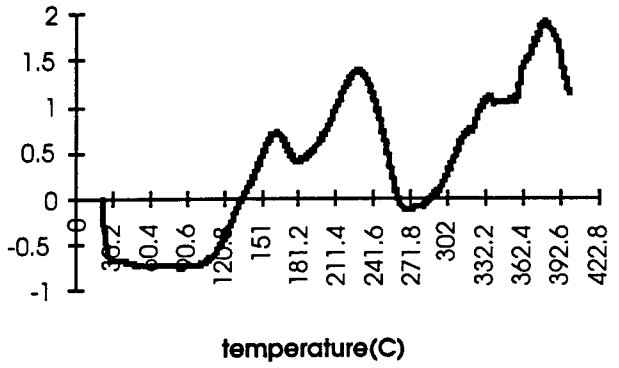

Figure 1.1 DSC of 3501-6 Epoxy

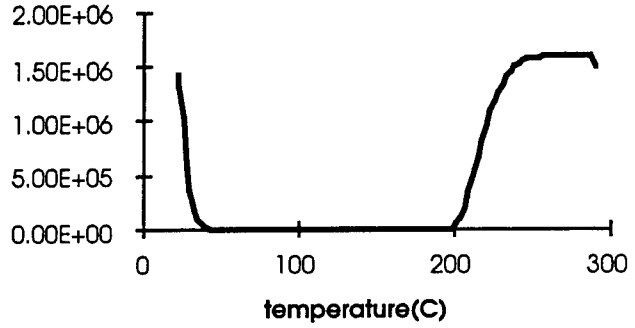

Figure 1.2 Rheometrics of 3501-6

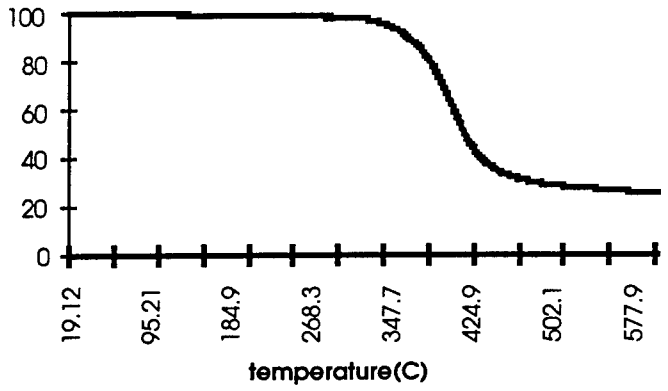

Figure 1.3 TGA of 3501-6

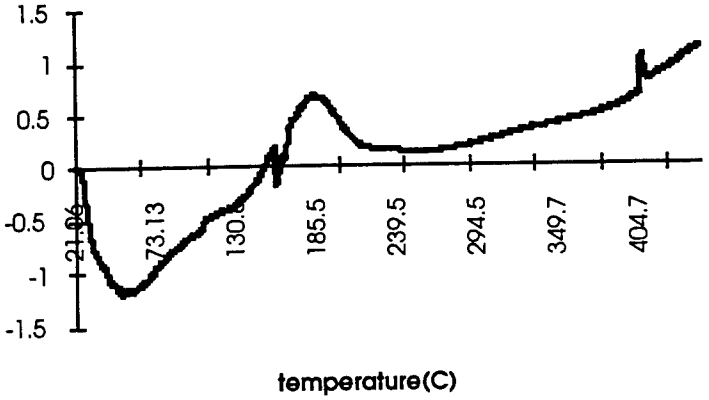

Figure 2.1 DSC of SC1008

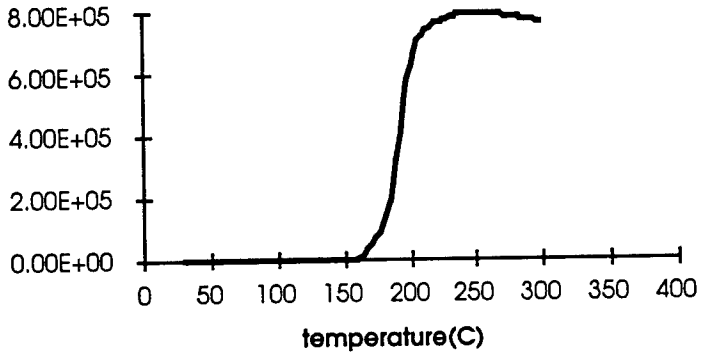

Figure 2.2 Rheometrics of SC1008

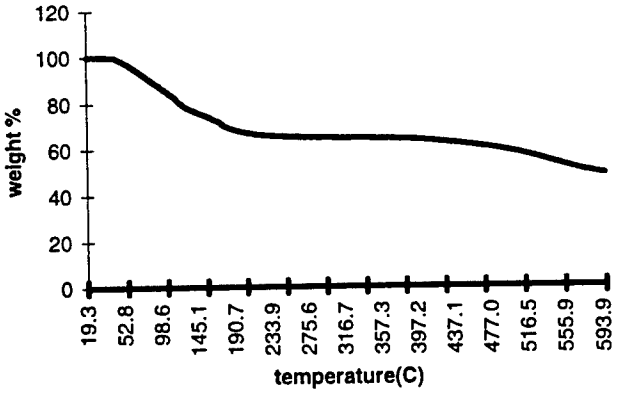

Figure 2.3 TGA of SC1008

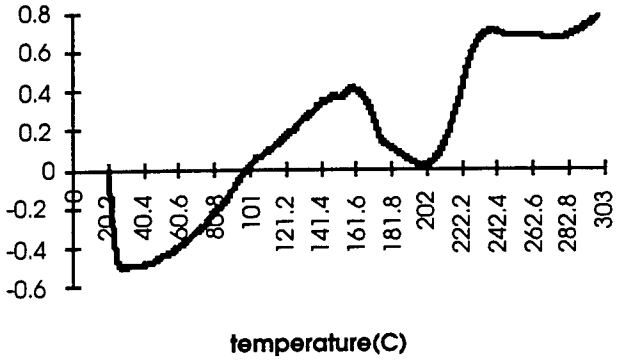

Figure 4.1 DSC of ACP

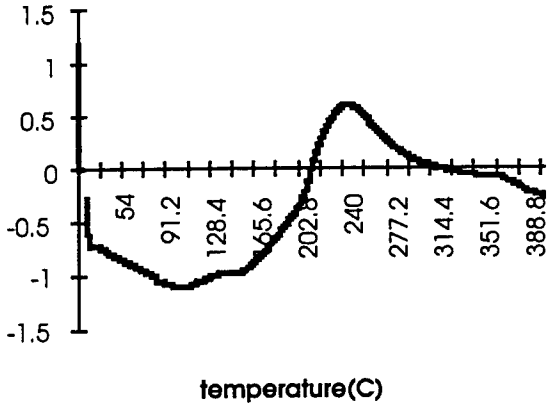

Figure 4.2 DSC of 3:1 A:PCP

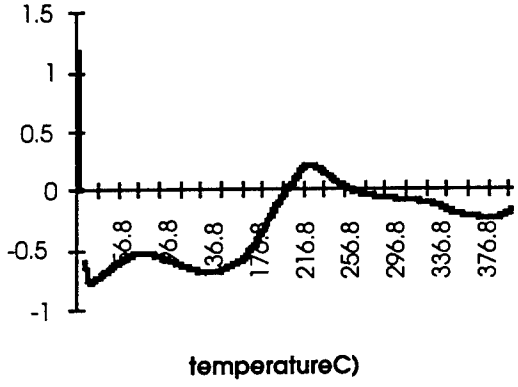

Figure 4.3 DSC of 1:1 A:PCP

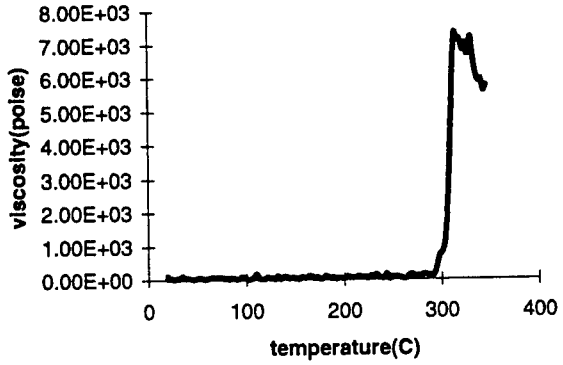

Figure 5.1 Rheometrics of ACP

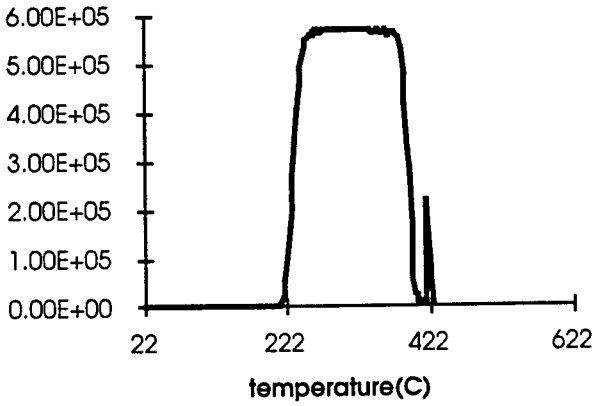

Figure 5.2 Rheometrics of 3:1 A:PCP

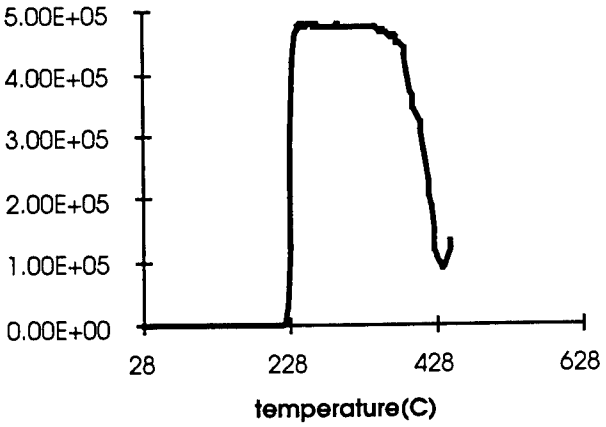

Figure 5.3 Rheometrics of 1:1 A:PCP

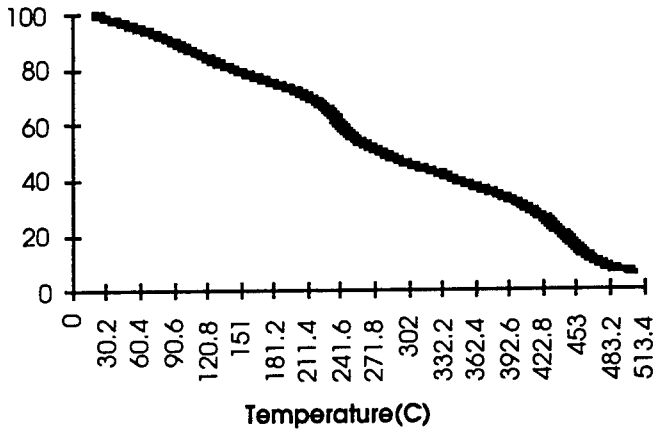

Figure 6.1 TGA of ACP

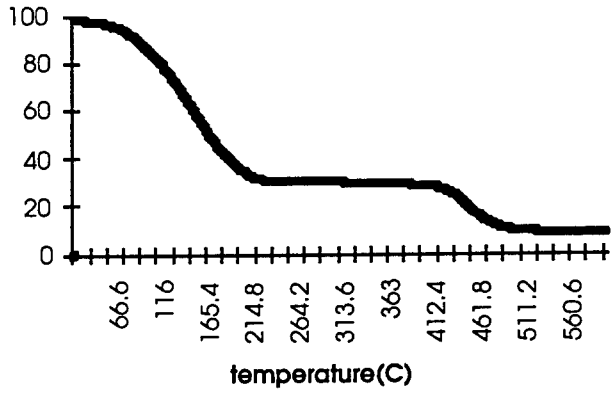

Figure 6.2 TGA of 3:1 A:PCP

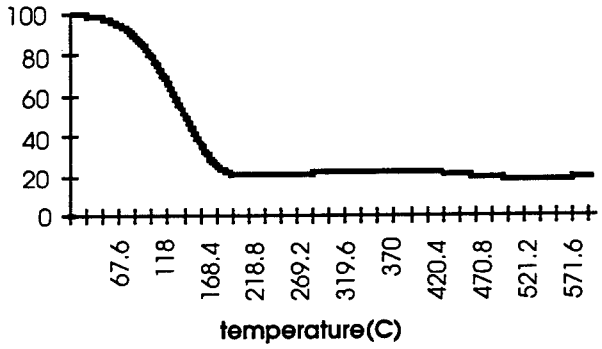

Figure 6.3 TGA of 1:1 A:PCP

References

1. Stoll K. Dirlikov, Chemtech, 32, (1942).

2. L. J. Mathias and J. Muthiah, Polymer Composites, 464, (1994).

3. D. Anderson, 21st Annual Conference on Composites, Materials and Structures(1997).

A STUDY OF THE PARTICULATE EMISSIONS OF A WELL-STIRRED RACTOR

Melissa R. Wilson
Graduate Student
Cloud and Aerosol Sciences Laboratory

University of Missouri, Rolla
G-7 Norwood Hall
Rolla, MO 65409-0430

Final Report for:
Graduate Student Research Program
Wright-Patterson AFB, Wright Laboratories

Sponsored by:
Air Force Office of Scientific Research
Bolling Air Force Base, DC

and

Wright Laboratories

September 1997

A STUDY OF THE PARTICULATE EMISSIONS OF A WELL-STIRRED REACTOR

Max B. Trueblood
Research Assistant Professor
Melissa R. Wilson
Graduate Student
Cloud and Aerosol Sciences Laboratory

Abstract

A well-stirred reactor system was constructed and a preliminary study of its particulate emissions was made using the University of Missouri-Rolla Mobile Aerosol Sampling system. The test matrix included hydrogen and hydrocarbon fuels where the fuel to air equivalence ratios were varied between lean stoichiometric and rich. Preliminary results indicate that particulate concentrations increased by several orders of magnitude as the equivalence ratio approached 1.0 compared to those for either lean or rich regimes. The size distributions were linear in shape between particle diameters of 10 and 250nm, with the peak at the smaller diameter. Results from this preliminary study were presented at the NASA Workshop on Aerosols, Cleveland Ohio, July 29-30 1997.

A STUDY OF THE PARTICULATE EMISSIONS OF A WELL-STIRRED REACTOR

Melissa R. Wilson

Introduction

The emission of particulates from jet engines has received significant interest from the atmosphere and emissions scientific community in recent years. Earlier this year, the EPA released a call-to-arms for particle characterization, citing the detrimental effects of small particulates on the human body[1-2]. This study was undertaken to examine the feasibility of using a well-defined laboratory experiment to represent data obtained from actual aircraft emission measurements, and to possibly provide a fuel formulation-based particle emission mitigation strategy. The Well-Stirred Reactor (WSR) was chosen as an appropriate lab-based test venue because it is currently the closest approximation available to an ideal, Perfectly-Stirred Reactor (PSR) i.e. a reactor in which mixing and transport effects have been minimized.

The data obtained at Wright-Patterson Air Force Base (WPAFB) this summer is an integral part of a much larger data set acquired with the University of Missouri, Rolla Mobile Air Sampling System (UMR/MASS) and other aerosol diagnostic tools employed as part of the following NASA sponsored projects: airborne field campaigns SONEX, POLINAT I & II, SNIFF and SUCCESS and ground-based measurement venues such as the AEDC and NASA LeRC PSL projects, SNIFF, and Air National Guard F-100 engine studies.[3-13]

Experimental

The UMR/MASS approach to aerosol characterization of combustion sources is well developed. A schematic diagram of the MASS is given in figure 1. It has been described extensively in the literature and has been used in many test venues. A description of the complete suite of measurements accessible with the UMR/MASS is given in Appendix 1. This preliminary study focused on total particle emissions as represented by the total differential concentration (TCN) and size distributions of particles emitted from the WSR using a range of fuels including H_2, CH_4, and Jet A. Additional data was collected on the soluble mass fraction, morphology, and elemental composition of the particle emissions.

The WSR (Figure 2) is a toroidal reactor in which the fuel is prevaporized and then premixed with air and injected into a toroidal combustion chamber. The fuel/air mixture undergoes tremendous turbulent mixing as combustion occurs. Characterization of mixing has been described elsewhere in the literature[14]. This stirring process makes the WSR a very good approximation of a PSR, and so a good model of ideal combustion conditions.

Progress

In the initial phase of this project, the final construction of the WSR was completed along with its interface to the UMR/MASS. Specifically the UMR team assisted Wright Lab personnel with the installation of (1) the oil-based temperature control system for the sampling probes; (2) the nitrogen delivery and control system; (3) the Horiba Emissions Analyzers, (4) type B, C and K thermocouples used in the experiment, and (5) the temperature control system for the heated

transfer lines used by UMR and Wright Labs. This installation process took approximately five weeks. All this installation work was essential prior to making particle measurements.

Calibration and Testing

When the reactor was completed, it was given several calibration runs, including one run with a 40% H_2 / 60% N_2 fuel, which was used to determine the system background particle emission level. The remaining calibrations used methane. Initial particle concentrations observed with methane were exceptionally high (30 million particles per cubic centimeter (pcc)); this was determined to be due to alumina particles baking off from the inside walls of the plug flow region (PFR). With continued heating of the internal surfaces of the reactor and the PFR these particle emissions were seen to fall to almost zero, at which point the tests began in earnest. Test fuels used were methane and Jet A. These fuels were varied in terms of fuel to air stoichiometric equivalence ratio ϕ at points below, at and above 1.

Results

Table 1

Fuel	Equivalence Ratio ϕ	TCN (particles pcc)
H_2N_2	1	3.07
CH_4	0.776	30,000
	1.00	1,700,000
	1.30	800,000
Jet A	1.00	18,000,000
	1.30	140,000,000

Discussion

The H_2/N_2 fuel mixture was studied approximately two weeks after the initial lighting of the WSR. Total particle concentrations, even at $\phi = 1$, were not above 5 particles pcc. This low concentration indicates little or no ablation occurred at the metal sampling probes which were inserted into the WSR. It also indicates no alumina was ablated off the ceramic lining in the WSR-PFR in the form of particulates, at least after the initial calibration runs with methane. In the hydrogen test the small concentrations precluded obtaining any meaningful size distribution data. It should be noted that the highest temperatures obtained with the hydrogen fuel were approximately 1000°C, much lower than the 1700°C typically seen during runs with methane and Jet A. Although a higher percentage of hydrogen would have yielded a higher temperature, this avenue was not pursued for safety reasons.

Methane was the most common fuel used during the present study because of cost, safety, and ease of use. A large set of this data was obtained: well over two hundred size distributions and more than thirty hours of total concentrations logged. The methane data presented in Table 1 were taken on 26 July, 1997 and are representative of data taken at other times. Inspection of Table 1 shows that as f increases from 0.776 to 1.3, the TCN goes from 30,000 to 1,700,000 to 800,000 pcc.

Size distributions obtained for methane (Figures 3 and 4) suggest high particle counts at the lower sizes, possibly even below 1 nm To increase the sampling range of the MASS at those particle sizes, another pump was added to the system early in the test program. This enabled

particle characterizations at very low particle sizes (below 10 nm). The distributions were almost linear on a log-log plot, indicating the highest concentrations at the lowest sizes, a result often seen in jet exhaust for more conventional fuels.

Jet A was found to have much higher TCN's than methane, by an order of magnitude or more. This was an expected result, as Jet A is a complex mixture of hydrocarbons, which have a high carbon to hydrogen ratio and thus a greater sooting capacity. Methane is the simplest hydrocarbon, having only a single carbon to four hydrogens, and thus less carbon and less soot production capacity per mole of fuel.

The size distributions obtained for Jet A (Figs. 5 and 6) indicate a higher mean particle diameter, and demonstrate a more "log-normal" shape than the methane distributions. The concentrations peaked at 20-30 nm as opposed to the 10 nm and lower peaks observed for methane.

Deliquescence data, used to determine the soluble mass fraction, was taken on both methane and Jet A, and is currently being analyzed.

Conclusions

The following conclusions can be drawn from this preliminary study:

1. The WSR can readily be interfaced to the UMR/MASS thus lending the WSR to MASS type analysis.

2. It was possible to passivate the alumina surfaces within the WSR-PFR to spurious particle production. This was achieved by burning methane in the WSR while monitoring the rate of change of particle emission. Passivation is achieved when the particle emission rate falls to a constant value for a given equivalence ratio and fuel flow rate.
3. Following passivation, background emissions observed using a hydrogen flame were negligible.
4. Particle concentrations varied as a function of fuel to air equivalence ratio peaking at stoichiometric ratios.
5. Particle concentrations varied with fuel formulation increasing with decreasing hydrogen carbon ratios.
6. Size distributions for methane are linear in shape with peaks at low particle sizes. Distributions for Jet A are closer to "log-normal" shape.
7. These preliminary results clearly demonstrate that a valuable database on particle emissions can be developed with further studies where the MASS is interfaced to a WSR.
8. These are first of a kind and unique data where particle emissions from a well defined laboratory burner have been physically characterized in terms of concentration, size distribution, hydration and growth properties and chemical composition.
9. The preliminary results of this study have been presented at the NASA Workshop on Aerosols, Cleveland Ohio, July 29-30 1997, and will be presented at the American Chemical Society Regional Meeting, October 29 - November 1, 1997.

Appendix 1

Aerosol characteristics accessible with the UMR/MASS.

Total Number Concentration N_{tot} - Because of the relative importance of this measurement total particle concentrations are determined by two methods. First, directly, by sending the incoming sample directly to a CN counter. This is a realtime measurement where all particles of effective diameters > 3nm are detected a minimum sample time of 1 sec. Secondly, the total aerosol concentration, N_{tot}, can be determined indirectly through the integral of the aerosol size distribution function (see subsection on size distributions below):

$$N_{tot} = \int_0^\infty (dN/dx)\, dx \qquad (1)$$

Excellent agreement between the direct measurement and size distribution function integration methods is achieved. These data with concomitant CO_2 measurements permit the calculation of the aerosol-related emission index (EI = #particles/kg fuel) for aerosols in any given sample taken from aircraft exhaust plumes or other combustion exhaust flow. The MASS has its own i.r. absorption CO_2 detector for realtime EI determination.

Non-Volatile Aerosol Concentration (N_{NVCN}) - This parameter is obtained both directly and indirectly as described for N_{tot} . In this case however the incoming sample is passed through an oven en-route to the CN counter. The temperature of the oven and the residence time of the

sample in the oven are controlled such that complete evaporation of all materials with boiling points below that of the oven temperature is assured. The incoming sample flow is split prior to the oven in order to permit simultaneous measurement of N_{tot} and N_{NVCN} and intercomparison of the two CN counters employed. The non-volatile component of the aerosol in exhaust flow is representative of the soot emissions of the source

Total Mass Concentration - Another primary aerosol parameter, total aerosol mass concentration, can likewise be extracted from the non-volatile CN size distribution, assuming an average density for soot:

$$M = \int_0^\infty \left(\frac{4\pi}{3} \right) \rho(x)\, x^3\, (dN/dx)\, dx \qquad (2)$$

This then, with concomitant CO_2 measurements permits the calculation of the mass-related emission index (EI=g aerosol/kg).

Size Distribution - The aerosol size distribution is an essential aerosol characteristic. The size distribution is the apportionment of aerosol into different size (diameter) categories. This is usually expressed in terms of the differential concentration, dN/dx, which normally is dependent on particle diameter x. (dN/dx)dx represents the particle concentration in the diameter range from x to x+dx.

Aerosol sizing in the diameter range 3nm - 300nm is achieved using differential mobility techniques. For diameters >300nm optical particle sizing techniques are employed.

Fixed Size Aerosol Concentration N_{FIX} - The differential mobility technique is also used to monitor, in real time, a fixed size aerosol. In this case the incoming sample is split of into another channel where a fixed diameter is selected through differential mobility analysis. This concentration is as described above using a CN counter.

Reactivity (Growth and/or Hydration Properties) - The growth and/or hydration properties of the aerosol must be characterized. These properties will control the ability of the aerosols to condense water or other species when they are exposed to moisture and other jet exhaust products. The total aerosol mass is subject to rapid changes in response to humidity variations. In turn this condensed water will control the chemical reactivity of the hydrated particle and influence its final evolution in the atmosphere. The hydration properties are usually represented in terms of the dry aerosol's soluble mass fraction (the fraction of the particle's total mass which is soluble in water) or critical supersaturation. A particle's critical supersaturation identifies the relative humidity (greater than 100%) which will cause the particle to become a freely growing droplet. Aerosol hydration properties are usually measured by observing the aerosol's response to different supersaturations in a cloud chamber, i.e. their critical supersaturation spectrum, or to 100% relative humidity conditions in a haze chamber, the deliquescence. The latter approach is employed in the MASS.

Threshold Soluble Mass Fraction Aerosol concentration N_{TSMF} - In this case the deliquescence technique is employed to monitor in real time the concentration of aerosols of fixed dry size that have a threshold soluble mass fraction.

Particle Morphology, Elemental Composition, and Molecular Composition - Other physical and chemical characteristics of the exhaust aerosols will be accessed. These will include Particle Morphology, Elemental Composition, and Molecular Composition. Here the strategy will be to collect aerosol samples on slides and/or filters for subsequent analysis, employing techniques such as SEM, FTIR microscopy and ultra-trace analysis separations mass spectroscopy, at analytical laboratories at UMR.

Acknowledgments

The authors would like to thank the following people for their help and support during this study: Cpt. Robert Mantz, Lt. Cary Baird, Dr. Melvin Roquemore, Mr. James Blust, Mr. Greg Tibbs, Mr. Greg Conrad *(AFWL)*, Dr. Philip Whitefield, Dr. Donald Hagen *(UMR)*, RDL.

References

1. http://www.c-ka.com/naaqs.htm

2. http://www.envirobiz.com/newsdaily/961202e1.htm

3. Hagen, D.E., and P.D. Whitefield, "Particulate Missions in the Exhaust Plume from Commercial Jet Aircraft Under Cruise Conditions", J. Geophys. Res. Atmos. 101, 19551-19557 (1996).

4. Arnold, F., J. Schneider, H. Schlager, P. Schulte, P. Whitefield, D. Hagen and P. Van Velthoven, "Observation of upper tropospheric sulfuric dioxide- and acetone-pollution: Potential implications for hydroxyl radical and aerosol formation", Geophys. Res. Letts. *24*, 57-60 (1997).

5. Schlager, H., P. Konopka, P. Schulte, U. Schumann, H. Zereis, F. Arnold, D. Hagen, P. Whitefield and J. Ovarlez, "In situ Observations of Air traffic Emission Signatures in the North Atlantic Flight Corridor", J. Geophys. Res. 102, 10739-10750 (1997).

6. Hagen, D.E., P.D. Whitefield and Max B. Trueblood, "Particulate Characterization in the Near Field of Commercial Transport Aircraft Exhaust Plumes Using the UMR-MASS". Proceedings of the "International Scientific Colloquium on the Impact of Emissions From Aircraft and Space Craft Upon the Atmosphere," Cologne Germany, April 1994.

7. Experimental Characterization of Gas Turbine Emissions at Simulated Flight Altitude Conditions. Ed. Robert Howard, AEDC TR-96-3 June 1996.

8. Pollution from Aircraft Emissions in the North Atlantic Flight Corridor, Contract no. EV5V-CT93-0310(DG 12 DTEE) Ed. U. Schumann, Commission of European Communities Final Report August 1996.

9. Whitefield, P.D., and D.E. Hagen, "Particulates and Aerosols Sampling from Combustor rigs Using the UMR MASS". AIAA 95-0111 33rd Aerospace Sciences Meeting, Reno January 1995.

10. Lilenfeld, H.V., P.D. Whitefield and D.E. Hagen, "Soot Emissions from Jet Aircraft". AIAA 95-0110 33rd Aerospace Sciences Meeting, Reno January 1995.

11. Whitefield, P.D., M.B. Trueblood and D.E. Hagen, "Size and hydration Characteristics of Laboratory Simulated Jet Engine Combustion Aerosols". Particulate Sci. and Tech. 11, 25, 1993.

12. Lilenfeld, H.V., P.D. Whitefield and D.E. Hagen, "Soot Emissions from Jet Aircraft". (ICAS-96-4.1.3) 20th International Council Aeronautical Science Congress/AIAA Aircraft Systems Conference, Sorrento Sorrento Italy, September 1996.

13. Whitefield, P.D., D.E. Hagen, J. Paladino, M.B. Trueblood, and H.V. Lilenfeld, "Ground-based Measurements of Particulate emissions from Sub-sonic and Super-sonic Transports" Proceedings of the 30th Section Anniversary Technical meeting Central State Section of the Combustion Institute: Combustion Fundamentals and Applications (Paper #39), St. Louis May 1996.

14. Blust J. W., D.R. Ballal, and G.J. Sturgess, "Emissions Characteristics of Liquid Hydrocarbons in a Well Stirred Reactor," AIAA Paper No. 97-2710, 1997.

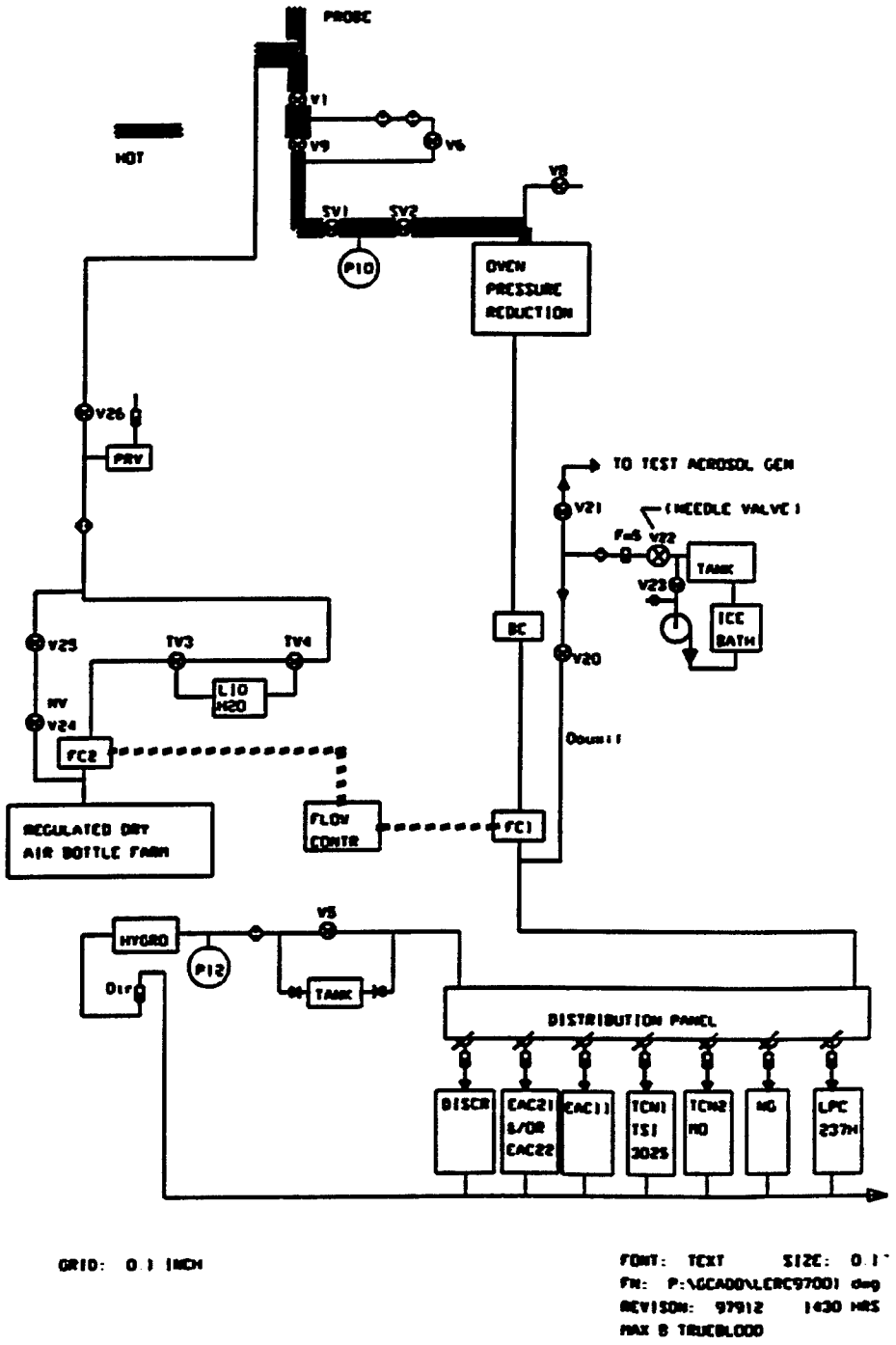

FIG 1. SCHEMATIC OF OVERALL AIR PLUMBING FOR UNIV OF MISSOURI - ROLLA MOBILE AEROSOL SAMPLING SYSTEM. MASS2. 97OCT.

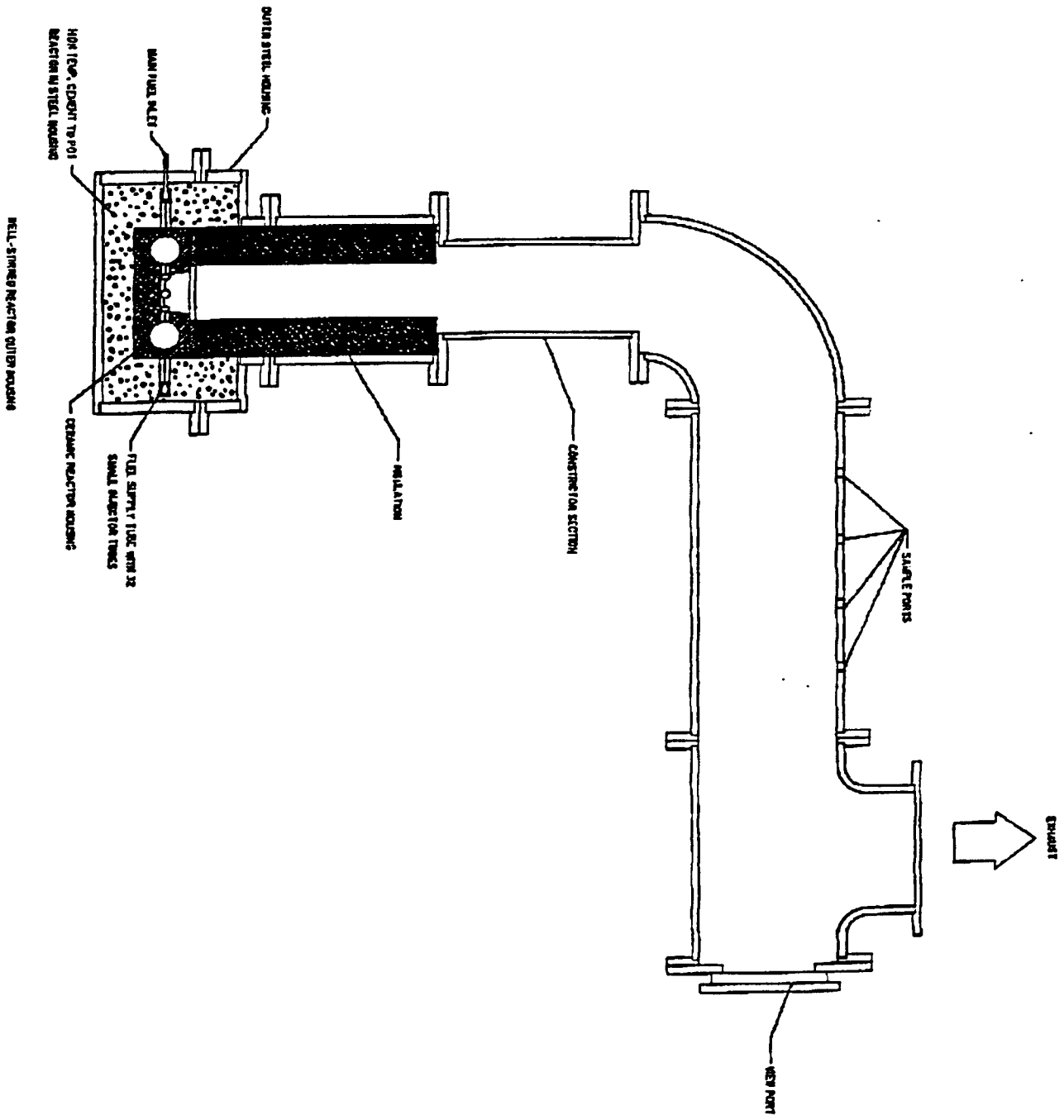
OUTER STEEL HOUSING
MAIN FUEL PELET
HOT TEMP. CEMENT TO FIX REACTOR IN STEEL HOUSING
WELL-STIRRED REACTOR OUTER HOUSING
CERAMIC REACTOR HOUSING
FUEL SUPPLY TUBE WITH 32 SMALL INJECTOR TUBES
INSULATION
COMBUSTION SECTION
SAMPLE PORTS
EXHAUST
USER PORT

Figure 2

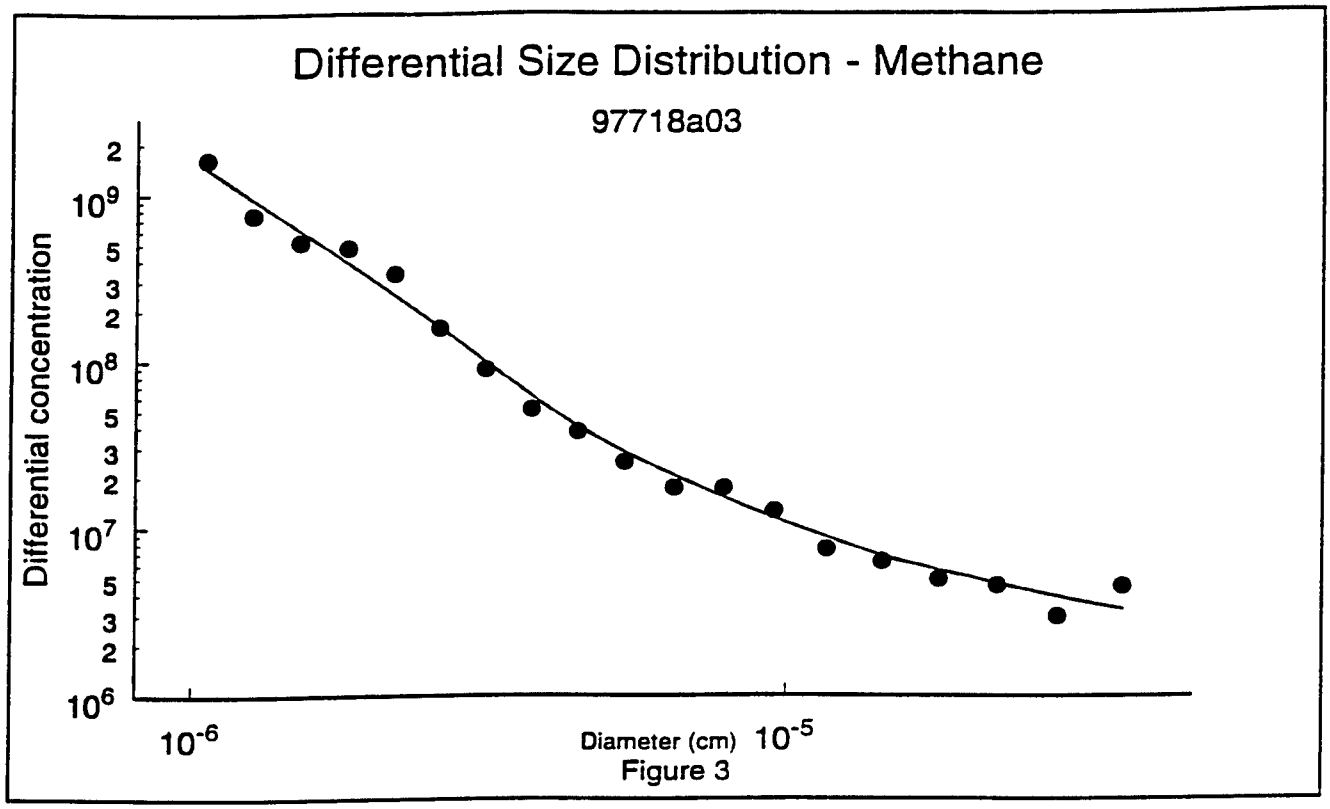

Figure 3

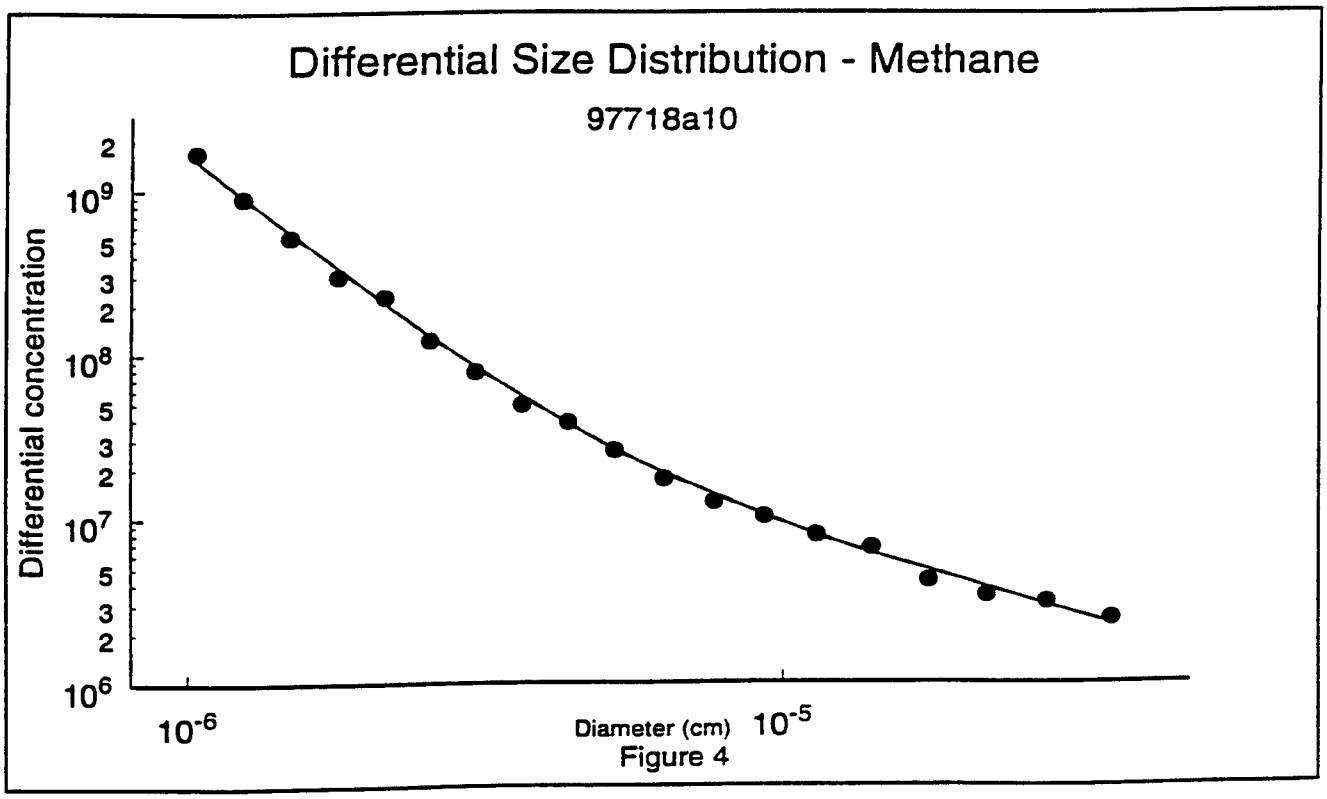

Figure 4

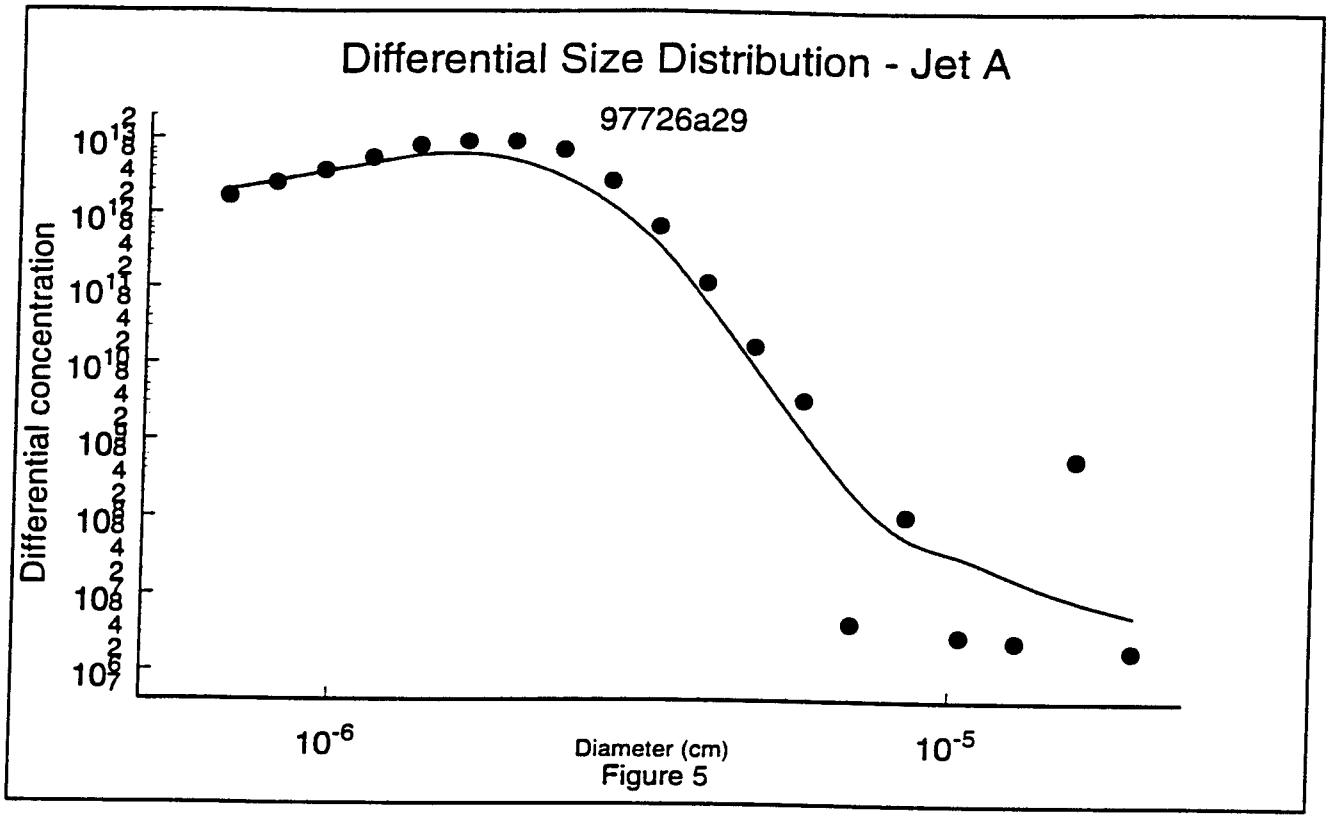

Figure 5

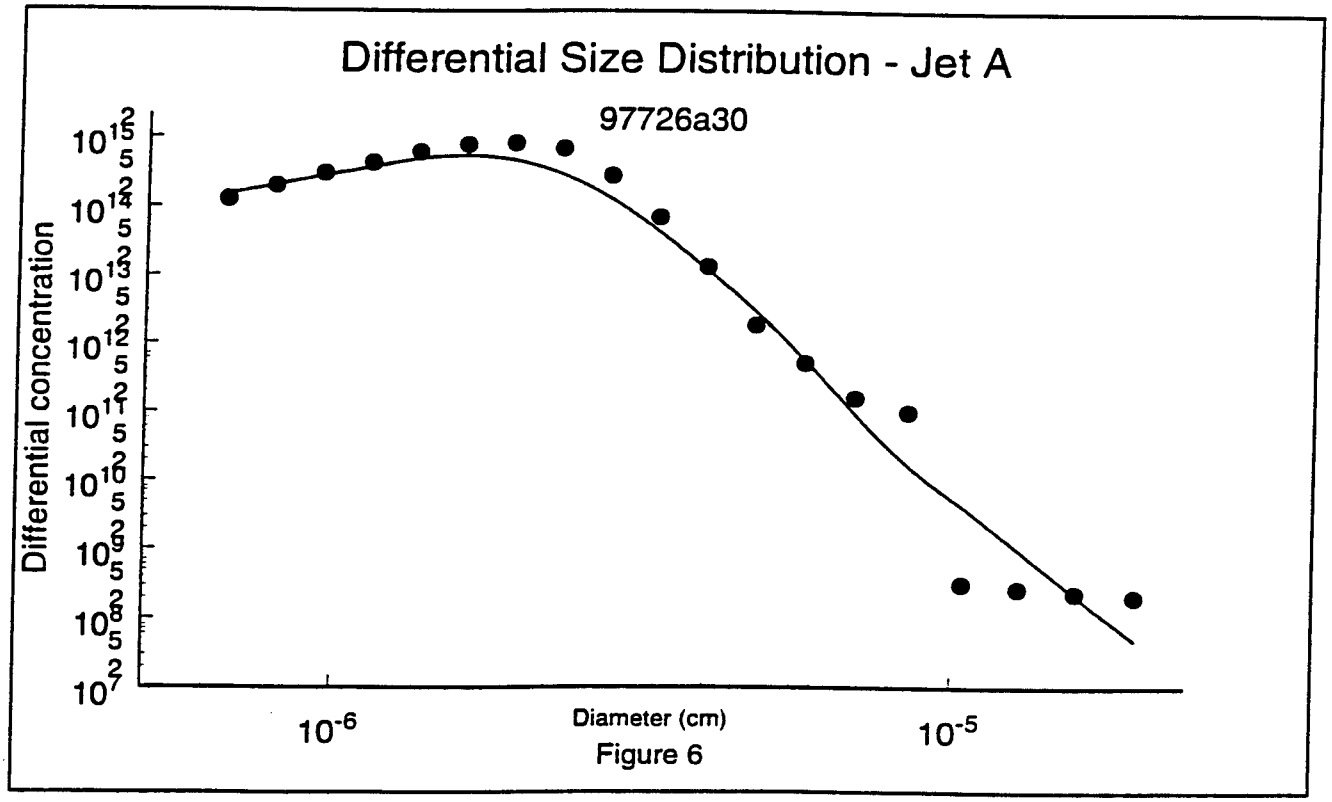

Figure 6

DEVELOP AN EXPLOSIVE SIMULATED TESTING APPARATUS FOR IMPACT PHYSICS RESEARCH AT WRIGHT LABORATORY

Sami Zendah
Graduate Student
Mechanical & Materials Engineering

Wright State University
3640 Colonel Glenn Highway
Dayton, Ohio 45435

Final Report for:
Summer Faculty Research Program
Wright Laboratory

Sponsored by:
Air Force Office of Scientific Research
Bolling Air Force Base, DC

and

Wright Laboratory

September 1997

DEVELOP AN EXPLOSIVE SIMULATED TESTING APPARATUS FOR IMPACT PHYSICS RESEARCH AT WRIGHT LABORATORY

Sami Zendah
Graduate Student
Mechanical & Materials Engineering
Wright State University

Abstract

The research task is intended to develop a simulated process that may be used to test different materials for resistance to failure from internal explosions. Theoretical derivations and analyses were made of the design of the test device. The equation for the stress intensity of multiple bar impact theory was evolved. The formula for reflective and transmitted stress intensity on varied areas for the impact was also derived. Three scaled down models were used to obtain pressure data in order to analyze the feasibility of the design, which will simulate the characteristics of the larger design. Various tests were conducted at Range A (Building 22B) of Wright Laboratory. An analysis was conducted in order to develop a full-scale model that will be eventually fabricated and tested.

DEVELOP AN EXPLOSIVE SIMULATED TESTING APPARATUS FOR IMPACT PHYSICS RESEARCH AT WRIGHT LABORATORY

Sami Zendah

Introduction

The use of real explosion processes to test plates of different materials for their resistance to failure is an expensive, time consuming, and hazardous task. The idea to develop a low cost and safe testing procedure to mimic a real explosion has been recommended by Dr. Arnold Mayer of Wright Laboratory. The purpose of this idea is to test plates of different materials for their resistance to failure when subjected to internal explosion. A good example to resist failure is the wing of an airplane to make up the fuel cell. To test the materials, a system is necessary which utilizes a cylindrical pressure tank. The tank will be filled with water, with a plunger in one end, and the test plate mounted on the opposite end. A stress pulse can be created by a projectile pressurized and released through a gun barrel that transmits the impulse to the water by striking the plunger in the cylinder.

As a preliminary step in this continuing project, three scaled-down devices were created to verify the feasibility of the full-scale test machine. The scaled-down devices were simplified, for it is only necessary to attain design parameters, not to test plates. The devices are composed of: 1) One piston and one projectile per test, 2) Three cylinders each with 0.5", 0.75" and 1.0" diameter bore, respectively, and 3) Two pressure transducers. These three cylinders were completely similar with exception of the internal diameter, or bore diameter. Three separate bore dimensions are necessary in order to study the effects of a smaller bullet striking larger plungers. Each cylinder configuration has a piston of the same diameter as its internal bore (i.e., 1/2", 3/4", and 1"). The pressure transducers were mounted in holes at the end and the side of each cylinder. The cylinder, bullets and pistons were all fabricated from carbon steel. The pressure transducers were purchased from Kistler.

A number of tests were conducted in the summer, ranging from low to medium projectile speeds, and from small pistons to large pistons at various helium pressures. Test data were analyzed and used for tuning the next tests. The results from the tests are to be utilized as the design criteria of the full-size impact machine.

Methodology

Figures 1 and 2 illustrate the testing system and the scaled-down cylinders. Each bored cylinder contains two mounting holes for pressure transducers (one on the sidewall and the other at the end), and two water holes on the top. Two types of pressure sensors from Kistler were used, one with a rated pressure of 15,000 psi and the other 70,000 psi. A transducer may require a high-insulation-resistance, a low-noise signal cable, a charge amplifier operating CHARGE mode. The system was connected to a Kontron data acquisition unit. A high-speed CCD camera and a VCR were used to record the impact between the bullet and plunger. Two different mounting schemes were recommended in Kistler's operation manual (see Figure 3). For real explosions where high-speed particles may be created, **Recess Mounting** should be utilized. In the earlier tests, the cylinders were fabricated based on this arrangement. **Flush Mounting** was later recommended due to the fact that there were no particles generated in the water during testing. All three cylinders were later modified based on the Flush Mount requirements (see Figure 4).

The setup procedure for each test includes the following steps:

1. Mount and align the cylinder on the supporting structures,
2. Measure and record the dimension and weight of bullet and plunger,
3. Insert two-third length of plunger into the cylinder,
4. Insert the bullet into the gun barrel until it reaches the front end,
5. Fill the water using the top holes into the cylinder until overflow,
6. Use set screws to cover and seal both water holes,
7. Connect the pressure transducers to the charge amplifier and check the setup,
8. Open the helium valve on the supply line of gun barrel,
9. Setup the high-speed camera on the PLAY mode,
10. Evacuate personnel to control room and close the security door,
11. Set the helium pressure to a desired value,
12. Setup the Kontron parameters: sampling times, channels, lasers, voltage levels, offsets, etc.,
13. Turn the security key, arm the system and shot the gun,
14. Calculate the bullet speed using $v = \Delta L/\Delta t$, where ΔL is the distance of two lasers, and Δt is the measured time between the lasers,
15. Zoom and examine the time history of each transducer channel and record the pressure data.

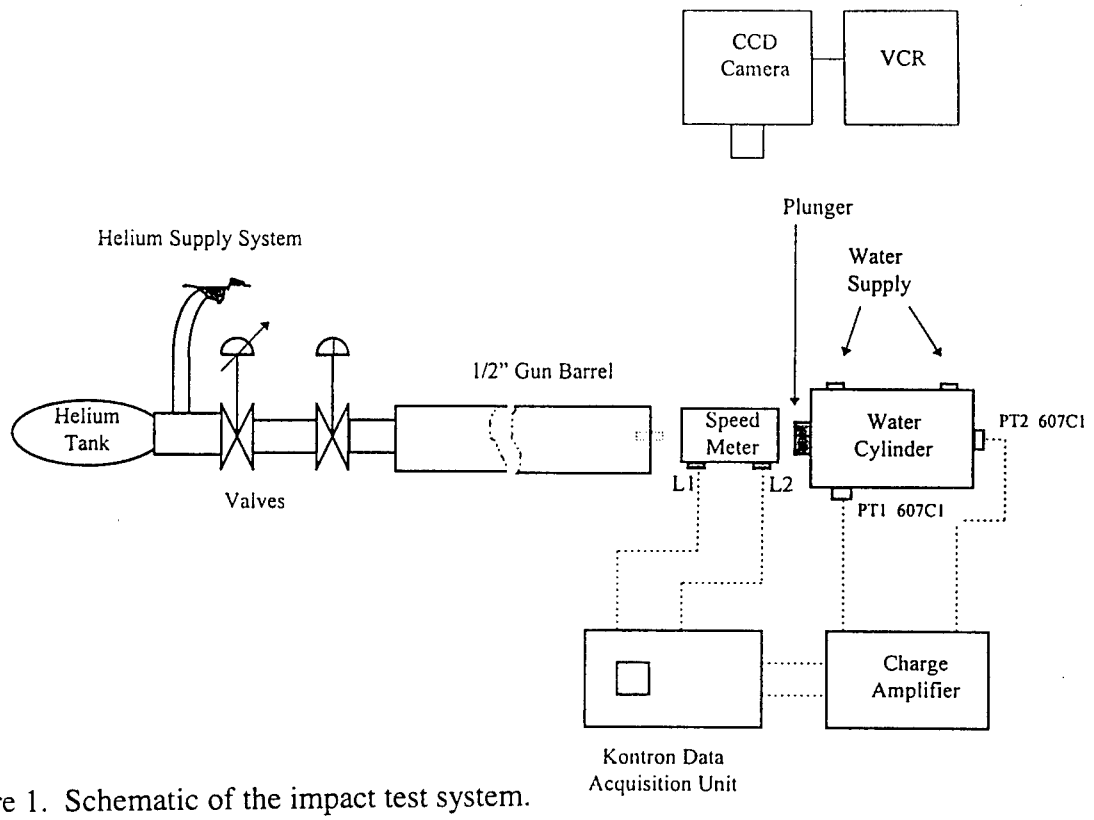

Figure 1. Schematic of the impact test system.

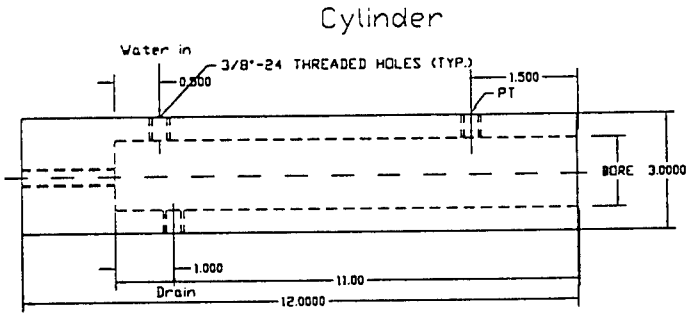

Figure 2. Original design of water cylinders.

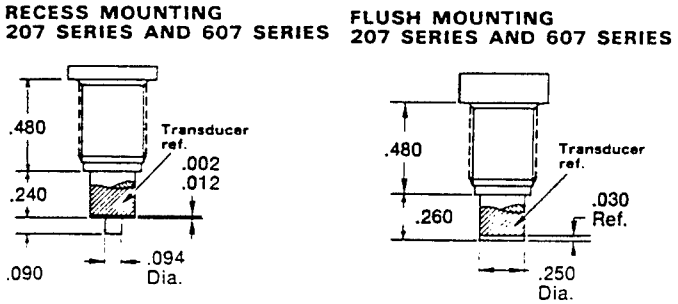

Figure 3. Pressure transducer mountings.

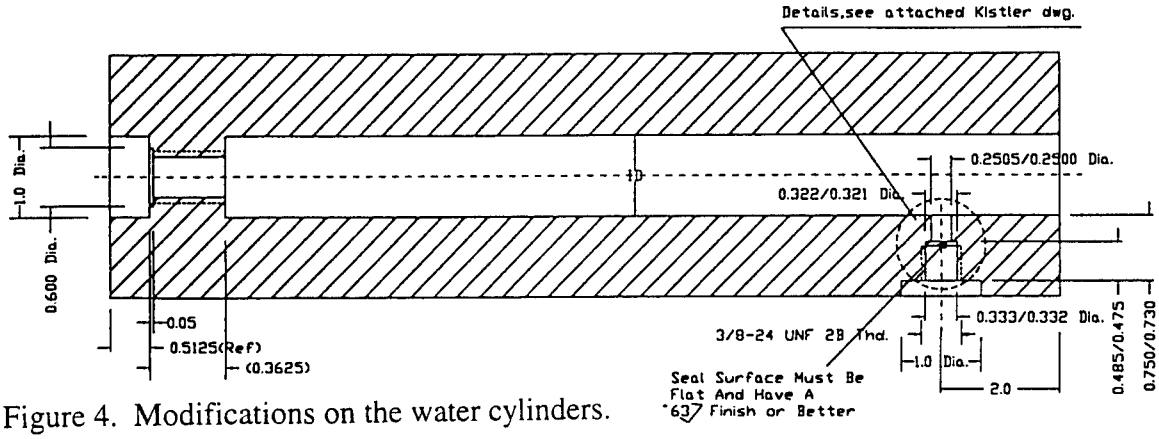

Figure 4. Modifications on the water cylinders.

Calculation of Cylinder Stresses

Denote the outer and inner radii as r_o an r_i, and the internal pressure as p_i, the radial and tangential stresses may be expressed as follows [1]:

$$\sigma_t = \frac{r_i^2 p_i}{r_o^2 - r_i^2}\left(1 + \frac{r_o^2}{r^2}\right) \tag{1}$$

$$\sigma_r = \frac{r_i^2 p_i}{r_o^2 - r_i^2}\left(1 - \frac{r_o^2}{r^2}\right) \tag{2}$$

Since both have maximum values at the inner surface, by substituting $r = r_i$ yields the maximum radial and tangential stresses as shown in Table 1.

Table 1. Max. tangential and radial stresses of the scaled-down cylinder models, (p_i = 10,000psi, r_o = 1.5"), material yield strength σ_y = 32,000 psi.

Stresses / r_i (Bore)	Tangential Stress (psi), σ_t	Radial Stress (psi), σ_r
0.250	10,570	-10,000
0.375	11,333	-10,000
0.500	12,500	-10,000

For a regular carbon steel with S_y = 32,000 psi, the above design is quite safe. For a small outer diameter (say d_o = 2.5"), the tangential stress will become 11,330, 13,270, 16,670 psi, respectively, with a safety factor of nearly 2.

Impact Theory

From the measured explosion data, the water pressure generated in the cylinder should rises up to 10,000 psi within 10 μsec and drops to 500 psi within 100 μsec. The theory used to obtain the conclusions of this section are an extension of theory derived about elementary one-dimensional elastic stress waves in long uniform bars due to impact [2,3]. The assumptions acquired narrow the scope of analysis to the coaxial collision of four bars of identical cross-sectional area but unequal impedance: an example of energy and momentum transmission. For the report, the initial assumptions were used:

- Identical cross-sectional area but unequal impedance ($\rho_o c$)
- Constrained with the condition that $l_1/c_1 = l_2/c_2 = l_3/c_3 = T$ (where l = length of a bar, and c = speed of the longitudinal stress wave in the material)

Figures 5(a) and (b) show the stress and speed situation at time $t=0$ and $t=T$. The compressive force and hence stress at the interface between the first and second bar during the period $0<t<T$ is the same in both bars. Denote the initial velocity of bar 1 is v_o, the following are the stresses at each interval. In period 1, $0 < t < T$:

$$\sigma_1 = \rho_1 c_1 (v_o - v_2) \tag{3}$$

$$\sigma_2 = \rho_2 c_2 v_2 \tag{4}$$

where both stresses are assumed to be the same, i.e., $\sigma_1 = \sigma_2$. v_2 is the particle speed in the second bar when supporting the stress σ_2. Hence,

$$v_2 = \frac{\rho_1 c_1}{\rho_1 c_1 + \rho_2 c_2} v_o \tag{5}$$

and

$$\sigma_2 = \sigma_1 = \frac{\rho_1 c_1 \rho_2 c_2}{\rho_1 c_1 + \rho_2 c_2} v_o \tag{6}$$

The head of the stress wave in each of the first and second bars reaches the end of the bar opposite to that at which impact took place, at the same instant and after time T. In period 2, $T<t<2T$:

(i) The compressive wave in the first bar reflected from its free end after $t=T$, as an unloading wave of tension; the first bar is completely stress free at $t=2T$. But each particle of the bar will have a speed to the left, see Figure 5(c), of

$$v_2 - (v_o - v_2) = 2v_2 - v_o = (\rho_1 c_1 - \rho_2 c_2) v_o / (\rho_1 c_1 + \rho_2 c_2) \tag{7}$$

(ii) Because the stress at the interface between the second and third bars is the same and if v_3 denotes the particle speed in the third bar when stressed to the level σ_3

$$\sigma_2' = \rho_2 c_2 (v_2 - v_3) \tag{8}$$

$$\sigma_3 = \rho_3 c_3 v_3 \tag{9}$$

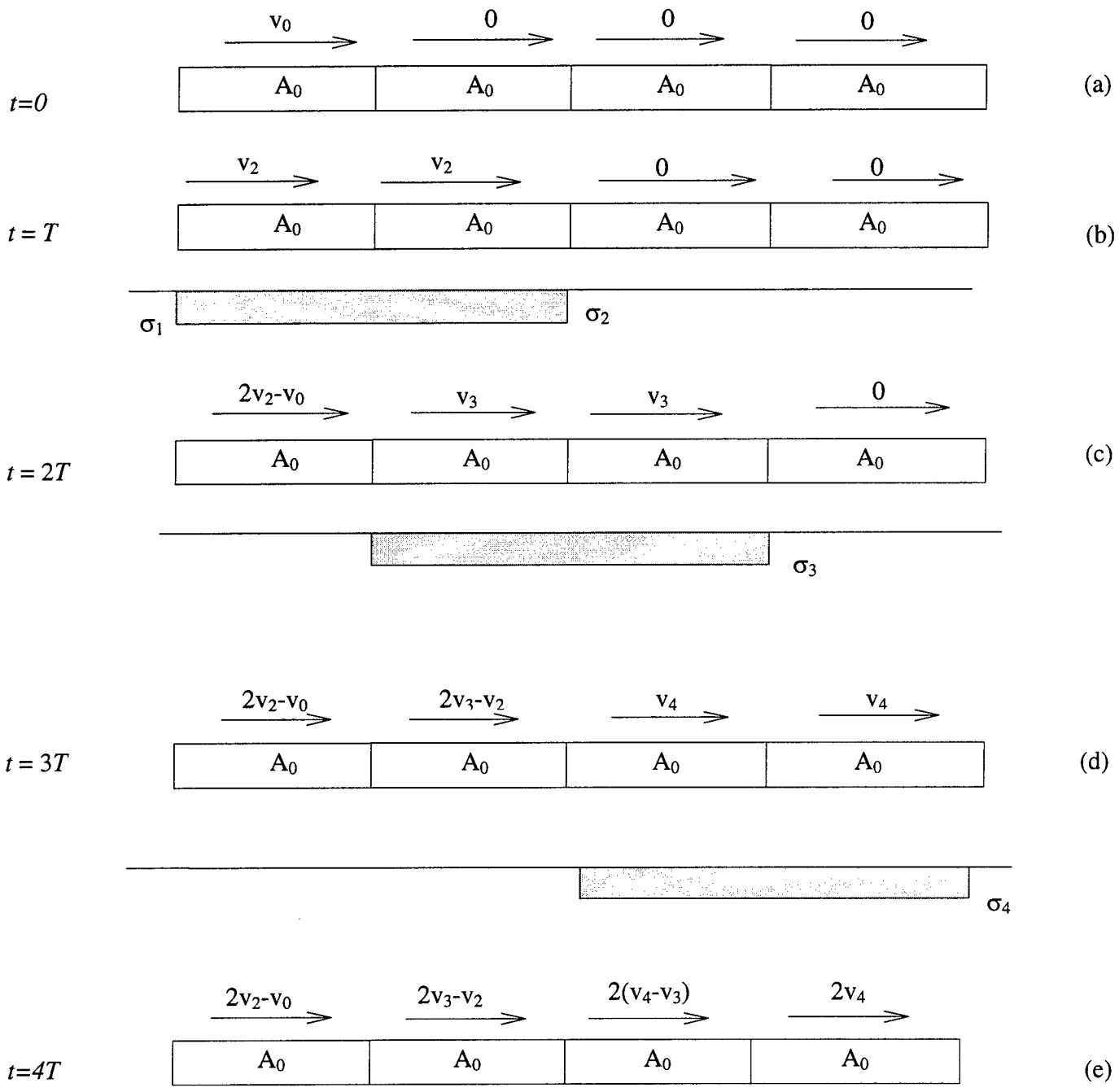

Figure 5. 4-bar impact diagram.

$$\sigma_3 = \sigma_2 + \sigma_2' \tag{10}$$

$$v_3 = \frac{2\rho_2 c_2}{\rho_2 c_2 + \rho_3 c_3} v_2$$

$$= \frac{2\rho_1 c_1 \rho_2 c_2}{(\rho_1 c_1 + \rho_2 c_2)(\rho_2 c_2 + \rho_3 c_3)} v_o \tag{11}$$

$$\sigma_3 = \frac{2\rho_1 c_1 \rho_2 c_2 \rho_3 c_3}{(\rho_1 c_1 + \rho_2 c_2)(\rho_2 c_2 + \rho_3 c_3)} v_o \tag{12}$$

The above 3-bar theory can be easily extended to obtain 4-bar equations, i.e. for the period $2T < t < 3T$, the wave from bar 3 reaches the interface of bars 3 and 4. Bar 4 will get a speed v_4, and a stress acting on the surface between bars 3 and 4 is

$$\sigma_3' = \rho_3 c_3 (v_3 - v_4) \tag{13}$$

$$\sigma_4 = \rho_4 c_4 v_4 \tag{14}$$

But $\sigma_4 = \sigma_3 + \sigma_3$ therefore,

$$v_4 = \frac{2\rho_3 c_3}{\rho_3 c_3 + \rho_4 c_4} v_3 = \frac{4\rho_1 c_1 \rho_2 c_2 \rho_3 c_3}{(\rho_1 c_1 + \rho_2 c_2)(\rho_2 c_2 + \rho_3 c_3)(\rho_3 c_3 + \rho_4 c_4)} v_o \tag{15}$$

$$\sigma_4 = \frac{4\rho_1 c_1 \rho_2 c_2 \rho_3 c_3 \rho_4 c_4}{(\rho_1 c_1 + \rho_2 c_2)(\rho_2 c_2 + \rho_3 c_3)(\rho_3 c_3 + \rho_4 c_4)} v_o \tag{16}$$

Stress Transmission in Varied Cross Sections

Use an approach concerning longitudinal wave propagation and consider the momentum to acquire a relationship between stress and area (see Figure 6).

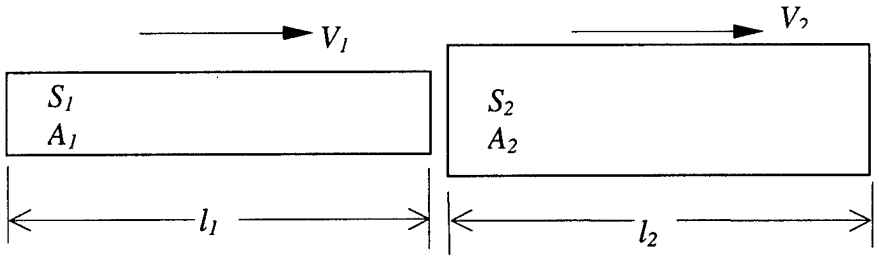

Figure 6. Bar S_1 and S_2 coaxial impact ($A1 \neq A2$, $v_1 > v_2$).

Let u_o be the speed common to both bars after S_1 and S_2 coaxial impact. The force acting on both bars at the common interface is the same. Denote σ_1 and σ_2 the stresses generated, then

$$A_1\sigma_1 = A_2\sigma_2 \tag{17}$$

and

$$A_1\,\rho_1\,c_1(v_1 - u_o) = A_2\rho_2 c_2(u_o - v_2) \tag{18}$$

It yields

$$u_o = \frac{v_2 + \dfrac{A_1\rho_1 c_1}{A_2\rho_2 c_2}v_1}{1 + \dfrac{A_1\rho_1 c_1}{A_2\rho_2 c_2}} \tag{19}$$

It is now straightforward to calculate σ_1 and σ_2 resulting in

$$\sigma_1 = \frac{\rho_1 c_1 v_1}{1 + \dfrac{A_1\rho_1 c_1}{A_2\rho_2 c_2}}\left[1 - \frac{v_2}{v_1}\right] \tag{20}$$

and

$$\sigma_2 = \frac{\rho_2 c_2 v_2}{1 + \dfrac{A_1\rho_1 c_1}{A_2\rho_2 c_2}}\left[\frac{v_1}{v_2} - 1\right]\frac{A_1\rho_1 c_1}{A_2\rho_2 c_2} \tag{21}$$

Assume $\rho_1 c_1 = \rho_2 c_2 = \rho\, c$, and define the area ratio as $\mu = A_1/A_2$, then

$$u_o = \frac{v_2 + \mu v_1}{1 + \mu} \tag{22}$$

If the starting speed of bar S_2 is zero (i.e., $v_2 = 0$),

$$u_o = \frac{\mu}{1 + \mu}v_1 \tag{23}$$

then,

$$\sigma_1 = \rho c v_1 \frac{1}{1 + \mu} \tag{24}$$

$$\sigma_2 = \rho c v_1 \frac{\mu}{1 + \mu} \tag{25}$$

Now consider an incident elastic wave of compressive stress of intensity $\boldsymbol{\sigma_I}$ moving to the right (See Figure 7), through a stationary bar of material S_1 of cross-sectional area A_1. The stress is partially transmitted and partially reflected at the surface of discontinuity AB where the second

bar of material S_2 and cross-sectional area A_2 is perfectly attached to S_1. Note that if A_2 were zero the wave would be wholly reflected while if S_1 and S_2 were identical the wave would be wholly transmitted. Since S_1 and S_2 are of different areas and materials, then, at AB, the incident wave must be both reflected and transmitted.

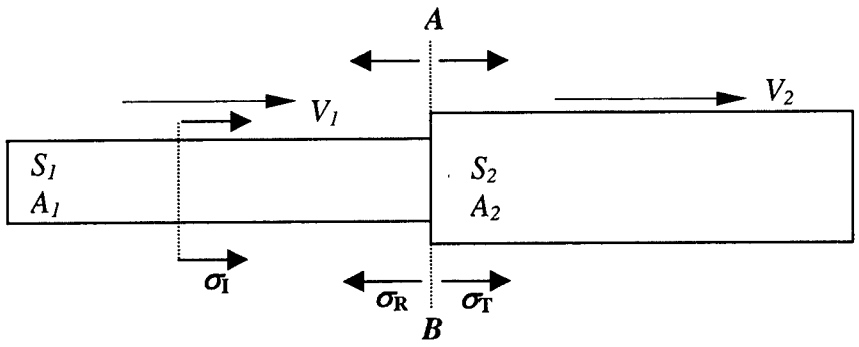

Figure 7. The relationship of σ_I, σ_T, and σ_R in elastic wave transmission.

The transmitted stress wave intensity through S_2 is defined as σ_T, and that reflected back through S_1 is σ_R. With $\sigma_o=\rho_o c_L v_o$, it may be found that the conditions to be satisfied at AB are: (1) The force on plane AB acting on S_1 and S_2 are at all the time equal; (2) The particle velocity in plane AB, in the material, for S_1 and S_2 are equal. If both σ_R and σ_T are taken to be compressive then

$$A_1(\sigma_I + \sigma_R) = A_2\sigma_T \tag{26}$$

Noting that σ_I and σ_R are associated with waves traveling in opposite directions, therefore,

$$v_I - v_R = v_T \quad \text{or} \quad \rho_1 c_1(\sigma_I - \sigma_R) = \rho_2 c_2 \sigma_T \tag{27}$$

in which v denotes the particle speed and subscripts I, R and T refer to the incidence, refection and transmission, respectively. Hence,

$$\sigma_R = \frac{A_2\rho_2 c_2 - A_1\rho_1 c_1}{A_2\rho_2 c_2 + A_1\rho_1 c_1}\sigma_I \tag{28}$$

$$\sigma_T = \frac{2A_1\rho_2 c_2}{A_2\rho_2 c_2 + A_1\rho_1 c_1}\sigma_I \tag{29}$$

In case same material is used, i.e., $\rho_1 = \rho_2$ and $c_1 = c_2$, the transmitted and reflective stresses may be simplified as

$$\sigma_R = \frac{1-\mu}{1+\mu}\sigma_I = \frac{A_2 - A_1}{A_2 + A_1}\sigma_I \tag{30}$$

$$\sigma_T = \frac{2\mu}{1+\mu}\sigma_I = \frac{2A_1}{A_2 + A_1}\sigma_I \qquad (31)$$

Empirical Data and Calculations

The data collected during testing at Wright-Patterson Range A are listed in full in the Appendix. The comparisons that follow show the relationships necessary to verify the feasibility of the full-scale test device. A tabulation of data acquired to show velocity relationships of the bullets to pressure is shown in the Appendix. These relationships were necessary to determine which pressures were required for the tests.

The data acquired from the tests are compared to theoretical calculations from the theory section in the Table 2 that follow. Figures 8, 9, and 10 show a graphical representation of the data.

Table 2. Comparison between empirical and theoretical data.

(a) 0.5" BULLET - 0.5" PISTON,

test date	bullet (ft/s)	measured σ (psi)	calculated σ (psi)	error (%)
7/23/97	182	10360	10926	5
7/23/97	190	9180	11446	20
7/23/97	186	10480	11176	6
7/24/97	267	18622	16069	16
7/24/97	193	13200	11590	14
7/24/97	183	9000	10994	18
8/20/97	180	13356	10799	24
8/20/97	186	16340	11184	46
8/20/97	189	14113	11373	24
8/20/97	153	9048	9192	2
8/21/97	168	13330	10116	32

(b)0.5" BULLET - 0.75" PISTON,

test date	bullet (ft/s)	measured σ (psi)	calculated σ (psi)	error (%)
7/24/97	182	7600	7285	4
7/24/97	191	7680	7666	0
8/19/97	183	12960	7325	77
8/19/97	220	12640	8822	43
8/19/97	202	17600	8120	117
8/19/97	180	20320	7238	181
8/20/97	185	11362	7427	53
8/20/97	182	11760	7284	61
8/20/97	211	14352	8477	69
8/20/97	197	0	7904	100

(c) 0.5" BULLET – 1.0" PISTON

test date	bullet (ft/s)	measured σ (psi)	calculated σ (psi)	error (%)
8/21/97	183	18235	5492	232
8/21/97	182	6909	5479	26
8/21/97	177	0	5324	100
8/21/97	188	6644	5654	17
8/22/97	190	6112	5724	7
8/22/97	170	10365	5118	103
8/22/97	171	11693	5137	128

Although some of the data were erratic due to the defective pressure transducers (15,000psi), it seems that the desired criteria can be reached. More tests will be needed in order to design a full-scaled model.

CONCLUSIONS AND SUGGESTIONS

A number of tests were conducted, ranging from low to medium high helium pressures, and from small to large plungers. The objective was intended to verify the impact theories, and to use the data as the design criteria for a full-scale cylinder model. Although the data acquired does not completely compare evenly with the theoretical calculations, a trend can be shown that follows the theory. The large discrepancy is partially due to the defective pressure transducers. It is also possible that the calibration and other technical errors within the data acquisition setup could cause this difference. Environmental factors and air in the water along with differences in the consistency of the other materials also add to error. In order to reduce the amount of air in the sensor area it is suggested that the sensor be mounted flush. A mobile support is also recommended, as to allow the placement of the sensors be changed to deal with the problem of air near the sensors. With all problems set aside, the full-scale project should proceed with the calculations provided from the scaling section. It is shown that all criteria are satisfied and the project is feasible. In summary, the following improvements are needed for accurate results:

(1) All pressure transducers used in the study should be calibrated to avoid uncertainties.

(2) A low-pass filter should be installed to eliminate unnecessary noise (see Appendix D).

(3) The Kontron acquisition unit should be calibrated (or upgraded) to prevent potential bias.

(4) A careful setup procedure is needed to avoid human errors that may induce testing errors. Typical example is the contamination in the transducer body and connectors.

(5) More tests are needed after the above conditions being corrected. The design of a full-scale model may include the parameters for pressure rise and decay time.

References

1. Shigley JE and Mischke CR, Mechanical Engineering Design, 5th Edition, McGraw-Hill, New York, 1989.

2. Meyers M, Dynamic Behavior of Materials, John Wiley & Sons, New York, 1994.

3. Johnson W, Impact Strength of Materials, Edward Arnold Ltd., London, 1972.

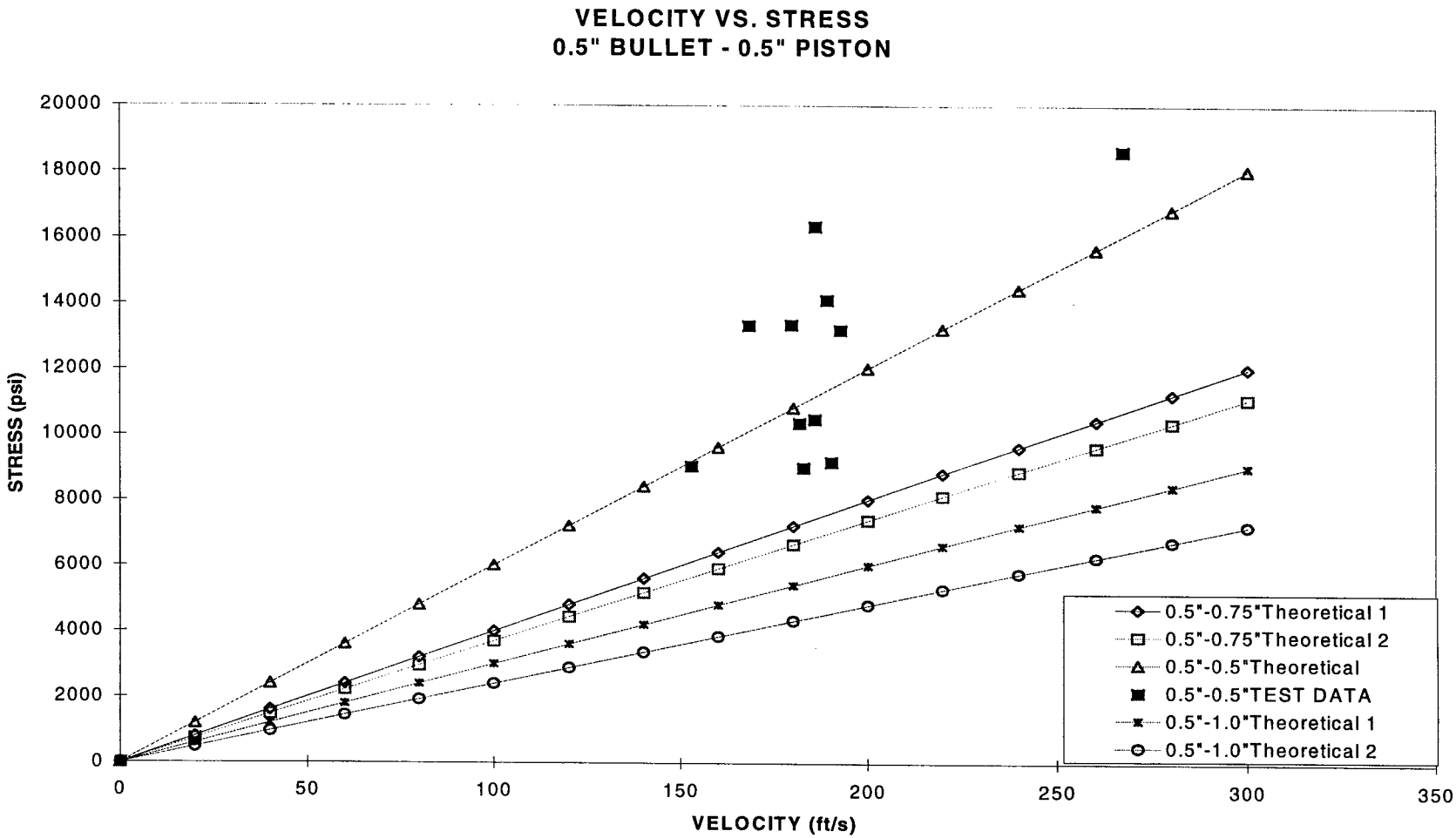

Figure 8. Comparison between empirical and theoretical data for 0.5"-0.5" impact.

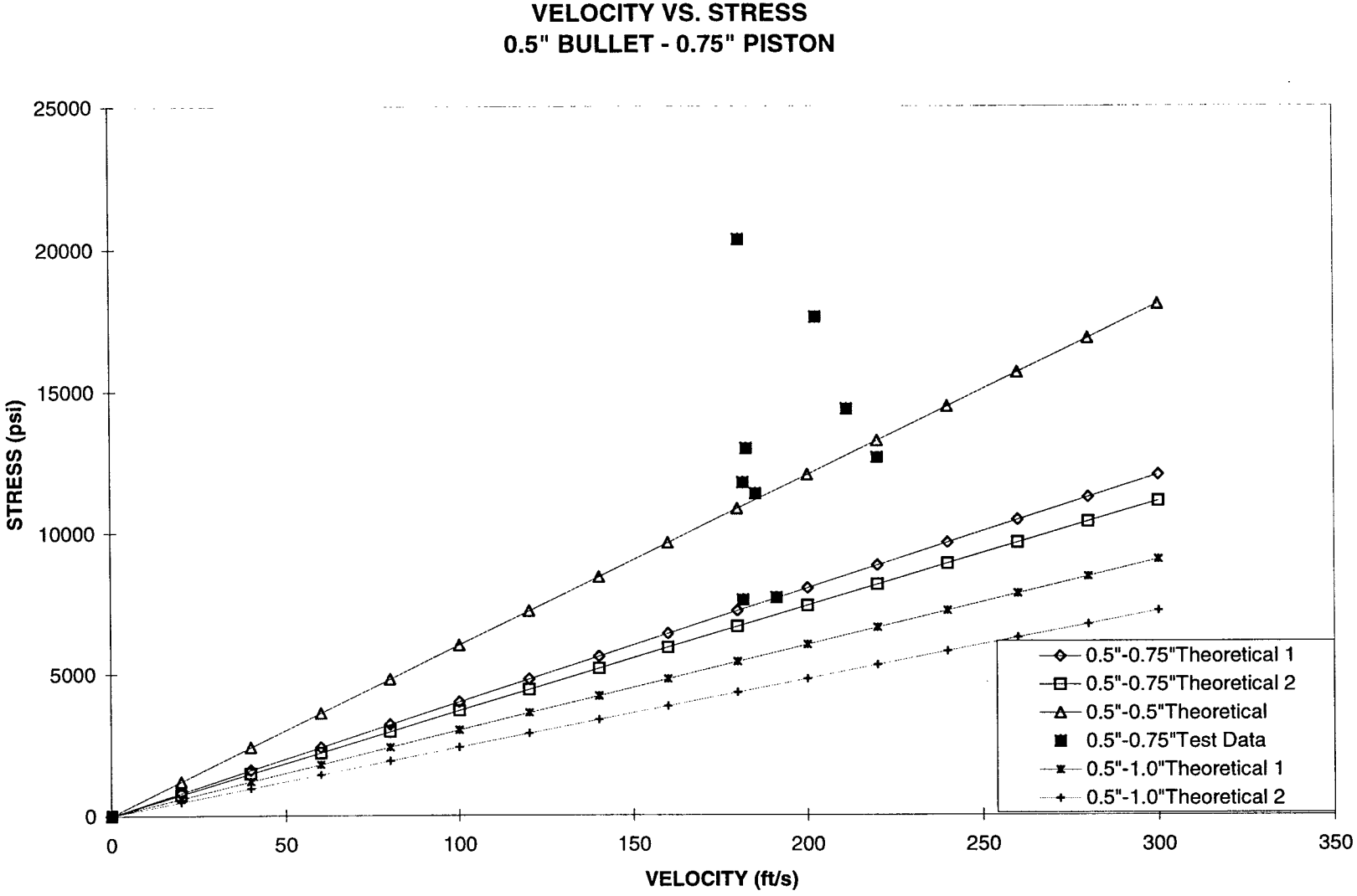

Figure 9. Comparison between empirical and theoretical data for 0.5"-0.75" impact.

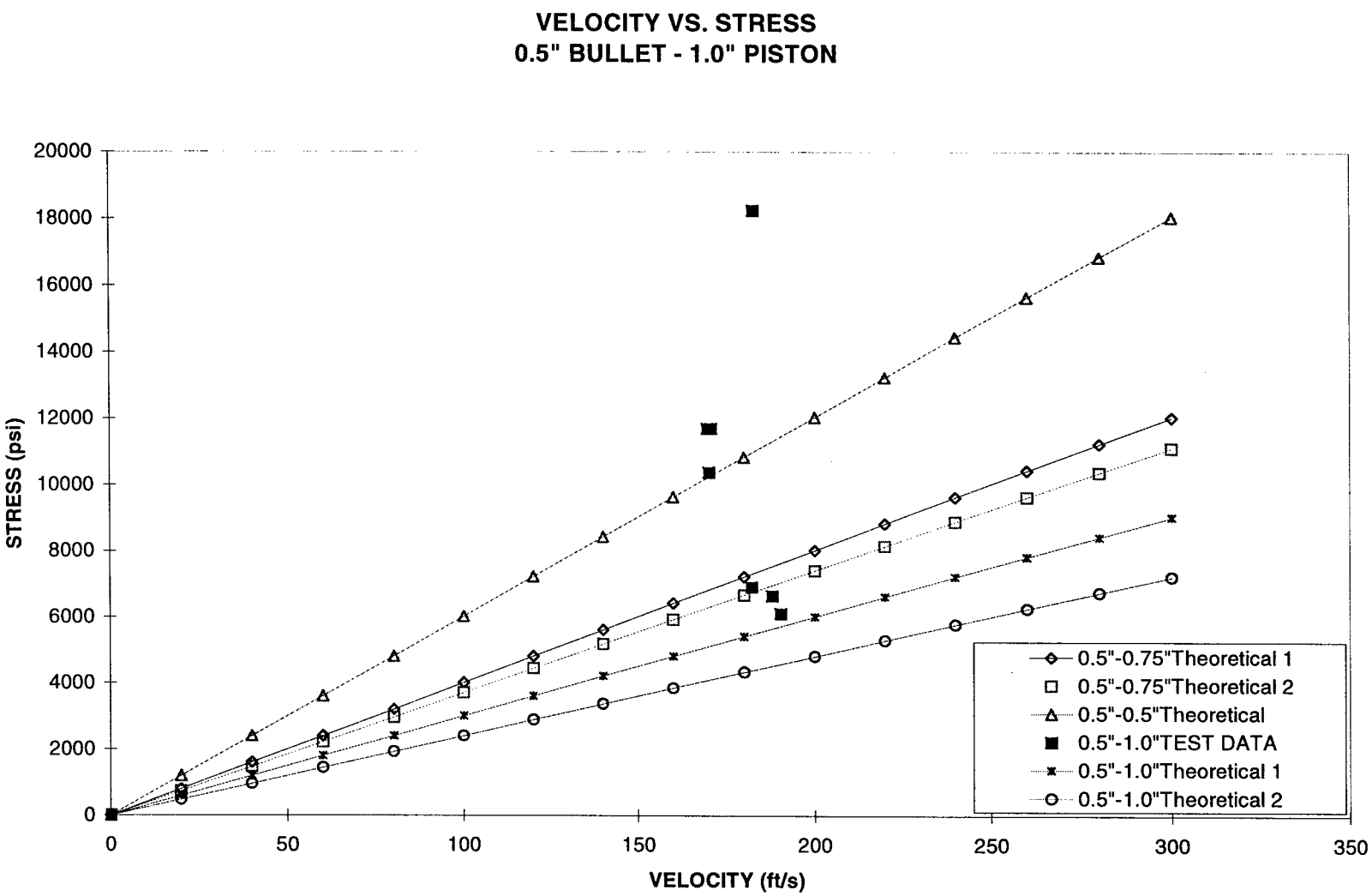

Figure 10. Comparison between empirical and theoretical data for 0.5"-1.0" impact.

Appendix A: Actual Testing Data

ACTUAL DATA

test date	test no.	BULLET dia.(in)	L (in)	mass (g)	PISTON dia.(in)	L (in)	mass (g)	B/P area ratio	pressure	1_2 v(ft/s)	1_2 TIME(ms)	Actual Stress in Water P.T. 1 (psi)	P.T. 2 (psi)
									0	0			
7/23/97	1	0.5	1.011	25.35	0.5	1	25	1	50.4	181.611	0.001606	10360	
7/23/97	2	0.5	1.015	25.45	0.5	1	25	1	50.2	190.259	0.001533	9180	
7/23/97	3	0.5	1.022	25.65	0.5	1	25	1	50.6	185.775	0.00157	10480	
7/24/97	1	0.5	1.512	38	0.5			1	125.8	267.094	0.001092	18622	
7/24/97	2	0.5	1.015	25.49	0.5			1	50.4	192.646	0.001514	13200	11000
7/24/97	3	0.5	1.02	25.6	0.5			1	50.1	182.749	0.001596	9000	15040
7/24/97	4	0.5	1.05	25.06	0.75	1.501	84.66	2.25	50.4	181.633	0.001606	7600	17741
7/24/97	5	0.5	1	24.84	0.75	1.526	85	2.25	60.2	191.131	0.001526	7680	
8/19/97	1	0.5	0.997	24.84	0.75	1.504	85	2.25	50.2	182.646	0.001597	12960	
8/19/97	2	0.5	0.998	24.99	0.75	1.525	85.13	2.25	70.4	219.96	0.001326	12640	
8/19/97	3	0.5	0.997	24.91	0.75	1.499	84.81	2.25	60.2	202.462	0.001441	17600	
8/19/97	4	0.5	1.005	25.27	0.75	1.506	85.23	2.25	70	180.476	0.001616	20320	
8/20/97	1	0.5	1	24.94	0.75	1.498	84.86	2.25	50.8	185.185	0.001575	11362	
8/20/97	2	0.5	1	24.99	0.75	1.498	84.86	2.25	50.2	181.622	0.001606	11760	
8/20/97	3	0.5	0.998	24.93	0.75	1.498	84.86	2.25	60.2	211.353	0.00138	14352	
8/20/97	4	0.5	0.998	24.94	0.75	1.499	84.85	2.25	60.2	197.072	0.00148		
8/20/97	5	0.5	0.995	24.95	0.5	1.5	37.52	1	50.8	179.5		13356	
8/20/97	6	0.5	1.002	25.09	0.5	1.499	37.54	1	50.2	185.9		16340	
8/20/97	7	0.5	1	25.03	0.5	1.504	37.55	1	50.3	189.038	0.001543	14113	
8/20/97	8	0.5	1.504	37.55	0.5	1.504	37.55	1	50.8	152.785	0.001909	9048	
8/21/97	1	0.5	1	25	0.5	1.5	37.58	1	50	168.146	0.001735	13330	
8/21/97	2	0.5	1	25	1	1.5	150.8	4	50.1	182.577	0.001598	18235	
8/21/97	3	0.5	1	25.02	1	1.504	151	4	50.4	182.15		6909	
8/21/97	4	0.5	1	25.28	1	1.5	150.77	4	50	177			
8/21/97	5	0.5	1	24.97	1	1.5	150.45	4	50.3	187.978	0.001552	6644	
8/22/97	1	0.5	1	25	1	1.5	150.8	4	50.5	190.296	0.001533	6112	
8/22/97	2	0.5	1.496	37.5	1	1.497	150.79	4	60.3	170.153	0.001714	10365	
8/22/97	3	0.5	1.497	37.49	1	1.5	150.17	4	60.3	170.775	0.001708	11693	
8/22/97	4	0.5	1.5	37.5	1	1.5	150.17	4	60.2	169.7		11690	

Appendix B: Theoretical Data

THEORETICAL DATA

test date	test no.	momentun p (g ft/S)	AREA REL stress in water (psi) th	stress in water (psi) M. Meyers	Stress in wa (psi)	error percentage		time for wave to travel 1l of water	2l of water	1l of bullet	1l of piston	barrel pressure (psi)	A1	A2
7/23/97	1	4603.829	10925.91892	10925.91892	10925.919	5.1796	5.1796002	0.0001711	0.00034228	4.9852E-06	4.93E-06	51.5	0.19635	0.19635
7/23/97	2	4842.085	11446.20077	11446.20077	11446.201	19.79872	19.7987159	0.0001711	0.00034228	5.0049E-06	4.93E-06	119.4	0.19635	0.19635
7/23/97	3	4765.127	11176.44954	11176.44954	11176.45	6.231402	6.23140238	0.0001711	0.00034228	5.0394E-06	4.93E-06		0.19635	0.19635
7/24/97	1	10149.57	16068.70493	16068.70493	16068.705	15.88986	15.8898622	0.0001711	0.00034228	7.4556E-06	0		0.19635	0.19635
7/24/97	2	4910.557	11589.8453	11589.8453	11589.845	13.89281	13.8928058	0.0001711	0.00034228	5.0049E-06	0		0.19635	0.19635
7/24/97	3	4678.363	10994.37706	10994.37706	10994.377	18.13997	18.1399732	0.0001711	0.00034228	5.0296E-06	0		0.19635	0.19635
7/24/97	4	4551.729	7284.85315	6724.479831	10927.28	4.326056	13.0198943	0.0001711	0.00034228	5.1775E-06	7.4E-06	45.25	0.19635	0.441786
7/24/97	5	4747.706	7665.804186	7076.126941	11498.706	0.185184	8.53394893	0.0001711	0.00034228	4.931E-06	7.52E-06		0.19635	0.441786
8/19/97	1	4536.915	7325.453809	6761.957362	10988.181	76.91737	91.6604809	0.0001711	0.00034228	4.9162E-06	7.42E-06		0.19635	0.441786
8/19/97	2	5496.795	8822.034078	8143.416072	13233.051	43.27761	55.217416	0.0001711	0.00034228	4.9211E-06	7.52E-06		0.19635	0.441786
8/19/97	3	5043.327	8120.239614	7495.605798	12180.359	116.7424	134.804237	0.0001711	0.00034228	4.9162E-06	7.39E-06		0.19635	0.441786
8/19/97	4	4560.619	7238.4241	6681.622246	10857.636	180.7241	204.117761	0.0001711	0.00034228	4.9556E-06	7.43E-06		0.19635	0.441786
8/20/97	1	4618.519	7427.3125	6855.980769	11140.969	52.97593	65.7239188	0.0001711	0.00034228	4.931E-06	7.39E-06		0.19635	0.441786
8/20/97	2	4538.732	7284.399519	6724.061095	10926.599	61.4409	74.8943062	0.0001711	0.00034228	4.931E-06	7.39E-06		0.19635	0.441786
8/20/97	3	5269.022	8476.824049	7824.760661	12715.236	69.30869	83.4177507	0.0001711	0.00034228	4.9211E-06	7.39E-06		0.19635	0.441786
8/20/97	4	4914.977	7904.065667	7296.060616	11856.099	100	100	0.0001711	0.00034228	4.9211E-06	7.39E-06		0.19635	0.441786
8/20/97	5	4478.525	10798.94101	10798.94101	10798.941	23.67879	23.6787939	0.0001711	0.00034228	4.9063E-06	7.4E-06		0.19635	0.19635
8/20/97	6	4664.231	11183.97289	11183.97289	11183.973	46.10193	46.1019278	0.0001711	0.00034228	4.9408E-06	7.39E-06		0.19635	0.19635
8/20/97	7	4731.62	11372.75636	11372.75636	11372.756	24.09481	24.0948066	0.0001711	0.00034228	4.931E-06	7.42E-06		0.19635	0.19635
8/20/97	8	5737.079	9191.736921	9191.736921	9191.7369	1.563762	1.56376234	0.0001711	0.00034228	7.4162E-06	7.42E-06		0.19635	0.19635
8/21/97	1	4203.659	10115.89172	10115.89172	10115.892	31.77286	31.7728616	0.0001711	0.00034228	4.931E-06	7.4E-06		0.19635	0.19635
8/21/97	2	4564.424	5492.026849	4393.621479	10984.054	232.0268	315.033477	0.0001711	0.00034228	4.931E-06	7.4E-06		0.19635	0.785398
8/21/97	3	4557.393	5479.184136	4383.347309	10958.368	26.09542	57.6192693	0.0001711	0.00034228	4.931E-06	7.42E-06		0.19635	0.785398
8/21/97	4	4474.56	5324.268966	4259.415173	10648.538	100	100	0.0001711	0.00034228	4.931E-06	7.4E-06		0.19635	0.785398
8/21/97	5	4693.811	5654.494	4523.5952	11308.988	17.49946	46.8743269	0.0001711	0.00034228	4.931E-06	7.4E-06		0.19635	0.785398
8/22/97	1	4757.4	5724.220585	4579.376468	11448.441	6.774362	33.4679523	0.0001711	0.00034228	4.931E-06	7.4E-06		0.19635	0.785398
8/22/97	2	6380.751	5118.317577	4094.654061	10236.635	102.508	153.134938	0.0001711	0.00034228	7.3767E-06	7.38E-06		0.19635	0.785398
8/22/97	3	6402.356	5137.017911	4109.614329	10274.036	127.6223	184.527916	0.0001711	0.00034228	7.3817E-06	7.4E-06		0.19635	0.785398
8/22/97	4	6363.75	5104.680472	4083.744377	10209.361	129.0055	186.256899	0.0001711	0.00034228	7.3964E-06	7.4E-06		0.19635	0.785398

Appendix C: Material data

material	C (in/s)	ρ (lbm/in^3)
steel	202800	0.28
water	55510.8	0.0361
aluminum	200400	0.096